Technical University of Liberec
Faculty of Mechanical Engineering

Diagnostic Tool for Initial Fixation of Acetabular Implant

Dissertation

Study programme:	2301-Mechanical Engineering
Study branch:	3901V003-Applied Mechanics
Author:	Ing. Petr Henyš
Supervisor:	doc. Ing. Lukáš Čapek Ph.D

Department of Applied Mechanics
Czech Republic
July 2015

Declaration

I hereby certify that I have been informed the Act 121/2000, the Copyright Act of the Czech Republic, namely §60-Schoolwork, applies to my master thesis in full scope. I acknowledge that the Technical University of Liberec (TUL) does not infringe my copyrights by using my thesis for TUL's internal purposes. I am aware of my obligation to inform TUL on having used or licensed to use my thesis; in such a case TUL may require compensation of costs spent on creating the work at up to their actual amount. I have written my thesis myself using literature listed therein and consulting it with my thesis supervisor and my tutor. Concurrently I confirm that the printed version of my thesis is coincident with an electronic version, inserted into the IS STAG.

Date:

Signature:

Acknowledgement

I would like to thank all people, who contributed to this work. Especially I would like to express huge thanks for my supervisor doc. Ing. Lukáš Čapek Ph.D for his patient supervising and rich advices. I would like to express a big thank Ing. Jaroslav Fencl and Pavel Čoupek for their help with experiments for this thesis. And last but not least, I would like to thank orthopedist Egon Prochazka for thoroughly performed total hip replacement in vitro for purpose of this work.

Poděkování

Na tomto místě bych rád poděkoval za trpělivé a cenné vedení doc. Ing. Lukáše Čapka Ph.D. Dále bych rád poděkoval všem co se na této práci podíleli, především pak Ing. Jaroslavovi Fenclovi a Ing. Pavlovi Čoupkovi z firmy Beznoska s.r.o za ochotu darovat implantáty totální kyčelní náhrady na experimenty a za přípravu těchto experimentů. V neposlední řadě bych rád poděkoval panu MUDr. Petrovi Hájkovi z Ústavu Anatomie lékařské fakulty Univerzity Karlovy V Hradci Králové za spolupráci při in vitro experimentech. Dále bych rád poděkoval panu ortopedovi MUDr. Egonovi Procházkovi z Ortopedie v Hradci Králové za in vitro operaci totální náhrady kyčelního kloubu na kádaverech.

Abstract

Initial fixation of cementless components of Total Hip arthroplasty (THA) plays a crucial role for long term survival of implant and the overall success of the surgical procedure. Every year a million of THA is performed and objective intra – operative assessment of initial fixation has not been available for clinical use yet. Currently, surgeons have to rely on their clinical experience, however they have a sophisticated screening method, but not suitable for intra operative assessment of initial fixation. They can use RSA, EBRA or the radiographic analysis for checking the healing process of implant, evaluating implant migration or bone resorption and osteolysis around the bone – implant interface. These methods are suitable for follow - up studies, but do not assist the surgeon during implantation process.

Vibrational analysis has been recognized as a promising tool in biomechanics to identify mechanical properties of bone structure, to assess the primary and secondary stability of dental implants and to evaluate fracture healing of bone. In literature some studies dealing with intra – operative initial fixation assessment during THA can be found. Most of them are focused on femoral stem fixation, although acetabular component (AC) fails with the same rate as femoral stem or even frequently. The main objective of proposed work is to investigate the ability of vibrational methods reflect the initial fixation of acetabular implant in some measurable quantity. The bone - implant interface is recognized as one of the potential candidates that would explain the changes in dynamic response of bone - implant system undergoes an ambient excitation. The bone - implant interface is investigated trough numerical modeling. In the experimental part of thesis, different pres fitting forces are compared with the dynamic response of bone - implant system. From numerical analysis it follows that there is a different level of relation between shared contact area and modal parameters of system. Experimental part shows also the relation between evaluation of fixation of implant and its response parameters.

Keywords:
implant fixation; acetabular cup; total hip replacement; finite element analysis; modal analysis

Abstrakt

Počáteční fixace acetabulárního implantátu hraje důležitou roli v jeho dlouholetém přežití. Každý rok se provede milión implantací během níž neexituje zatím žádná metoda jež podala informaci o tom jak je implantát zaveden. V současnosti se musí operatér spolehnout na svoje zkušenosti přestože má k dispozici celou řadu sofistikovaných zobrazovacích technik, která však nejsou vhodné k intra operativnímu posouzení fixace implantátu. Mohou být spíše použity pro post operativní hodnocení stavu implantátu.

Vibrační metoda se dostala do popředí v oblasti diagnosticky fixace implantátu díky její úspěšné implementaci v dentální implantologii. Úspěšně se používá k hodnocení počáteční i průběžné fixqce implantátu. V oblasti totální kyčelní náhrady existuje řada seriózních prací zabívající se implementací této metody pro femorální komponentu. Nicméně, klinické reálné použití zatím ještě není k dispozici. Tato práce je zaměřena na implementaci této metody pro acetabulární komponentu jejíž fixace nebyla zatím touto metodou vyšetřována. Práce pojednává o rozhraní kosti a implantátu jako možném prediktoru počáteční fixace implantátu ve formě numerických simulací. Experimentální část je zaměřena na hledání vztahu mezi stupněm počáteční fixace a dynamickou odezvou soustavy kost - implantát. Simulace a experimenty ukazují, že dynamické parametry soustavy jsou ovlivněny změnami počáteční fixace implantátu a mohou být potentiálními ukazately počáteční fixace implantátu.

Klíčová slova:
fixace implantátu; acetabulární jamka; totální kyčelní náhrada; metoda konečných prvků; modální analýza

List of Figures

List of Tables

List of Operators

i	$i^2 = -1$
$\cdot^T$	matrix transpose
$\cdot^H$	matrix hermitian transpose
$\cdot^*$	complex conjugate
$\cdot^{-1}$	matrix inverse
$\mathbf{Real}(\cdot)$	real part of
$\mathbf{Imag}(\cdot)$	imaginary part of
$E\{X\}$	mathematical expectation of stochastic variable X
$\mathbf{var}(x)$	variance of scalar x as $E\{\|x - E\{x\}\|^2\}$
$\|\cdot\|$	absolute value of variable
$\|\|\cdot\|\|$	norm of vector or matrix
$A(f)$	frequency response
$F(f)$	Excitation force
∇	First order derivation operator
B_e	Derivation of shape function on finite element

List of symbols

N_i	number of inputs
N_o	number of outputs
n	order of a polynomial
m	m^{th} iteration step
N_s	number of samples
N_f	number of DFT frequencies
T_S	sampling period
f	frequency
f_s	sampling frequency
ω_f	angular frequency at frequency f
Ω	generalized transform variable
Ω_f	Ω evaluated in DFT f
W	Weighting matrix
N_m	Number of poles
pb	Probability that a true pole falls inside the probability circle
b_{kj}	Coefficients of numerator polynomial matrix
a_j	Coefficients of denominator polynomial
$\delta\theta$	Perturbation vector of parameters to optimize
e_m	m^{th} residual of objective function
g^{ij}	Metric tensor
N_e	Number of finite elements
p^i	Updated parameter
x_s, x^s	Box bounds

List of Abbreviations

DFT	Discrete Fourier Transform
DOF	Degree of Freedom
IRF	Impulse Response Function
MIMO	Multiple Input Multiple Output
ML	Maximum Likelihood
LSCF	Least Square Complex Frequency
PLSCF	Polyreference Least Square Complex Frequency
MFD	Matrix Fraction Description
SNR	Signal to Noise Ratio
SR	Sensitivity Ratio
SVD	Singular Value Decomposition
RMS	Root Mean Square
MAC	Modal Assurance Criterion
MPC	Modal Phase Colinearity
MVC	Modal Vector Complexity
MSF	Modal Scale Factor
THA	Total Hip Replacement
RSA	Radiostereometric Analysis
DXA	Dual- energy X - ray Absorptiometry
BMD	Bone Mineral Density
THR	Total Hip Replacement
EMA	Experimental Modal Analysis
SI	Sacroiliac
OA	Osteoarthritis
BMI	Body Mass Index
DDH	Developmental Dysplasia
PMMA	Poly (Methyl Methacrylate)
AC	Acetabular Cup
LVDT	Linear Variable Differential Transformer)
FE	Finite Element
FFT	Fast Fourier Transform
FRF	Frequency Response Function
CT	Computer Tomography
STL	STereoLithography graphical format
ACSM	Active Contour Segmentation Method
NURBS	Non - Uniform Rational Basis Spline

NSMM	Non - linear Squares Minimization Method
HU	Housefield Units
MKL	Math Kernel Library
GTLS	Generalized Total Least Squares
SLSQP	Sequential Least Squares Programming
SVM	Support Vector Machine
SISO	Single Output Single Input
PCR	Principal Component Regression
PLSR	Partial Least Square Regression

Dedication

For Žaneta and Antonín

Contents

Chapter 1

Introduction

This chapter contains the main introduction and the motivation for this thesis. The research context is introduced. In this section the main objective and hypothesis are defined also.

1.1 Research Contents

Total hip replacement is often called as "Surgery of century" [1]. It is one of the most success procedures in orthopedics. It solves the impact of degenerative pathologies of human hip joint by using a manufactured medical implant, which replaces a missing or damaged biological structure (ISO 13485). About a million procedures are performed a year [2]. One is believed that THA can protect a major part of patients from pain and increase the quality of patient's live for the period 10 – 20 years. Despite the modern surgical procedure, sophisticated tools and active biomaterials the survival rate is not one hundred percent. The revision operation after failure is often needed. It brings an increased risk of complications and the results and prognosis are poorer than in primary THA [3]. The implant ten-year revision - free survival for younger patients is estimated in range from 72 % in Finland to 86 % in Sweden by Kaplan – Meier method [4]. In another study it can be found the survival rate 90 % (3 to 20 years range) [5, 6], [7]. There was even found the rate of success around 97 % at 3 years follow – up studies [8] and 92 % at 10 years [9].

Aseptic loosening is considered to be the most common reasons of THA fail [10], [11], [12]. The percentage range of aseptic loosening is around 50 % to 90 % [13]. Following revision THA is not only costly but it is also associated with an increasing risk of complications [14], [15]. Aseptic loosening is a failure that occurs in a relatively long time after primary THA [16]. Possible scenarios of aseptic loosening were introduced in the last decades: the accumulated damage; failed bonding; the particulate reaction; destructive wear; stress shielding and stress bypass scenario [17]. Proposed scenarios are not independent to each other, but they are related [18]. A recent study shows that another cause of implant loosening would be a fluid pressure at the bone - implant interface during the micromotion [19].

Orthopaedic implant is mechanically stabilized in bone by press – fitting procedure or cementing techniques. Enough implant stability is fundamental assumption for correct physiological transfer and long – term outcomes of surgery. Especially in case of cementless component the press – fit level is critical. If the surgeon does not press – fit enough the implant than the implant is not stable and probably fails due to aseptic loosening, concretely, the migration phenomenon, osteolysis or excessive micromotion can occur [20], [21]. On the other hand, excessive press fitting would lead to periprothetic fractures (2 % - 28 %) [22], [23], [13]. An optimal press – fitting level strongly depends on surgeon's experience. The optimal mechanical stability of the implant is a condition for osseointegration process. According [24], osseointegration process would be defined as a direct structural and functional connection between surrounding bone and implant surface. Osseointegration means also the direct mechanical connection without progressive relative movement [25], [26]. Initial implant stability is measured in term of periprothetic micromotion that is directly related to osseointegration process. If the initial stability is not achieved, excessive micromotion during the daily activities occurs at the periprothetic interface [27], [28], [28]. Micromotion than stimulates

osteoclastic response of bone which leads to periprothetic osteolysis and consequently to implant failure [29], [30]. Both the micromotion and osteolysis with wear particle increase implant failure [31], [32]. Design of implant and press fit process should prevent exceed the micromotion around 150 μm to keep bone ingrowth [33].

The stability measurement is a critical procedure important for early implant loosening detection and prediction. Since the micromotion is taken as a right indicator of the implant stability, the full evaluation useful in vivo is difficult [34]. A complete evaluation of micromotion requires into account physiological conditions (muscle forces, skeletal forces and patient activities) [35]. Currently, the diagnosis of status of implant loosening is mainly based on the qualitative information from traditional methods (X - rays, RSA, etc.) [36], [37]. Although the diagnostic methods are very sophisticated, a diagnostic with one hundred percent accuracy is not possible to achieve [38], [39]. The migration phenomenon could be captured by the traditional methods and seems to be as a good predictor of implant stability. It has been found that early migration has a predictive value for long term success of implant [30]. Radiographic signs were correlated with implant instability. Another author suggested that the migration higher than two millimetres at two years could be a good predictor of aseptic loosening [40]. It has been also reported that radiolucent lines cover more than 50 % of the bone – implant interface could estimate the implant stability [41]. The use of radiolucent lines as the implant stability predictor for revision decision also has been reported [42]. However there are cases of implants that migrated significantly but after a year they get stabilized. No complications were reported. In another work authors argued that radiolucent lines are not definitive hallmark of aseptic loosening in range 2 to 5 years follow – up [43].

Roentgen stereophotogrammetric analysis is an imaging technique with ability to precise measure the implant migration in order of millimeters or better [44]. The using of tantalum markers may be difficult and sometimes even impossible. The new techniques based on digital contouring of traditional RSA are extensively developed [45], [46].

X – Ray based methods provide an assessment of loosening of THA components are plain radiography, scintigraphy, substraction and nuclear arthrography [47], [48].

Dual x – ray absorptiometry (DXA) gives a value of BMD (bone mineral density), which is related to osseointegration and remodeling bone process and, consequently, to assess the implant stability [49].

Unfortunately, none of previously mentioned methods has an ability to be appropriate for detecting the primary fixation of orthopaedic implants during surgery. The combination the traditional methods with computer simulation models could be used as an alternative tool for pre – clinical trial. Nowadays, there is no objective method of THR stability measuring, although the implant stability significantly influences the rate of implant success.

A diagnostic method based on mechanical vibration is used by engineers to investigate material properties or structural integrity. Damage and health monitoring of structures are main

application of vibrational analysis. It is used for a large variety of an engineering problems such air planes, automotive, building and bridges [50]. Vibration analysis was successfully used to quantify the stability of dental implants by [51], [52],[53], [54], [55]. The frequency shift is directly related to the implant stability. This method is used in commercially available device (Osstell^{TM}, Integration Diagnosis AB, Goteborg, Sweden). Although the vibration analysis works well for dental implant, the use for any other implants, especially for THR, is still a challenge. Probably due to conditions for THR implants that are different from dental implants and would be much more difficult to get sufficient reliability and feasibility of this method for real clinical trial. The THR stability measurement protocol based on vibrational technique was established by several authors [56], [57], [58]. All of them are focused on femoral stem, although the survival rate of the acetabular cup is similar and the radiological diagnosis is even more difficult and poorer [59], [60], [61]. Previous works have an experimental device and support by numerical approach, but suffer from insufficient clinical testing and clear determination of influencing factors and the limitations of method.

1.2 Research Hypothesis, Focus and Organization of the Thesis

This work is focused on the assessment of the initial fixation stability of acetabular implants in THR. The study is funded by TACR (Technological Foundation of the Czech Republic) – ALFA 1401. Measurement protocol is built and tested on the cementless acetabular component – a type SF manufactured by Beznoska (Beznoska s.r.o, Kladno, Czech Republic). The main objective of the study was to investigate an usefulness of vibrational method for measuring the initial fixation of acetabular implant and subsequently design an experimental device for intra - operatively assessment of the initial fixation of acetabular implant.

Research direction was formulated in several hypotheses:

- Interfacial contact surface influences a dynamic response of bone - implant system.
- The implant – bone structure behaves rather as quasi- linear system with an exception in case of completely unstable implant.
- Between modal parameters and fixation level of an implant a relation exists.
- Alternative relation between fixation level of the implant and an evaluation of its frequency response function would be find by data mining technique.
- More complex modes are more sensitive to change in bone - implant interface.

Research questions:

- Can vibrational method be a useful tool for estimating the initial fixation of acetabular component?
- What are the limitations of vibrational method for press fitted acetabular implant?

The organization of the work is proposed in the figure 1.1.

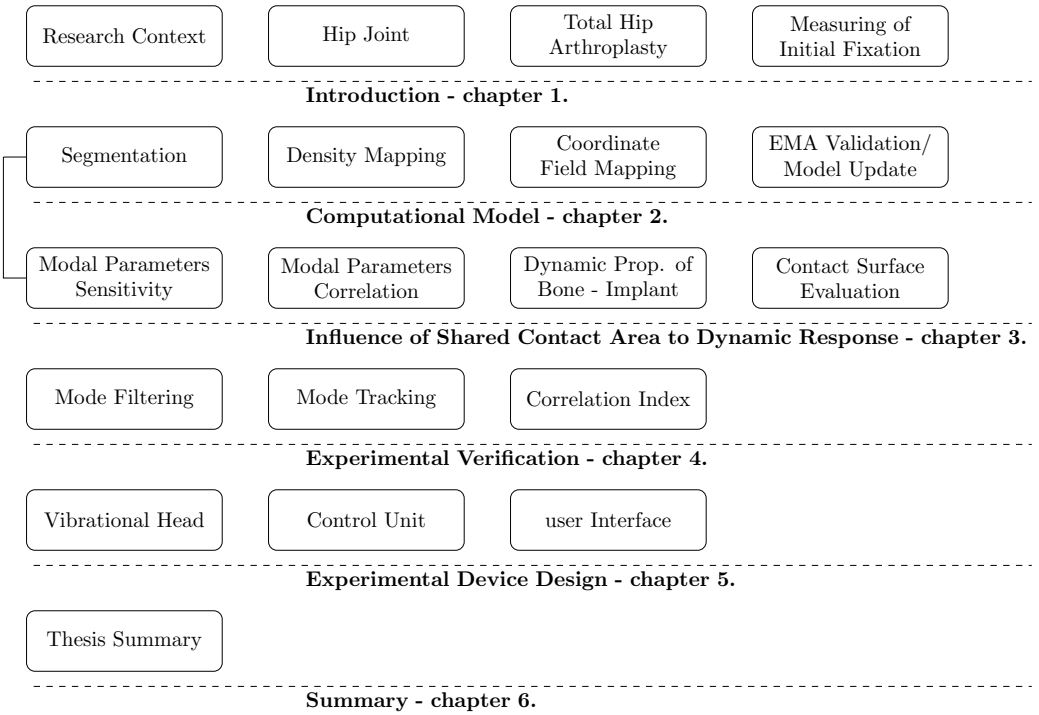

Figure 1.1: Thesis outline

1.3 Original Contribution in this Work

Original contributions in this work go in two different ways. In experimental way, a novel concept of vibration mechanism was explored based on the positioned vibrational head with the excitation and acquire transducer in one part. The head is completely washable, sterilize or treatable with plasma. The mechanism of the head has an ability to be connected to both THA component: acetabular and femoral component.

Experimental identification of modal properties of pelvis bone with cup and correlation with press fit level of acetabular cup have never been investigated. This work brings an important investigation of relation of resonant frequencies, damping and even modal shapes with fixation level expressed as an impact force and a polar gap. Apart from modal parameters,

an evaluation of the frequency response for every fixation level was examined by multivariate supervised techniques based on Principal Component and Partial Least Square regressions.

The numerical way express the series of a computer simulations mainly done for support the conducted hypothesis. For simulation purposes, a novel simple approach was taken in the modeling of orthotropic material properties of curved composite structure as bone is. This method generates complex material field based on the curvature, thickness and real material properties of bone. The method was successfully validated with experimental modal analysis (EMA) and updated with optimization framework for material properties. The industrial identification algorithms in field of experimental modal analysis were successfully applied in biomechanics of the pelvis bone and implant.

1.4 Hip Joint Anatomy

The hip is a ball – and – socket joint with powerful surrounding muscles. It is a structural link between the lower extremities and the axial skeleton and it allows greatest mobility and stability. It is composed from joint cavity, articular cartilage, synovial membrane and surrounding ligamentous capsule (figure 1.2). The hip has a very important biomechanical function. It supports a major part of human body ($\sim 2/3$ of total bodyweight) and simultaneously serves smooth articulation of the limbs to enable bi – pedal gait. During daily activities, transfer forces can exceed the body weight even 5.5 times. [62],[63], [64], [65].

The pelvis bone is formed from three bones: the ilium, ischium and pubis. They fuse together and form the ox coxae. At the point of fusing the acetabulum is formed. Adjacent joints to the pelvis are sacroiliac (SI) and pubis joint. The posterior and superior margins of the acetabulum are reinforced with cortical bone, which enhances the stability of the joint during weight bearing from flexed and extended positions [66]. The bony structure of the pelvis is similar to a composite material. It consists of a dense, stiff and thin shell of cortical bone. The thick of cortical bone is in the range 0.7 to 3.2 mm. [67]. The inner part of pelvis is filled by much less dense trabecular bone.

The femur is the longest and strongest bone in the human body. It is composed from head and a neck proximally, a diaphysis, two condyles distally. The diaphysis of femur has cylindrical structure. Proximal part of femur has an irregular shape consists from spherical head, neck and greater and lesser trochanter. Cortical bone along the diaphysis of femur has a thick up to 7 mm and supports large tensile and compressive loads from hip loading [68]. Both joint surfaces are covered with a strong lubricated layer of hyaline cartilage ranging from 1.2 to 2.3 mm thick in normal adults [69]. The articular cartilage on the acetabulum forms an incomplete marginal ring called lunate surface [70].

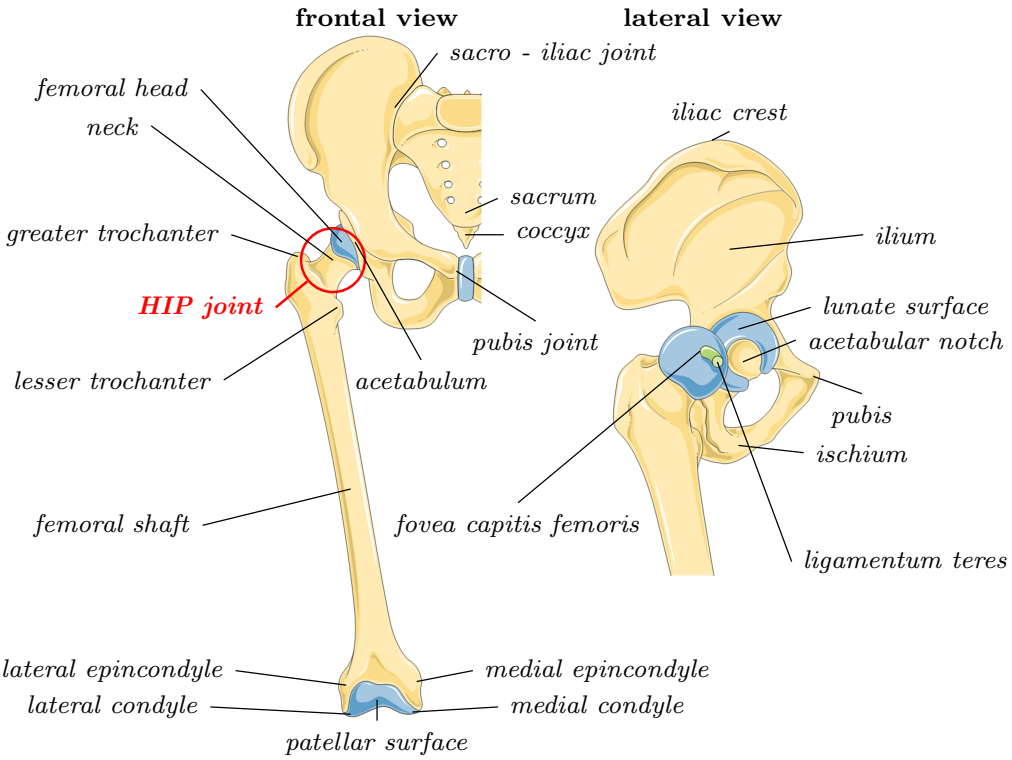

Figure 1.2: Hip joint anatomy

1.5 Hip Joint Diseases

The most common disorders include osteoarthritis, avascular necrosis, slipped epiphysis, bursitis and developmental dysplasia.

Osteoarthritis (OA) is a degenerative disease associated with the wearing of the cartilage covering bone – ends [71]. It involves the entire joint: cartilage, bone, synovium, labrum and capsule. The typical manifestation of OA is a loss of cartilage in the load bearing surface of the joint and proliferative response associated with osteophytosis [72]. This process is followed by subsequent thickening of subchondral bone and mild – to – moderate synovial inflammation. OA of the hip is recognized as a primary (idiopathic) or secondary (systemic or localized) disease. Risk factors of primary OA are following: age (older is higher risk); high bone mass; a genetic predisposition; increased body mass index (BMI); participation in weight – bearing sports. The risks for secondary OA are: hemochromatosis; hyperparathyroidism; hypothyroidism and more [73], [74].

Developmental dysplasia of the hip (DDH) is characterized by malorientation and reduction of contact area between femoral head and acetabulum [75]. Subluxation caused by DDH increases the mechanical stresses in the hip joint during the gait load cycle. It is though that

DDH causes the early damage of the hip cartilages and bones and, consequently leads to early hip osteoarthritis. Surgical procedure of the anatomic abnormalities caused by DDH is done by pelvis osteotomy, which involves cutting the socket free from the pelvis and rotating it to a new position [76].

1.6 Total Hip Arthroplasty

1.6.1 Introduction

Total hip arthroplasty becomes one of the most successful surgical procedures in last decades. THA gives a solution for patients suffering from pain, movement reduction, rigidity or deformity. It is also the solution in case of osteoarthritis (OA), avascular necrosis, developmental dysplasia (DDH), traumas and tumors. The surgical procedure has several ways how to be performed. The most commonly performed methods for THA include the anterior (Smith - Petersen), anterolateral (Watson - Jones), muscle splitting lateral (Hardinge), transtrochanteric lateral (Charnley) and posterior approaches (Moore, Gibson) [77]. The basic idea is depicted in figure 1.3. The damaged hip joint is replaced by an artificial acetabular cup (AC) and femoral head. Together these two components replace damaged natural articulation surfaces. The AC is anchored in the pelvis bone and femoral head is connected with the femoral bone by the stem anchored in the medullary canal [78]. This presented work is primary focused on the cementless acetabular cup. The following chapters describe mainly the THR in mean of cementless acetabular cup.

1.6.2 Implant Design

THA procedure includes a large variety of solution in mean of implant shape, size, modularity and kind of purposes. The choice depends on surgeon's skills and patient's state. Nowadays, THA implants are modular: polyethylene liner, hemispherical socket fixed onto the acetabulum, ceramic (or metallic) head, metallic neck and femoral stem. The modularity of implants provides a possible adapting the implant geometry to the patient's joint morphology, which mean much more flexibility during the primary and revision THA [79], [80]. The modularity of the implant is useful during the DDH and when a mini approach is performed [81], [82]. The modular design allows using different materials with properties suitable for their function [83], [84].

Nowadays, most cementless acetabular cup has a porous coated surface over their entire circumference for bone ingrowth. They differ commonly in kind of initial fixation. Fixation of porous shell with transacetabular screws is a common technique, but carries a risk to intraplevic vessels and viscera (figure 1.4). It requires flexible instruments for screw insertion [85].

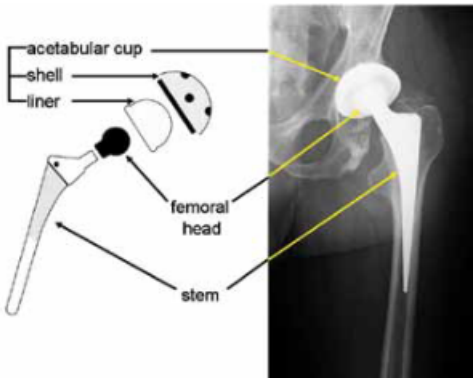

Figure 1.3: Modular construction of total hip implant [78]

Figure 1.4: Universal acetabular component (Biomet, Warsaw, Ind – left, SF, Beznoska s.r.o, Czech Republic - right). Titanium plasma spray coating with dome and rim screw fixation options

Pegs and spikes placed on the cup shell surface provide a rotational stability, but less than in case of using the screws (figure 1.5). These features are especially important in patients with marginal bone quality and when the cementless cup is repositioned after initial insertion [86].

Other devices have a dual geometry or an enlarged peripheral rim that can be press fitted without any ancillary fixation devices (figure 1.6) [85].

Several analyses of THR survival with supplementary AC fixation features show good results with fixation screws, pegs [87], [88], [89]. Although there are studies that show no increase of AC survival with screws [90], [91].

Press fitting technique is currently a common method for ensure good initial stability of cementless AC [92], [93]. With the press-fit fixation technique, a hemispherical porous-coated

Figure 1.5: Duraloc acetabular component. Sharp spikes are driven through subchondral bone to improve initial stability (Courtesy of Johnson & Johnson, DePuy, Warsaw, Ind.)

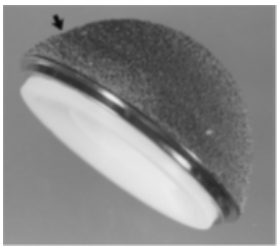

Figure 1.6: Interfit acetabular component - hemispherical design with gradual transition to enlargement in peripheral rim for improved initial stability and peripheral stress transfer (Courtesy of Smith & Nephew, Memphis, Tenn.)

acetabular component, typically 1 to 4 mm larger than the last reamer used to prepare the acetabulum, is forcefully impacted into the acetabulum [94]. It is essential that the surgeon have an exact knowledge of the geometry of the cementless acetabular component they are using, as this will have an effect on the amount of under-reaming necessary to obtain the desired degree of interference fit and full seating of the component. Modular cups frequently have screw holes or a central "polar hole" that allows for visual confirmation that the cup is fully seated and well apposed to host bone after insertion [86].

1.6.3 Cemented versus Cementless Technique

Basically, there are two major types of artificial hip replacements: cemented and uncemented. Both are widely used. Cemented prostheses are the oldest form of THA. The principle lies in fulfilling the prepared bone bed by epoxy cement (PMMA) that attaches the stem to the bone. Good clinical results at 10 years are achievable with this method [95]. Although there are complications related to the PMMA behaviour. The PMMA degrades over time and generates the cement debris causes inflammation of surrounding bone and, consequently the loose of periprothetic interface [96]. In case of revision surgery the lack of bulk cancellous bone during the first surgery could bring a problem. It is though that for older (65 and older - [97]) patients with poorer or osteoporotic bone the cemented implant could bring stronger initial fixation of implant [98].

The cementless technique is an alternative for suppressing the problems associated with cemented implants. The essential stability of the implant is achieved by press – fit technique. The last rasped (or reamed) cavity has a smaller diameter than the final implant. The frictional and compressive forces caused by press – fit are responsible to adequate load transfer during the gait cycle. The earlier generation of cementless THA has poorer performance than cemented [99], but current concepts of implants have a similar survival rate to their cemented counterparts [100].

1.6.4 Loosening of Acetabular Component

Aseptic loosening and osteolysis are a major reason for acetabular component fail. The range of aseptic loosening (wear, AC migration) of porous coated anatomic cup (PCA) is from 7 % to 30 %. However range of fail in PCA is relatively high, there are studies that show the success of Harris – Galante AC (Ti shell with fiber metal mesh bonded to the shell) much better. The long term results (more than 10 year) are excellent with a range of aseptic loosening from 0 % to 4 % [101]. A recently published study by Della Valle and associates evaluated 20-year follow-up of patients with the HG - 1 porous acetabular component [102]. A total of 114 patients of the original cohort of 204 patients were available for review. Kaplan-Meier survivorship of the acetabular component was 96 % in terms of revision for aseptic loosening or radiographic evidence of loosening as an endpoint. Fourteen hips (12.3 %) with well-fixed acetabular shells underwent revision for a modular liner exchange. The authors concluded that wear-related complications continue to be the major mode of failure [103]. Another kind of AC was investigated by [104]. Their recently 20 – years follow up study reported the survival rate of coated RM cementless AC. This AC was manufactured from ultrahigh molecular weight polyethylene coated with a thin layer of Ti particles. Ninety-three primary THA were performed with a survivorship of 94 % (17.4 to 20.9 years). Mainly reason for revision THA were osteolysis and polyethylene wear. In table 1.1 another studies of acetabular cup performance are provided for comparison.

Table 1.1: The acetabular cup performance

Author	Mean Length of Follow–up [year]	Number of Cups	Radiographically Loose, n [%]	Revised for Loosening, n
Bojescul [105]	15.6	64	19 (30)	17
Hastings [106]	10.3	73	13 (18)	17
Healy [107]	12.3	53	6 (11)	6
Kawamura[108]	12	187	12 (6)	8
Kim [109]	11.3	116	8 (7)	8

The survivorship of the cementless AC stabilized with press fit technique was reported in several studies. Another author reported the result from 10 – year follow up study where the survival rate was 99.1 % with revision with the conclusion that the press fit socket is associated with a low rate of osteolysis [110]. The most common reasons for reoperation were still wear and disassociation of the polyethylene insert. They confirm the findings in work done by Kwong that there is no significantly difference in stability between HG porous coated AC with 1 mm press fit with or without supplementary screws [111]. Associated problem with press fit implantation is periprothetic fractures. Fracture of acetabulum has been reported in cadaveric studies. Sharkey demonstrated that acetabular fracture can clinically occur during

uncemented cup insertion and it can lead to serious complications (9 fractures from 13 cases) [112]. The fracture can occur during the variety of cup oversizing (2, 4 mm) [113], [114].

1.6.5 Initial Fixation of Cementless Acetabular Cup

Initial stability of the cementless acetabular component would be defined as the lack of relative micromotion between shell surface and bone bed [115], [116], [117]. The initial stability is essential for bone ingrowth and long time performance of acetabular cup and to prevent aseptic loosening. Sufficient initial stability is achieved by press fitted acetabular cup with optional screws. The contact area between shell surface and surrounding bone must be maximal to achieve an optimal distribution of stress [118]. Roth demonstrated that cups with higher contact area have higher the initial stability measured by the pull – out test [119]. Curtis recommend for achieving the best initial stability the press fit in range 2 to 3 mm [114]. In this manner the cup is fixed at the outer diameter of the acetabulum, which leads to a uniform transfer of load and homogenous, approximately physiological loading of the acetabulum.

The micromotion and strains on the interface is a subject of studies in mean of implant fixation and movement during the physiological gait cycle. The measuring in vivo is difficult [120], however they have been carried out in vitro experimentally [111], [117], [116] and using the FE modelling [121], [122], [123]. In most reported experimental studies the acetabular cup micromotion was obtained by unidirectional LVDT in three axes. Kluess attempted to validate the FE model of micromotion prediction by optical markers but they did not achieve acceptable accuracy [121]. Zinkovic validated their FE model by six LVDTs probes under a chair – rising loading [124]. Clarke tried to validate their FE model with experimental result obtained by digitalization arm [125]. All of mentioned studies show in average a good accuracy of micromotion and strains measuring and validation of FE model.

The threshold value of micromotion, above which fibrous layer forms, has been studied by several authors. From literature review for bone – dental implant interface it was found the range of micromotion 50 to 150 μm [126]. Maloney reported the axial micromotion value 40 μm in study on eleven femoral specimens retriever at autopsy. Histological investigation showed intimate osseointegration at the bone – implant interface with only rare intervening fibrous tissue [127]. Engh found the similar magnitude of micromotion in case of cementless femoral components with bone ingrowth at porous – coated implant. The higher micromotion (150 μm) was found in on areas of failed bone ingrowth [128]. Whiteside reported the micromotion value around 80 μm on investigation the difference between AML and the Mallory Head prosthesis. From noticed works can be concluded that the range of micromotion for bony ingrowth process could not exceed 150 μm [129].

As it was mentioned, the computer simulations were used for the investigation of micromotion and fibrous layer formation. In a study of influence of various fibrous thicknesses

the micromotion the thickness 58 μm was found to be sufficient to increase the micromotion excess the threshold value (200 μm) for ingrowth process [130]. In a similar study authors demonstrated that the viable region for bone ingrowth was completely eliminated for the fibrous tissue layer with thick 300 μm [131].

1.7 Current Concepts of Initial fixation Measurements

1.7.1 Pull – out and torque resistance test

The radiological based methods are currently the first step of investigation in post-operative THR [132], [133]. However radiological method can provide the information about migration, dislocation and cup position, the intraoperative ability to assess the initial stability of cup is not available. The most of described analyses of initial fixation of AC are based on the pull – out and torque resistance test and vibrational analysis. Olory performed in their analysis the pull – out test of eleven cups and obtained that the pull out strength varies from 7.63 to 55.46 Nm. He also noted that the hemisphere has the better contact to keep a good initial stability and the highest pull - out strength force is associated with the highest initial stability [118]. The observation the relation between contact area and initial stability is consistent with radiological findings, where the higher peripheral contact is associated with decreasing of peripheral radiolucencies [134], [93]. In another study Fehring quantified the initial stability of acetabular cup with torsional load (*e.g.* the forces required to move the AC greater than 150 μm) [135]. The results show unclear behaviour of acetabular cup (high degree of variability in resisting load). Although the torque and pull- out test can provide sufficient information about the initial stability due to micromotion and peripheral contact area, it is not possible to use it in vivo. It is a destructive test. However, the combination of those in vitro test and numerical analysis of micromotion, it would be obtained an interesting alternative assessment of initial stability of acetabular component with focus on the interfacial parameters such friction, micromotion [136], [137], [138], [139], deformation [140] and [141].

1.7.2 Vibrational Test

Vibration analysis is widely used in engineering problems to investigate structural properties. There are many methods to determine the structural behavior. There are based on the modal analysis, resonance frequency shift, harmonic distortion, and acoustic emission. The abilities of vibrational methods in biomechanics were demonstrated firstly in determining of bone mechanical properties [142], [143], [144], [145] and clinical monitoring of fracture healing [146], [147].The first report of vibrational analysis related to the implant fixation has been established in dental and craniofacial medicine [148], [149]. It has been found the strong relation between quality implant fixation and resonance frequency shift. The base idea is depicted at figure 1.7. A transducer is attached to the implant. In opposite face the acceleration sensor

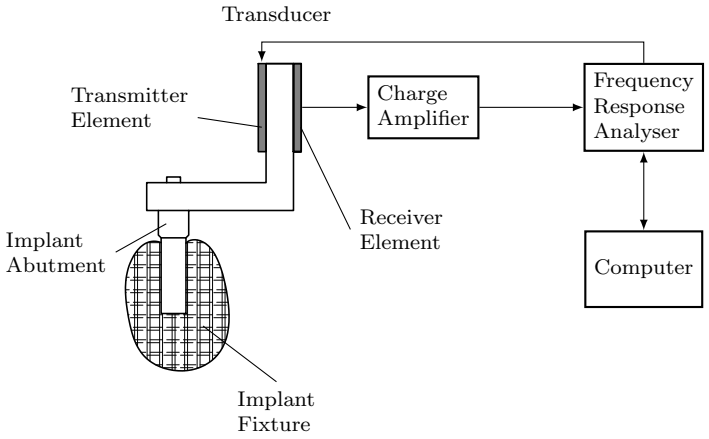

Figure 1.7: Principle of measuring the stability by Osstell device

is attached to acquire the response. The first bending resonance frequency is measured. Sufficient initial fixation increases this first bending resonance frequency and has a potential to assess early implant failure. Currently, this method is used in commercially available device (Osstell, Integration Diagnosis AB, Goteborg, Sweden).

Osstell device converts the resonance frequency shift to a unique unit called ISQ (Implant Stability Quotient). The range is from zero to 100 points and higher value means better implant fixation. However, it has been proved the relations between resonance shift and initial fixation in vivo and between torque test in vitro, there are still question about the sensitivity of this method to parameters such direction of measurements, density of bone, implant makrodesign and micro design parameters. Čapek demonstrated the resonance frequency depending on the direct of measuring and concluded that is necessary to keep the orientation of transducer unlike there is not clear if it is measured the first or second resonance frequency [150]. In addition, Huang found that the boundary height, width and the density of specimen influence significantly the resonance frequencies [151]. Another method for dental implant stability assessment is based on the similar method as Osstell device. It is named Periotest (Medizintechnik Gulden e. K., Germany). Periotest consists of small headpises probe with rod inside. Using the electromagnetic accelerator the rod strikes an implant 16 times in 4 seconds at a velocity of 0.2 ms^{-1}. The contact times between rod and the implant is measured and converted into Periotest value [152]. In comparison between Osstell and Periotest, Zix shown that Periotest is less sensitive than the Osstell device [153]. Finally, in a recent study, Wijaya introduced the device called Implant movement checker [154] - figure 1.8. It is based on the assumption that mechanical mobility of the implant is directly related to response function

Figure 1.8: Implant movement checker [154]

written as:

$$\lambda(f) = \frac{1}{i2\pi f}\frac{A(f)}{F(f)} \tag{1.1}$$

Where the force amplitude is constant.

Although there are more methods to assess the implant fixation by the vibrational principle [155], [156], these three mentioned devices based on the vibration analysis have the ability to use in clinical environment. However, the first version of Osstell device has suffered from bad usability due to sterilization process. The last update of Osstell device uses wireless probes and does not need to be connected physically to the implant (Osstell Mentor – SmartPeg probe). In another study, Shao designed the in vivo / in vitro measurement protocol of osseointegration of trans - femoral implants (figure 1.9). The implant was excited with a small mechanical shaker and the response was recorded by an accelerometer. The response was analyzed using FFT (Fast Fourier Transform.) to obtain natural frequency. They concluded that higher interfacial elastic modulus corresponds to a higher natural frequency. He also demonstrated the influence of boundary conditions on the natural frequency [157].

The previous work was extended by Cairns, who measured also the natural shapes and demonstrated their sensitivity to interfacial changes [158]. The conditions for using the vi-

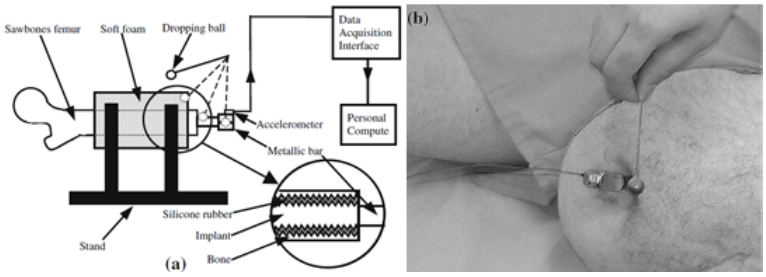

Figure 1.9: Measuring the stability of trans - femoral implant [157]

Figure 1.10: Measuring the stability with the force applied to knee [159]

brational method in THR are much more different from in case of dental and trans - femoral implants. Especially that the THR implant is immediately covered after implantation and there is no more access until the revision THR. A several studies deal with the vibrational analysis of THR. Georgiou developed the diagnosis protocol and compared it to radiographic findings as one of the first. The vibration technique does not need to expose the femoral implant, because the vibration force is applied to the knee and the response is acquired on the subcutaneous greater trochanter [159].

He focused on the number of resonant frequencies, the amplitudes of the first and second harmonics and the number of remaining harmonics. For femoral component during the in vivo study, they found the vibrational analysis is more sensitive than radiographs (up 20 % more). However also they pointed that the accuracy in case of acetabular component is comparable with radiological findings (sensitivity around 50 %), which is, of course, great challenge to improve.

Li focused his experiment on the cemented femoral component. The femoral bone and implanted femoral stem was excited by the sinusoidal waveform. The information about stem stability was extracted from amplitude in frequency domain and from the distortion of the response signal. The response was obtained for 21 secure systems, 17 were loosened and 14 showed in the spectral analysis several distorted frequencies [160]. However, the relation between early stem loosening and signal distortion was not clearly 100 %. They suggested future improvement of the vibrational technique and concluded that the tissue fibrous layer cement fractures are not vibrational detectable [161].

Recent studies were based on the two assumptions, that the difference in vibrational behavior is increased with the complexity of the modal modes and is thus, the more complex modes are more sensitive to interaction femur- stem system and the ability to detect the insertion point of the stem [162], [163] and [164].

Study was done on the sawbones of femur with implanted stem (figure 1.11). The used

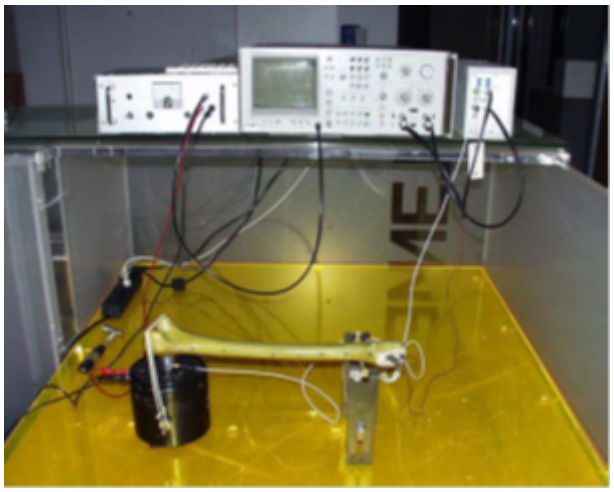

Figure 1.11: Measuring the stability of femoral stem [163]

methods to assess the fixation quality are based on the frequency shift and the vibrational modes. They found, that the sensitivity to a first bending mode to fixation status is very low (frequency shift about 50 Hz). Generally, they confirm that most sensitive band is above 1000 Hz, which is in accordance with previous work [165], where the authors suggested the most sensitive band to observed the interfacial effect in the femur – stem is above 2500 Hz. The previous work was extended to a vivo test by Pastrav [166]. They tested two groups with cemented and uncemented prostheses and found that FRF evaluation is dependent on the cement curing. They conclude that the vibrational technique would assess a critical step during the insertion of stem (end point of insertion – prevent to fracture of bone).

The previous works are based on the bending vibration and are direction dependent [167]. Lannocca established the vibration protocol that uses the torsional stiffness measuring by vibration as a predictive value of initial fixation of stem. The method uses excitation in torsion [168]. The correlation between micromotion test and peak amplitude is significant (table 1.2).

1.7.3 Summary

Vibrational analysis as a toll to assess the initial stability of femoral stem has been investigated in many forms. Basically, most of the cited studies use as a predictive variable the frequency response function of the bone – stem. The use of the FRF expects the linear or quasi-linear behavior of investigated system, which was demonstrated in [161], [160], [170], [171], [172] and [166]. Spectral analysis used by Li has an ability to find the clinically mobile implant due to harmonic distortion, but also shows that early loosening is rather linear than non – linear and consequently not detectable by harmonic distortion. The femoral stem and bone interaction were demonstrated in finite element simulation to show the sensitivity

of vibrational modes to interfacial conditions [165], [166]. The findings show the increasing sensitivity of vibrational modes with more complex structures in range of frequencies around 1000 - 2500 Hz.

The stability of the acetabular cup is investigated generally much less than the femoral component. Georgiou found a poor sensitivity of the vibrational method (50 %) [159]. Pastrav investigated in his PhD thesis modal frequencies of acetabular cup in different insertion step on several demonstration experiments, but without deeper insight [173]. The acetabular component was investigated in sawbone experiments by Rieger. They focused on the acetabular cup – femoral stem as a whole body, thus, the direct possibilities of vibrational technique was not clear [169].

Most of the previous works use the measuring structure mechanical stimulation – acceleration response. The ability to detect the difference could be decreased with additional soft tissue, the direct of excitation and the power of excitation. The wireless approach of measuring with no mechanical contact has been investigated. Puers and Marschner tried to build the telemetry of response data transferring from the electronics placed into the head of the femoral implant. In vitro, or in vivo experiments was not available [174], [175]. In another work, the femoral implant has self-exciting system based on the pendulum and the response is measured by the accelerometer [176], [177]. The ultrasound (Doppler effect), laser vibrometry, acoustic emissivity and modal parameter extraction have been investigated as the potential determinant of the implant stability [178], [179], [180], [181], [182], [183].

Table 1.2: The Summary of the vibrational analysis in field of implant stability

Author	Method	Excitation - Response	Analysis	Conclusion
Li 1995 [161]	Spectral analysis – distortion, frequency response	Sinusoidal force applied to the distal end of the femur. Response is acquired by accelerometer placed near to great trochanter	sawbone	In 21 secure prostheses were two or less resonances. From 21 specimens, 20 showed increased number of resonance peaks. Early loosening was detected only in three from eight specimens.
Li 1996 [160]	Spectral analysis – distortion, frequency response	Sinusoidal force was applied to the distal metaphyseal – diaphyseal junction of the femur. An accelerometer was placed close to greater trochanter	sawbone	In 21 secure prosthesis were two or on resonances. From 17 macroscopically loosened stems, 14 showed increased resonances. Early loosening was detectable in 3 specimens from 16.
Georgiou [159]	Frequency response vs. radiographic comparison	Vibration shaker placed on the knee, accelerometer is placed on the subcutaneous greater trochanter	in vivo	80 % sensitivity to assess stem failure, 50 % to assess the cup failure was observed. In comparison the vibrational technique is 20 % more sensitive than radiograph.
Pastrav [166]	Frequency response measurement (FRF)	The shaker was attached to the stem neck. The force was measured by the impedance head at the same place	in vivo	In 45 cases from 53, it was observed important difference between cemented and uncemented stems. Detection of insertion end point.
Varini [167]	Frequency response vs. micromotion	Vibrational head connected to the stem	in vitro	A strong correlation between the highest peak amplitude and micromotion was observed. $R^2 = 0.71, p < 0.00001$
Rieger [169]	Frequency response, Peak count analysis, integration of FRF	Chirp pulse at the lateral condyle. Laser vibrometry, accelerometers placed on the medical knee condyle, on the top pf great trochanter and at the crest of ilium	sawbone	FRF magnitude did not provide an useful information; Integral analysis is sensitive to stem loosening, the Peak count analysis is sensitive to cup loosening

Chapter 2

Computational Model of Pelvis Bone and Acetabular Cup

This chapter is focused on the computational model of pelvis bone and acetabular cup implant. The first section gives a way how a pelvis geometry and a material field were extracted. A new method to describe an orthotropic material field with respect to curvature of a outer pelvis surface is introduced. In the next section the computational model of the pelvis bone is validated with experimental modal analysis. For this purpose, class of stochastic/deterministic multi - variable identification algorithms was successfully applied in an identification of the modal properties of the pelvis bone. A modal updating optimization procedure of the elastic properties was developed for further refine of the elastic properties.

2.1 The Rationale

In order to investigate an influence of bone - implant interface on their dynamic response, a computational model was developed. The modeling process composes from three basic steps. The first step contains extracting a real geometry of the pelvis bone from the same model used in experiments. The geometry of pelvis bone is scanned with a CT and consequently segmented to create a 3D model. The second step consists of a method to extract a material field of the pelvis bone. Material properties are extracted from the CT data and mapped to a new field of material properties *elastic modulus* E $[MPa]$, *density* ρ $[\frac{m^3}{kg}]$ and *Poisson ratio* ν $[-]$. A synthetic bone was used for experiments and also for the computational model. This kind of bone (Sawbones, The USA) is an orthotropic composite, thus the material properties must be adequately described. The last step belongs to an updating of the computational model. The model is calibrated and validated against experimental modal analysis, because this is a method for dynamical testing and is rather suitable validation technique than the static one for purposes in this work. Since the material properties of bone are expected to be density dependent ones, they are expressed as two coefficients power law.

2.2 Preparing of Computational Model

2.2.1 Geometry and Basic Material Properties

The geometry of the pelvis bone was obtained by CT scanning (Phillips Brilliance 64, Phillips) of the sawbone. The parameters of the CT scan procedure are described in table 2.1:

Table 2.1: Parameters of the CT scanner

Slice number	473
Slice thickness	1 mm
KVP	120 kV
Spacing between slides	0.5 mm
Rows	768
Columns	768
Pixel spacing	x = 0.308593 mm, y = 0.308593 mm, z = 0.5 mm
Origin	x = -118.5 mm, y = 73.5 mm, z = -804.7 mm
Intensity range	-1024 to 1618

The bone is shown on figure 2.1. It is a composite bone suitable fo biomechanical testing. It is two layered structure, where the outer part is a mixture of glass fibres and epoxy resin. The inner part is a solid rigid polyurethane foam. The material of these two components have similar properties as real bone structure. Material properties of synthetic pelvis bone are described in table 2.2. Discretized bone structure and geometry were as an input to

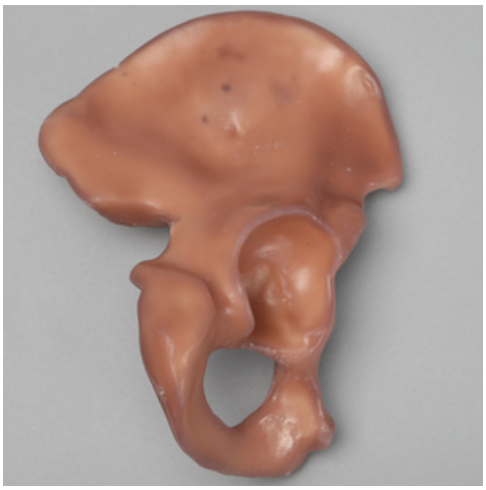

Figure 2.1: Synthetic left pelvis bone (Sawbone, USA)

Table 2.2: Material properties of sawbone

Cortical bone (Short fibre filled epoxy)				
	Longitudinal Tensile		Compressive	
Density[$\frac{m^3}{kg}$]	Strength [MPa]	Modulus [MPa]	Strength [MPa]	Modulus [MPa]
1640	106	16000	157	16700
	Transverse Tensile			
	93	10000		
Cancellous bone (Rigid polyurethane foam)				
Density[$\frac{m^3}{kg}$]			Strength [MPa]	Modulus [MPa]
270			6	155

the segmentation procedure. Segmentation was done by software TurtleSeg (TurtleSeg.org, [184]) and ITK-SNAP [185]. The histogram of gray density distribution was interpreted by Gaussian mixture data clustering. Three clusters were recognized: background (-1004.6 $\pm$ 134.6), cortical bone (577.6 $\pm$ 582.6) and cancellous bone (-882.1 $\pm$ 752.1) with the weight 0.33 for all of them (figure 2.2). The automatic 3D segmentation process was finish by the snake algorithm based on the active contour segmentation method (ACSM) [186]. The result binary mask was manually corrected for small avoids in sites of very thin bone by manual segmentation with the help of the interactive TurtleSeg Spotlight procedure [187]. The bone was scanned before reaming the acetabular cavity.

The output from the segmentation procedure is a surface model of the bones (cortical and cancellous part) in STL format and the mask of the cortical and trabecular bone. The triangularization process generated 1, 700 000 triangles. Due to high memory consuming, the decimation process was applied. The number of triangles was decreased to 10 % (170 000 triangles). After decimation, Laplacian smoothing was applied. In order to get the para-

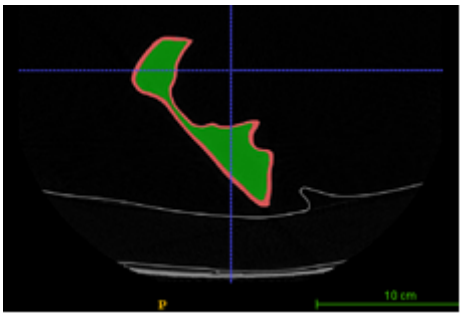

Figure 2.2: Mask generated with cluster analysis: red - cortical bone, green - cancellous bone

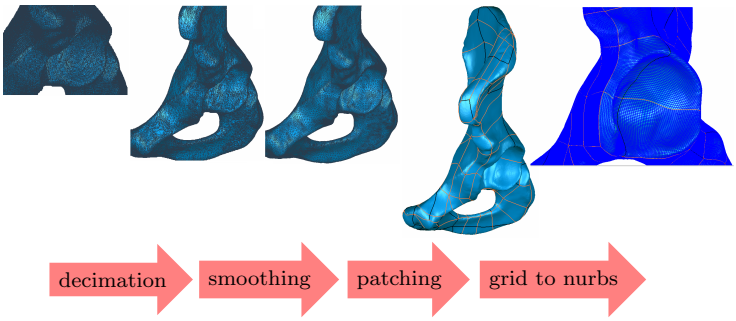

Figure 2.3: Construction of CAD model from raw tessellated data

metric model of the bone, a surface fitting procedure was applied (Geomagic Studio 12, 3D Systems, USA). Finally, the surface model of pelvis bone and the acetabular cup model were imported into the finite element software (Comsol AB, Sweden). The finite element model was used as reference model to validate the custom made finite element framework for updating purposes. The updating framework accepts the finite element mesh from Comsol and also the mesh generated directly from the CT and segmentation data. The CT based meshing framework is built on CGAL platform (CGAL, Computational Geometry Algorithms Library, http://www.cgal.org -[188]). The meshing based with CGAl avoids the expensive CAD generation model and permits generate a high quality tetrahedral mesh directly from CT data. A deviation of normal distance was computed to compare the initial mesh model with NURBS model (figure 2.4). Due to high curvature around the peripheral rim, the deviation is higher in this site (0.2 mm). The parameters of distribution of deviation are 0.021 $\pm$ 0.025 mm (maximum 0.457 mm at iliac tuberosity – red landmark). It is taken as sufficient accuracy of the surface fitting procedure against the initial mesh model. The thickness of the cortical bone is measured via the algorithm that minimizes the distance between the outer cortex surface and the interface surface between cortical and cancellous bone. The thickness is varied from to 0.5 to 5.42 mm (figure 2.5).

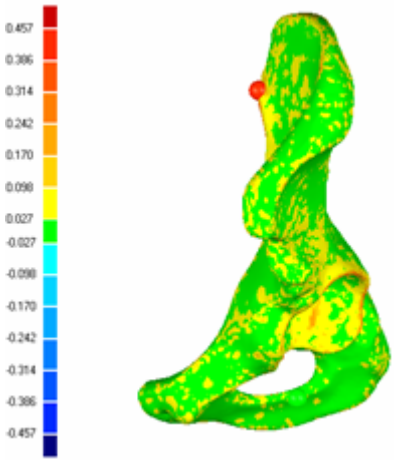

Figure 2.4: Deviation between Stl mesh and surface model [mm]

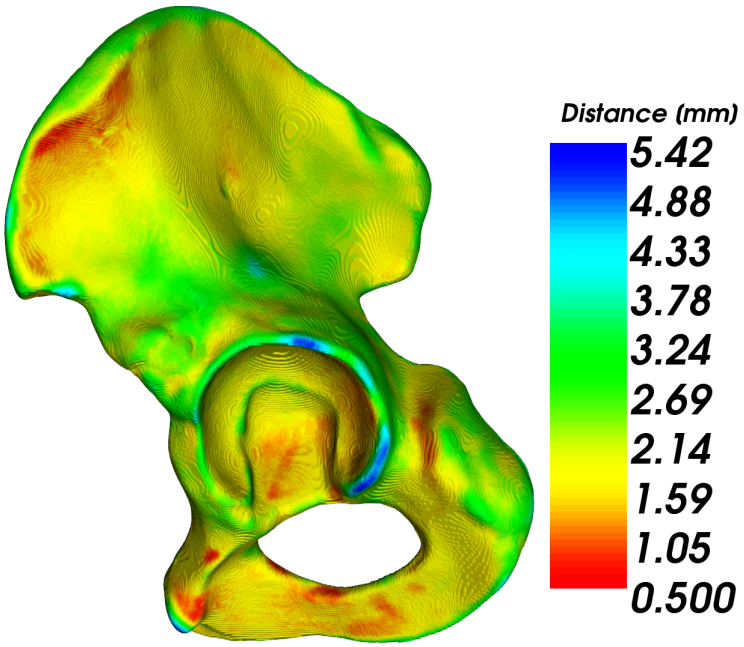

Figure 2.5: Thickness of cortical shell

2.2.2 Coordinate system

Anatomical markers are provided for building the coordinate system and for measuring procedure. Around the peripheral part of acetabula, the four landmarks were extracted (red and violin landmarkers – figure 2.6):

- **Landmark 7**: The most inferior point of the anterior end of the lunate surface of the acetabulum.
- **Landmark 8**: Point on the acetabulum margin corresponding to where ilium and *ilio-pubic ramus* meet.
- **Landmark 9**: Point on the acetabulum margin furthest away from landmark 7.
- **Landmark 10**: Point on the acetabulum margin furthest away from landmark 8.

The landmark number seven is associated with x - axis of the coordinate system. The rest landmarkers are follow:

- **Landmark 1**: Prominent point on the Pubis.
- **Landmark 2**: *ASIS* - the most superior point of the *illiac* spine.
- **Landmark 3**: The most anterior superior point of *illiac* crest.
- **Landmark 4**: *PSIS* - apex of the posterior superior *illiac* spine.
- **Landmark 5**: The most inferior point on *ischial* tuberosity.
- **Landmark 6**: The most inferior point on *ischial ramus*.

The global coordinate frame is based on the radiological planes. A linear affine transform was applied to get the coordinate system O_{GCS} suitable for positioning of the acetabular component. Translation vector is provided by location of fictions acetabular sphere. The radius and center was obtained with fitting procedure in sense of Non - linear Squares Method Minimization (NSMM) [189]. Rotation matrix was obtained through the built a plane XY from four points (7, 8, 9 and 10) placed on the acetabular rim. The normal vector of fitted plane was obtained by singular value decomposition technique (SVD) [190], [191]. Final rest two rotation vectors were obtain from the assumption that axe x is associated with the point 7 and due to orthogonal basic the third vector is a cross product of previous two. The graphical representation and transformation was provided with open source visualization library VTK (Kitware Inc., USA, Python wrapper. [192])

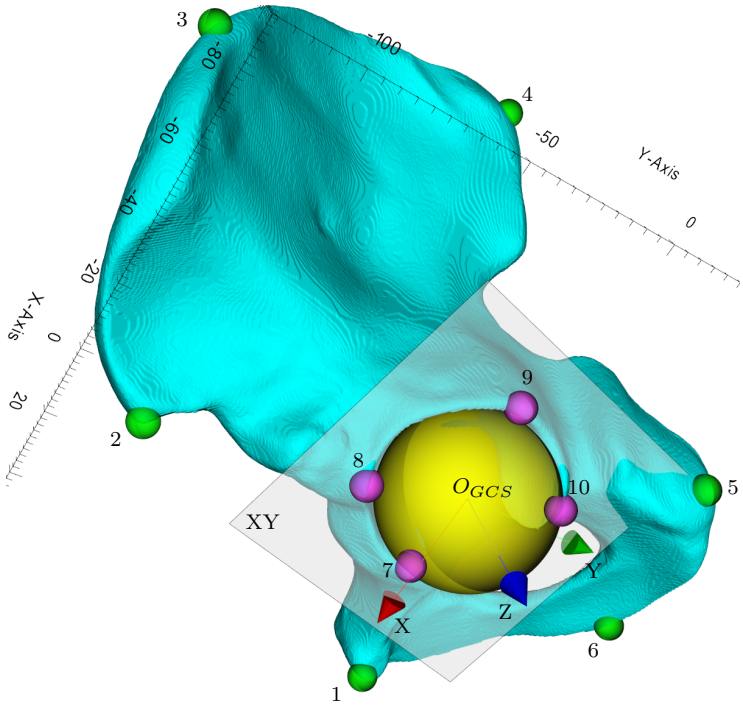

Figure 2.6: Anatomical landmarks on the pelvis model

2.3 Modeling of Material Field Based on Real Structural Data

Modeling of bone material properties consists of two important steps. Due to inhomogeneous bone structure, one can not use a simple approach based on the Young modulus constant on whole material domain. In the second step, typically, bone material properties are direct dependent, *i.e.* rather than using an isotropic model is much more accurate to account an orthotropic one or at least transversally isotropic one. With a combination of curved and closed structure like sandwich and mentioned steps, an accurate modeling of material field needs more carefully look. The modeling of bone anisotropy in sense of locally isotropic material properties is a common technique in many works [193], [194], [195]. Generally, it gives good results validated on static tests with small specimens. Works dealing with comparison the local isotropy and orthotropy show that there could be a significant accuracy improvement obtained using the orthotropic material model. The major discussion goes around the definition of principal direction of material. Often, the material directions are based on the principal stress direction or on technique of minimal/maximal variation of the density or fabric tensor of direction [196], [197], [198], [199]. These methods are employed to estimate the orthotropic properties, however there are various works, that successfully describe the bone as a transversally isotropic material. The transverse isotropy was successfully formulated for both part of the bone, i.e cortical and cancellous one [200], [201] and [202]. In this study on the

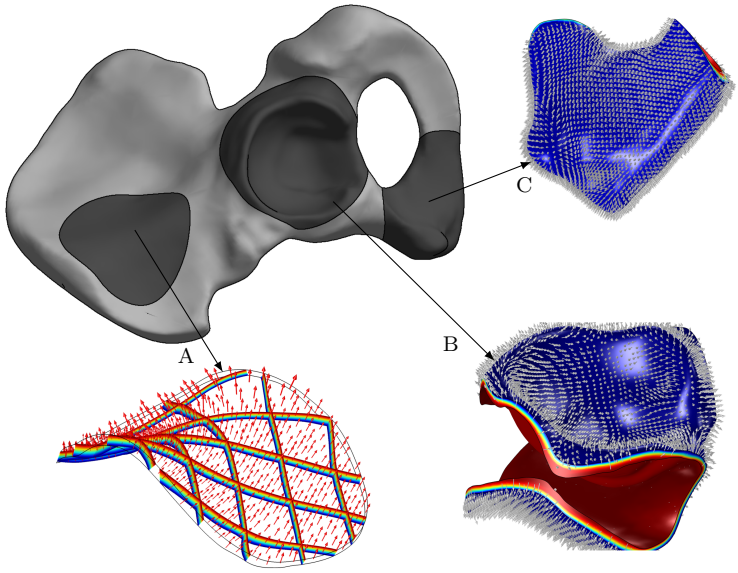

Figure 2.7: First principal vector derived from gradient of scalar field

synthetic pelvis bone, it will not be used pointed methods to describe material orientation, but the simple approach which could be more easy implement to a commercial software. The idea of this simple approach is based on the synthetically modeled coordinate field extracted from suitable sets of partial differential equations. The choose of suitable partial differential equations is in accordance with physical background (suitable scalar, vector or tensor field). These scalar, vector or tensor fields must fulfill defined requirements on boundaries and on directions of coordinates.

2.3.1 Simple Approach to Model Vector Field of Coordinates

The main idea is to find a vector field that is perpendicular to boundary normals. The basic dimensionless Laplace's partial differential equation is computed on the pelvis domain $\Omega \in R^3$. The details are provided in 2.7.3.

In the figure 2.7, three samples of cortical shell are depicted. The location A is selected on the *ischium* bone, the second one B is selected close to acetabular ring and the last one C is selected on the *ramus* bone. The surface coming from *ischium* part is quite flat without any significant curvature. On the other hand, the curvature of part coming from location B and C is very significant. It can be seen that vector field between inner and outer surfaces fulfills the request of a gradient direction suitable to define the first coordinate direction. The whole coordinate system is depicted in figure 2.8.

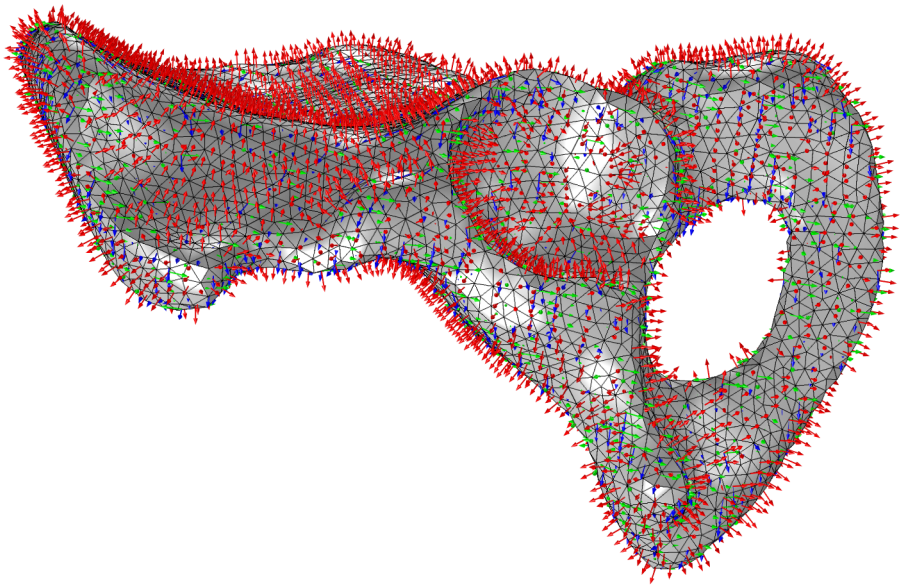

Figure 2.8: Principal vectors of coordinate field

2.3.2 Scalar Field of Material Properties

After defining the coordinate vector field, the next step is to define the scalar material field. The common procedure is based on the relationship between the CT gray values and bone density. After calibrating the CT scale (figure 2.9), the structural density and elasticity modulus could be directly gained from gray intensity according to:

$$\rho(x, y, z) = grayvalues_{three\ dim.array} \tag{2.1}$$

Parameters of orthotropic elasticity ($E_{11},\ E_{22} = E_{33}$) are defined as constants. Poisson ratio vector ($\nu_{12},\ \nu_{13},\ \nu_{23}$) is set to be a constant (0.3, 0.3, 0.3), *i.e.* independent on the structural density. Shear modulus $G_{12} = G_{13}$ is also taken to be a constant. The shear modulus G_{23} is computed as:

$$G_{23} = \frac{E_{22}}{2(1 + \nu_{12})} \tag{2.2}$$

The shear modulus G_{12} is not available in technical sheet of sawbone. Thus, initial values are taken from the literature [203], [204]:

$$G_{12} = 4.3\ GPa \tag{2.3}$$

Material density field represented in three dimensional grid points was interpolated by trilinear interpolation method. This method was preferred to Least Square fitting procedure for better performance with very similar results. Practically, due to a discretization error and a large scatter in structural density of each bone part, the calibration coefficients (figure 2.9)

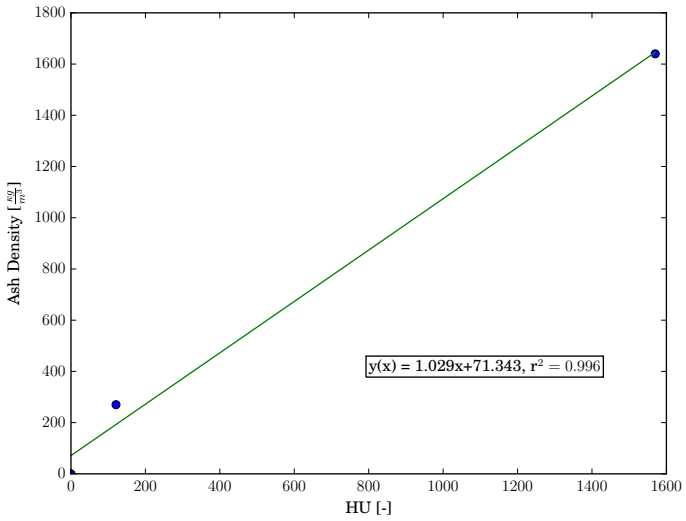

Figure 2.9: Relationship between CT HU and material density

are computed in such way, that a difference between real and model mass is minimized (for 1M mesh: difference 1.17 g, 125k mesh: 8.06 g). Nominal values of density are taken as mean ones. The adopted statistical approach (cluster analysis) simply explains why the magnitude of density on figure 2.10 is not equal to nominal one. In the figure 2.10 an example of the scalar field of density is shown for a raw FE mesh generated by CGAL Mesher. The mesh consists of around 1M linear elements. The field is interpolated by trilinear interpolation core and integrated in gauss points of mesh. The lower range of density is cut of, because due to small gaps in the model (technological gaps in synthetic pelvis bone). So, there should not be an element with density equal to zero.

2.4 Validation and Update of the Numerical Model

In order to validate and calibrate numerical model of the pelvis, the experimental modal analysis were performed. The modal analysis as comparison criterion was chosen because it is not a destructive test. Experimental results are compared with the numerical modal analysis of the computational model. The following steps were considered to take as the most accurate comparing as possible:

- Compute modal parameters from finite element model of the pelvis.
- Perform experimental modal analysis(EMA).
- Extract modal parameters from EMA by MIMO identification algorithms.
- Validation EMA results.
- Compare EMA results with numerical ones and consequently update numerical model.

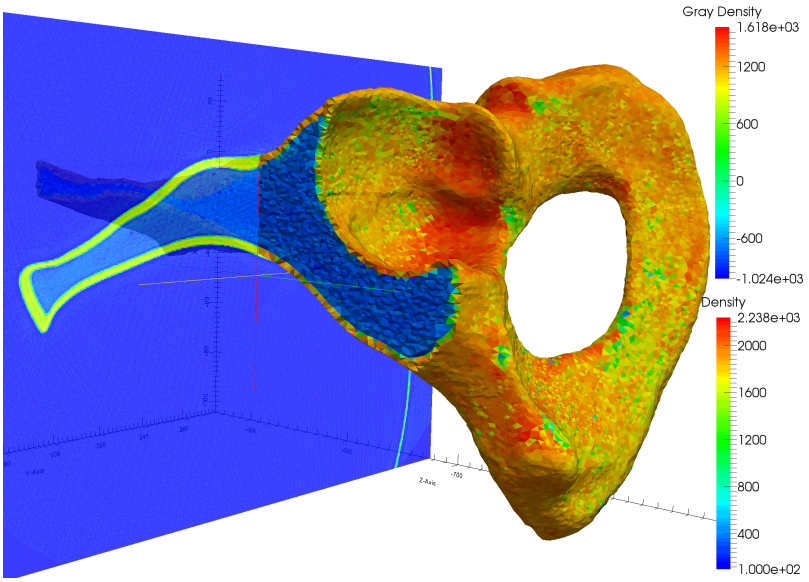

Figure 2.10: Scalar field of density $[\frac{kg}{m^3}]$

2.4.1 Numerical Modal Analysis of the Pelvis Bone Model

Finite element model was created in Comsol software (Comsol AB). Mesh convergence expressed at L_2 norm was monitored for the first five deformable modes. The convergence tolerance was set to 5 %. Two cases of mesh quality were considered. The best one consists of 2M elements with average length 0.6 mm for cortical shell and 4 mm for cancellous core. This mesh was taken as the converged one and it was referred with EMA results. The worst mesh consists of 100 000 elements with average length 4 mm for both part of the bone (figure 2.11). Boundary conditions are very simple. The model is in free-free mode that is suitable to sufficient replicate in real model. Geometry is replicated according to CT data. Material properties are modeled according to previous section 2.3. Linear tetrahedral element was selected. Energy dissipation was not considered. The solution was obtained with direct solver (MUMPS). The results are shown in table 2.3 and the convergence plot for first five modes in figure 2.12. Corresponding modal vectors are shown in figure 2.13. The vectors were normalized to M - norm ($v^T M v = 1$). It can be clearly recognized that the first mode is torsional, where the middle part (around acetabulum) makes a node and the ischium and ramus part are moving in anti - phase. The next modes are much more complicated, but it can still be recognized the combination of the bending and torsional shape.

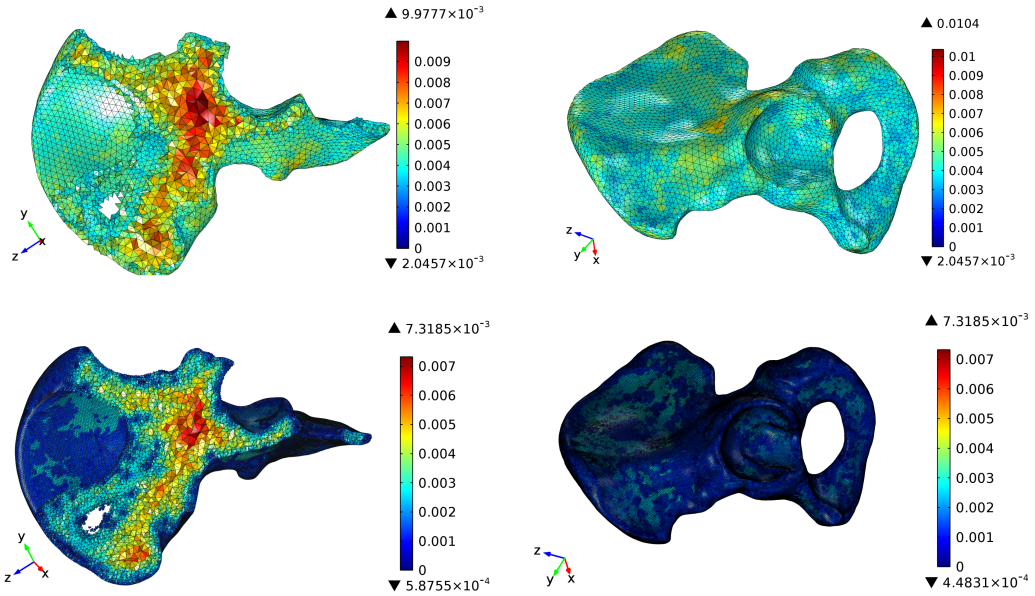

Figure 2.11: Finite element mesh scenarios [m]

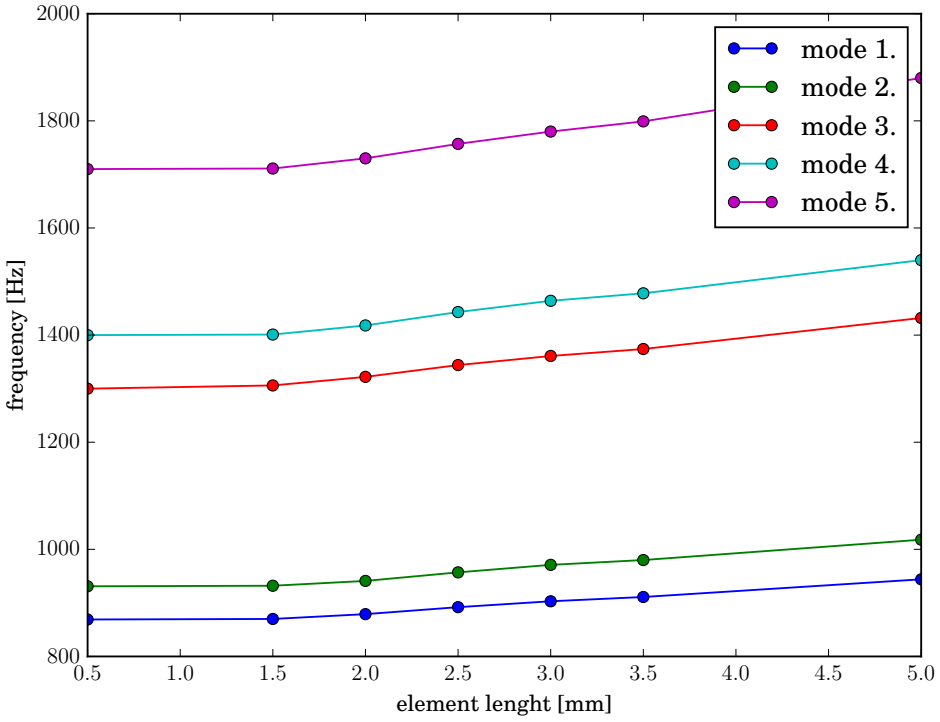

Figure 2.12: Convergence plot for the first five modes

Table 2.3: Natural frequencies of the numerical model [Hz]

# mode	converged mesh	worst mesh	error [%]
1.	870	944	8.51
2.	932	1018	9.23
3.	1306	1432	9.65
4.	1401	1540	9.92
5.	1711	1880	9.88

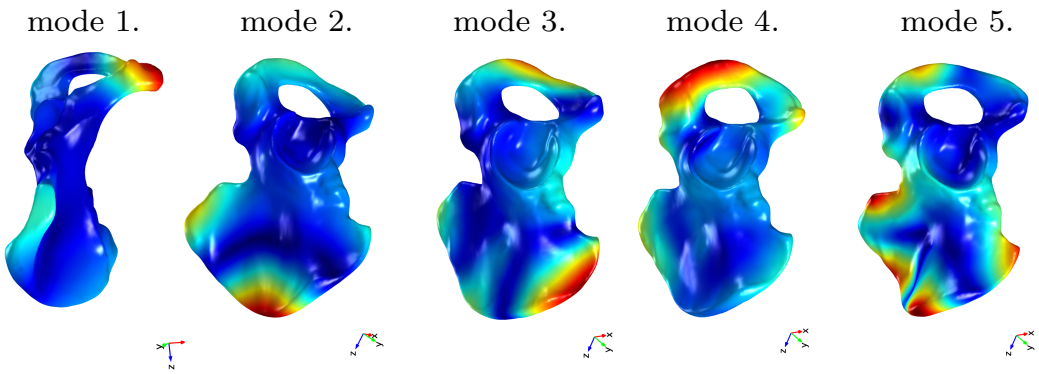

Figure 2.13: Modal shape vector of pelvis model from numerical analysis

2.4.2 Experimental modal analysis of the pelvis sawbone

Experimental modal analysis (EMA) was performed on the sawbone of the right hemipelvis. As excitation source, an impact hammer with hard tip was used. The chosen of only one driven point seems to be enough for accurate description of dynamical behavior of the pelvis bone. For adequate acquiring, 228 points were excited. These 228 points are normal degree of freedom (DOF). Obtained response is always just the projection of the response to a surface normal as the excitation as well. The points were selected in grid with approximate distance (10 mm) between each nodes (figure 2.14). Modal analysis were performed with configuration in table 2.4. The output of frequency response estimator is composed from real, imaginary part and coherence function formulated according H_1. The pelvis bone was placed on a soft foam. First rigid mode starts in frequency at 18 Hz. This is far enough from the first deformable mode (879.23 Hz), thus it could be taken as a boundary that does not affect the free - free configuration of the pelvis model. The mass loading effect could not occur because the used accelerometer is only 3 g weight. The whole pelvis is 317.29 g. The reciprocity test showed the correlation between two FRFs $r^2 = 92$ % ($p < 0.001$).

(a) Experimental configuration(DAQ, accelerometer and impact hammer)

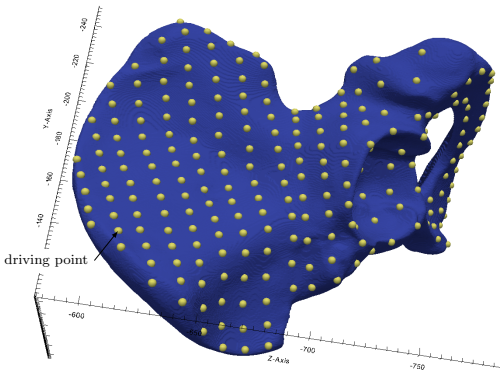

(b) Measuring grid

Figure 2.14: Measuring configuration and virtual grid on the geometry of pelvis

Table 2.4: Configuration of modal analysis experiment

sampling frequency [Hz]	4000
FFT block size[samples]	4000
window	exponential
trigger level [N]	10 %
pre-trigger samples [samples]	100
FRF estimator	H_1
averaging	RMS
number of hint	10
weighting mode	linear

2.4.3 MIMO Identification of Modal Parameters

The modal parameters were extracted from frequency response at each normal DOF. For this purpose the algorithm based on the least square complex frequency (LSCF) was employed. To refine the results (add FRF (co)variances), extended iterative stochastic algorithm in sense of Maximum likelihood (ML) was developed [205], [206], [207], [208], [209]. All algorithms are coded in Python language (www.python.org), critical part are implemented in C, with Math Kernel Library support (MKL). An average of all FRFs is shown in bode plot depicted in figure 2.15. The natural frequency, damping ratio, residues and uncertainty parameters were extracted (table 2.5). For finite model update, proportional damping scalar coefficients were calculated ($\alpha = 0.589674332,\ \beta = 1.48727709e-06$). The identified frequencies are clearly seen in so called stabilization diagram (figure 2.16). Where red dots mean poles which are not stable (i.e., real part is positive). Green dots mean the stable pole, but the damping ratio is out of range (0.05 - 10 %). Finally, black circles mean the stable physical pole. The

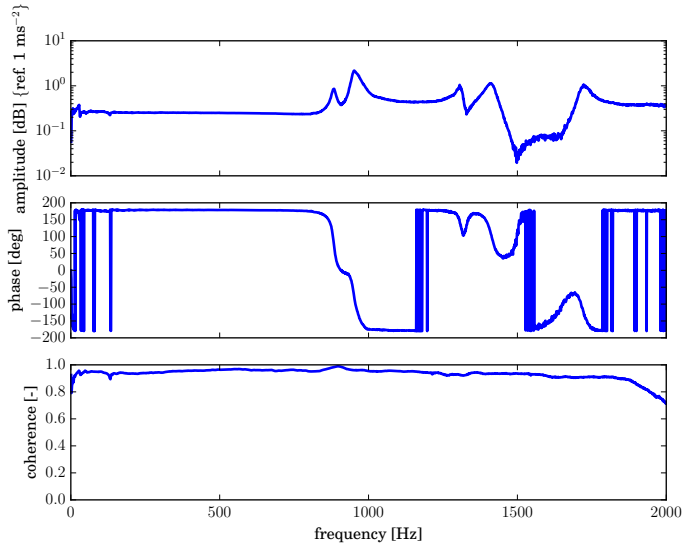

Figure 2.15: Bode plot for averaged FRF

Table 2.5: Identified Modal Parameters

# mode	f [Hz]	σ_f [Hz]	ξ [%]	σ_ξ [%]	MPC [-]
1.	879.23	0.09363	0.8315	0.0106	0.9826
2.	952.51	0.07241	0.9454	0.00753	0.9201
3.	1304.63	0.1919	1.048	0.0143	0.9715
4.	1408.76	0.2814	1.286	0.0197	0.9398
5.	1719.93	0.2415	1.259	0.013	0.9712

stabilization diagram was constructed for 25 orders of the polynomial base. However it is clear that the order of this system is much smaller (fifth order), the over modeling is acceptable to recognize unstable computational poles from stable physical ones. The stabilization diagram shows the average of all FRFs. For real polynomial coefficients, the desired order is reached with the doubled one.

2.4.4 Validation EMA Results

To achieve high quality modal model, it is necessary to validate modal parameters. For this purpose, there are several approaches based on the correlation between each modal shape vectors [210], [211], [212]. Due to low level excitation or low SNR ratio, the mode could not be well excited and than it could face the low degree of orthogonality to the others modes. The idea of vector orthogonality is used in MAC (modal assurance criterion). Another criteria, developed for the shape vector, is MVC (Modal Vector Complexity), MPC (Modal Phase Collinearity) which basically mean the degree of the vector complexity. The auto MAC matrix

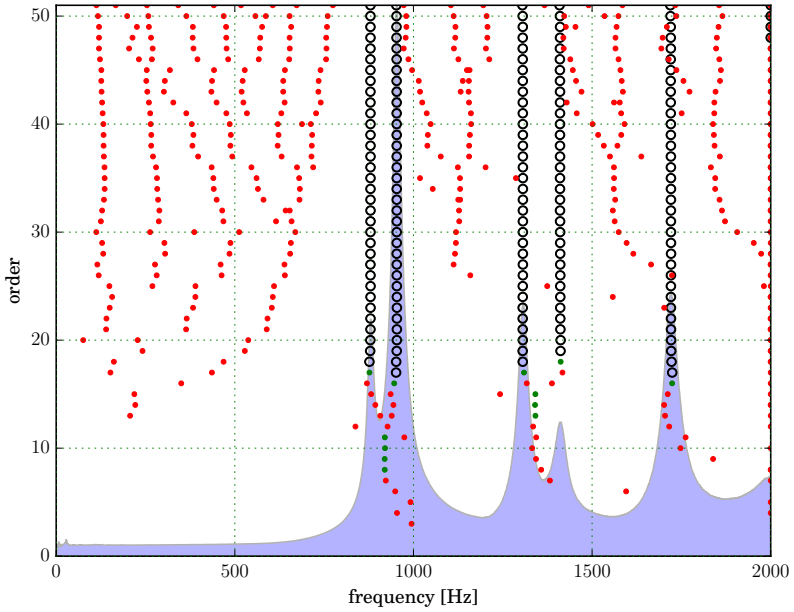

Figure 2.16: Stabilization plot up to twenty fiftieth order

is represented by the bar graph (figure 2.17). The value close to one means no orthogonality between two vectors and the value close to zero means existing orthogonality between two vectors. In the picture is clearly seen that are almost orthogonal. The MSF (Modal Scale Factor) gives the additional information about the proportionality between two vectors(figure 2.17). The vector complexity is graphically shown in figure 2.18. It can be seen that second mode is slightly more complex.

2.4.5 Comparing

The modal frequency and modal shape vector from experimental modal analysis are correlated with the numerical modal output. The frequency correlation is expressed in relative error term in table 2.6. Modal shapes correlation is expressed in MAC values (figure 2.19) and visual

Table 2.6: Relative error between experimental and numerical results (natural frequency [Hz])

# mode	experimental	numerical (converged mesh)	error [%]
1.	879.23	870.33	1.02
2.	952.51	932.94	2.11
3.	1304.63	1306.12	0.15
4.	1408.76	1401.22	0.49
5.	1719.93	1711.54	0.47

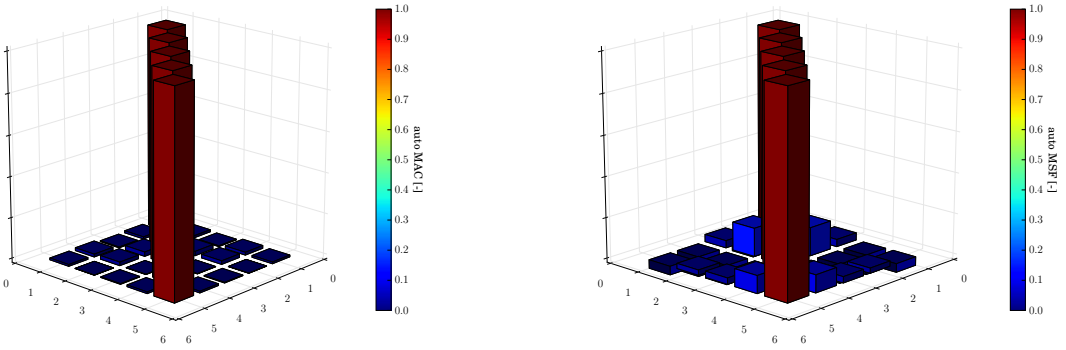

(a) Auto MAC

(b) Auto MSF

Figure 2.17: Auto MAC and auto MSF of identified modal shape vectors

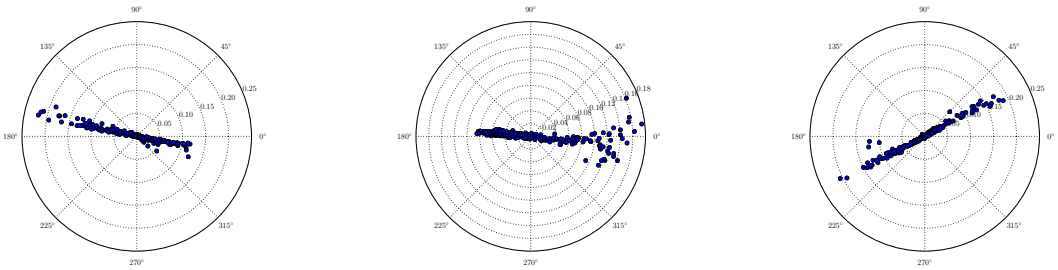

(a) mode 1.

(b) mode 2.

(c) mode 3.

(d) mode 4.

(e) mode 5.

Figure 2.18: Modal vector complexity

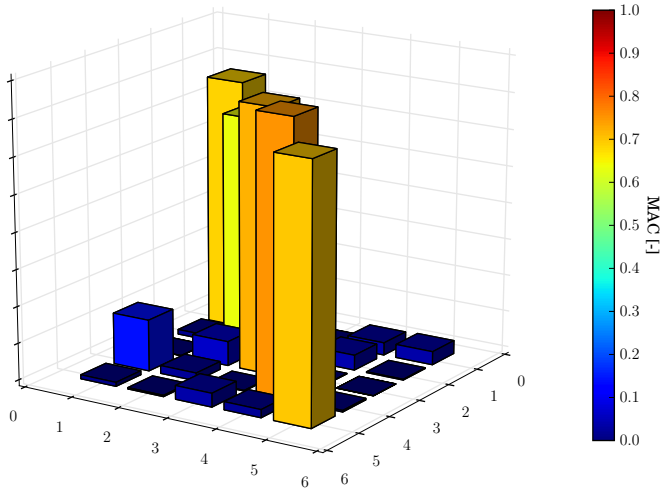

Figure 2.19: MAC correlation between EMA and numerical results

correlation (figure 2.20). Because the experimental shape vectors are obtained in the normal DOF (in outer normals of pelvis surface), also the numerical modes have to be projected to the normals of the outer surface. The experimental modal shapes correlated well with numerical ones, computed in Comsol. The worst correlation was found for the second mode (MAC = 65 %). Usually the threshold 65 % is taken as the bottom range to recognize the mode as correlated.

2.5 Update of FE Model

However the model is accurate with the initial parameters, the model would be updated with experimental results from modal analysis. In this thesis, an update technique based on sensitivity analysis is employed. The updating procedure is described in chapter 2.7.4. Basically, it is an optimization process, where the objective function is minimized in sense of natural frequency from EMA and FE model. The material constants described in previous section are the minimization parameters. After obtaining a converged solution of iteration solver (usually 3 - 10 iterations, figures 2.21, 2.22), the updated material parameters are gained (table 2.7). Together with sensitivity analysis (figure 2.23) and assumptions that material parameters are normally distributed, standard deviation can be optionally described (tabs. 2.7 and 2.8).

Table 2.7: Updated material parameter [GPa]

G_{12}	$\sigma_{G_{12}}$
4.531	0.0122

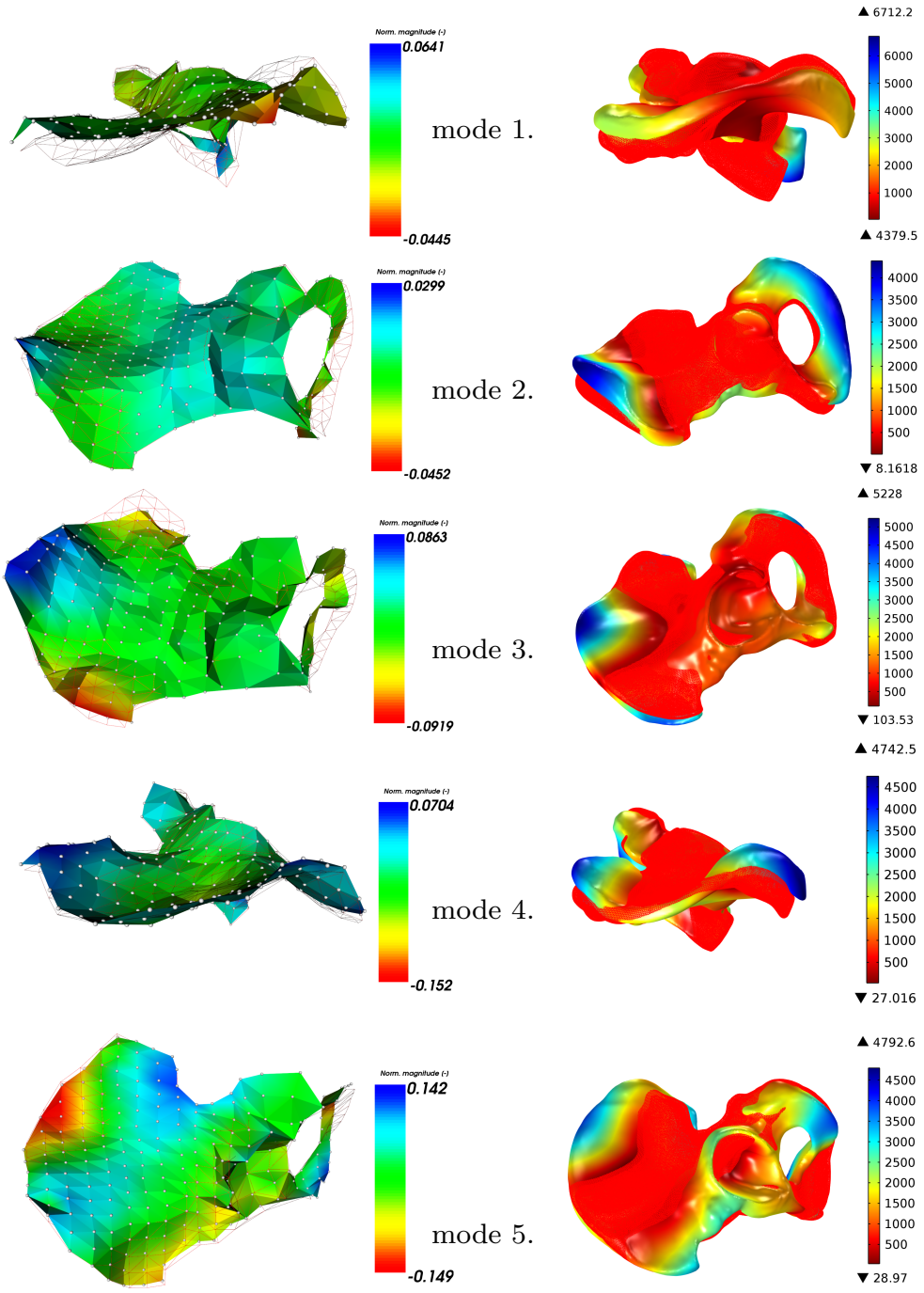

Figure 2.20: Modal shape vectors from EMA and from numerical modal analysis

```
-----------------------------------------------Start Iterations-----------------------------------------------

                                                                  --Num. of Calls--                --Time Elaps.--
Step     StabPar.   SubCost fun   epsF.     epsX.     Cond       Fun       Jac       Success    FEM        SENS.
-------------------------------------------------------------------------------------------------------------------
0        1.0        1.44e-07      0.00497   0.0443    10.4       120       20        1          26.3       1.06e+02
1        1.0        5.27e-08      0.00373   0.0338    10.5       120       20        1          27.1       1.07e+02
2        1.0        5.3e-14       8.53e-05  0.0012    10.7       114       19        1          26.5       1.06e+02
3        1.0        1.65e-17      1.09e-07  1.31e-06  10.7       101       15        1          29.2       1.06e+02
4        1.0        1.23e-17      1.17e-09  2.05e-09  10.7       29        3         1          27.3       1.08e+02
5        1.0        1.23e-17      1.21e-09  6.66e-20  10.7       17        1         1          27.6       1.08e+02
-----------------------------------------------SOLUTION CONVERGED-----------------------------------------------
```

Figure 2.21: Iteration solver output - a converged solution

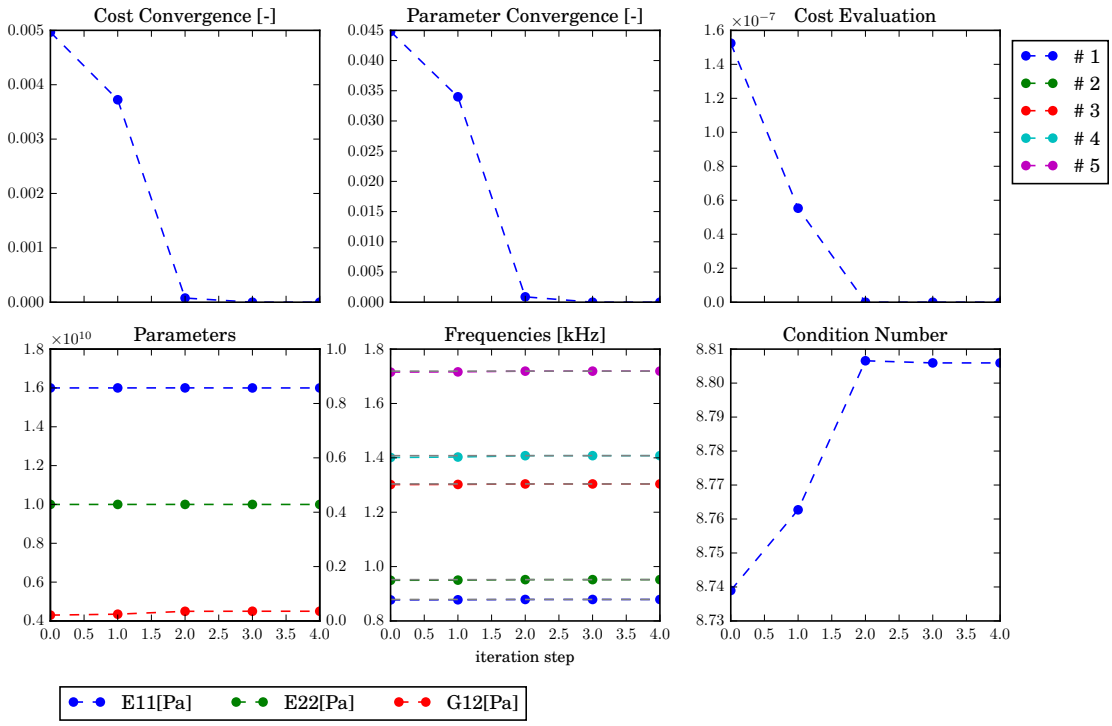

Figure 2.22: Solver performance - a converged solution

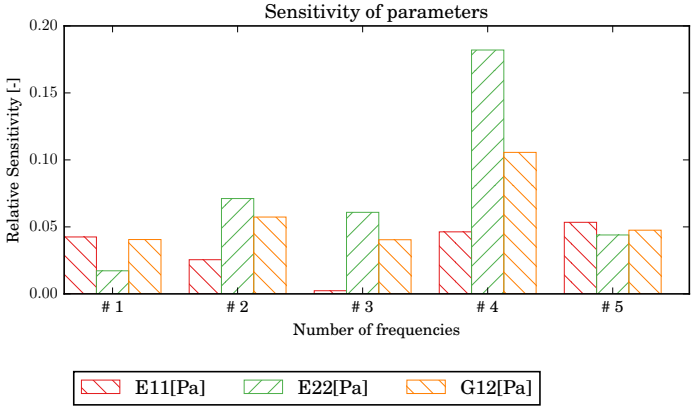

Figure 2.23: Parameter sensitivity - a converged solution

Table 2.8: Updated relative error between experimental and numerical results (natural frequency [Hz])

# mode	experimental	numerical (converged mesh)	error [%]
1.	879.23	879.21	0.002
2.	952.51	952.01	0.053
3.	1304.63	1304.98	0.027
4.	1408.76	1408.95	0.014
5.	1719.93	1719.11	0.048

2.6 Summary

This section describes a complete survey of modeling and validation of computational model of the pelvis. The computational model is represented in discretized form suitable for finite element method. It provides a complex material properties based on the real bone. In this case the real data are based on the simplified synthetic bone model. The real bone data are not available yet and even are not suitable for the first validation process, which is mainly focused on the proposed algorithm. But, in the possible future work, the use of data from real bone could increase the model versatility. The geometry of the pelvis bone was segmented with semi automatic process based on the sophisticate machine learning and graph cut algorithms. The orthotropic material behavior of the bone was modeled with approach based on the like - diffusion process. This implementation requires only small amount of the computational time because of solving just simple Laplace equation with easy boundary conditions. It would be pointed out that it is a method, which not reflects the real physical behavior, but just fits the orthonormal direction of the material field as well as possible in contrast the method that are based on the Wolf's law or haversian system orientation [197], [213]. The material field generated with diffusion equation could be problematic in some very sharp corners. It is possible to make some tune up with the coefficients or use it another class of equations which have a similar properties suitable for modeling the vector coordinate field. The composite structure of the bone was modeled as inner and outer surface by manual way - this is a drawback of proposed model of vector field, which needs specify the boundaries explicitly. In a future work a more robust solution based on the combination of the finite element meshing algorithm, graph cut partitioning to formulate appropriate boundaries automatically would be used. Validation process based on the experimental modal analysis was used because it is non destructive test, however possible just in the sense of expectation of the linear properties of the specimen under the test. The modal analysis has been recognized useful in problematic pelvis bone in real in vitro environment, but with some limitation [214], [215], [216]. The pelvis bone has a quite difficult geometry and the damping properties are not available yet. It is a time consuming process, but it leads to very important results to help to understand

the biomechanical behavior of the pelvis bone. In this chapter the EMA was successfully used to correlate finite element model with experimental results with very good agreement (MAC in range 65 - 85 %). Also the simple damping properties were extracted (damping ratio or Rayleigh coefficients). This model expects the proportional damping, however some shape vectors were slightly complex. It suggest some errors in validation process, or the non proportional behavior of the damping. In case of real pelvis bone it is necessary to refine the damping model and use more sophisticated registration of measuring grid. In this experimental modal analysis the stochastic/deterministic identification algorithms successfully used in common structural engineering were employed. The refinement of material properties was done by the sensitivity based optimization scheme. This update leads to an accurate identification of linear material properties with uncertainty level including the uncertainties of experimental frequencies, initial material guess and discretization process.

2.7 Theoretical Background

2.7.1 Estimation of Modal Parameters

Formulation of Transfer Matrix

The estimation framework is based on the optimization procedure on the experimental frequency response of linear invariant system in so called *Matrix Description formulation*. Consider Newton's equation of motion:

$$M\ddot{x}(t) + C\dot{x}(t) + Kx(t) = f(t) \tag{2.4}$$

With M, C and K respectively the mass, damping and stiffness matrices, and $f(t)$, $x(t)$ the applied force and structural response vector. The frequency equivalent given by the Laplace transform is formulated as:

$$G(s)X(s) = F(s) \tag{2.5}$$

where $G(s) = Ms^2 + Cs + K$ is the dynamic stiffness. After a matrix inversion this yields

$$F(s)H(s) = X(s) \tag{2.6}$$

With $H(s)$ the transfer function matrix. This can by further expressed as

$$H(s) = G(s)^{-1} = \frac{G_{adf}(s)}{|G(s)|} \tag{2.7}$$

The numerator G_{adj} is an $(N_m \times N_m)$ matrix of polynomials of order $2(N_m - 1)$. The denominator is a polynomial of order $2N_m$. Both are in the s - domain. Therefore, Eq. (2.7) could

be rewritten

$$H(s) = \frac{B(s)}{A(s)} = \frac{\begin{pmatrix} B_{1,1}(s) & \cdots & B_{1,N_m}(s) \\ \vdots & \ddots & \vdots \\ B_{N_m,1}(s) & \cdots & B_{N_m,N_m}(s) \end{pmatrix}}{A(s)} \tag{2.8}$$

This formulation of the transfer function matrix is also called *common denominator model* and it is a special case of the more general Matrix Fraction Description (MFD) applied in Polyreference Least Square Complex Frequency Estimator (PLSCF) [217], [218]. In order to get the modal residue matrices, a pole - residue parametrization is useful.

$$H(s) = \sum_{r=1}^{N_m} \frac{R_r}{s - p_r} + \sum_{r=1}^{N_m} \frac{R_r^*}{s - p_r^*} \tag{2.9}$$

with p_r and R_r the poles and $(N_m \times N_m)$ residue matrices of r^{th} mode. Further, to get the modal shape ϕ_r and modal participation factor vector L_r, the non defective residue matrix can be decomposed as [219]

$$R_r = Q_r \phi_r \phi_r^T = \phi_r L_r^T \tag{2.10}$$

The estimation model according Eq. (2.8) at discrete frequency f between output o and input i is modeled as

$$\hat{H}_k(\Omega_f, \vartheta) = \frac{B_k(\Omega_f, \vartheta)}{A(\Omega_f, \vartheta)} \tag{2.11}$$

where

$$B_k(\Omega_f, \vartheta) = \sum_{j=0}^{n} b_{kj} \Omega_f^j, \;\; A(\Omega_f, \vartheta) = \sum_{j=0}^{n} a_j \Omega_f^j \tag{2.12}$$

for $k = 1, 2, ..., N_o N_i$ and order n. The coefficients $a_j, \; b_{kj}$ are the unknown parameters ϑ to be estimated. A discrete time domain model with generalized transform variable Ω_f is used.

$$\Omega_f = e^{-i\omega_f T_s} \tag{2.13}$$

To obtain non - trivial solution of Eq. (2.11), the constraint must be imposed, for example, fixing the highest denominator coefficient , *i.e.* $a_n = 1$. After linearisation proposed in [220], the model from Eq. (2.11) can be estimated as

$$W_k(\omega_f) \left(\sum_{j=0}^{n} b_{kj} \Omega_f^j - \sum_{j=0}^{n} a_j \Omega_f^j H_k(\omega_f) \right) \approx 0 \tag{2.14}$$

for $k = 1, ...N_o N_i$ and $f = 1, ...N_f$ the number of spectral lines. The quality of the estimation in sense least squares and further maximum likelihood is improved by introducing weighting function $W_k(\omega_f)$. The choice of this function is discussed later. The cost function to minimize

according to least square sense is given

$$l(\vartheta)_{LS} = \sum_{k=1}^{N_o N_i} \sum_{f=1}^{N_f} |B_k(\Omega_f, \vartheta) W_k(\omega_f) - A(\Omega_f, \vartheta) H_k(\omega_f) W_k(\omega_f)|^2 \tag{2.15}$$

Linearized Least Square Solution

A least square solution of Eq. (2.15) is formulated with explicit Jacobi matrix J as

$$J^H J \vartheta = 0 \tag{2.16}$$

where the expression $J^H J$ has a following structure

$$J^H J = \begin{pmatrix} \Gamma_1^H \Gamma_1 & 0 & \cdots & \Gamma_1^H \Phi_1 \\ 0 & \Gamma_2^H \Gamma_2 & \cdots & \Gamma_2^H \Phi_2 \\ \vdots & \vdots & \ddots & \vdots \\ \Phi_1^H \Gamma_1 & \Phi_2^H \Gamma_2 & \cdots & \sum_{k=1}^{N_o N_i} \Phi_k^H \Phi_k \end{pmatrix} \tag{2.17}$$

With the entries of the submatrices given as

$$\begin{aligned} [\Gamma_k^H \Gamma_k]_{rs} &= \sum_{f=1}^{N_f} |W_k(\omega_f)|^2 {\Omega_f^{r-1}}^H \Omega_f^{s-1} \\ [\Phi_k^H \Phi_k]_{rs} &= \sum_{f=1}^{N_f} |W_k(\omega_f) H_k(\omega_f)|^2 {\Omega_f^{r-1}}^H \Omega_f^{s-1} \\ [\Gamma_k^H \Phi_k]_{rs} &= -\sum_{f=1}^{N_f} |W_k(\omega_f)|^2 H_k(\omega_f) {\Omega_f^{r-1}}^H \Omega_f^{s-1} \end{aligned} \tag{2.18}$$

The structure of these submatrices is a Toeplitz one and could be efficiently constructed by the FFT algorithm. Since the submatrices $\Gamma_k^H \Gamma_k$ are not subjected to errors and the parameter constraint affected only the denominator coefficients ϑ_A, the numerator coefficients ϑ_{B_k}can be eliminated from the Eqs. (2.17).

$$\vartheta_{B_k} = -[\Gamma_k^H \Gamma_k]^{-1} [\Gamma_k^H \Phi_k] \vartheta_A \tag{2.19}$$

and therefore, the solution for the denominator coefficients ϑ_A

$$\left[\sum_{k=1}^{N_o N_i} [\Phi_k^H \Phi_k] - [\Gamma_k^H \Phi_k]^H [\Gamma_k^H \Gamma_k]^{-1} [\Gamma_k^H \Phi_k] \right] \vartheta_A = D \vartheta_A \approx 0 \tag{2.20}$$

Which is found as

$$\vartheta_{A_{LS}} = \begin{pmatrix} -D[1:n, 1:n]^{-1} D[1:n, n+1] \\ 1 \end{pmatrix} \tag{2.21}$$

Another possibility solution for denominator coefficients is to force the norm $A^T A = 1$. This yields to a generalized eigenvalue problem with diagonalized covariance matrix on the right side(Generalized mixed Least Square - GTLS).

The roots of the computed denominator polynomial $A(\Omega, \vartheta_A)$ have to be transformed to the Laplace domain in sense of impulse - invariant transformation ($z = e^{sT_s}$). Than, from the poles (roots) p_r ($r = 1, ..., N_m$) the modal damped frequency f_{dr} and damping ratio ζ_r are obtained

$$f_{dr} = \frac{\mathbf{Im}(p_r)}{2\pi}, \ \zeta_r = \frac{\mathbf{Re}(p_r)}{|p_r|} \tag{2.22}$$

Residue matrix R_r ($N_o \times N_i$) is computed from the coefficients ϑ as

$$R_{kr} = \lim_{\Omega \to p_r} \hat{H}_k(\Omega, \vartheta)(\Omega - p_r) \tag{2.23}$$

Maximum Likelihood Estimator

With assumption that model uncorrelated FRFs are complex normally distributed, the maximum likelihood cost function is

$$l(\vartheta) = \sum_{k=1}^{N_o N_i} \sum_{f=1}^{N_f} W_k(\omega_f)^2 \frac{|\hat{H}_k(\Omega_f, \vartheta) - H_k(\omega_f)|^2}{\mathbf{var}(H_k(\omega_f))} \tag{2.24}$$

The solution is obtained by minimization of the non - linear cost function Eq.(2.24) respect to the parameters ϑ. Due to quadratic cost function, the Gauss - Newton like algorithm is used to solve the optimization problem. The m^{th} G - S iteration step solved for $\delta\vartheta$ is given as

$$J_m^H J_m \delta\vartheta = -J_m^H e_m \tag{2.25}$$

where e_m is the residual vector and J_m the Jacobian matrix. The residual vector is defined as

$$e(\vartheta) = \begin{pmatrix} W_1(\omega_1)\dfrac{\hat{H}_1(\omega_1,\vartheta) - H_1(\omega_1)}{\mathbf{var}(H_1(\omega_1))} \\ \vdots \\ W_1(\omega_{N_f})\dfrac{\hat{H}_1(\omega_{N_f},\vartheta) - H_1(\omega_{N_f})}{\mathbf{var}(H_1(\omega_{N_f}))} \\ W_2(\omega_1)\dfrac{\hat{H}_2(\omega_1,\vartheta) - H_2(\omega_1)}{\mathbf{var}(H_2(\omega_1))} \\ \vdots \\ W_{N_oN_i}(\omega_{N_f})\dfrac{\hat{H}_{N_oN_i}(\omega_{N_f},\vartheta) - H_{N_oN_i}(\omega_{N_f})}{\mathbf{var}(H_{N_oN_i}(\omega_{N_f}))} \end{pmatrix} \tag{2.26}$$

The explicit Jacobi matrix has the same block structure as Jacobi matrix (2.17) with submatrices Γ_k and Φ_k.

$$\Gamma_k = \begin{pmatrix} W_k(\omega_1)\dfrac{\Omega^0(\omega_1)}{\sqrt{\mathbf{var}(H_k(\omega_1))}A(\omega_1,\vartheta)} & \cdots & W_k(\omega_1)\dfrac{\Omega^n(\omega_1)}{\sqrt{\mathbf{var}(H_k(\omega_1))}A(\omega_1,\vartheta)} \\ \vdots & \cdots & \vdots \\ W_k(\omega_{N_f})\dfrac{\Omega^0(\omega_{N_f})}{\sqrt{\mathbf{var}(H_k(\omega_{N_f}))}A(\omega_{N_f},\vartheta)} & \cdots & W_k(\omega_{N_f})\dfrac{\Omega^n(\omega_{N_f})}{\sqrt{\mathbf{var}(H_k(\omega_{N_f}))}A(\omega_{N_f},\vartheta)} \end{pmatrix} \tag{2.27}$$

and

$$\Phi_k = \begin{pmatrix} -W_k(\omega_1)\dfrac{\Omega^0(\omega_1)B_k(\omega_1,\vartheta)}{\sqrt{\mathbf{var}(H_k(\omega_1))}|A(\omega_1,\vartheta)|^2} & \cdots & -W_k(\omega_1)\dfrac{\Omega^n(\omega_1)B_k(\omega_1,\vartheta)}{\sqrt{\mathbf{var}(H_k(\omega_1))}|A(\omega_1,\vartheta)|^2} \\ \vdots & \cdots & \vdots \\ -W_k(\omega_{N_f})\dfrac{\Omega^0(\omega_{N_f})B_k(\omega_{N_f},\vartheta)}{\sqrt{\mathbf{var}(H_k(\omega_{N_f}))}|A(\omega_{N_f},\vartheta)|^2} & \cdots & -W_k(\omega_{N_f})\dfrac{\Omega^n(\omega_{N_f})B_k(\omega_{N_f},\vartheta)}{\sqrt{\mathbf{var}(H_k(\omega_{N_f}))}|A(\omega_{N_f},\vartheta)|^2} \end{pmatrix} \tag{2.28}$$

Thus, the solution is rewritten as

$$\begin{pmatrix} \Gamma_1^H\Gamma_1 & 0 & \cdots & \Gamma_1^H\Phi_1 \\ 0 & \Gamma_2^H\Gamma_2 & \cdots & \Gamma_2^H\Phi_2 \\ \vdots & \vdots & \ddots & \vdots \\ \Phi_1^H\Gamma_1 & \Phi_2^H\Gamma_2 & \cdots & \sum_{k=1}^{N_oN_i}\Phi_k^H\Phi_k \end{pmatrix} \begin{pmatrix} \delta\vartheta_{B_1} \\ \delta\vartheta_{B_2} \\ \vdots \\ \delta\vartheta_{B_{N_oN_i}} \\ \delta\vartheta_A \end{pmatrix} = - \begin{pmatrix} \Phi_1^H\Phi_1 e_1 \\ \Phi_2^H\Phi_2 e_2 \\ \vdots \\ \Phi_{N_oN_i}^H\Phi_{N_oN_i}e_{N_oN_i} \\ \sum_{k=1}^{N_oN_i}\Phi_k^H e_k \end{pmatrix} \tag{2.29}$$

According to decoupling denominator and numerator parameters in Eq. (2.19), the perturbation $\delta\vartheta_{B_k}$ of the parameters ϑ_{B_k} can be computed

$$\delta\vartheta_{B_k} = -[\Gamma_k^H\Gamma_k]^{-1}\left([\Phi_k^H\Phi_k]^H e_k + [\Gamma_k^H\Phi_k]\delta\vartheta_A\right) \tag{2.30}$$

And finally, the solution of the perturbation $\delta\vartheta_A$ can be computed according to elimination on Eqs. (2.25) and (2.30)

$$\left[\sum_{k=1}^{N_oN_i}[\Phi_k^H\Phi_k] - [\Gamma_k^H\Phi_k]^H[\Gamma_k^H\Gamma_k]^{-1}[\Gamma_k^H\Phi_k]\right]\delta\vartheta_A = -\left[\sum_{k=1}^{N_oN_i}\Phi_k^H - [\Gamma_k^H\Phi_k]^H[\Gamma_k^H\Gamma_k]^{-1}\Gamma_k^H\right]e_k \tag{2.31}$$

Choice of Weighting Function

The weighting function improves the LS estimator performance. In this estimator, a deterministic weighting function was selected according to [221] for the iterative approach as function of parameters from previous step

$$W_k^2(\omega_f) = \frac{1}{|A(\omega_f,\vartheta_{m-1})|^2} \tag{2.32}$$

In the case of linear solution, the weighting function is [222]

$$W_k^2(\omega_f) = \frac{|H_k(\omega_f)|^2}{\mathbf{var}(H_k(\omega_f))} \tag{2.33}$$

Computational Notes

The expression of the ϑ_A coefficients is done by substituting the Eq. (2.19) to the last $n+1$ equations in Eq. (2.16). The G - S iteration scheme uses the well known algorithm named Levenberg - Marquardt with additional Fletcher's modification. The main advantages of proposed algorithm is the adaptive control of the iteration step (*i.e.* it is a combination of the Gauss - Newton and gradient descent method) [223], [224], [225]. More information about the implementation remarks can be found in [226], [227] and [228].

Estimation of Uncertainties

The uncertainty propagation framework is based on the [229], [230], [231]. Due to statistical nature of ML estimator, it is possible derive the Gaussian uncertainties of the modal parameters from the covariance matrix of common denominator parameters in the last converged iteration step. Thus, the covariance matrix of poles is computed by linearisation as

$$Cov(z) \approx \frac{\partial z}{\partial d}Cov(d)\left(\frac{\partial z}{\partial d}\right)^T \tag{2.34}$$

Where the differentiation of poles z respect to denominator coefficients d is computed according to [232]. After transforming the covariance matrix of poles into Laplace domain via Impulse Invariant Transform, the variance of poles, frequency and damping can be computed.

2.7.2 Modal Quality Factors

Modal Assurance Criterion (MAC)

The reliability and quality of the estimated model is expressed in a well known comparing of two vectors, in modal analysis called as MAC (Modal Assurance Criterion). This evaluating variable is formulated for the two real or complex valued vectors as

$$MAC(\psi_1, \psi_2) = \frac{\left(\mid \psi_1^H \cdot \psi_2| + |\psi_1^T \cdot \psi_2|\right)^2}{\left(\psi_1^H \cdot \psi_1 + |\psi_1^T \cdot \psi_1|\right)\left(\psi_2^H \cdot \psi_2 + |\psi_2^T \cdot \psi_2|\right)} \tag{2.35}$$

This is an extended expression of the MAC from [210]. It avoids some drawbacks of the classical MAC.

Modal Phase Collinearity (MPC)

In order to quantify if the vector is monophase (close to real valued vector), the variances and covariances between real and imaginary part is evaluated [233], which results to a simple expression

$$MPC(\psi) = \left(\frac{\mid \psi^H \cdot \psi^*|}{\|\psi\| \cdot \|\psi^*\|}\right)^2 \tag{2.36}$$

Modal Scale Factor (MSF)

The function of modal scale factor provides a normalized estimate of modal participation factors for two references of a specified mode [211].

$$MSF(\psi_1, \psi_2) = \frac{\psi_1^H \cdot \psi_2^*}{\psi_1^H \cdot \psi_1^*} \tag{2.37}$$

2.7.3 Coordinate Field Formulation

The coordinate field was interpreted as a simple vector field, where only normal component is computed from scalar field defined by the Laplace equation presented a potential field.

$$-\nabla \cdot (\nabla U) = 0 \tag{2.38}$$

With adequate Dirichlet boundary condition on opposite faces $\partial\Omega^a, \partial\Omega^b$

$$U = 0 \; on \; \partial\Omega^a \; and \; U = 1 \; on \; \partial\Omega^b \tag{2.39}$$

and Neumann type boundary at any other boundary

$$n \cdot (\nabla U) = 0 \tag{2.40}$$

The solution U represents a scalar field and its gradient

$$-\nabla U \tag{2.41}$$

Solution of the potential field was found with Galerkin finite element method.

Transformation Rules

The base vector starts from the first basis vector v obtained from as the gradient or vector from solving the previous equalizations on given domain Ω. The first base vector is defined as

$$e_1 = \frac{v}{|v|} \tag{2.42}$$

The second base vector is defined:

$$e_2 = \frac{\bar{v} - (\bar{v} \cdot e_1)e_1}{|\bar{v} - (\bar{v} \cdot e_1)e_1|} \tag{2.43}$$

where $\bar{v}$ represents a vector defined by user. Usually, $\bar{v}$ is one of the global base vector. And finally, the third base vector is a cross product of previous two ones.

$$e_3 = e_1 \times e_2 \tag{2.44}$$

In order to recognize a different quantification of the mathematical object such vector or tensor undergoes non orthonormal transformation, it is useful to note contravariant and covariant transformation.

Lets begin with example of transformation in sense of tensor transformation and write down it in Einstein summation notation.

$$T_n = n_i T^i \tag{2.45}$$

The superscript indicates *contravariant* indicies and subscript indicates *covariant* indices. More, precisely - contravariant formulation:

$$T^{i,x} = \frac{\partial u_i}{\partial x_j} T^{j,u} \tag{2.46}$$

or - covariant formulation

$$T_{i,x} = \frac{\partial x_j}{\partial u_i} T_{j,u} \tag{2.47}$$

Metric tensor g is also formulated in two manner:

$$g^{ij} = (e^i, e^j) = \frac{\partial u^i}{\partial x_k} \frac{\partial u^j}{\partial x_k} \; or \; g_{ij} = (e_i, e_j) = \frac{\partial x_k}{\partial u_i} \frac{\partial x_k}{\partial u_j} \tag{2.48}$$

Transformation is than given by the three orthonormal column vectors. Although, if the transformation is orthonormal, than the both formulation coincidence and the metric tensor is identity. This assumption of orthonormality is required and fulfilled. Than, the transformation matrix is given by three orthonormal base column vectors.

$$n = \begin{pmatrix} e_{11} & e_{12} & e_{13} \\ e_{21} & e_{22} & e_{23} \\ e_{31} & e_{32} & e_{33} \end{pmatrix} \tag{2.49}$$

And any vector or tensor is transformed according to transformation rule (2.45).

2.7.4 Experimental - Numerical Model Updating

Problem Formulation

The finite model is updated by natural frequencies from EMA. The identification procedure forces the cost function to be minimized.

$$\Theta = \sum_{i=1}^{I} W_i \left(\frac{\hat{f}_i - f_i}{\hat{f}_i} \right)^2 \tag{2.50}$$

with the weighting matrix

$$W_i = \begin{pmatrix} \frac{1}{\mathbf{var}(\hat{f}_1)} & & 0 \\ & \ddots & \\ 0 & & \frac{1}{\mathbf{var}(\hat{f}_I)} \end{pmatrix} \tag{2.51}$$

The Eq. (2.50) is minimized in LS sense, which needs the differentiation of natural frequencies λ respect to the design variables p. After finite element discretization, the discrete algebraic equations are obtained in the matrix form

$$K\Psi + M\Psi\Lambda = 0 \tag{2.52}$$

After rearranging the Eq. (2.52) and pre - multiplying by the i^{th} eigenvector

$$\Psi_i^T(K + M\lambda_i)\Psi_i = 0 \tag{2.53}$$

Differentiating of Eq. (2.53) respect to design variables p_i and taking the symmetry of stiffness and mass matrices yields

$$2\frac{\partial \Psi_i^T}{\partial p_j}\left(K - \lambda_i M\right)\Psi_i + \Psi_i^T\left(\frac{\partial K}{\partial p_j} - \frac{\partial \lambda_i}{\partial p_j}M - \lambda_i\frac{\partial M}{\partial p_j}\right)\Psi_i = 0 \tag{2.54}$$

Fulfill the Eq. (2.53) requests that differentiation of eigenvector respect to design variables must be zero. Further assuming that eigenvectors are mass normalized and mass matrices are design variable independent, the differentiation of natural frequencies respect to design variables is

$$\frac{\partial f_i}{\partial p_j} = \frac{1}{8\pi^2 f_i}\left(\Psi_i^T\frac{\partial K}{\partial p_j}\Psi_i\right) \tag{2.55}$$

with $\lambda_i = (2\pi f_i)^2$ Assuming K_e element matrix contains the operators B_e independent on design variables, differentiation reduces to

$$\frac{\partial f_i}{\partial p_j} = \frac{1}{8\pi^2 f_i}\sum_{e=1}^{Ne}\left((\Psi_i^T)_e\int_{V_e} B_e^T\frac{\partial C_e}{\partial p_j}B_e dV_e(\Psi_i)_e\right) \tag{2.56}$$

This expression results to an important first order linearized model response in terms of sensitivity coefficients S_{ij}. Due to ill conditioned sensitivity matrix (different magnitude between the design variables), every coefficient S_{ij} is expressed as

$$S_{ij} = \frac{\partial f_i}{\partial p_j}\frac{p_j}{f_i} \tag{2.57}$$

Build the quadratic cost function from sensitivity matrix S with penalization matrix W results to a local quadratic approximation of cost function

$$e = (Sx - \Delta f)^T W(Sx - \Delta f) \tag{2.58}$$

where $\Delta f = \frac{f^{new} - f^{old}}{f^{old}}$ and $x = \frac{p^{new} - p^{old}}{p^{old}}$ are vectors containing relative changes of objective and design variables.

Bounds and Constraints

The bounds must be formulated for the relative change of criteria in optimization routine. The box constraints for maximum allowable parameter change during one iteration step and absolute value of parameters are imposed. The second sets of constraint must be handled in

parameter correction. The bounds are

$$x \geq x_s \; and \; x \leq x^s \tag{2.59}$$

with respect to updated parameters

$$p^{k+1} = (1 + x)p^k \tag{2.60}$$

It follows that absolute bounds must be imposed as

$$x \geq \frac{p_s}{p^k} - 1 \; and \; x \leq \frac{p^s}{p^k} - 1 \tag{2.61}$$

In order to preserve the positive definiteness of elasticity matrix, non - linear constraints must be imposed such

$$|\mu_{12}| > \sqrt{\frac{E_1}{E_2}}; \; |\mu_{23}| > \sqrt{\frac{E_2}{E_3}}; \; |\mu_{31}| > \sqrt{\frac{E_3}{E_1}} \tag{2.62}$$

and linear constraints

$$E_{11} > 0; \; E_{22} > 0; \; E_{33} > 0; \; G_{12} > 0; \; G_{23} > 0; \; G_{31} > 0 \tag{2.63}$$

Solution of Cost Function

The evaluation of cost function is based on the FE model. The finite element model is fomulated via Galerking method with linear tetrahedral elements. The generalized eigenvalue problem is solved with Davidson type eigen solver implemented in SLEPc library [234], [235], [236] and [237]. The minimization of the cost function formulated in eq. (2.7.4) is solved by Sequential Least Squares Programming optimization method (SLSQP). Unlike searching global minimum of cost function, the minimum of local approximation is searched. This approach avoids expensive FE evaluation in every steps [238], [239], [240] and [241]. The identification framework was written in python language with Numpy/Scipy modules [242], [243], [244] and [245]. The fast algorithmic differentiation of elasticity matrix was solved via Theano package [246], [247].

Chapter 3

Influence of Shared Contact Area to Dynamic Response

This chapter provides a numerical analysis of pelvis bone - implant - probe analysis with various contact conditions. These conditions are changed in mean of different depth of reaming of acetabular bed. This leads to a parametric change of shared contact area. For every level of reaming, numerical modal analysis is performed. Computational model is based on model proposed in chapter 2. Results show a potential correlation of modal parameters and contact area.

3.1 Introduction

Behavior of a bone - implant interface in time or frequency domain under various conditions can reflect the anchoring of an implant in a bone bed. There could be expected that a factor influencing a response of the system is quite complex. One could have to account phenomenon of the stress stiffening, contact surface varying, material properties distribution in a bone around the implant and phenomenon of friction in the interface. However, modeling of those phenomenons together is an expensive task with possible uncertain results. Especially, a combination of strong non - linearities such friction with stiffening effect would be a challenge. In this part of thesis, a much more clear and reliable simulation is presented. It is based on a validated computational model (chapter 2) with different reaming conditions of acetabular bed. Although this model does not account complicated frictional contact behavior, it can still gives an important information how the different shared contact area impacts a dynamic properties of bone - implant - probe system.

3.2 Method

3.2.1 Computational Model

Geometrical and material model of the pelvis bone is taken from chapter 2. The acetabular implant is SF - type (Beznoska, Czech Republic). The diameter of the implant is 58 mm. A measuring device is connected through the thread placed in the central hole to the implant. This beam represents a measuring probe of the initial fixation (figure 3.1). The connected beam is 100 mm length and diameter is 10 mm. The material properties are in table 3.1. The measuring probe is taken as an essential part of measuring strategy. This solution preferable because there is no other option how measure an initial fixation of acetabular implant after insertion in a patient. Numerical model was formulated with finite element method (Comsol

Table 3.1: Material properties of implant - probe system

	Young modulus [MPa]	Poisson ratio [-]	density $[\frac{kg}{m^3}]$
implant (Ti alloy 6Al–4V)	110000	0.3	4500
probe (Steel)	210000	0.3	7800

Multiphysics, Comsol AB). The implant and the probe were discretized with linear tetrahedral elements. The mesh of bone was taken from chapter 2 with additional convergence study (figure 3.2).

The bone is in free - free conditions for modal analysis. Hemispherical cup of implant is positioned at 45° abduction and 25° anteversion [122]. The coordinates and orientation of the implant are recomputed according to local coordinate system defined in chapter 2. The material properties of implant and probe are assumed to be linear and homogeneous.

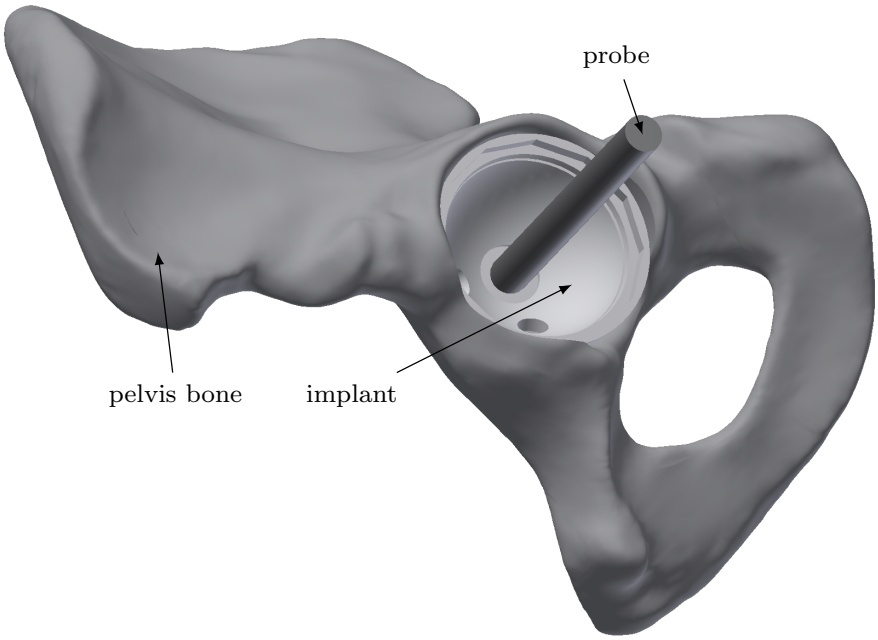

Figure 3.1: Computational model of the pelvis - implant - probe

3.2.2 Modal Parameters Sensitivity and Correlation

To find out whether the modal parameters are influenced by the parametrized reaming depth, a sensitivity and a correlation analysis are performed. The sensitivity analysis for the i^{th} damped modal frequency f_i, modal shape vector(magnitude, shape) ϕ_i and further Q_i quality factor, modal participation factors ($u_i,\ v_i,\ w_i$). The last two variables are additional for monitoring of changes in energy losses and relative change in modal shape contribution. Due to problematic formulation of the explicit sensitivity matrix, the parametric sensitivity was taken into account. This method employs a so called sensitivity ratio SR as:

$$SR = \frac{\partial F(x)}{\partial x} \frac{x_0}{F_0}\bigg|_{x=x_0} \tag{3.1}$$

This expression means local normalized partial derivation in normal point. The perturbation around the normal point is usually 5 % [248],[249]. In order to account global sensitivity amount, a modified version of SR is proposed.

$$SR_{global} = \frac{1}{N} \sum_{i=1}^{i=N} SR_i^2 \tag{3.2}$$

Where N means number of evaluation points. The correlation between the contact area and the modal parameters is expressed in terms of linear regression including a determination

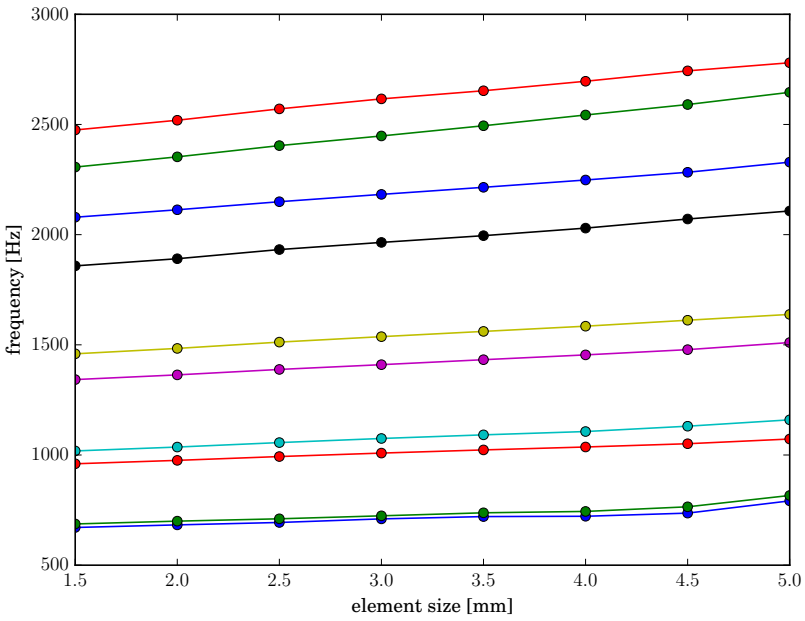

Figure 3.2: Convergence plot of first ten modes of computational model

parameter and non - parametric Spearman rank - order correlation coefficient [250], [251], [252].

3.3 Results

3.3.1 Dynamic Properties of Implant - Probe

In order to identify and properly match the modal shape vectors and frequencies to each component, the separate modal parameters of the hemispherical cup implant and assembly implant - probe were investigated. The models of the implant and the assembly were in free - free conditions to capture their behavior after implanting into a bone. First modes were selected in according to the experimental frequency range. In the figure 3.3, the modal shape vector of the implant are depicted In the figure 3.4 the modal shapes of the assembly are depicted. The modal shapes and associated modal frequencies are show in figure 3.5. According to shape and contribution of each mode, the modes were associated with every part of measured system (*i.e.* bone, implant, beam). First five modal solution without rigid modes were extracted and identified to be possibly excitable by the experimental device. As one can see, the first natural frequencies of the implant starts in significantly higher frequency range compared to the implant - probe system. Due to strong symmetry of the implant, the shapes are symmetric too. In the case of the beam connected to the implant, its modal shapes are also symmetric with mainly bending mode. The whole system (bone - implant - probe)

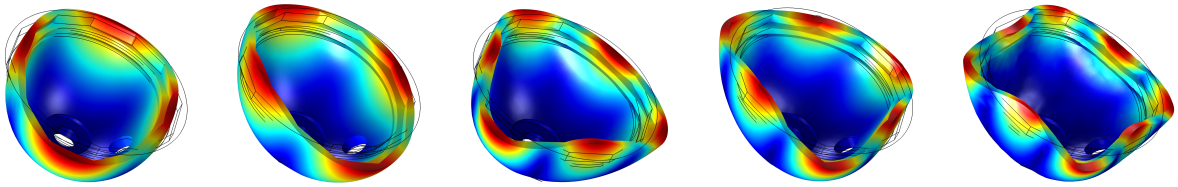

(a) mode 1. 4591 Hz (b) mode 2. 4599 Hz (c) mode 3. 112081 Hz (d) mode 4. 11241 Hz (e) mode 5. 19346 Hz

Figure 3.3: Modal shape vectors and frequencies of the implant

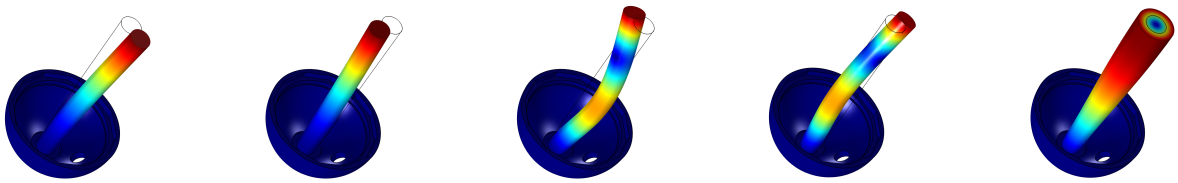

(a) mode 1. 694 Hz (b) mode 2. 695 Hz (c) mode 3 4238 Hz (d) mode 4. 4239 Hz (e) mode 5. 7935 Hz

Figure 3.4: Modal shape vectors and frequencies of the implant - probe

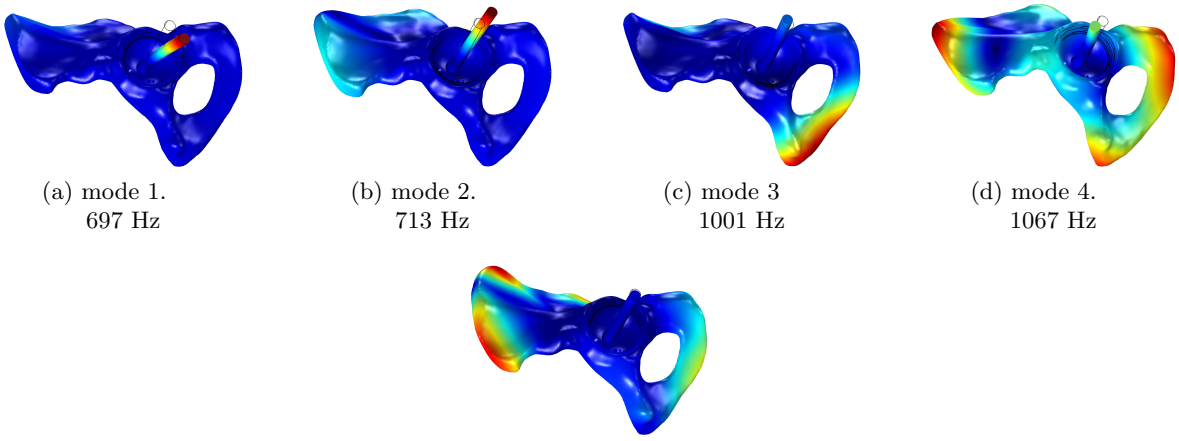

(a) mode 1. 697 Hz (b) mode 2. 713 Hz (c) mode 3 1001 Hz (d) mode 4. 1067 Hz

(e) mode 5. 1401 Hz

Figure 3.5: Modal shape vectors and frequencies of the bone - implant - probe

shows that the modal properties of the bone are strong influenced by the added mass from cup - beam system and also the additional stiffness coming from the implant (implant and bone surfaces are bonded).

3.3.2 Contact surface influence

Contact interface is recognized as the one of the possible factor influencing the stiffness of the contact interface. In that order, the contact surface should be investigated to quantify the influence of the contact surface area on the response of the bone - implant - probe system. For that, the implant system is placed into the different depth of reamed cavity around the rotational axis of the implant - probe. The different inserting depth of implant reflects the different amount of the shared contact area between the implant and the bone. The contact level statuses are depicted in figure 3.6. The graphical representation of the surface contact area is shown on figure 3.7. It is clear that due to composite structure of the bone, the different evaluation of the partial contributions of both cortical and trabecular surface are seen. The sensitivity of the modal parameters to shared contact surface was investigated.

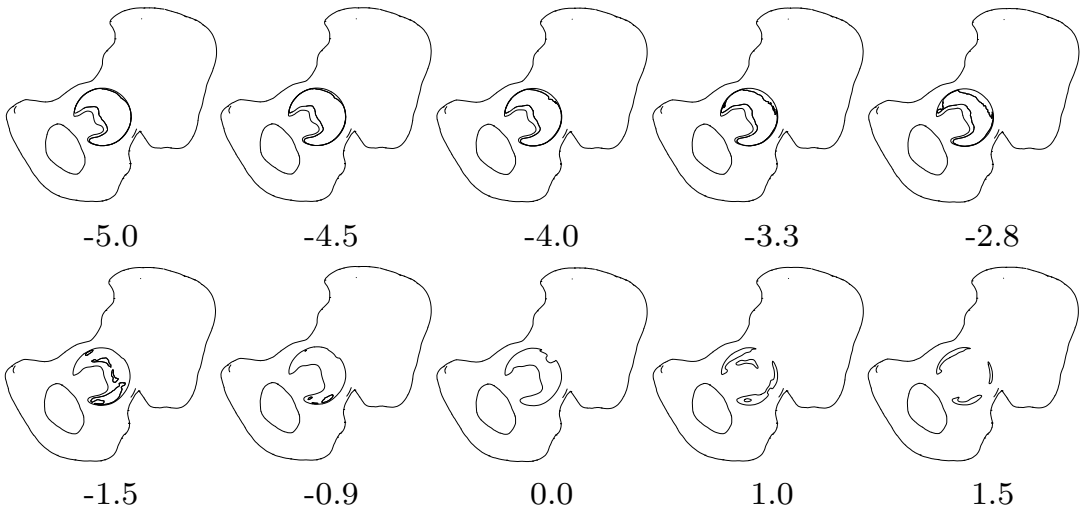

Figure 3.6: Evaluation of shared contact surface between implant and bone in dependence on the reaming distance [mm]

In the global sense, the sensitivity was evaluated on the whole model to see the difference in global parameters such modal i^{th} quality factor Q_i, participation factors $r_i(u, v, w)$ and modal damped natural frequency f. The first five deformable modes were searched. In special cases, the frequency range was extended to account the eigenvalues of the acetabular cup itself. The special attention was paid in investigation of the change in modal shape vectors. The modal shape vectors are compared in different acetabular cup implant and beam separately.

Table 3.2: Shared contact area between implant and bone

reamed cavity [mm]	S_{cort} $[mm^2]$	S_{trab} $[mm^2]$	S $[mm^2]$
-5.0	948.661	3307.465	4256.126
-4.5	1026.307	3127.361	4153.668
-4.0	1137.974	2916.448	4054.422
-3.3	1405.884	2506.943	3912.827
-2.8	1674.152	2097.585	3771.737
-1.5	2825.755	644.754	3470.509
-0.9	3179.401	117.215	3296.616
0.0	2926.972	0	2926.972
1.0	1502.596	0	1502.596
1.5	969.189	0	969.189

The sensitivity of undamped natural frequency, participation factors and quality factor to change of contact area is shown on the figure 3.7. From the scatter plot (figure 3.7) it is seen that there is probably non significant influence of the distance parameter to the modal parameters. The most sensitive parameters are participation factors, but there is attention necessity, because the order of the magnitude of the participation factor is close to numerical instability. Other parameters are not sensitive to distance parameter. This fact is also seen in the figure 3.8. The sensitivity ratio SR is evaluated in two critical points (the highest change of the contact area and the inflection point on the curve represented the cortical area evaluation). In both cases the sensitivity of the participation factors is much higher than the sensitivity of the quality factor and damped frequency. The correlation between distance parameters and modal ones is significant only for the damped frequency. The variance of the parameters (figure 3.7 - a) is most significant for participation factors, where the maximum is reached in participation factor w (var = 0.45) in third mode. The variance of the quality factor and frequency is much lower (maximum variance is for the quality factor in fifth mode, var = 0.0011). Determination coefficient (figure 3.7 - b) shows the best linear correlation for the damped frequency for every mode except the third one(range from 0.35 to 0.48). Sensitivity ratio (figure 3.7 - c, d) for two evaluating points shows the highest sensitivity for the participation factors, where the highest value is reached in second mode, for the variable w and distance -0.9 mm. Cumulative sensitivity 3.7 - e) has a similar evaluating as a variance and also gives information that the participation factors are most sensitive to change in distance parameter. The last description parameter 3.7 - f) shows rank order correlation as the best for the damped frequency (maximum 0.7 for the first mode). The sensitivity of the modal shape vectors was analyzed for the acetabular cup itself and for the beam. The correlation matrix based on the MAC criterion is shown in figure 3.9 and 3.11 for every mode. It is evident that modes are very similar in all orthogonal direction, the mac values is around 0.8 - 0.99 for non diagonal members. The case of the acetabular cup itself, there is

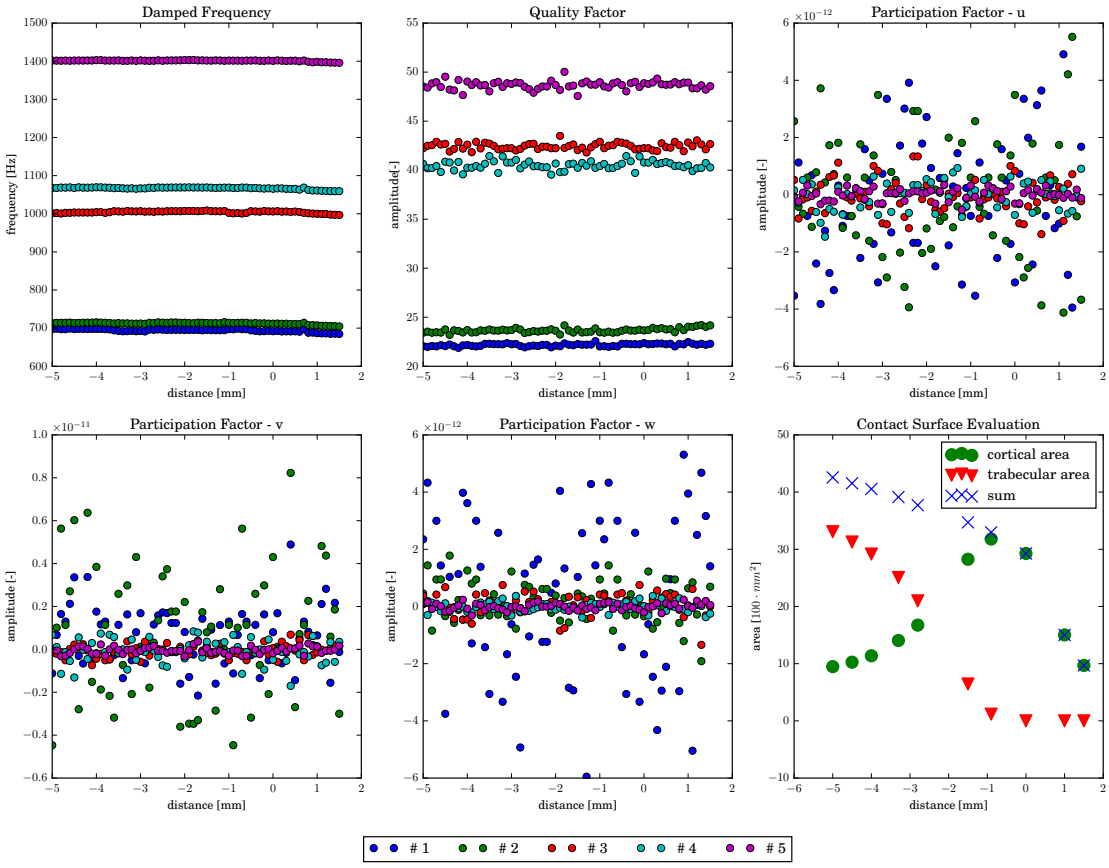

Figure 3.7: Scatter plots of modal parameters as a function of contact area

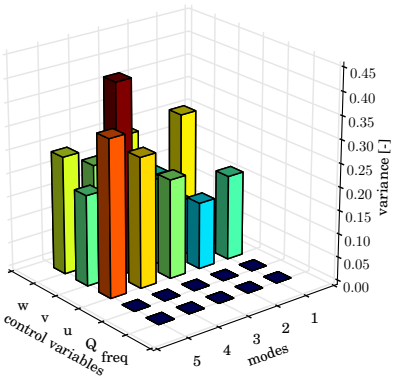

(a) Variance

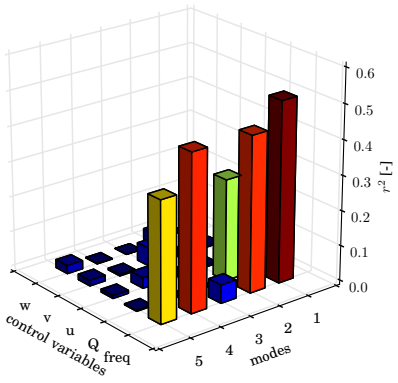

(b) Determination coefficient

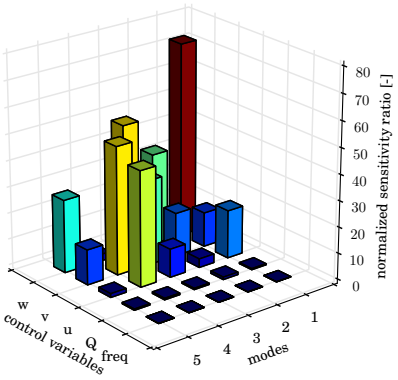

(c) Sensitivity ratio (-2.8)

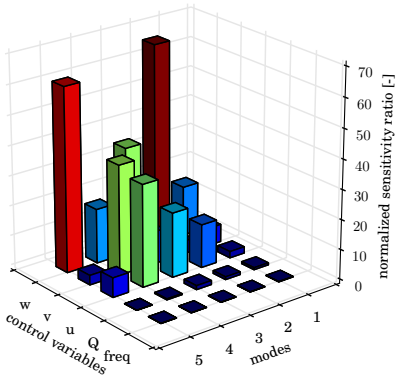

(d) Sensitivity ratio (-0.9)

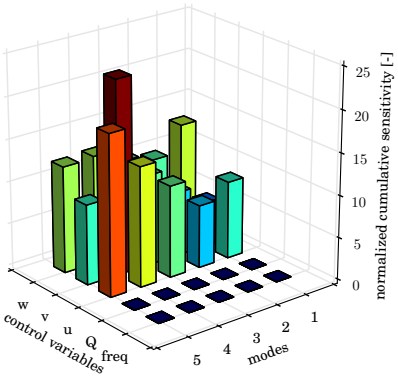

(e) Cumulative sensitivity

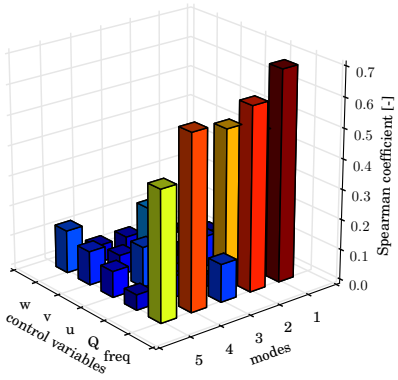

(f) Rank - order correlation coeff.

Figure 3.8: Control variables

a significant difference between shape vector component - w of the second mode. The most difference is in range of distance from 4.1 to 5.0 mm. The case of the beam has a similar evaluation as the cup. In the second mode of the vector component w, the mac matrix show significant difference between vectors in range of distance 4.1 to 5.0 mm. On the figure 3.10 is shown the evaluating of the MAC with modal shape complexity increasing. It is clearly seen, that the more complex modal vectors are more sensitive to changes in contact area.

3.4 Summary

This chapter provides a look inside to the one possible explanation of relations between the dynamic response of the system bone - implant - beam and the interfacial conditions. One can see the strong correlation between the resonance frequency and the interfacial stiffness in dental implantology, where this method is commonly used. The direct influence of the interfacial contact surface on the dynamic response of bone - implant system has not been investigated yet. Thus, the contact surface amount was taken as control parameter during the performing of numerical modal analysis. From the simulations of different contact area it was not proven the significant influence of modal parameters. The modal frequency change was smaller than 1 % (var = 0.0011). The quality factor indicator was also not proven to be sensitive variable to change in contact are. The change in participation factors of every mode was little bit harder to understand due to relative small contribution of deformable modes in free - free conditions. Although, there was no proven the relation with the contact surface area changing, the sensitivity to the change was relative high, but possibly in order of numerical instability (local SR = 0.73, var = 0.48). Although the determination and rank - order coefficients show possible relationship between natural damped frequency and distance parameter, the frequency change is probably very small compared to the reliability error occurs in real situation.

A special effort is taken in case of modal shape vector and its maximal value. The sensitivity of modal shape vector was calculated for the acetabular cup itself and for the model composed the beam. The direct comparison of every mode vector was taken, ie every mode was compared with the others. From the shape point of view, there was not proven a significant difference between the modal vectors and the change in contact surface amount in whole range of distance parameter. The highest difference was found in range of parameter from 4.1 to 5.0 mm, where the correlation between modes was very low, ie around 10 %. This result was found for both of the configuration (acetabular cup and beam). This behavior was not expected, because there is not probably reason for those relative high changes in component of modal shape vector. However, taken the closer look into an extended frequency range (see appendix A), one can seen the significant sensitivity increasing of the modal shape vector with increasing its complexity. This implies to account the wide frequency band in measuring

and not to focus just on the low frequency band, where the shape modes are not so sensitive. This fact could be also supported by the extended results of sensitivity of the damped natural frequency, quality factor and modal participation factors. These variables don't change their behavior significantly in higher modes. From figure 3.10 is clear the previous mentioned hypothesis that increasing shape complexity provides a higher sensitivity to the changes shared contact area. However, expression of the correlation between shapes and contact area was not investigated yet.

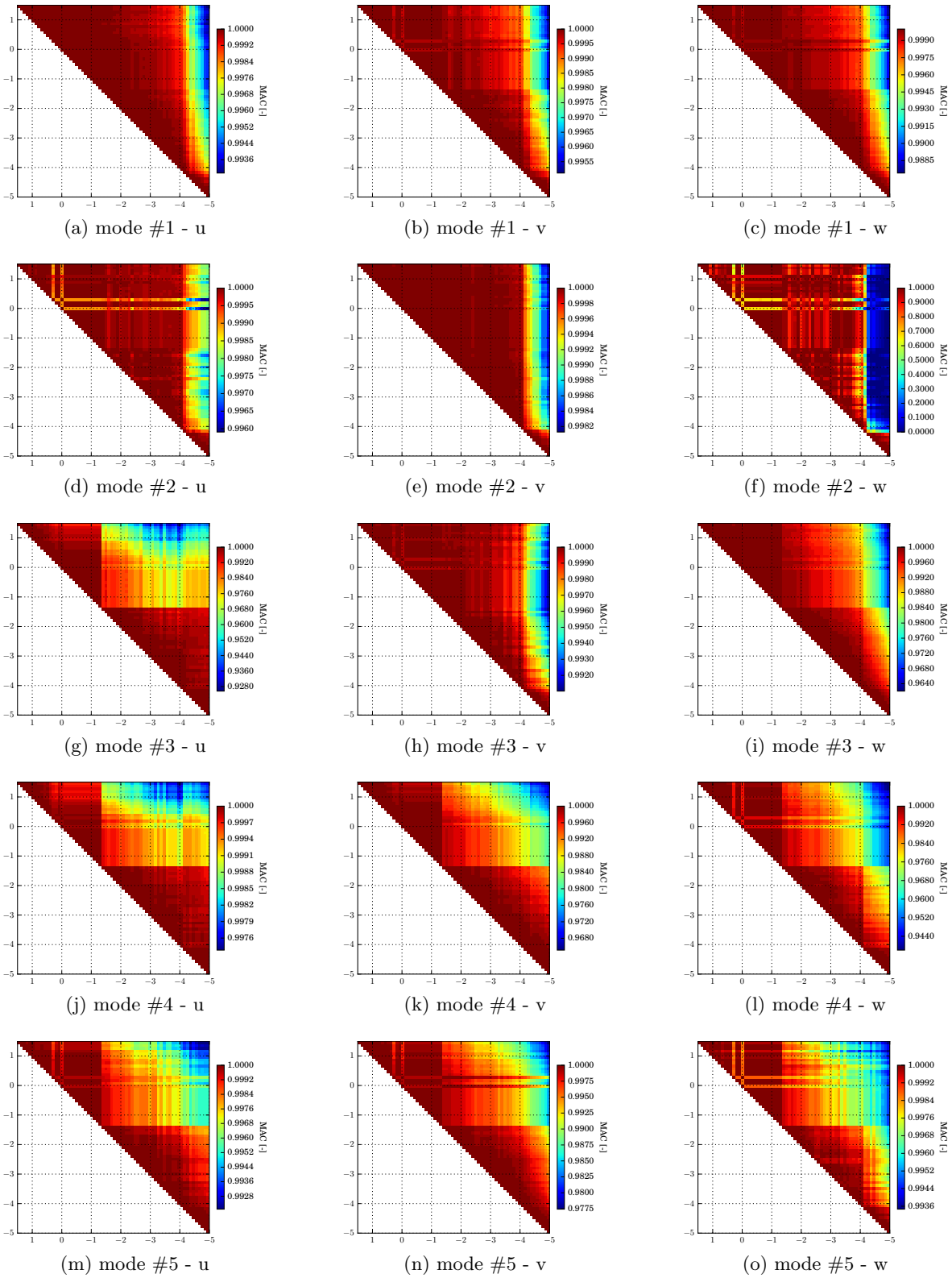

(a) mode #1 - u (b) mode #1 - v (c) mode #1 - w

(d) mode #2 - u (e) mode #2 - v (f) mode #2 - w

(g) mode #3 - u (h) mode #3 - v (i) mode #3 - w

(j) mode #4 - u (k) mode #4 - v (l) mode #4 - w

(m) mode #5 - u (n) mode #5 - v (o) mode #5 - w

Figure 3.9: MAC for acetabular cup - 5 modes

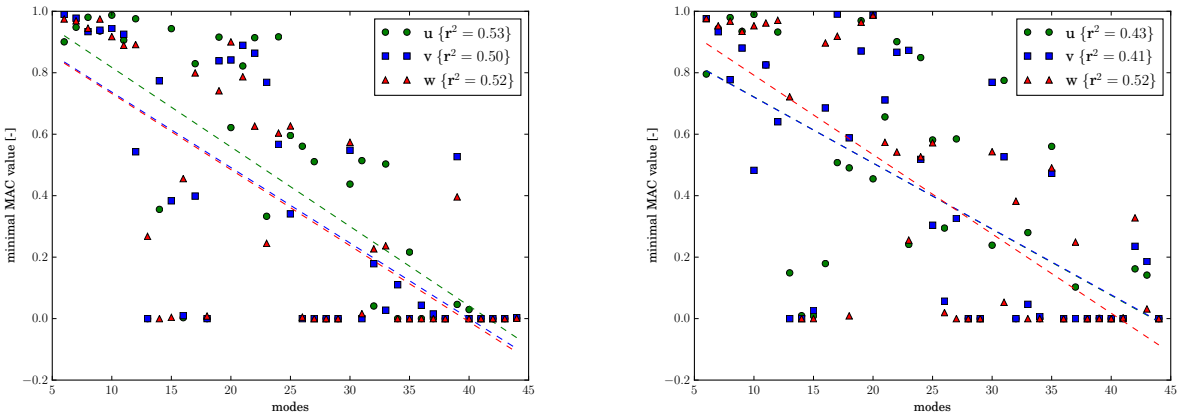

(a) cup (b) beam

Figure 3.10: MAC decreasing with the modal shape complexity

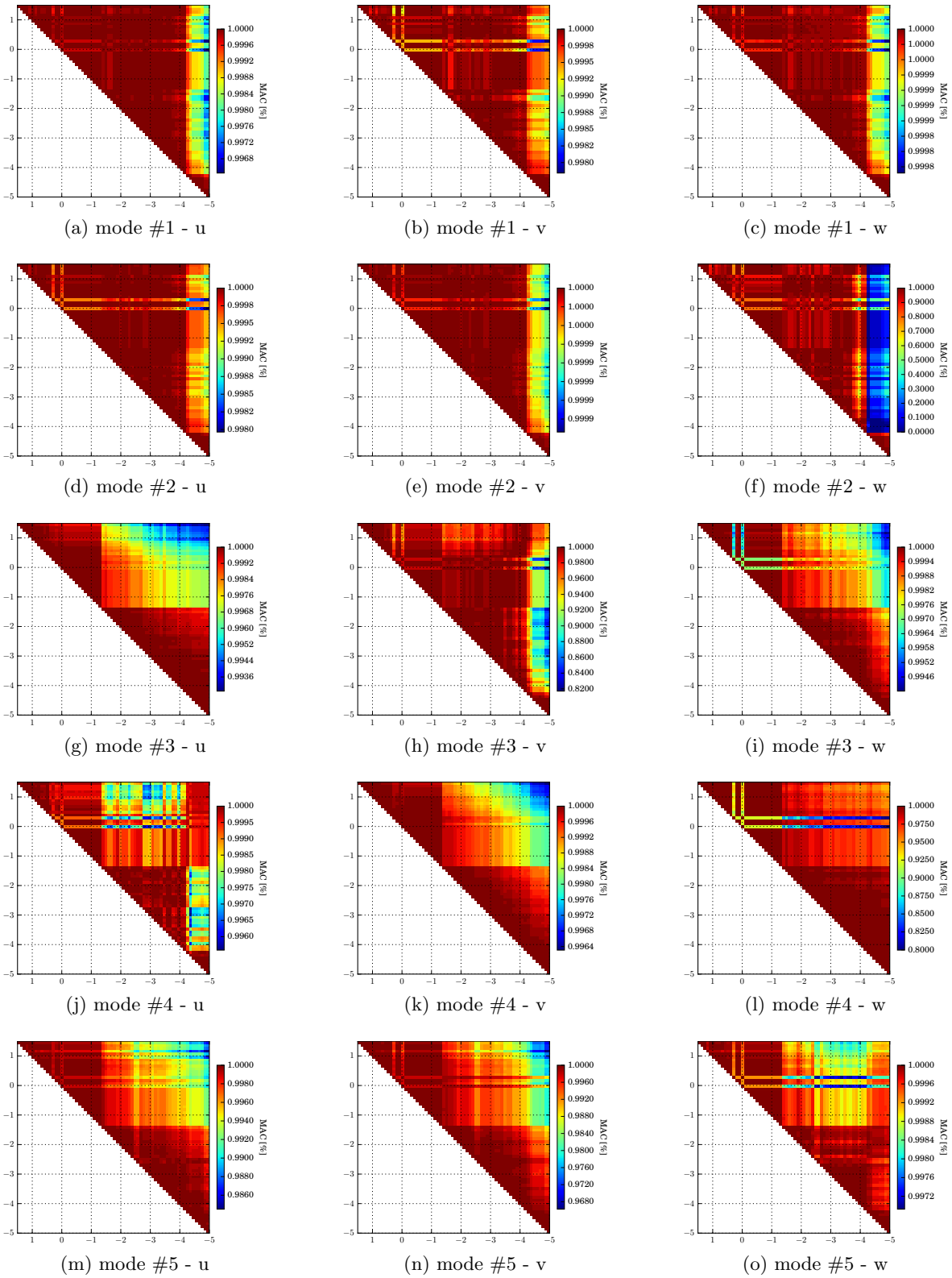

(a) mode #1 - u (b) mode #1 - v (c) mode #1 - w

(d) mode #2 - u (e) mode #2 - v (f) mode #2 - w

(g) mode #3 - u (h) mode #3 - v (i) mode #3 - w

(j) mode #4 - u (k) mode #4 - v (l) mode #4 - w

(m) mode #5 - u (n) mode #5 - v (o) mode #5 - w

Figure 3.11: MAC for beam - 5 modes

Chapter 4

Experimental Verification

The main part of this thesis is described in this chapter - experimental protocol for measuring of initial fixation. The acetabular cup implant is press fitted into the reamed acetabula cavity with different reamer diameter to account different press fit level in range from 0 mm (clinically mobile implant) to 1.5 mm. The upper range is taken as a completely stable cup implant. In the first stage, the experiments are done on the sawbone pelvic bone with real geometry. On this bone are reamed a different press fit levels with one type of the acetabular cup. For every press fit level, the modal properties with impact hammer on the outer surface along the peripheral rim of the acetabular cup are measured. To find patterns characterizes the changes in FRFs, the class of machine learning algorithm is employed to try to predict the initial fixation of the acetabular implant.

4.1 Experiment Aim and setup

The level of initial fixation is related to the common used press fit implantation technique. The main idea of the experimental part is to find out any relation between level of initial fixation and dynamic response of the acetabular cup. Thus, experimental modal analysis was performed on the acetabular cup for every fixation level. For every impact, the impact force and polar gap distance are measured and together present an energy needed to insert the acetabular cup into the acetabular bed. It is hypothesized that this energy positively correlates with the interfacial stiffness and thus with the initial fixation of the implant.

The experiment was performed on the three acetabular cups with the same initial diameter 57.4 mm (without plasma spraying) and with one reamer with diameter 57 mm. And finally, three press fit levels was obtained with three different thickness of plasma surface:

1. pressfit 0.5 mm (AC diameter: 57.5 ÷ 57.6 mm)
2. pressfit 1.0 mm (AC diameter: 58.0 ÷ 58.1 mm)
3. pressfit 1.5 mm (AC diameter: 58.5 ÷ 58.6 mm)

Figure 4.1: Three type of cups used at experiment

The higher press fit than 1.5 mm caused a rapture of peripheral rim of bone and neither was not considered in this experiment. A hemispherical cup was used (Beznoska, Czech Republic, type SF, nominal diameter 58 mm, figure 4.1). The implant was approximately positioned at 45° abduction and 25° anteversion. The polar gap in the notch is always expected. The clinically mobile cup is taken at initial configuration, where is no press fit, *i.e* zero press fit. The minimal polar gap value for completely inserted cup was found to be 4.9 mm. It is a threshold that the polar gap distance is changed less than 5 % during the impacting (figure 4.2). The experimental protocol is composed from five steps:

1. Initialize the press fit: reaming the cavity $\longrightarrow$ insert the implant (with impact) into the pelvis bone.
2. Measure the axial displacement (figure 4.3) Δs, force response F(t)

3. Modal test on peripheral ring of the cup: perform modal analysis on twelve points regularly spaced on the ring (figure 4.4). Each point includes two degrees of freedom (axial and radial).

4. Extract frequency series from response and excitation.

5. Finish the modal measuring: repeat the first step with the new press fit level.

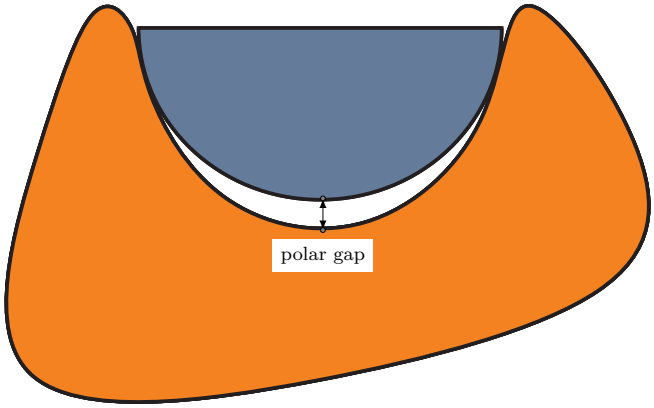

Figure 4.2: Measuring position for polar gap

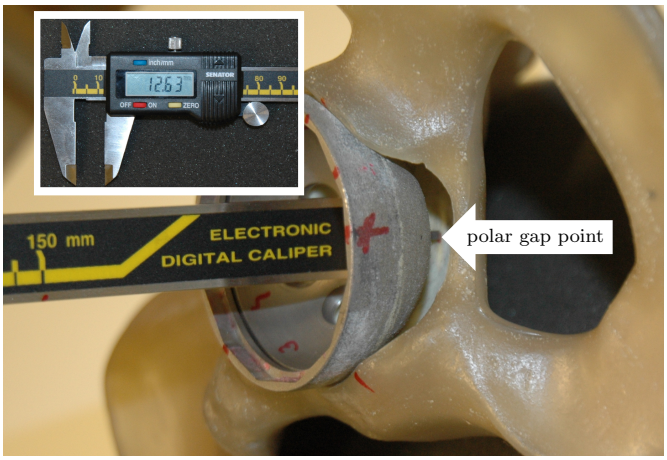

Figure 4.3: Cup displacement according to polar gap value in axial direct of AC

The overall mechanical tools are shown on figure 4.5. Polar gap value is measured by digital caliper at centering point on reamed acetabular surface. The impact force for the cup inserting and for the modal analysis is measured by the impact hammer Kistler 9724A5000 with maximal force range 5 kN. The acceleration response is measured by the small weight

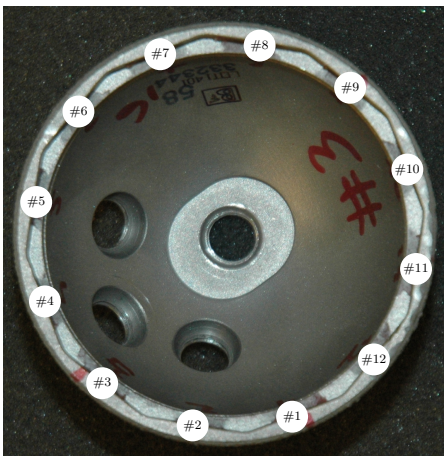

Figure 4.4: Measuring points on AC peripheral rim

Table 4.1: Configuration of modal analysis measuring

sampling frequency [Hz]	10000
FFT block size [samples]	10000
window	exponential
trigger level [N]	10 %
pre - trigger samples [samples]	1000
FRF estimator	H_1
averaging	RMS
number of hints	10
weighting mode	linear

accelerometer Kistler 5812794. Raw data are acquired by specialized measuring device DAQ 4431 (National Instruments, Czech Republic). Modal analysis is performed by home made software written in Labview 2012 (National Instrument) and the setup of the modal program is shown in table 4.1.

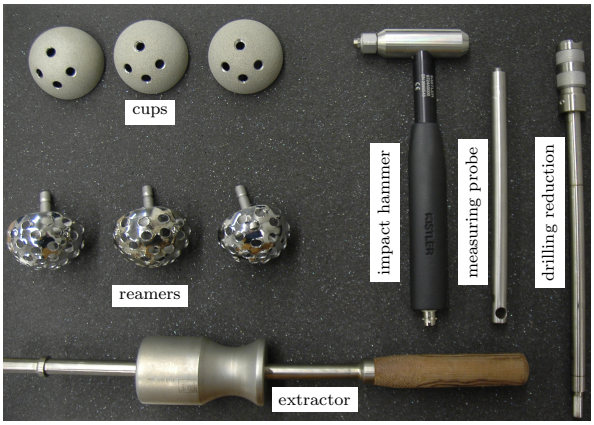

(a) Mechanical tools used in experiments

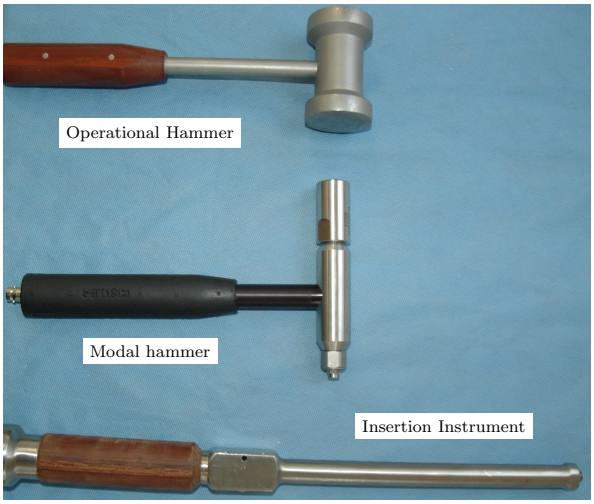

(b) Additional Tools - Operational Hammer and Insertion Instrument

(c) Inserting step

Figure 4.5: Tools used in experiment

4.1.1 Mode Filtering

Every change in structure is reflected in changes of modal parameters. The recognition ability if the pole is physical or structural is strongly dependent on identification procedure, the quality of structural response. From the results is clearly seen that basically there are two frequency ranges where the observed FRFs are different in their quality. In range from 100 to 2100 Hz the FRFs have a good quality, but in the range from 2100 to 5000 Hz, the quality is poor (figure 4.6). Due to a large amount of FRFs from different fixation levels, an

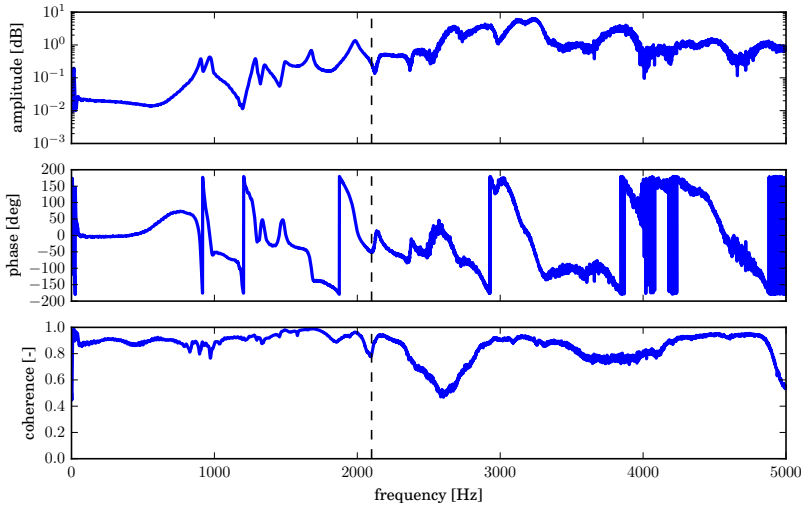

Figure 4.6: Typical bode plot of FRFs

autonomous qualification of physical modes is necessary. A similar approach introduced in [207], [226], [253] and [254] is used. Firstly, the typical results are shown in figure 4.7. The MLE uses the log - like cost function with better convergence behavior. Maximum allowable iteration is 100, which usually leads to converged solution of MLE. The modal data are firstly filtered by physical threshold. This means the 3% of frequency cut off around the band edges. Poles with a damping ration smaller than 0.01 % and higher than 10 % were removed. Due to large discrete over - modeling, computational modes are presented in the model. This is the reason for using a next level of filtering. The filter consists of stochastic and deterministic criteria. The stochastic criteria based on the MLE natural statistic properties are defined:

- **Frequency and damping variance** - σ_f , σ_ξ are used as criteria. Poorly excited physical modes or computational modes have a large variance.
- **Pole - zero interaction**. Computing an uncertainty circle of r^{th} pole p for counting how many zeros z_k fall inside the circle can help recognize computational mode, since computational pole has a large number of zeros inside its uncertainty circle of pole.

$$R = \sqrt{-2log(1-p_b)}\sigma_{p_r} \tag{4.1}$$

$$I_{p_r} = |p_r - z_k| \leq R \tag{4.2}$$

- **Individual SISO analysis**. Counting how many times the tracked pole occurs in the individual frf in uncertainty circle of globally estimated pole This can prevent the misclassifying the real mode in case of local or poorly excited mode. Mathematically written as:

$$K_{p_r} = |p_r - p_{k_{SISO}}| \leq R \tag{4.3}$$

  where *pb* means the probability that a true pole falls inside the circle. According to work [226], the typical standard deviation of a computational mode is around 10 - 100 higher than for physical one. This was proven in this thesis where common value of standard deviation of computational pole is around 5 - 72 times higher than common value of standard deviation for physical pole.

The stochastic criteria are robust to noisy data, however it can still happen that in case of poorly excited modes, the stochastic criteria recognizes the physical pole as computational one. For this reason, a class of deterministic criterion is used. Namely:

- **Mode Phase Collinearity (MPC)**. This variable is defined in chapter 2. MPC describes the possible linear relation ship between the real and imaginary part of pole. For case of real or slightly complex modes, the value is close to unity.

- **Enhanced Modal Assurance Criterion** (MAC - described in 2). High non-diagonal MAC values around the r^{th} mode can indicate its quality with defined threshold, which was taken as 0.1.

The SISO analysis provides a useful insight into individual mode quality. In the figure 4.8 is a typical Nyquist plot of poles after physical thresholding with varying of each SISO analysis. The indexing numbers corresponds with Figure 4.7. The color of circles corresponds with actual number of global pole. The radius corresponds with pole variance scaled five times to be bigger for better visualizing. The real part is transformed to positive values and logarithmically scaled. However the MPC variable can fail in some of computational modes, where it detects a higher value common for physical pole. The variables describing the behavior of pole are the arguments of a supervised machine learning algorithm. Next algorithm arguments are two states belongs to decision if the pole is computational or physical. The variables are firstly rescaled to unity with subtracted minimum. A typical evaluation of variables is in Figure 4.9. There are several machine learning algorithms used in identification of physical poles. Many of them are based on cluster analysis (hierarchical and portioning clustering) [255], [256],[257] or a combination of cluster and support machine vector method [258]. In this thesis, a class of fuzzy cluster analysis (Scikit - fuzzy) is used for improving of quality of training data. Modal data are partitioned into two clusters that separate surely

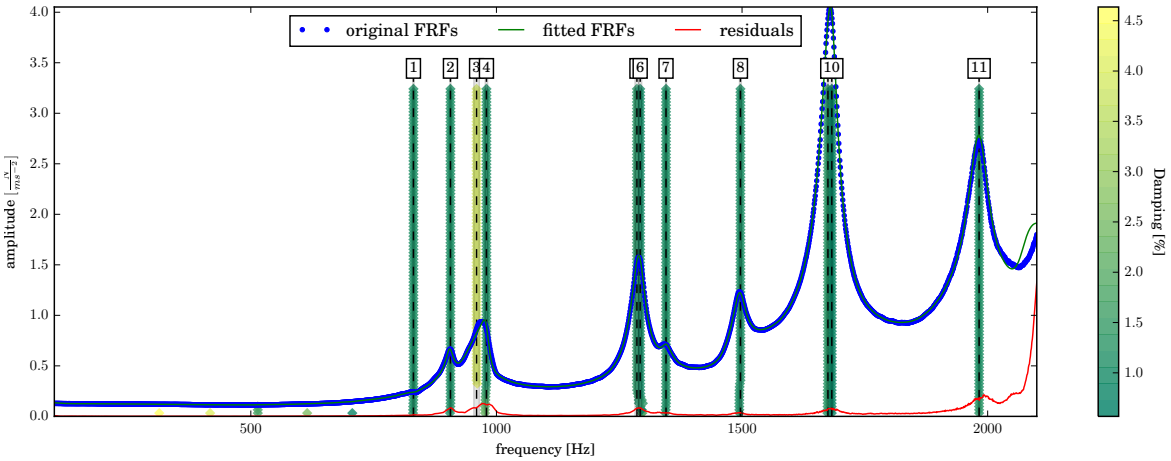

(a) 100 - 2100 Hz - typical stablization analysis

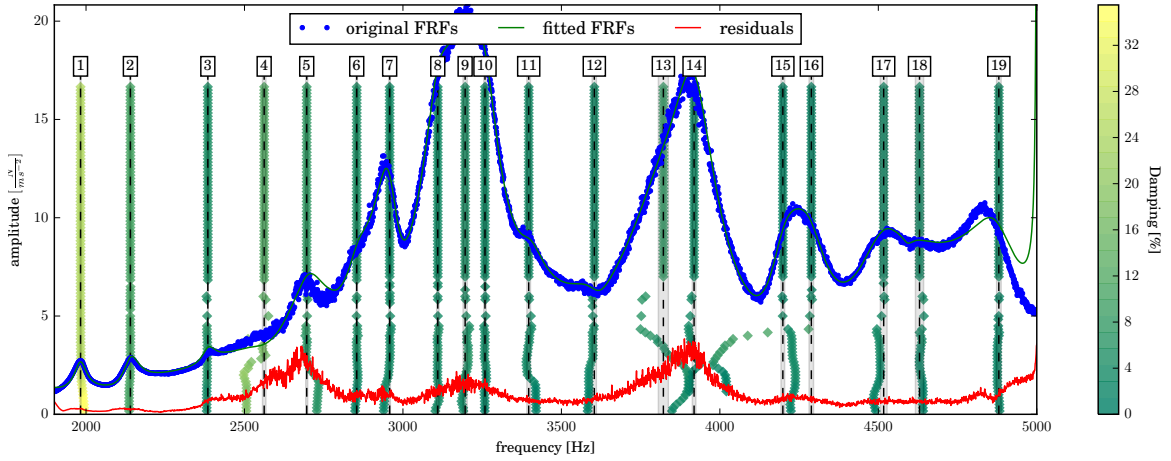

(b) 1900 - 5000 Hz - typical stablization analysis

Figure 4.7: Typical identification results from MLE algorithm

spurious and probably physical poles according their numerical behavior. After preparing training sets, the simple SVM (Scikit-learn [259]) is trained to predict a new set of modal data. The training data are taken from measuring with the smallest implant. The training set is composed of several identification runs with different order of system and noise contribution. This approach seems to be sufficient, since modal data come from similar structural analysis in all cases of experiments. A performance of the trained svm estimator is presented in figure 4.10, where the cross validation score and confusion matrix show a good estimation behavior. The figure also shows the planar space of training data, obtained by projecting of feature vectors in the space formulated by the two principal axes of the original feature space (PCA analysis). As it is expected, the spurious and physical modes occur in two separable clusters easily detectable with a cluster analysis or with SVM technique. The SVM is validated by Random permutation cross - validation and tunned by Grid search method (both available in Scikit-learn).

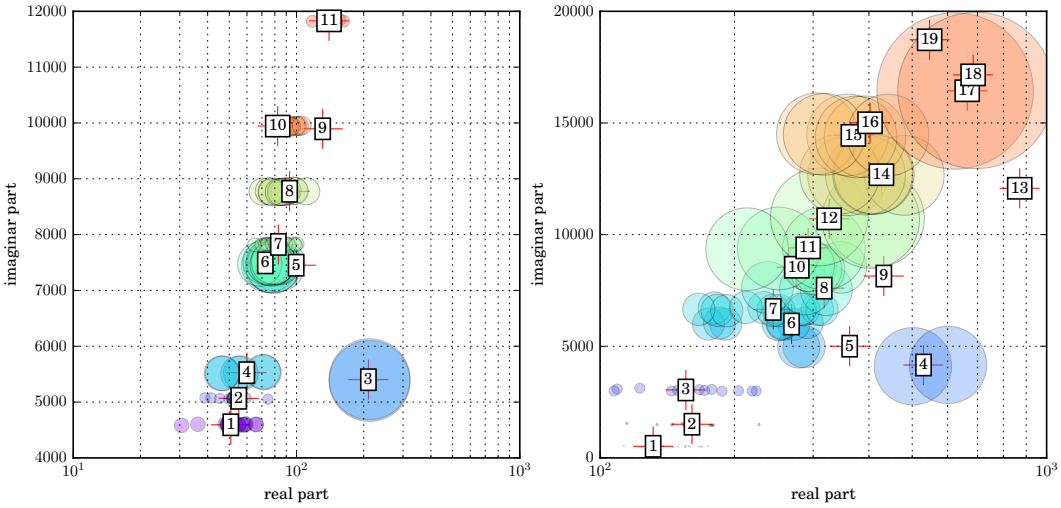

(a) 100 - 2100 Hz (b) 1900 - 5000 Hz

Figure 4.8: SISO pole analysis

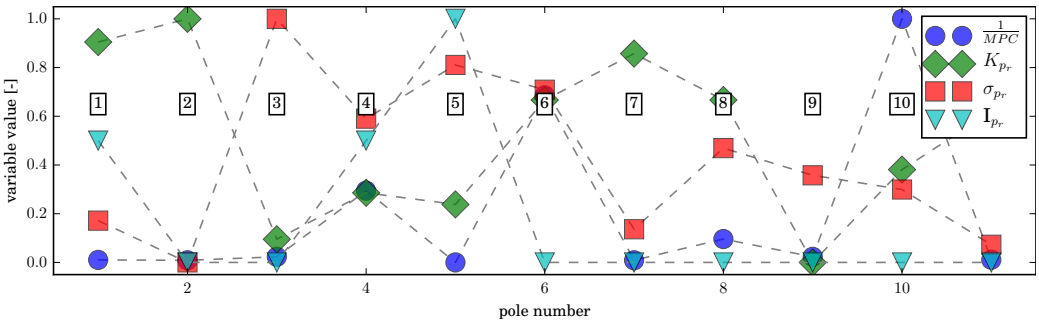

(a) 100 - 2100 Hz

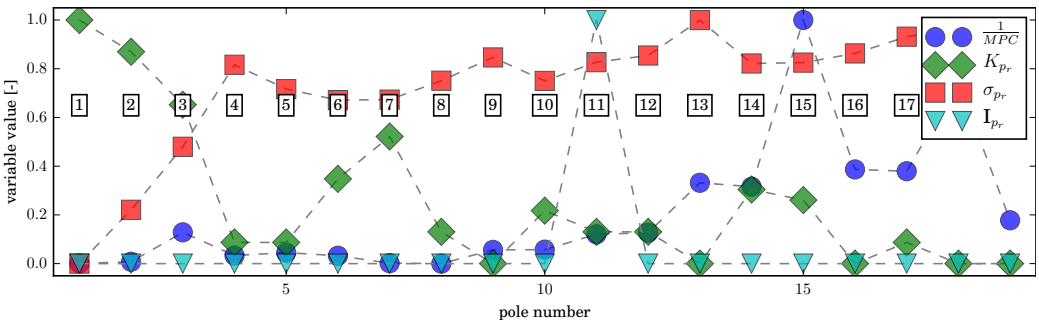

(b) 1900 - 5000 Hz

Figure 4.9: Variables for learning algorithm

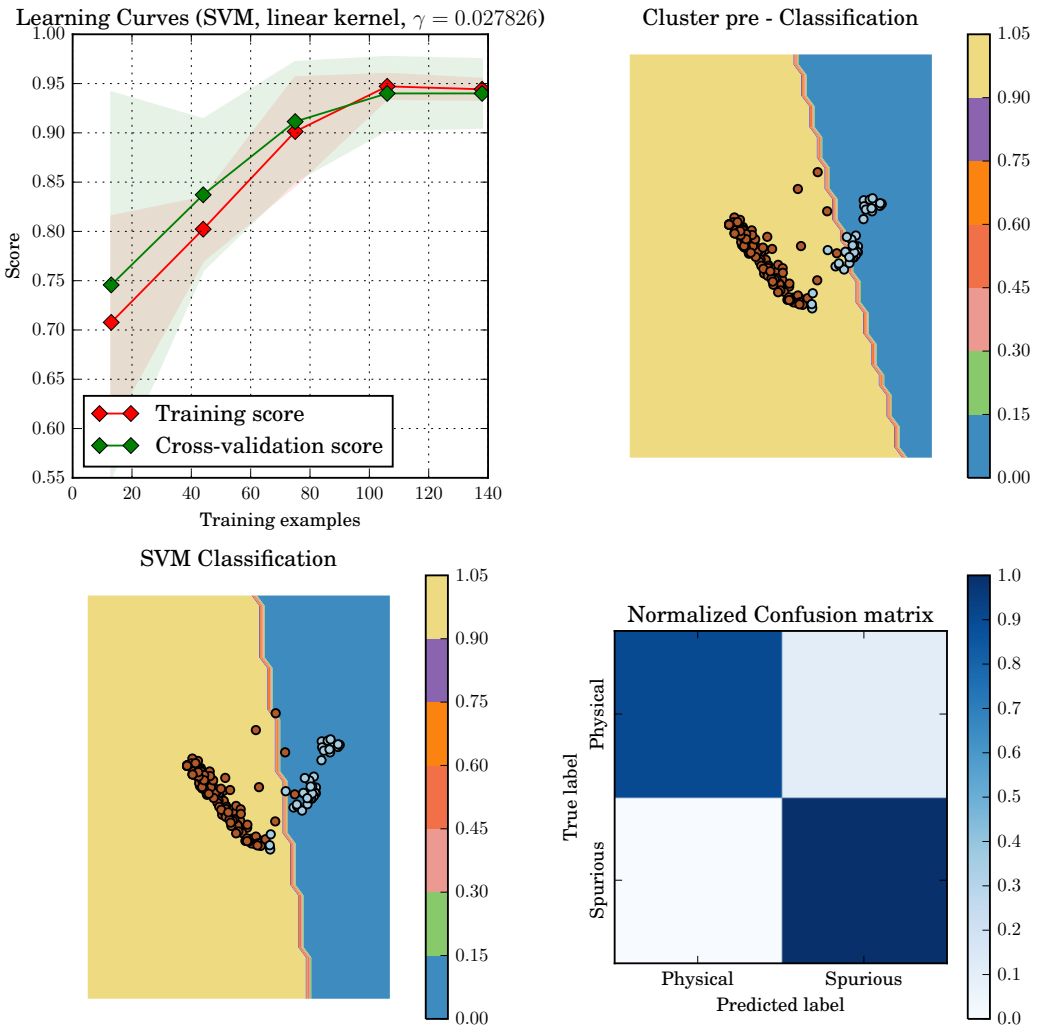

Figure 4.10: Classification performance of SVM

4.1.2 Mode Tracking

Due to structural changes in different fixation levels, there is a possibility that modes cross each other. This crossing is necessary to catch and consequently switch crossing modes index. The tracking algorithm is based on the MAC criterion [260]. Another way, in case of small number of sensors, is based on the residual matrix distance approach [226]. In this thesis, the first mentioned solution is used, because of sufficient number of sensors and simple implementation. In the figure 4.11 a typical MAC evaluation for eight levels in frequency range 100 - 2100 Hz of fixation is shown. After thresholding (usually 0.3 - 0.8), some modes are switched, *i.e.* mode 5 and 6 in the second level and so one. The mode tracking algorithm changes the evaluation of the modal properties at each fixation level. The switched mode evaluation

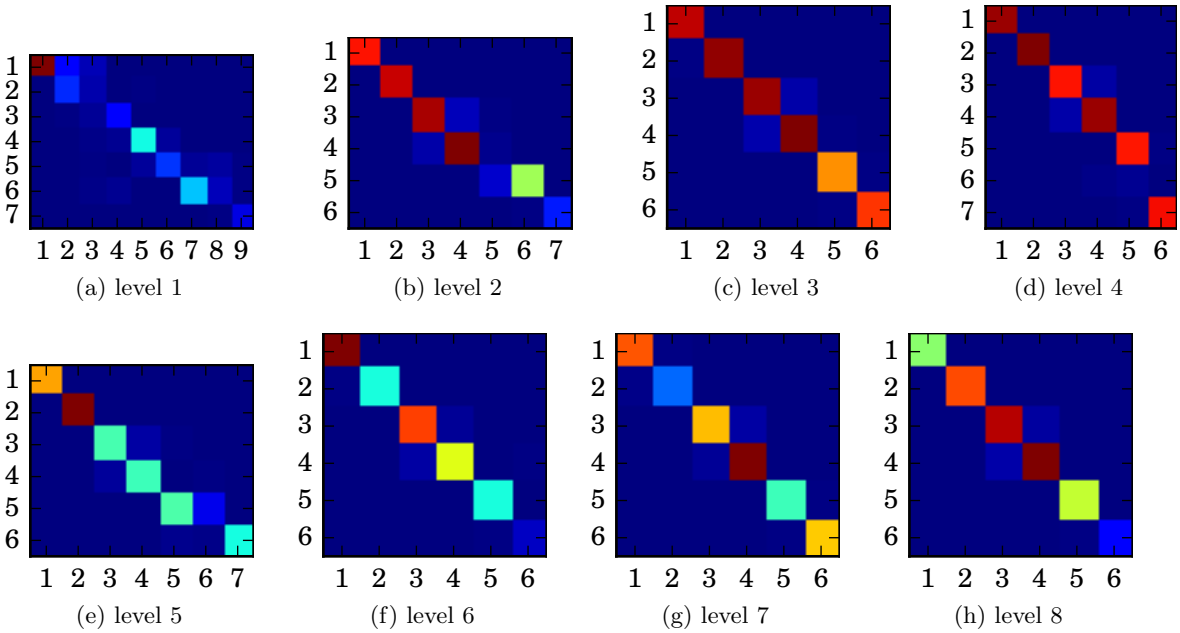

Figure 4.11: MAC matrices for mode tracking

example is shown in figure 4.12 for frequency and damping ratio. Almost modes are tracked well except the mode number seven. This mode is a result from tracking algorithm that was not filtered with the threshold how many times the mode must be tracked to be qualified as a traceable mode. The threshold is usually $N - 2$, where N is the level number. Thus, the mode number seven after thresholding will be rejected. The need of tracking algorithm is clearly seen in case of damping evaluation, where due to switching of modes, damping ratio can be successfully tracked.

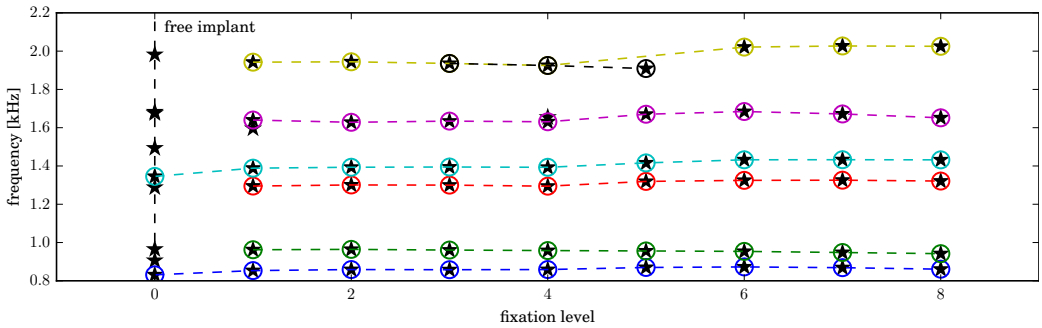

(a) frequency evaluation

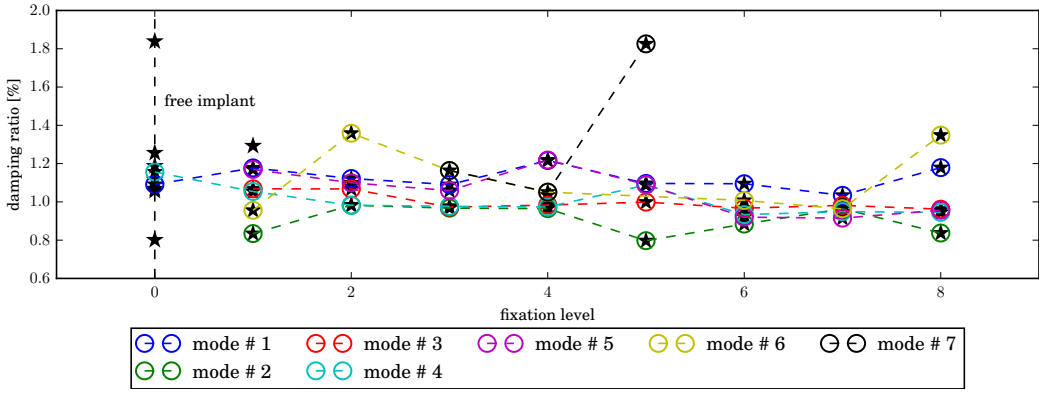

(b) damping ratio evaluation

Figure 4.12: Tracking process of modal parameters

4.1.3 Correlation Step

After having identified and properly matched modal parameters, the set of the those ones enter into the correlation phase, which is based on unsupervised methods. First, the cross correlation method was used to explore relation between impact force, gap distance, modal frequency and damping at each fixation level. This leads to a weighted correlation matrix for each identified and tracked physical mode in both frequency ranges. The Spearmann's rank coefficient was used as a metric. As an independent variable the impact force is chosen. However, statistical properties of correlation coefficient are not taken as an descriptive information since the data are not statistically valuable (small sample). Due to high dimensionality of Modal shapes and FRFs frequency data, an exploratory analysis based on a cluster and PCA analyses is used. A possible relation between inserted energy (impact force and gap distance), shape modes and FRFs data is searched in reduced feature space. The idea of correlation between levels of gaps and impact force and the shape of every modal vector is following:

1. **Formulate distance matrix** from observations of every modal shapes in measured DOFs. As a metric, the MAC criterion is chosen.

2. **Perform linear dimensional reduction** into the first eight principal component with

highest eigenvalues.

3. **Calculate linear regression** coefficients on the projected data.
4. **Transform regression coefficients** back in to the original space.
5. **Perform cross validation** process and evaluate estimator quality.

This formulation of regression process is known as a Principal Component Regression (PCR) with cosine metric as distance one. The regression models must be adequately validated. In this thesis, a common validation method was used, namely cross validation with outliers detection and interpretation. The cross validation helps to determine which component has the best correlation potential and whether the correlation is meaningful.

4.2 Results

First of all, due to rapture of the pelvis bone during the early insertion phase of the third implant, the data coming from this experiment are considered to be unfinished and would be comparable only from normalized energy (figure 4.13). The evaluation of the insertion phase for every implant is shown in figure 4.14. In the graph is clearly seen the phase of rapture of the bone. Probably the crack was initiated during the extraction phase of the smaller implants, but without any visual significance. The polar gap and impact(cumulated) force shows a correspondence, which is confirmed by a strong correlation after all. Polar gap was measured with a statistical manner and qualified as a normally distributed variable (10 samples). The confidence intervals are also shown in the figure 4.14. For every diameter of

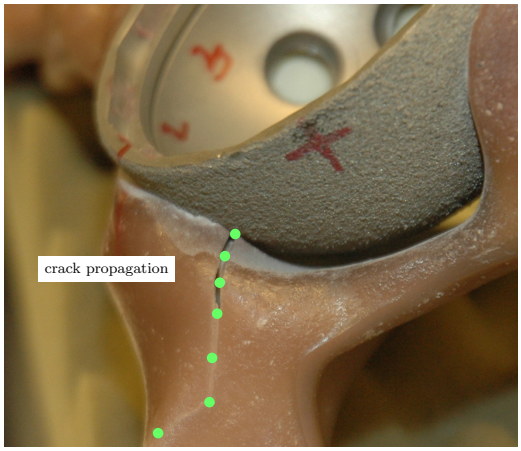

Figure 4.13: Bone rapture after insertion impact

implant the initial polar gap was measured. The initial polar gap values are shown in table 4.2, there is clearly seen that bigger diameter corresponds with bigger initial polar gap.

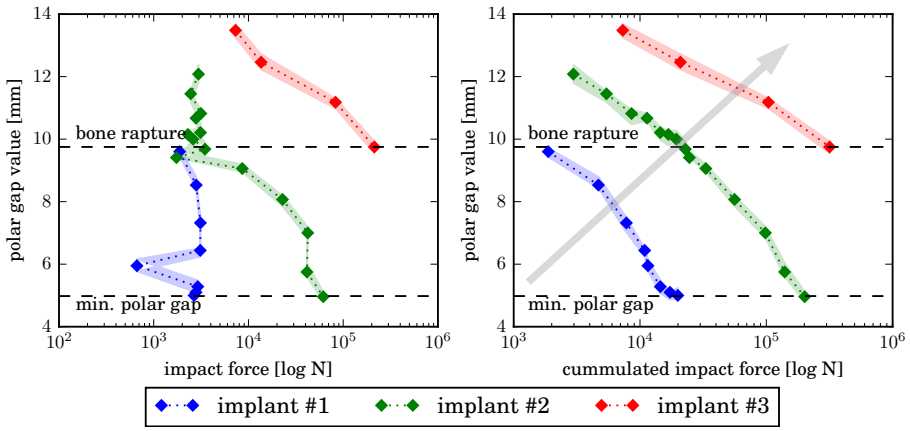

Figure 4.14: Evaluation of mechanical response of the cup to the impact force

In the experiments, 576 FRFs were obtained from modal analysis including three implants and 24 fixation levels. Due to limited excitations performance of modal impact hammer in range higher than 2500 Hz, the frequency range was split into two. The first frequency range is 100 - 2100 Hz and second is 1900 - 5000 Hz. The order of the system in the first frequency range was reduced from initial 25 to 18. The order of system in the second frequency range was always set up to 25. The maximum allowable iteration of MLE was set to 100. Filtering criteria for the first frequency range was taken from 4.1.1. In the second frequency range, the allowable standard deviation of the frequency and damping must be doubled. Thus, from every fixation level the modal parameters are extracted and matched by tracking mechanism. This leads to sets of parameters which are correlated each other.

Table 4.2: Initial polar gap value [mm]

implant #1	implant #2	implant #3
10.74	13.54	15.28

4.2.1 Frequency and Damping Correlation

The evaluation of modal parameters is in figure 4.15. There are always four graphs with modal frequencies and damping on a vertical axis and with gap distance and impact force on a horizontal axis. Those graphs contain two frequency bands as was mentioned in the experimental set up for each value of diameter of implant. In the figure 4.15 only data for the first implant is shown. The rest of two implants data is in appendix D. In the first frequency range 100 - 2100 Hz six, eight and seven modes were recognized suitable for correlation for implant number one, two and three. In the range 1900 - 500 Hz fourteen, fifteen and fourteen modes were recognized for implant number one, two and three. Every mode was tracked during each fixation level. In the figure 4.15 one can seen that modal data somehow corresponds

with changes of fixation level. An evaluation of natural frequencies in both frequency ranges shows a variability every mode for all tested implants due to change of fixation level. Natural frequencies vary from 10 to 200 Hz within the first frequency band (100 - 2100 Hz) for both gap distance and impact force. The frequency changes for the band 2100 - 5000 Hz are much higher and commonly reach 1kHz difference. The damping ratio evaluation is significantly more sensitive than natural frequencies. As is expected (better data quality and low damping), in the low frequency range the ramping ratio i usually around 0.8 - 2.4 for all implants. In the second frequency band, the damping ratio is much higher, even more than 80 % (mode 1 - implant 1) or 40 % (mode 1 - implant 2) or 42 % (mode 1 - implant 3). These high values of damping are not a real character of mode, but it is a results of behavior of the identification procedure. For this reason, both frequency ranges should overlap. However the modal data does not always monotonically correspond with gap and force variables, an interesting corresponding is obtained in the value of polar gap distance (around 6 mm). In this fixation phase, the impact force is decreased(or constant for implant 2). This suggests that the implant reaches position, where the stiffness of interface decreases. It could suggest that a crack is initiated (not found for implant 1 and 2) or during the last insertion phase the implant passes the acetabular rim edge that is a main stiffness contributor. A similar phenomenon Pastrav found in his thesis [173].

In order to quantify relations between fixation variables(polar gap and impact force) and modal parameters, correlation matrices with Spearman's coefficients was built. In the figure 4.16 one can see the correlation structure for the first implant. The rest of implants is in appendix E. In almost cases the modal frequencies, damping ratios and fixation variables correlate. In the lower frequency range (100 - 2100 Hz), the correlation tends to be higher than in range 2100 - 5000 Hz. Also, the modal frequencies are correlated more often than damping ratios.

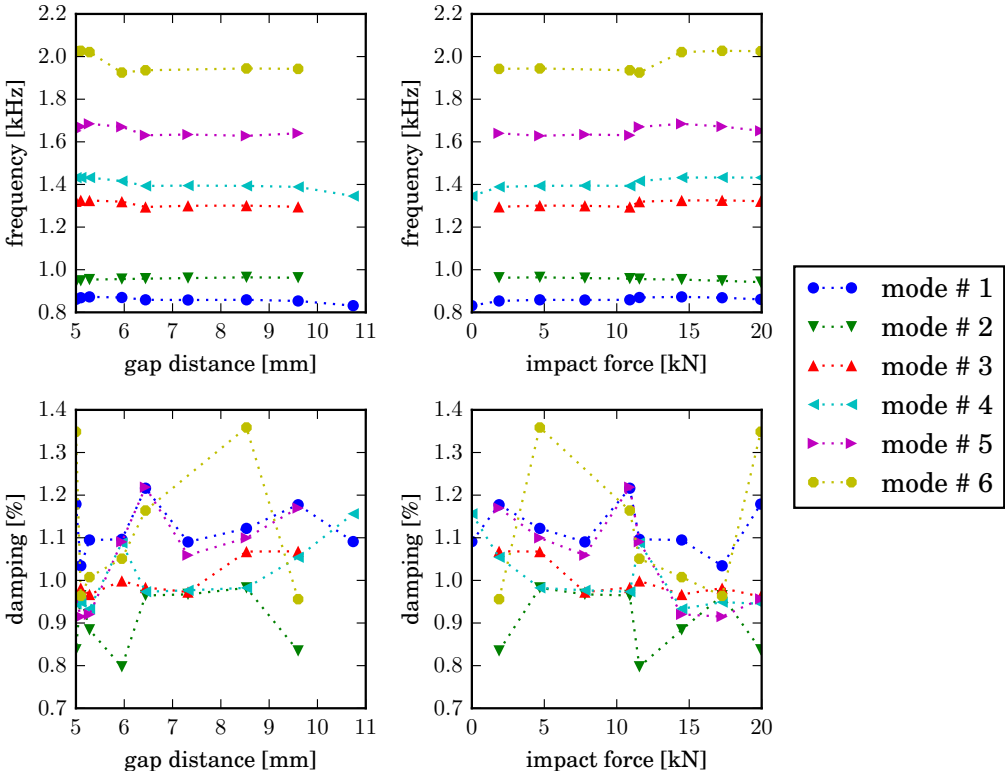

(a) frequency range 100 - 2100 Hz

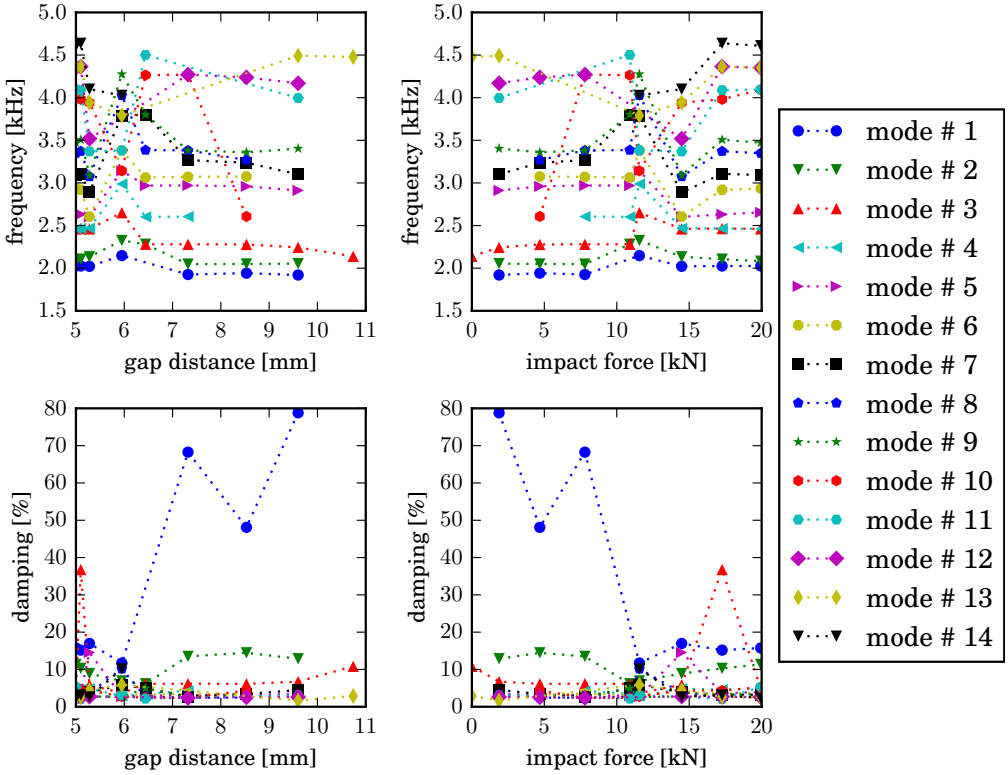

(b) frequency range 1900 - 5000 Hz

Figure 4.15: Evaluation of modal properties for implant # 1

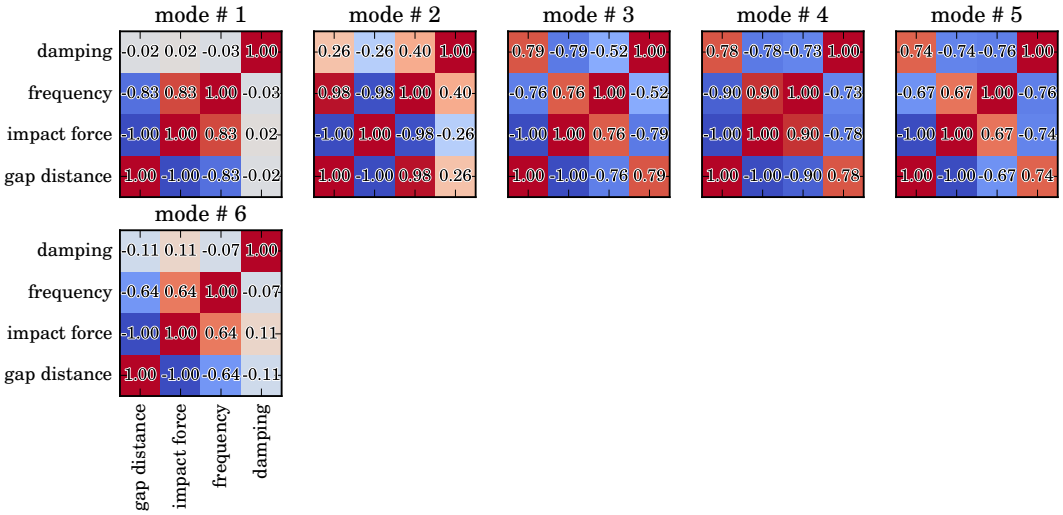

(a) frequency range 100 - 2100 Hz

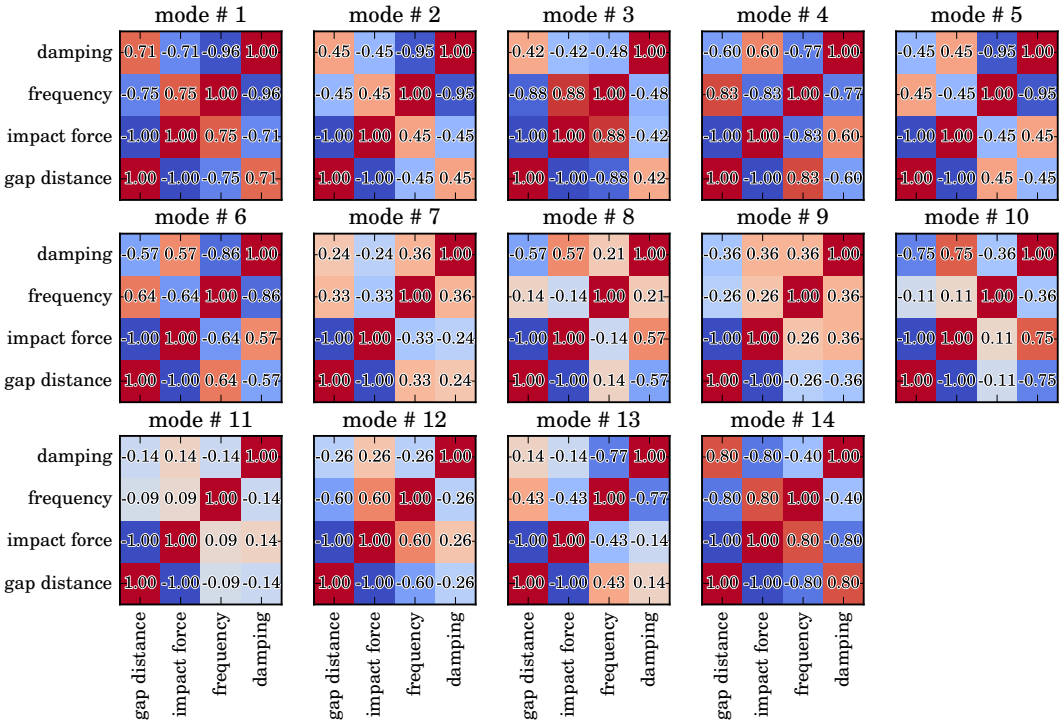

(b) frequency range 1900 - 5000 Hz

Figure 4.16: Evaluation of modal properties for implant # 1

4.2.2 Modal Shape Correlation

A correlation between modes shape is formulated with multivariate analysis. Typical normalized shapes of modes for the first implant are depicted in figures 4.17 and 4.18. Only peripheral ring is shown with deformed status projected into three planes. Due to a complex character of shape vectors, modes are shown at the initial time $t = 0$. Green marker shows the center of implant rim. Blue markers show the first two measure points (from right to left) in clock wise direction. These markers ensures the orientation of rim on real implant. The red curves mean a deformed status of the rim. In the first frequency range, the estimation quality of the modes is higher than in second one. This fact explains a weird deformation of modes in the second range (comparing to modes from computational model of acetabular cup in chapter **??**), especially in the axial direction. However in modes of the acetabular cup, the overall modes (of pelvis) are projected also, which distorts modes of acetabular cup itself.

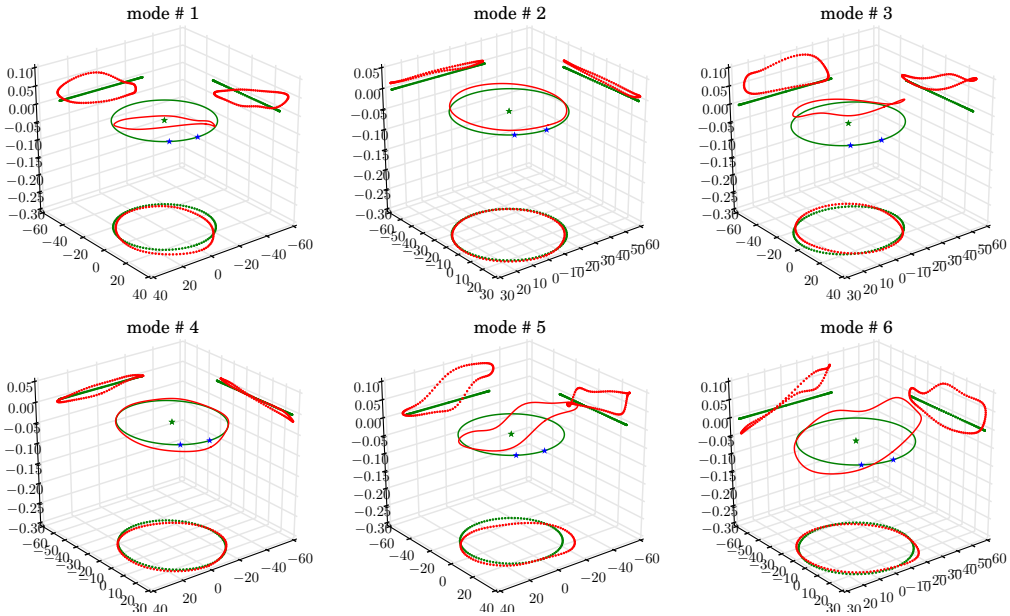

Figure 4.17: Modal Shape for implant # 1

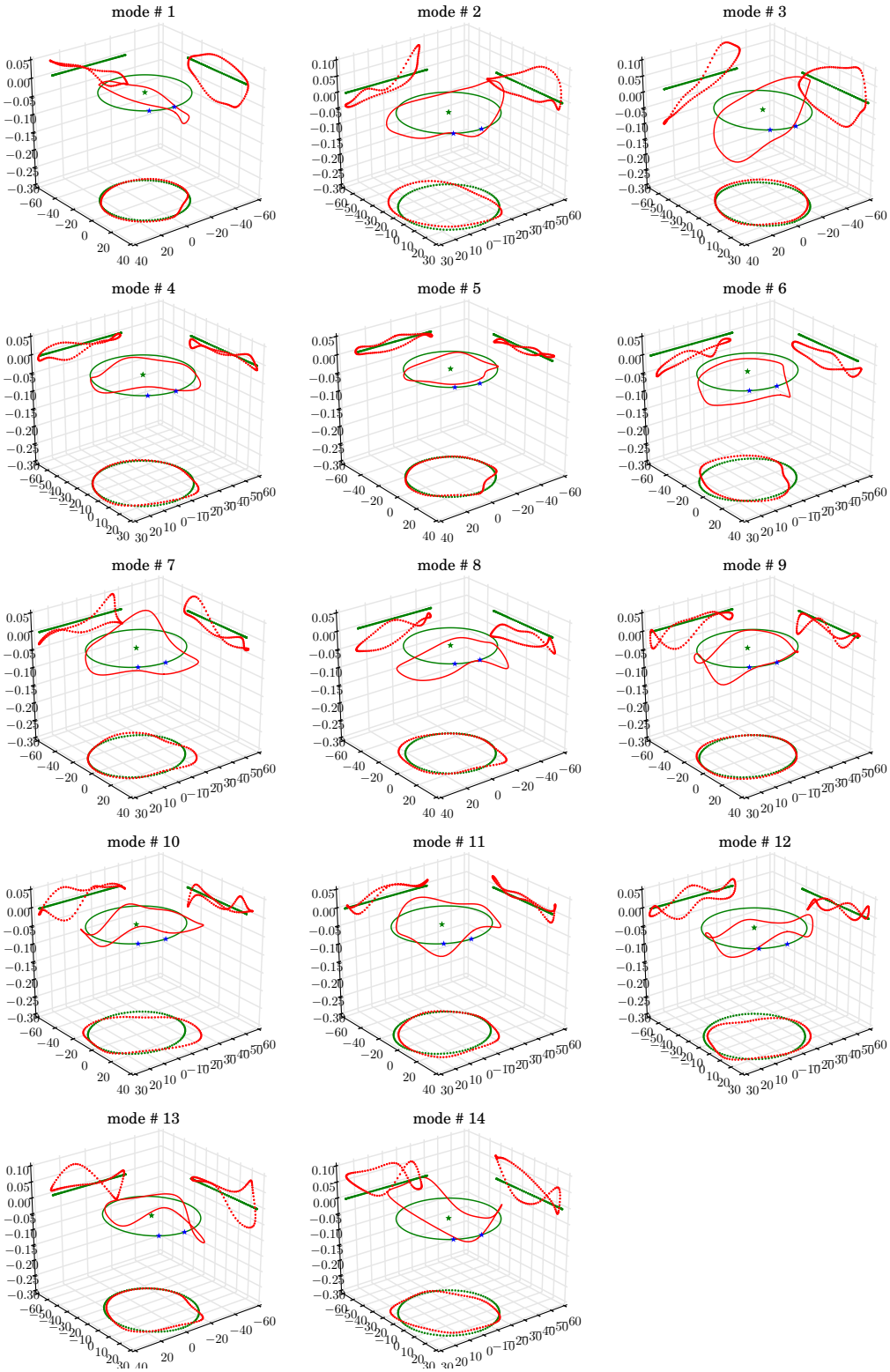

Figure 4.18: Modal Shape for implant # 1

The possible relations between modes and fixation levels presented by gap distance and impact force are shown in figures 4.19, 4.20, 4.21. Where one can see a number of graphs showing a predictive performance of PCR for every mode. Correlation coefficients are shown only for the best matched principal component (tables 4.3, 4.4,4.5, 4.6). The potential real correlation in mode shapes is quite difficult to derive. For this purpose, the determination coefficient, number of correlated principal component and predictive performance are monitored. Filter criterion is based on the number of principal component (max. third component) and coefficient of determination (min. 0.75) of the validated model. Due to a small sample number (10 samples) and high features vector (3000 features), the regression technique tends to perform poor fit with over - fitting. This drawback of experiment will be discussed later. From the performance plots of PCR a general relation of modal shapes and fixation variables can be seen, however with some PCR behavior keeping in mind. Higher principal component explains more local variance or even a noise in a data. For some dummy uncorrelated data, the highest component shows a high linear correlation but the validation of model predictability always shows no any performance. In the tables the fitting parameters are described for both calibrated and validated model. For the first frequency range (100 - 2100 Hz) of implant # 1, the first (polar gap), second (impact force) and fourth (impact force) mode was selected to be the most related to fixation variables. The second frequency range (2100 - 5000 Hz) contains the first (impact force) and second (impact force) mode that potential correlated. Similar results were obtained for implant # 2, where the number of potentially correlated modes is even smaller compared to the first implant.

Table 4.3: Regression parameters for implant # 1 - frequency range 100 - 2100 Hz and gap distance [mm]

	Calibration				Validation			
# mode	Slope [-]	interp. [mm]	RMSE [mm]	R^2[−]	Slope [-]	interp. [mm]	RMSE [mm]	R^2[−]
1.	0.89	0.86	1.01	0.84	0.56	1.93	10.15	0.53
2.	0.86	0.90	0.58	0.86	0.47	3.67	1.11	0.62
3.	0.81	1.21	0.68	0.81	0.64	2.32	0.99	0.69
4.	0.96	0.27	0.38	0.96	0.66	2.22	0.91	0.83
5.	0.37	4.18	1.26	0.37	0.08	6.15	1.58	0.23
6.	0.33	4.34	1.36	0.33	0.04	6.51	1.85	0.10

Table 4.4: Regression parameters for implant # 1 - frequency range 100 - 2100 Hz and impact force [N]

	Calibration				Validation			
# mode	Slope [-]	interp. [N]	RMSE [N]	R^2[−]	Slope [-]	interp. [N]	RMSE [N]	R^2[−]
1.	0.84	1.62e3	2.62e3	0.83	0.48	4.86e3	4.04e3	0.68
2.	0.94	650.97	1.39e3	0.94	0.61	4.25e3	2.71e3	0.82
3.	0.82	1.92e3	2.40e3	0.82	0.67	3.53e3	3.14e3	0.73
4.	0.97	267.47	1.06e3	0.97	0.68	3.63e3	2.93e3	0.83
5.	0.47	5.82e3	4.17e3	0.47	0.17	8.73e3	5.25e3	0.34
6.	0.48	5.95e3	4.31e3	0.48	0.20	8.28e3	5.95e3	0.28

Table 4.5: Regression parameters for implant # 1 - frequency range 2100 - 5000 Hz and gap distance [mm]

	Calibration				Validation			
# mode	Slope [-]	interp. [mm]	RMSE [mm]	R^2[−]	Slope [-]	interp. [mm]	RMSE [mm]	R^2[−]
1.	0.77	1.51	0.81	0.77	0.63	2.63	1.25	0.59
2.	0.73	1.76	0.81	0.73	0.52	3.15	1.12	0.61
3.	0.87	0.86	0.68	0.87	0.32	4.95	1.52	0.54
4.	0.83	0.94	0.33	0.83	0.43	3.09	0.66	0.55
5.	0.99	0.06	0.15	0.99	0.59	2.73	1.17	0.58
6.	0.79	1.29	0.55	0.79	0.44	3.54	0.86	0.62
7.	0.66	2.22	0.91	0.66	0.15	5.86	1.46	0.34
8.	0.26	4.55	1.03	0.26	-0.11	6.86	1.47	-
9.	0.23	5.05	1.39	0.23	-0.02	6.92	1.17	0.11
10.	0.21	4.91	1.07	0.21	-0.08	6.82	1.38	0.04
11.	0.99	0.02	0.09	0.99	-0.01	6.02	1.63	0.26
12.	0.99	8.81e-5	0.01	0.99	0.62	2.72	0.78	0.87
13.	0.99	0.006	0.07	0.99	-0.16	7.89	2.75	0.02
14.	0.96	0.16	0.06	0.96	-0.09	5.82	0.42	0.26

Table 4.6: Regression parameters for implant # 1 - frequency range 2100 - 5000 Hz and impact force[N]

	Calibration				Validation			
# mode	Slope [-]	interp. [N]	RMSE [N]	R^2[−]	Slope [-]	interp. [N]	RMSE [N]	R^2[−]
1.	0.89	1.13e3	1.91e3	0.89	0.81	1.62e3	2.82e3	0.84
2.	0.85	1.62e3	2.23e3	0.85	0.65	3.77e3	3.13e3	0.77
3.	0.91	863.56	1.92e3	0.91	0.19	5.95e3	6.06e3	0.32
4.	0.92	1.06e3	1.14e3	0.92	0.45	9.36e3	3.25e3	0.55
5.	0.99	35.23	327.45	0.99	0.69	3.37e3	3.09e3	0.78
6.	0.71	3.62e3	2.68e3	0.78	0.41	7.27e3	3.81e3	0.54
7.	0.75	2.67e3	2.88e3	0.75	0.21	8.11e3	4.98e3	0.43
8.	0.37	7.77e3	3.86e3	0.37	0.03	1.22e3	5.36e3	0.13
9.	0.23	8.45e3	5.02e3	0.23	-0.03	1.14e3	6.23e3	0.16
10.	0.06	1.15e3	4.74e3	0.06	-0.2	1.46e3	6.29e3	-
11.	0.96	504.23	1.11e3	0.96	0.08	1.28e3	5.61e3	0.32
12.	0.99	8.25	182.24	0.99	0.61	4.18e3	3.30e3	0.85
13.	0.98	133.93	828.65	0.98	-0.05	1.29e3	8.03e3	0.19
14.	0.99	23.46	119.97	0.99	0.06	1.51e3	2.97e3	0.48

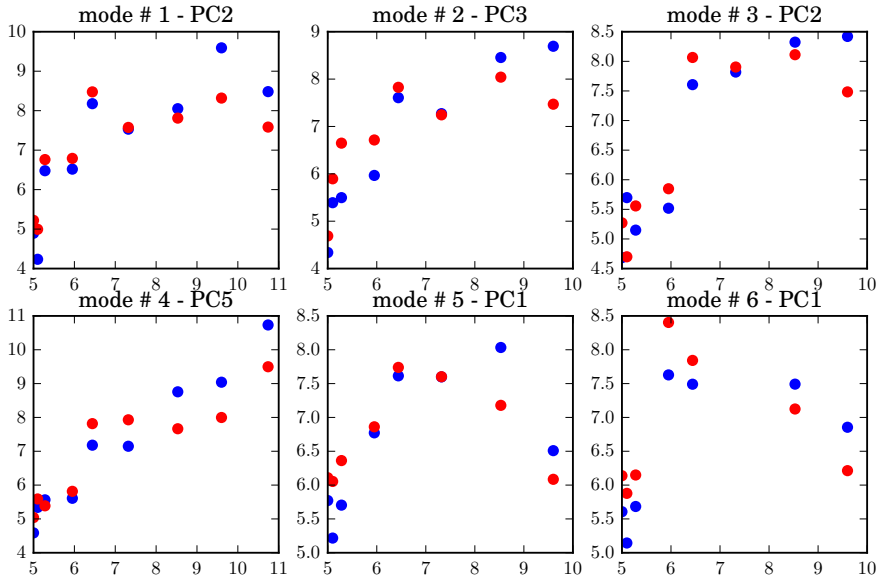

(a) gap distance

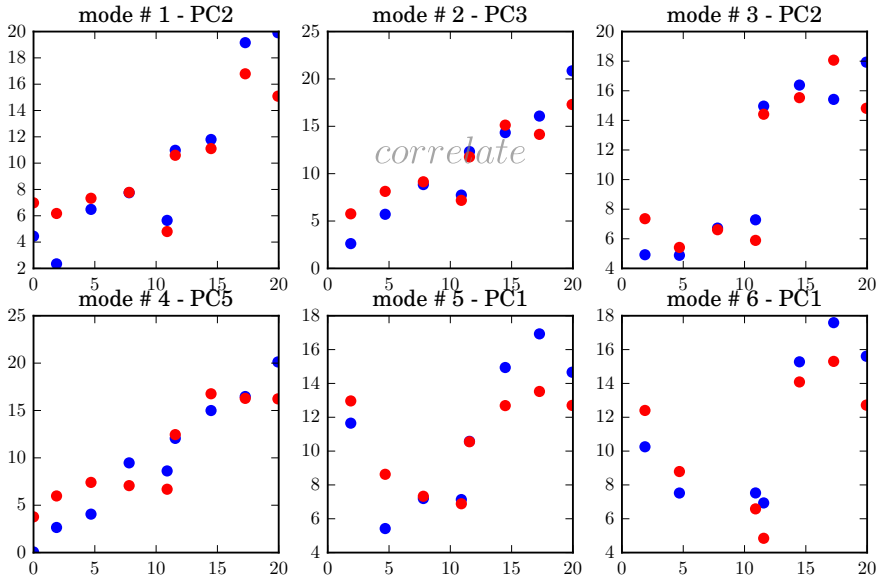

(b) impact force

Figure 4.19: Performance of PCR for implant # 1 in range 100 - 2100 Hz

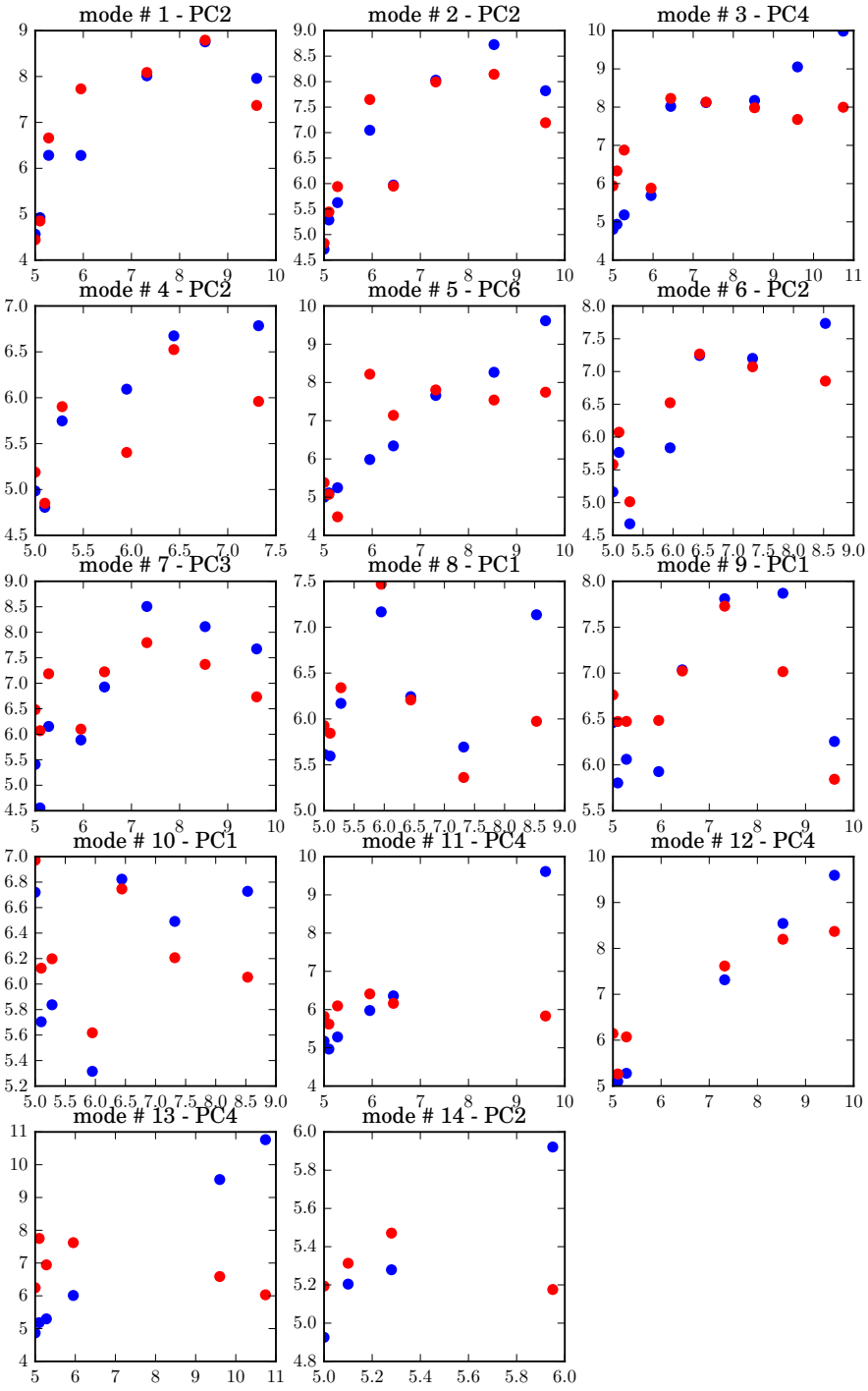

Figure 4.20: Performance of PCR for implant # 1 in range 2100 - 5000 Hz - gap distance [mm]

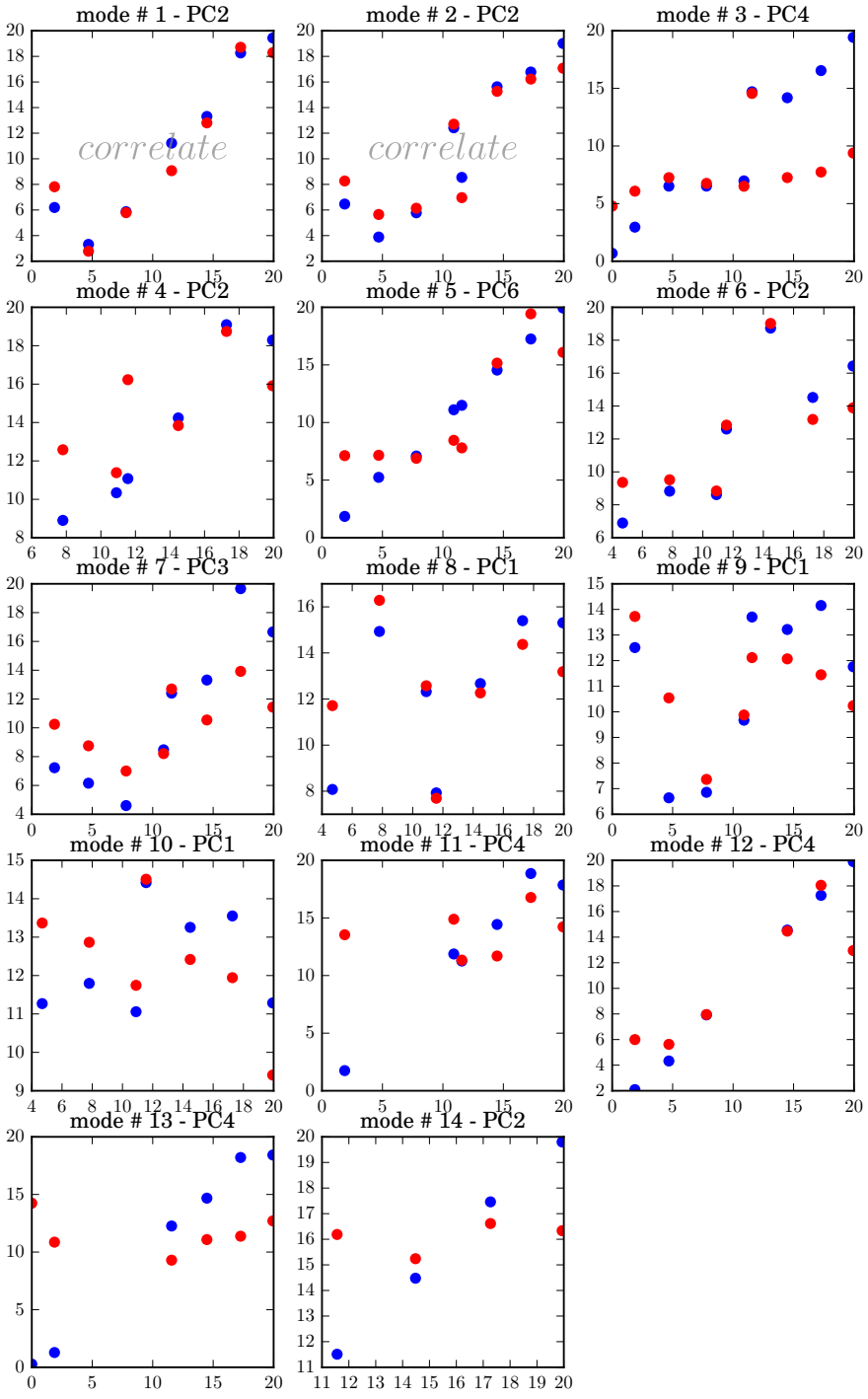

Figure 4.21: Performance of PCR for implant # 1 in range 2100 - 5000 Hz - impact force [kN]

4.2.3 FRF Raw Correlation

Previous correlation analysis are based on the data that come from the identification process and thus they depend on the estimator quality. The way how to overcome estimation quality is to perform exploratory analysis on the raw spectral data for each dof. This idea leads to a multidimensional correlation problem with possible collinear data. Such problem can be handled by similar technique as PCR named Partial Least Square Regression (PLSR). The raw FRF data is sorted according the spatial positions around the rim of acetabular implant and the direct of excitation source (radial and axial). Thus, 24 dofs are measured for every implant. The figures 4.22, 4.23 and 4.24, 4.25 show a polar spatial performance of the regression for both frequency bands and directions. The plots represent calibration and validation values for coefficient of determination (blue and red). Circles contains the number of principal component. The dof that fulfills the threshold criteria ($PC <= 3$ and $R^2 >= 0.75$) are marked by green color. The number of potentially correlated DOF with fixation variables is general higher for the radial direct (19 vs 9). Also, it seems to be that from the calibration values point of view, the second frequency band confirms a higher determination coefficients (blue structure). This could be given by the real assumption that higher modes are more correlated or just higher noise. However, the validation of regression models is still poor for all implants and frequency bands.

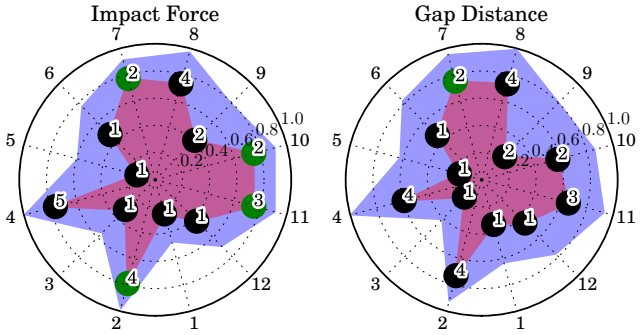

(a) frequency range 100 - 2100 Hz

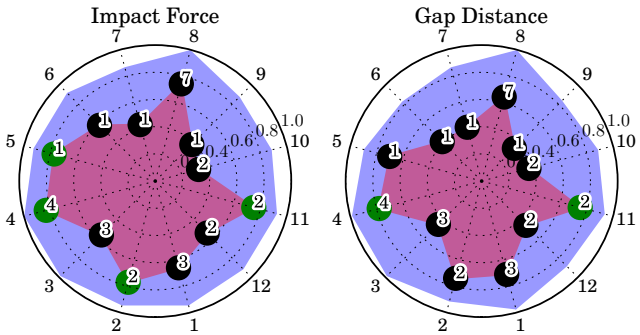

(b) frequency range 1900 - 5000 Hz

Figure 4.22: Correlation plot for implant # 1 - radial DOF

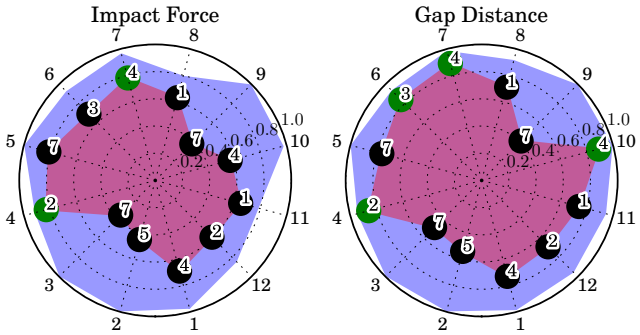

(a) frequency range 100 - 2100 Hz

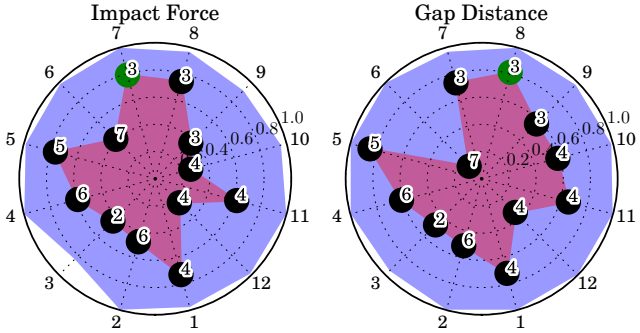

(b) frequency range 1900 - 5000 Hz

Figure 4.23: Correlation plot for implant # 2 - radial DOF

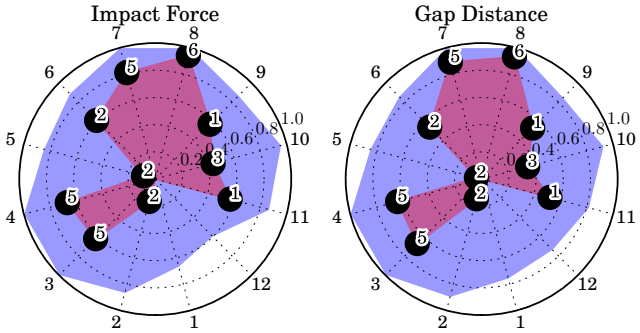

(a) frequency range 100 - 2100 Hz

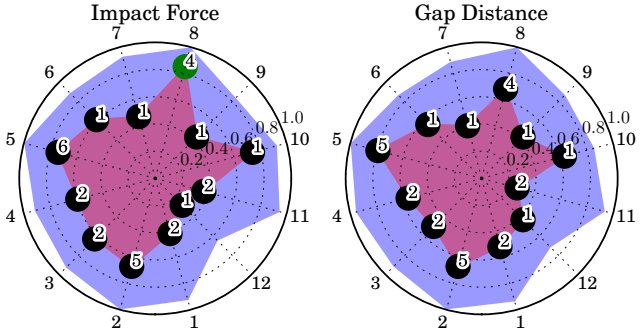

(b) frequency range 1900 - 5000 Hz

Figure 4.24: Correlation plot for implant # 1 - axial DOF

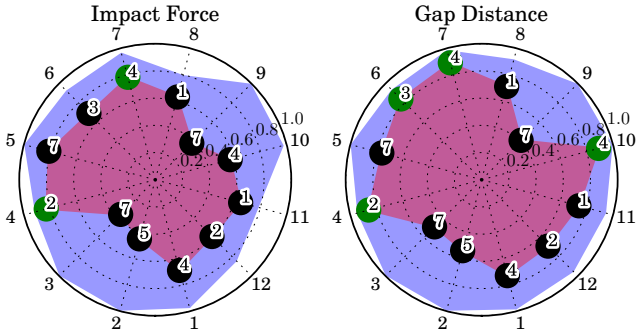

(a) frequency range 100 - 2100 Hz

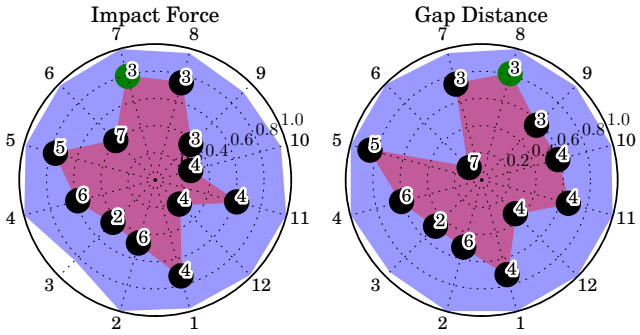

(b) frequency range 1900 - 5000 Hz

Figure 4.25: Correlation plot for implant # 2 - axial DOF

4.3 Summary

In this chapter, the complete experimental survey of correlation between initial fixation and modal properties was described. In the first part of the chapter the experimental protocol is built with respect to different initial fixation of the acetabular cup in saw bone pelvis. This assumption leads to simplified conditions which may not correspond with real situation in vivo, however in process of correlation, a complicated in - vivo conditions can generate difficulties. The overall model is composed from three different acetabular cups and with one type of pelvis bone with the same geometry and material properties distribution. Every cup is inserted into the pelvis acetabular and than the modal analysis is performed on cup rim. Modal analysis step is an important step since it is a key process which provides dynamic properties of the system. To correct identify measured mechanical system through its dynamic parameters, the MLE algorithm is employed. This identification process provides also statistical properties of dynamic parameters, which leads to better separation of physical and computational modes. After physical thresholding, most significant computational modes are removed and the rest of them is detected by trained machine learning algorithm. This approach seems to be an almost fully automated process of modal analysis. To properly match the modes in every insertion phase, a tracking process must be imposed. Due to limited applicability of the modal impact hammer, the frequency range was split into two ones. The first range contains a high quality FRF and the identification is very robust and efficient. On the other hand, the second range, unfortunately more important, has a poor quality and the results are impacted by high uncertainty, which is seen in the estimated variances estimated by MLE.

In this work, the algorithm based on the modified MAC criterion was successfully used to track modes. The algorithm also gives an additional information about bad identified modes, which usually have a small neighborhood connectivity in the tracking plot. Although, in the case of high noise data (second freq. range), mode tracking need manual verification and correction and it does not still guarantee the properly tracked modes. The fixation level of each cup is represented by impact force and polar gap distance. This description of level fixation is comparable with a classical definition of primary stability (as interface stiffness or push out test). Monitoring of both variables (polar gap and impact force) gives us the information about the bone - implant interface behavior and even from the geometry of acetabulum, diameter of implant and polar gap is possible to compute shared contact area theoretically. A potential relation between modal parameters (frequency and damping ratio) and fixation variables was investigated with help of correlation analysis based on the Spearman's criterion. A simple plot analysis and correlation method show that modal parameters are responsive to level of fixation. However the relation is not strictly linear or even monotonic in the case where rapid changes start in the interface stiffness. From the quantity point of view, the absolute frequency sensitivity especially in the second band are much more significant. It

would be a prove that higher modes (modes of acetabular cup) are more sensitive to changes in interface stiffness. On the other hand, it would be a result of poor data quality.

A possibility that modal shapes would be a candidate reflecting the initial fixation was investigated in a similar manner as modal frequencies and damping. To capture the multidimensional nature of shape vector, Principal Component Regression was used to investigate a possible correlation of modal shapes and fixation variables. The results from multidimensional regression analysis indicates a potential correlation of some modes, but in almost cases without sufficient validation. Similar results were obtained with regression analysis for raw FRF data. Since the interpretation of local changes is possible via the modal parameters, global changes are investigated on raw FRF data. Although the multidimensional analysis seems to be a promising tool to found a correlation, but it does tell a little or even nothing about physical background. This is because the reduced feature vector is hard to interpret.

Chapter 5

Measuring device design

In this chapter the author developed an experimental device for measuring the initial fixation of the acetabular and femoral component. The device is designed to fulfill medical norm requirements according to ISO 60601. The device is able to operate at the clinical environment. This is an essential step, which provides an advance in real clinical usability and opens the door to start performing real clinical experiments.

5.1 Introduction

Experimental device for the initial fixation measuring is composed mainly from three parts:

- Vibrational Head - measuring probe
- Control Unit
- User computer

Every part is designed according to ISO 60601. The main idea of the measuring is the vibrational principle.

5.2 Vibrational Head

The vibrational head is composed of three parts. The first part is a frame from medical steel with plastic cover. The mechanism of the fasting to the implant is very simple, base on the thread to lock up the system (figure 5.1). Firstly, the mechanism is disconnect to be than freely attached to the femoral neck or acetabular beam. After properly positioning the vibration head, the final position is fixed by the thread. The measuring head is designed as two channel

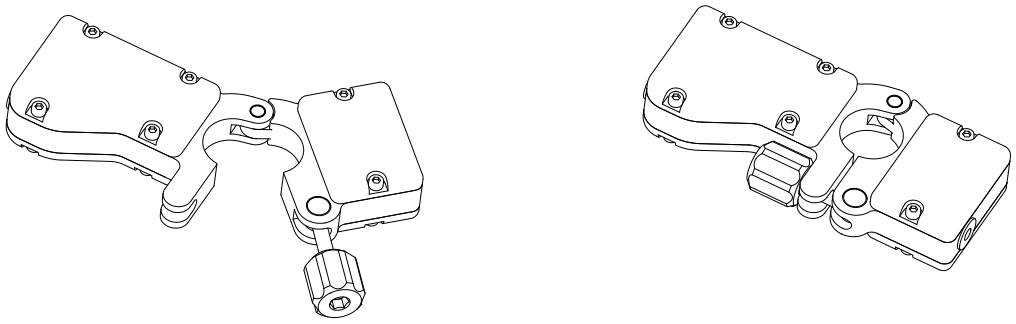

(a) Opened (b) Lock Up

Figure 5.1: Fixation mechanism

measuring probe. The one channel is the vibration signal to drive the electromechanical actuator and second one is dedicated to acquire the response the system to the vibration from actuator. The response is acquired by an accelerometer. The position of the measuring devices is depicted in figure 5.2.

The electromechanical actuator is a stacked piezoelectric block. The force is generated in reaction sense, thus, on the top of the actuator, the seismic mass (10 grams) is added. The actuator and accelerometer are isolated according to the norm by the ceramic insulator. The

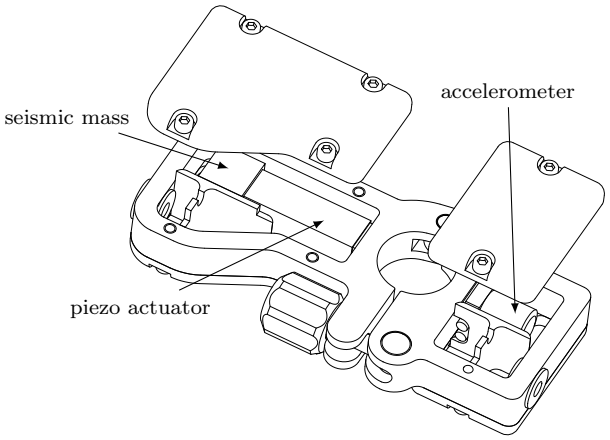

Figure 5.2: Position of the actuator and accelerometer

actuator is driven by the voltage driver up to 150 V. The maximal displacement is 17.4 μm. The accelerometer is based on the piezo principle. The sensitivity is 10 mV/g and the range is $\pm$500 g. The accelerometer and actuator are protected from the aggressive sterilizing process by the bio - silicone gasket.

5.3 Control Unit

The control unit has a function of generating and acquiring the signal. It is battery supplied electronics. the heart of the system is the microchip ATMEL x51 family, which provides the communication between external computer and the driven voltage generator for piezo actuator. The generation of the high voltage signal is provided by the specialized power MOSFET transistor. The wireless connectivity is provided by the specialized IO block OWS 451 with 60601 certification. The block scheme is depicted in figure 5.3. The energy for the

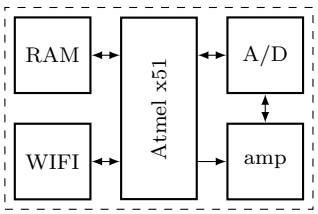

Figure 5.3: Block scheme of the control unit

piezo actuator is provided by two Li-pol batteries. Electromagnetic field compatibility is

secured with proper circuit topology and adequate external shield (aluminum chassis - figure 5.4).

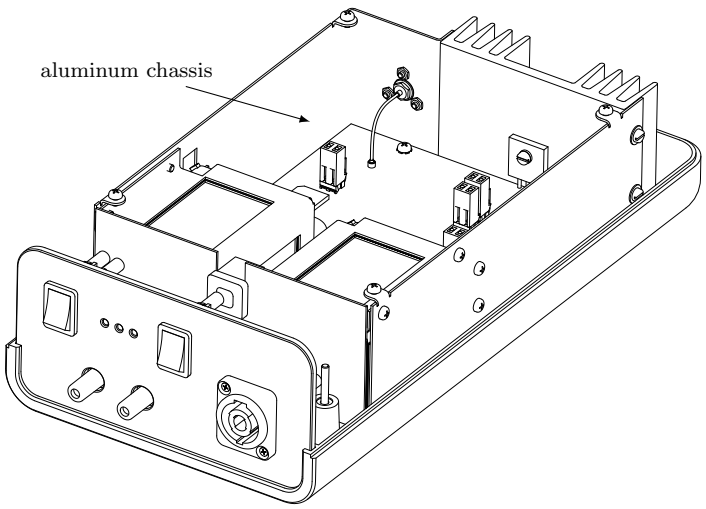

Figure 5.4: Control unit design

5.4 User Interface

The control unit communicates directly with the user interface composed of tablet with adequate software. The tablet is certified for the ISO 60601 and does not need further specification. The software provides basic functionality such internal communication protocol, generation of the excitation signal and acquiring. The software also controls the temperature in the control unit, properly connected measuring probe and status of wireless connection. Raw data from the control unit could be quickly evaluated in the provided software, but for more sophisticated evaluation, the external software is needed.

5.5 Summary

This chapter contains a quick introduction into the design of the experimental device used for measuring initial fixation of THR implants (figure 5.5). Main technologies were presented with focus on the vibrational head. The vibrational head is the most critical part of designing, because it is directly connected to the human body and it needs for its properly function a voltage source to driven a piezo stack. The technology and design of this device are patented in internal scope [261].

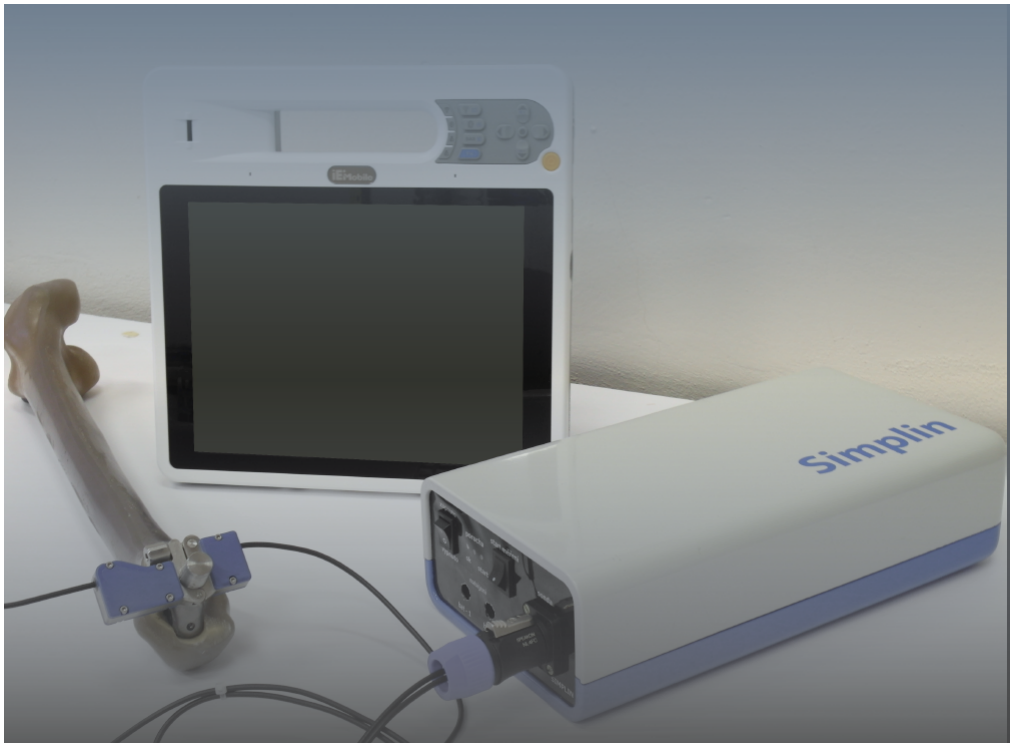

Figure 5.5: Final device design

Chapter 6

Summary

Assessment of the initial fixation of the acetabular cup in per operative conditions can bring an important information about its future survive. The social and economical benefit of this information for a surgeon and also for a patient is significant. The knowledge about the quality of implantation plays a crucial role in prevention the revision surgery. Decreasing the probability of revision surgery leads to an increasing of patient live quality and decreasing the price of THR surgery. However such information is not easy obtain. In dental surgery the environmental conditions permit the clear enter to the implant during the whole healing period. It was proven that dental implant shape is much more suitable to find a significant relation between the implant fixation and change in its dynamic parameters. However in other disciplines such orthopedic it is not easy implement, and, there is even a question if it would work in such a way. The most studies deal with the initial fixation of the femoral component, however the survival of the acetabular component is the same or even worst as it was found from literature studies. Another aspect that significantly contributes to decrease of the implant survival is a problematic radiographic evaluation of the implant performance. All of these problems lead to finding a new technique how to asses the implant performance that would outperform all drawbacks of traditional diagnostic methods. The initial fixation of the implant is taken as a promising variable to predict the implant performance. The initial fixation is taken as an amount of the micromotion at the bone - implant interface or as u micro deformation. These two variables strong correspond with the common stabilizing techniques (fixation with pegs, spikes and press fitting) during te insertion step. However the experiments are performed in vitro with precise experimental equipment. Also, the experiments itself often use a destructive testing, which is not acceptable in clinical environment.

Dynamic response of the measured system bone - implant - (probe) on the different fixation level was shown mainly in dental implantology, but also in the case of the femoral component. where the implant response was measured for different press fit level for bending and torsional modes. Although, the clinical using is not still available, probably due to problematic measuring mechanism usable in vivo. It can be hypothesize that femoral com-

ponent would be more suitable for this kind of initial fixation assessing due to its similar topology as the dental implant has. There is a lot of publications dealing with initial fixation related to the dynamic response, however there is a little about the why it should work, why a relation should exist between the fixation and dynamic response of implant. An attempt of explanation was perform in chapter 3, where the relation between shared contact area and the dynamic response of the system bone - implant - (probe) was investigated. The contact area is an essential measurable variable, which probably strong influences the initial fixation of the implant. It influences the mechanical properties as amount of micromotion, friction and even bio - integration process. From interface point of view, the surface also influences the interfacial stiffness. For accepting or rejecting hypotheses about the interfacial stiffness influences the dynamic response of the system, a mathematical model with various interfacial contact level was investigated. The modal analysis was performed for every contact level with different shared contact area. Output modal parameters were than correlated with the control parameter of insertion phase. The computational model confirms the hypothesis that dynamic properties of bone - implant - probe are influenced by a different amount of shared contact surface. This influence was demonstrated on the sensitivity analysis of modal parameters respect to the control insertion parameter. Investigating the complexity of modal shapes and its MAC criterion related to the control variable supports the hypothesis that more complex modes are more sensitive to changes in the bone - implant interface. This was shown through the relation between minimal value of MAC criterion of every mode and control variable. The results shows that the minimal value of MAC decreases with increasing the mode complexity.

The mathematical model takes as real data as possible to obtain relevant results. The synthetic model of the pelvis bone was firstly digitalized by the CT scanner and consequently reconstructed with sophisticated segmentation process. The material field is based on the linear elastic model with continuous material properties extracted from the density of raw CT data. Due to a simplified, nearly homogeneous properties of the synthetic bone with known material properties, there was not used a power relation between Young modulus and density, but only the boundary between the cancellous and cortical bone was adopted. The orthotropic nature of the outer cortical part was modeled by a simplified coordinate field based on the curvature of the shell and the thickness of the cortical bone. This assumption works well for this synthetic bone model, where the manufactures guarantee the transversally isotropic properties and the transversal direction is parallel to outer shell normal. In a real case the coordinate could be modeled rather from gray density data. The model consists of another three coordinate system (global anatomic, local acetabular and boundary). The global anatomical coordinate system is a base frame given by the position in the CT scanner. The local coordinate system was defined for the easier manipulation with the acetabular cup. The coordinate origin was placed at the acetabular sphere center, which was found by the

non linear optimization scheme. The coordinate base vectors were constructed with singular value decomposition with direction at an unique anatomical land markers. The position of the implant cup was then recomputed to the radiographic one. The boundary coordinate system was constructed from curvature properties of the bone surfaces.

The mathematical model of the pelvis - implant - probe was based on finite element method. The model was validated against the experimental modal analysis. The experimental modal analysis was performed on the synthetic pelvis bone in 228 measuring points with one driven point. This leads to an sufficient description of the modal vectors, damped modal frequencies and damping ratio. The maximum relative error in the damped frequencies was around 2% for the second mode. The modal vectors were compared with MAC criterion. The significant correlation was found for all measured modes (five modes) in frequency range 10 - 2000 Hz. The minimum correlation 65 % was found for the second mode, but it is taken as still sufficient correlation. This relative low correlation could reflect the errors between measuring position in real and digital model. Better results can be obtained with refinement on the measuring grids and normals. However modal vectors are complex, the complexity and phase collinearity show that the vectors are nearly monophasic. This implicates somewhat error in the measuring way - probably due to some bad impact or local damping. The computational model was successfully validated by the experimental modal analysis with the initial material parameters, however the refinement was applied via optimization scheme that allows account a possible spatial variation of Young modulus with structural density. After successful update of finite element model of the pelvis bone, the uncertainty of estimated parameters was computed via the first order sensitivity method.

Going back to purpose of the computational model, a parametric sensitivity of the modal properties of the system bone - implant - (probe) to a different contact area amount was investigated. The different contact area was obtained with parametric changes of the reamer position, this goes to the different uncovered portion of the cortical (subchondral) and trabecular bone. The different contact area amount always occur in the real situation and it is important know what influences the initial fixation. The origin position of the reamer lies in the plane rotated according a common surgical procedure. The reamer was positioned negatively close into a notch and also positively more out of the plane. These two opposite directions express a possible scenarios of the reamed cavity. With closer look how the contact are is changing during the different reamer displacement, there is seen the non linear dependence of the cortical and trabecular area. This simply mean that there exists a displacement position where the cortical area is dominant (if it is expected that shared cortical area has much more significant positive impact to the initial fixation). The sensitivity of the modal parameters was monitor through their variance and sensitivity ratio, since the direct explicit formulation of the sensitivity matrix was problematic. The participation factors seem very sensitive to change in contact area, but this result has to be taken with careful interpretation,

since their magnitude is in range of accuracy of the computational model. The change of the quality factor was also monitored for controlling purposes. The sensitivity of quality factor was not significant. The damped frequencies are sensitive to change of the contact area and even there exists a correlation with changing of contact area. The first five deformable modes were monitored for possible experimental comparing with impact hammer testing, however, the extending of the frequency range could uncover more complicated modes, which may be much more sensitive to a local changes in contact area. For example, there first five modes do not account the natural frequency of the cup itself, because it is in much higher frequency range (4.3 kHz - first deformable rim mode of the cup). The special attention was paid to quantify the changes in the modal shape vectors. The correlation matrix all to all was created for every parts of the modal shape vector. The shape vectors are sampled in gauss points on the one template mesh with adequate rigid transformation according to implant displacement change. Modal vectors were sampled also on the special beam, connected through the threat at cup pole. This measuring probe is expected to have an ability reflect the cup response in its dynamic properties. This solution was designed for easy manipulation and measuring in vivo. The frequencies of the modal probe is in similar range as frequencies of the pelvis. From the correlation matrices is seen that in almost cases, the shape vectors are not sensitive to change in contact area. But there are exceptions in case of the second deformable mode, which has a character of the bending mode with dominant deformation on the probe, the third coordinate of the shape vector seem to be sensitive to the changes in contact area. If one try to hypothesize that it is a relevant information, it would mean that there is a significant change in contact boundaries in defined direct. This would be a good observation and thus it needs more refinement and experimental background. The correlation matrices were constructed on the MAC criterion in all to all configuration. Another support interest is that increasing shape complexity corresponds with decreasing of the MAC values. This simply means that more complex modes are more sensitive to changes in bone - implant interface.

The experimental part is focused mainly on investigation of potential relation between input data, namely modal parameters (frequencies, damping and shapes), raw FRF data and output response defined as fixation variables (polar gap and impact force). It is supposed that response variables represent fixation level of implant. This assumption is based on the strong relation of impact force and pull out test commonly referred as a quantification of initial fixation. Putting these variables together, the axial stiffness could be obtained as another fixation description. Before implementing the main experimental protocol, algorithms for automatically performing modal analysis were developed. The main core of estimation of modal parameters is the Maximum likelihood estimator with uncertainty framework. The ability of uncertainty estimation is an advantage during the second step for detecting spurious modes. Classification of spurious and real modes is based on a combination of cluster analysis and support vector machine algorithm. The last step is to involve tracking mechanism to have

a properly matched identified modes for every fixation level. The algorithm is based on the enhanced MAC criterion. The main experimental protocol consists of three acetabular cups with different press fit level inserted into sawbone pelvis. During the insertion phase, every impact is recorded by impact hammer and the polar gap is measured with in a statistical manner. Experimental modal analysis is performed for 24 dofs (12 radial and 12 axial) on cup rim. The results from experimental modal analysis are split into two frequency bands, because of different quality of frequency responses. All results from the second band are impacted by much lower quality and this is taken as one of the important drawback of experimental protocol. The lower quality of frf data is cased by the insufficient ability of excitation hammer to work in higher frequency (i.e. higher than 2500 Hz). Despite to high uncertainty in the FRFs, robust log MLE with machine learning recognition of physical modes identified properly most modal parameters. The problem of quality was a little more significant in case of tracking mechanism, especially in the higher frequencies. After having tracked modes, the correlation analysis goes to be the next step. Generally, the correlation analysis was performed in a local and a global sense. Modal parameters such frequency and damping ratio have a local character. The global behavior is more referred to modal shapes and raw FRF data. In order to account multidimensional character of shape vectors and FRF data, regression methods (Principal Component Regression (PCR) and Partial Least Square Regression (PLSR)) were used to determine the relation in the frequency data. Correlation analysis for local and global variables as well shows potential relations that would be candidates describing the initial fixation of acetabular implants. Although, the regression models were always validated, the sample size is one of the factors negatively influencing the quality of regression models. Another, very important drawback of the correlation study, is a difficult physical interpretation of reduced data (PCA). This leads to focus only on quantifying the relation rather than qualifying.

At the final chapter, the real clinical device is designed and tested according to ISO 60601. The capability of designed device opens wide possibilities how to get the real clinical data and thus how to describe real fixation of the bone much more accurate. The uniqueness of the designed device is that it can measure initial fixation of the both part of THR, *i.e.* femoral and acetabular component. The device contains vibrational head and control unit. The control unit communicates with common medical tablets by wireless way.

The using of experimental modal analysis confirms the hypothesis that bone - implants can be taken as a linear system. From computer simulations and experiment done in this thesis it can be concluded, that the level of initial fixation of acetabular implant correlates with dynamic properties of the bone - implant - (probe) system. All modal properties and the raw FRF data were potentially correlated with insertion force and polar gap distance. Modal parameters (mainly natural frequencies or amplitudes) are commonly used for investigating the initial stability of implant, however without proper handling of uncertainties

and modal shapes. The importance of modal shapes for initial fixation of implant has never been accounted, partially because obtaining of modal shapes can be a time consuming operation. The known modal shapes bring important information about the possible switch of closely spaced modes (mode tracking). Insufficient mode tracking can lead to an misinterpretation of modal parameters and consequently distorts the correlation phase. In this thesis a precise modal analysis was performed with mode tracking. All modal parameters (natural frequencies, damping and shapes) and their uncertainties were monitored and correlated with insertion variables of implantation process.

All hypotheses about vibration method for assessment of initial fixation of acetabular implant were supported with computational and experimental investigation. Modal parameters and raw FRF data can potentially reflect the initial fixation level of cup. The raw FRF data as description parameters of implant stability is a novel approach and could overcome the traditional approach based on the modal parameters. Using sophisticated machine learning techniques (in this thesis regression methods were used) would bring a new look including a complicated correlation in spectral data and shapes of FRF response. The response data from vibrational measuring for machine learning algorithms must not be necessarily in the frequency domain. This is another advantage against the traditional approach based on the modal analysis, which expects that measured system is linear one. The next step in the developing of the device measuring real initial fixation of acetabular implant is to employ machine learning techniques on the data obtained from designed device in clinical environment.

Publications

Main publications related to the thesis:

- Petr Henys, Lukas Capek, Jaroslav Fencl, and Egon Prochazka. Evaluation of acetabular cup initial fixation by using resonance frequency principle. *Proceedings of the Institution of Mechanical Engineers, Part H: Journal of Engineering in Medicine*, 229(1):3–8, 2015
- Petr Henyš and Lukáš Čpek. Numerical and experimental results from measuring spinal implant stability. *Journal of Vibroengineering*, 15(2), 2013
- P. Henyš and L. Čapek. Measuring primary stability of cervical implant. *Computer methods in biomechanics and biomedical engineering*, 15(sup1):340–342, 2012

Other publications:

- L. Dzan, P. Henyš, L. Čapek, and A. Šimůnek. Makrodesign implantátu-typy a tvary používaných závitů a jejich hodnocení metodou konečných prvků. *Czech Stomatology & Practical Dentistry/Česká stomatologie a praktické zubní lékařství*, 113(4), 2013
- L. Capek, A. Simunek, P. Henys, and L. Dzan. The role of implant's surface treatment to its preload. *Computer methods in biomechanics and biomedical engineering*, 17(sup1):8–9, 2014

Conference papers:

- Michal Ackermann, Lukáš Čapek, Petr Henyš, and Cyril Dody. Evaluation of contact pressure by using pressurex films. In *14th Conference on Human Biomechanics*, page 2, 2012
- Maxime Billon, Lukáš Čapek, Martin Kaláb, Petr Henyš, and Petr Hájek. Analysis of the force needed for the closure of the sternum after median sternotomy. In *14th Conference on Human Biomechanics*, page 3, 2012
- Enrico Schileo, Cristina Falcinelli, Luca Balistreri, Petr Henys, Fabio Baruffaldi, Sigurdur Sigurdsson, Vilmundur Gudnason, Stephanie Boutroy, and Fulvia Taddei. Association of ct-based finite element estimates of femur strength with fracture status in three clinical studies on post-menopausal women. 2014

Patents:

- L. Čapek, P. Henyš, and Fencl J. Tool for measuring of implant stability, 2014

Bibliography

[1] Ian D. Learmonth, Claire Young, and Cecil Rorabeck. The operation of the century: total hip replacement. *The Lancet*, 370(9597):1508–1519, 2007.

[2] American Academy of Orthopaedic Surgeons. *American Academy of Orthopaedic Surgeons: National Center for Health Statistics*. American Academy of Orthopaedic Surgeons, 1999.

[3] B. F. Kavanagh, D. M. Ilstrup, and R. H. Fitzgerald. Revision total hip arthroplasty. *The Journal of Bone and Joint Surgery*, 67(4):517–526, 1985.

[4] Kelly L. Corbett, Elena Losina, Akosua A. Nti, Julian J. Z. Prokopetz, and Jeffrey N. Katz. Population-based rates of revision of primary total hip arthroplasty: A systematic review. *PLoS ONE*, 5(10):e13520, 10 2010.

[5] L. Ahnfelt, P. Herberts, H. Malchau, and G. B. J Andersson. Prognosis of total hip replacement: A swedish multicenter study of 4,664 revisions. *Acta Orthopaedica*, 61:2–26, 1990.

[6] Richard Iorio, William L. Healy, and Anthony H. Presutti. A prospective outcomes analysis of femoral component fixation in revision total hip arthroplasty. *The Journal of Arthroplasty*, 23(5):662 – 669, 2008.

[7] John Older. Charnley low-friction arthroplasty: A worldwide retrospective review at 15 to 20 years. *The Journal of Arthroplasty*, 17(6):675 – 680, 2002.

[8] A. R. Britton, D. W. Murray, C. J. Bulstrode, K. McPherson, and R. A. Denham. Long-term comparison of charnley and stanmore design total hip replacements. *Journal of Bone and Joint Surgery, British Volume*, 78-B(5):802–808, 1996.

[9] Ulf Lucht. The danish hip arthroplasty register. *Acta Orthopaedica*, 71(5):433–439, 2000. PMID: 11186396.

[10] W. H. Harris. Aseptic loosening in total hip arthroplasty secondary to osteolysis induced by wear debris from titanium-alloy modular femoral heads. *The Journal of Bone and Joint Surgery*, 73(3):470–472, 1991.

[11] Seneki Kobayashi, Kunio Takaoka, Naoto Saito, and Kenji Hisa. Factors affecting aseptic failure of fixation after primary charnley total hip arthroplasty. multivariate survival analysis*. *The Journal of Bone and Joint Surgery*, 79(11):1618–1627, 1997.

[12] A. V. Lombardi, T. H. Mallory, B. K. Vaughn, and P. Drouillard. Aseptic loosening in total hip arthroplasty secondary to osteolysis induced by wear debris from titanium-alloy modular femoral heads. *The Journal of Bone and Joint Surgery*, 71(9):1337–1342, 1989.

[13] Steven H. Weeden and Wayne G. Paprosky. Minimal 11-year follow-up of extensively porous-coated stems in femoral revision total hip arthroplasty. *The Journal of Arthroplasty*, 17(4, Supplement 1):134 – 137, 2002.

[14] Nizar N. Mahomed, Jane A. Barrett, Jeffrey N. Katz, Charlotte B. Phillips, Elena Losina, Robert A. Lew, Edward Guadagnoli, William H. Harris, Robert Poss, and John A. Baron. Rates and outcomes of primary and revision total hip replacement in the united states medicare population. *The Journal of Bone & Joint Surgery*, 85(1):27–32, 2003.

[15] Kevin L. Ong, Edmund Lau, Jeremy Suggs, Steven M. Kurtz, and Michael T. Manley. Risk of subsequent revision after primary and revision total joint arthroplasty. *Clinical Orthopaedics and Related Research®*, 468(11):3070–3076, 2010.

[16] Slif D. Ulrich, Thorsten M. Seyler, Derek Bennett, Ronald E. Delanois, Khaled J. Saleh, Issada Thongtrangan, Michael Kuskowski, Edward Y. Cheng, Peter F. Sharkey, Javad Parvizi, James B. Stiehl, and Michael A. Mont. Total hip arthroplasties: What are the reasons for revision? *International Orthopaedics*, 32(5):597–604, 2008.

[17] Rik Huiskes. Failed innovation in total hip replacement: Diagnosis and proposals for a cure. *Acta Orthopaedica*, 64(6):699–716, 1993.

[18] T. W. Bauer and Jean Schils. The pathology of total joint arthroplasty. *Skeletal Radiology*, 28(9):483–497, 1999.

[19] Anna Fahlgren, Mathias P. G. Bostrom, Xu Yang, Lars Johansson, Ulf Edlund, Fredrik Agholme, and Per Aspenberg. Fluid pressure and flow as a cause of bone resorption. *Acta Orthopaedica*, 81(4):508–516, 2010. PMID: 20718695.

[20] Stuart B. Goodman, Enrique Gómez Barrena, Michiaki Takagi, and Yrjo T. Konttinen. Biocompatibility of total joint replacements: A review. *Journal of Biomedical Materials Research Part A*, 90A(2):603–618, 2009.

[21] M. Viceconti, R. Muccini, M Bernakiewicz, M. Baleani, and L. Cristofolini. Large-sliding contact elements accurately predict levels of bone–implant micromotion relevant to osseointegration. *Journal of Biomechanics*, 33(12):1611 – 1618, 2000.

[22] Paul F. Lachiewicz and Elizabeth S. Soileau. Changing indications for revision total hip arthroplasty. *Journal of surgical orthopaedic advances*, 14(2):82—84, 2005.

[23] John C. Clohisy, George Calvert, Frank Tull, Douglas McDonald, and William .J Maloney. Reasons for revision hip surgery: A retrospective review. *Clinical Orthopaedics and Related Research*, 429, 2004.

[24] P. I. BRANEMARK. Osseointegrated implants in the treatment of the edentulous jaw. experience from a 10-year period. scand. *J. Plast. Reconstr Surg*, 16:1–132, 1977.

[25] T. Albrektsson, P. I. Brånemark, H. A. Hansson, and J. Lindström. Osseointegrated titanium implants: Requirements for ensuring a long-lasting, direct bone-to-implant anchorage in man. *Acta Orthopaedica*, 52(2):155–170, 1981.

[26] R. Branemark, P. I. Branemark, B. Rydevik, and Robert R. Myers. Osseointegration in skeletal reconstruction and rehabilitation. *Journal of Rehabilitation Research and Development*, 38(2):175–181, 2001.

[27] R. J. Haddad, S. D. Cook, and K. A. Thomas. Biological fixation of porous-coated implants. *The Journal of Bone and Joint Surgery*, 69(9):1459–1466, 1987.

[28] Jay A. Mandell, Dennis R. Carter, Stuart B. Goodman, Stuart B. Schurman, and Gary S. Beaupré. A conical-collared intramedullary stem can improve stress transfer and limit micromotion. *Clinical Biomechanics*, 19(7):695 – 703, 2004.

[29] Vincent A. Stadelmann, Alexandre Terrier, and Dominique P. Pioletti. Microstimulation at the bone–implant interface upregulates osteoclast activation pathways. *Bone*, 42(2):358 – 364, 2008.

[30] J. Karrholm, B. Borssen, G. Lowenhielm, and F. Snorrason. Does early micromotion of femoral stem prostheses matter? 4-7-year stereoradiographic follow-up of 84 cemented prostheses. *Journal of Bone and Joint Surgery, British Volume*, 76-B(6):912–917, 1994.

[31] I. C. Clarke, P. Campbell, and N. Kossovsky. Debris - mediated osteolysis - a cascade-phenomenom involving motion, wear, particulates, macrophage induction, and bone lysis. *In: St. John KR (ed). Particulate debris from medical implants: mechanisms of formation and biological consequences, ASTM STP 1144. Philadelphia, American Society for Testing and materials*, 1992.

[32] Mariko Horikoshi, William Macaulay, Robert E. Booth, Lawrence S. Crossett, and Harry E. Rubash. Comparison of interface membranes obtained from failed cemented and cementless hip and knee prostheses. *Clinical Orthopaedics and Related Research*, 309:69–87, 1994.

[33] R. M. Pilliar, J. M. Lee, and C. Maniatopoulos. Observations on the effect of movement on bone ingrowth into porous-surfaced implants. *Clinical Orthopaedics and Related Research*, 208:108–113, 1986.

[34] Jan H. Kuiper and Rik Huiskes. Friction and stem stiffness affect dynamic interface motion in total hip replacement. *Journal of Orthopaedic Research*, 14(1):36–43, 1996.

[35] Jean-Pierre Kassi, Markus O. Heller, Ulrich Stoeckle, Carsten Perka, and Georg N. Duda. Stair climbing is more critical than walking in pre-clinical assessment of primary stability in cementless {THA} in vitro. *Journal of Biomechanics*, 38(5):1143 – 1154, 2005.

[36] T. A. Gruen. *Radiographic criteria for the clinical performance of uncemented total joint replacements.* In Lemons JE (ed): Quantitative characterization and performance of porous implants for hard tissue applications. ASTM STP 953. American Society for Testing Materials, Philadelphia, USA., 1999.

[37] Yongde Zhang, Aaron W. Putnam, Anneliese D. Heiner, John J. Callaghan, and Thomas D. Brown. Reliability of detecting prosthesis/cement interface radiolucencies in total hip arthroplasty. *Journal of Orthopaedic Research*, 20(4):683–687, 2002.

[38] Olivier P. P. Temmerman, Pieter G. H. M. Raijmakers, Johannes Berkhof, Erik F. L. David, Rik Pijpers, Marinus A. Molenaar, Otto S. Hoekstra, Gerrit J. J. Teule, and Ide C. Heyligers. Diagnostic accuracy and interobserver variability of plain radiography, subtraction arthrography, nuclear arthrography, and bone scintigraphy in the assessment of aseptic femoral component loosening. *Archives of Orthopaedic and Trauma Surgery*, 126(5):316–323, 2006.

[39] Henrik Malchau, Johan Kärrholm, Yu Xing Wang, and Peter Herberts. Accuracy of migration analysis in hip arthroplasty digitized and conventional radiography, compared to radiostereometry in 51 patients. *Acta Orthopaedica*, 66(5):418–424, 1995.

[40] A. Kobayashi, W. J. Donnelly, G. Scott, and M. A. R. Freeman. Early radiological observations may predict the long-term survival of femoral hip prostheses. *Journal of Bone and Joint Surgery, British Volume*, 79-B(4):583–589, 1997.

[41] Edward J. Vresilovic, William J. Hozack, and Richard H. Rothman. Radiographic assessment of cementless femoral components: Correlation with intraoperative mechanical stability. *The Journal of Arthroplasty*, 9(2):137 – 141, 1994.

[42] Cyna Khalily and Leo A. Whiteside. Predictive value of early radiographic findings in cementless total hip arthroplasty femoral components: An 8- to 12-year follow-up. *The Journal of Arthroplasty*, 13(7):768 – 773, 1998.

[43] Ilkka A. Lautiainen, Jaakko Joukainen, and E.Antero Mäkelä. Clinical and roentgenographic results of cementless total hip arthroplasty. *The Journal of Arthroplasty*, 9(6):653 – 660, 1994.

[44] Selvik G. Roentgen stereophotogrammetry: a method for the study of kinematics of the skeletal system. *Acta ortoapedica Scandinavica*, 60, 1989.

[45] E. R. Valstar, F.W. de Jong, H. A. Vrooman, P. M. Rozing, and J. H. C. Reiber. Model-based roentgen stereophotogrammetry of orthopaedic implants. *Journal of Biomechanics*, 34(6):715 – 722, 2001.

[46] Edward R. Valstar, Rob G. H. H. Nelissen, Johan H. C. Reiber, and Piet M. Rozing. The use of roentgen stereophotogrammetry to study micromotion of orthopaedic implants. {*ISPRS*} *Journal of Photogrammetry and Remote Sensing*, 56(5–6):376 – 389, 2002. Theme Issue: Medical Imaging and Photogrammetry.

[47] Wim J. G. Oyen, J. Albert M. Lemmens, Roland A. M. J. Claessens, James R. van Horn, Tom J. J. H. Slooff, and Frans H. M. Corstens. Nuclear arthrography: Combined scintigraphic and radiographic procedure for diagnosis of total hip prosthesis loosening. *Journal of Nuclear Medicine*, 37(1):62–70, 1996.

[48] Olivier P. P. Temmerman, Pieter G. H. M. Raijmakers, Johannes Berkhof, Erik F. L. David, Rik Pijpers, Marinus A. Molenaar, Otto S. Hoekstra, Gerrit J. J. Teule, and Ide C. Heyligers. Diagnostic accuracy and interobserver variability of plain radiography, subtraction arthrography, nuclear arthrography, and bone scintigraphy in the assessment of aseptic femoral component loosening. *Archives of Orthopaedic and Trauma Surgery*, 126(5):316–323, 2006.

[49] Jenny B. Kiratli, Mary M. Checovich, Andrew A. McBeath, Michael A. Wilson, and John P. Heiner. Measurement of bone mineral density by dual-energy x-ray absorptiometry in patients with the wisconsin hip, an uncemented femoral stem. *The Journal of Arthroplasty*, 11(2):184 – 193, 1996.

[50] S. W. Doebling, C. R. Farrar, M. B. Prime, and D. W. Shevitz. *Damage identification and health monitoring of structural and mechanical systems from changes in their vibration characteristics: A literature review.* May 1996.

[51] N. Meredith, D. Alleyne, and P. Cawley. Quantitative determination of the stability of the implant-tissue interface using resonance frequency analysis. *Clinical Oral Implants Research*, 7(3):261–267, 1996.

[52] N. Meredith, K. Books, B. Fribergs, T. Jemt, and L. Sennerby. Resonance frequency measurements of implant stability in viva. a cross-sectional and longitudinal study of resonance frequency measurements on implants in the edentulous and partially dentate maxilla. *Clinical Oral Implants Research*, 8(3):226–233, 1997.

[53] N. Meredith, F. Shagaldi, D. Alleyne, L. Sennerby, and P. Cawley. The application of resonance frequency measurements to study the stability of titanium implants during healing in the rabbit tibia. *Clinical Oral Implants Research*, 8(3):234–243, 1997.

[54] S. J. Heo, L. Sennerby, M. Odersjö, G. Granström, A. Tjellström, and N. Meredith. Stability measurements of craniofacial implants by means of resonance frequency analysis. a clinical pilot study. *The Journal of Laryngology and Otology*, 112:537–542, 6 1998.

[55] L. Rasmusson, M. Meredith, I. H. Cho, and L. Sennerby. The influence of simultaneous versus delayed placement on the stability of titanium implants in onlay bone grafts: A histologic and biomechanic study in the rabbit. *International Journal of Oral and Maxillofacial Surgery*, 28(3):224 – 231, 1999.

[56] L. Cristofolini, E. Varini, I. Pelgreffi, A. Cappello, and A. Toni. Device to measure intraoperatively the primary stability of cementless hip stems. *Medical Engineering and Physics*, 28(5):475 – 482, 2006.

[57] A. P. Georgiou and J. L Cunningham. Accurate diagnosis of hip prosthesis loosening using a vibrational technique. *Clinical Biomechanics*, 16(4):315 – 323, 2001.

[58] S. Jaecques, C. Pastrav, and G. Zahariuc, A. Van der Perre. Analysis of the fixation quality of cementless hip prostheses using a vibrational technique. *In: Sas, P. and De Munck, M. (Eds.), ISMA 2004, International Conference on Noise and vibration engineering. K.U.Leuven, Leuven, Belgium*, 2004.

[59] P. Lieberman, M. H. Huo, R. Schneider, E. A. Salvati, and S. Rodi. Evaluation of painful hip arthroplasties. are technetium bone scans necessary? *Journal of Bone and Joint Surgery, British Volume*, 75-B(3):475–478, 1993.

[60] G. Köster, D. L. Munz, and H. P. Köhler. Clinical value of combined contrast and radionuclide arthrography in suspected loosening of hip prostheses. *Archives of Orthopaedic and Trauma Surgery*, 112(5):247–254, 1993.

[61] Ole Ovesen, Per Riegels-Nielsen, Sten Lindequist, Ib Jensen, Troels Munkner, Trine Torfing, and Jens Marving. The diagnostic value of digital subtraction arthrography and radionuclide bone scan in revision hip arthroplasty. *The Journal of Arthroplasty*, 18(6):735 – 740, 2003.

[62] G. Bergmann, G. Deuretzbacher, M. Heller, F. Graichen, A. Rohlmann, J. Strauss, and G. N. Duda. Hip contact forces and gait patterns from routine activities. *Journal of Biomechanics*, 34(7):859 – 871, 2001.

[63] W. A. Hodge, R. S. Fijan, K. L. Carlson, R. G. Burgess, W. H. Harris, and R. W. Mann. Contact pressures in the human hip joint measured in vivo. *Proceedings of the National Academy of Sciences*, 83(9):2879–2883, 1986.

[64] D. P. Byrne, K.J. Mulhall, and J. F Baker. Anatomy and biomechanics of the hip. *The Open Sports Medicine Journal*, 10, 2010.

[65] M. P. T. Dutton. *Orthopaedic Examination, Evaluation, and Intervention. Second Endition.* The McGraw-Hill Companies, 2008.

[66] Leigh C. Anderson and Donna Jo Blake. The anatomy and biomechanics of the hip joint. *Journal of Back and Musculoskeletal Rehabilitation*, 4, 1994.

[67] M. Dalstra, R. Huiskes, and L. van Erning. Development and validation of a three-dimensional finite element model of the pelvic bone. *Journal of Biomechanical Engineering*, 117, 1995.

[68] M. F. Ericksen. Aging changes in thickness of the proximal femoral cortex. *American Journal of Physical Anthropology*, 59(2):121–130, 1982.

[69] D. E. T. Shepherd and B. B. Seedhom. Thickness of human articular cartilage in joints of the lower limb. *Annals of the rheumatic diseases*, 58(1):27–34, 1999.

[70] Henry Gray. *Anatomy of the human body.* Lea & Febiger, 1918.

[71] Mohammed Rafiq Abdul Kadir. *Computational Biomechanics of the Hip Joint.* Springer, 2013.

[72] E. L. Radin, D. B. Burr, B. Caterson, D. Fyhrie, T. D. Brown, and R. D. Boyd. Mechanical determinants of osteoarthrosis. In *Seminars in arthritis and rheumatism*, volume 21, pages 12–21. Elsevier, 1991.

[73] M. Nevitt. Risk factors for knee, hip and hand osteoarthritis. *Osteoarthritis Handbook*, page 23, 2005.

[74] Nancy E. Lane. Osteoarthritis of the hip. *New England Journal of Medicine*, 357(14):1413–1421, 2007.

[75] Daniel A. Michaeli, Stephen B. Murphy, and John A. Hipp. Comparison of predicted and measured contact pressures in normal and dysplastic hips. *Medical engineering & physics*, 19(2):180–186, 1997.

[76] Masahiko Nozawa, Katsuo Shitoto, Kejii Matsuda, Katuhiko Maezawa, and Hisashi Kurosawa. Rotational acetabular osteotomy for acetabular dysplasia a follow-up for more than ten years. *Journal of Bone & Joint Surgery, British Volume*, 84(1):59–65, 2002.

[77] Michael L. Parks and William Macaulay. Operative approaches for total hip replacement. *Operative Techniques in Orthopaedics*, 10(2):106–114, 2000.

[78] Uwe Holzwarth and Giulio Cotogno. *Total Hip Arthroplasty: State of the Art, Challenges and Prospects*. Publications Office, 2012.

[79] J. Dennis Bobyn, Michael Tanzer, Jan J. Krygier, Ariel R. Dujovne, and C. Emerson Brooks. Concerns with modularity in total hip arthroplasty. *Clinical orthopaedics and related research*, 298:27–36, 1994.

[80] Hugh U. Cameron. Orthopaedic crossfire®—stem modularity is unnecessary in revision total hip arthroplasty: In opposition. *The Journal of arthroplasty*, 18(3):101–103, 2003.

[81] Philip C. Noble, Emir Kamaric, Nobuhiko Sugano, Masaaki Matsubara, Yoshitada Harada, Kenji Ohzono, and Vibor Paravic. Otto aufranc award: Three-dimensional shape of the dysplastic femur: Implications for thr. *Clinical orthopaedics and related research*, 417:27–40, 2003.

[82] Robert E. Kennon, John M. Keggi, Robert S. Wetmore, Laurine E. Zatorski, Michael H. Huo, and Kristaps J. Keggi. Total hip arthroplasty through a minimally invasive anterior surgical approach. *The Journal of Bone & Joint Surgery*, 85(suppl_4):39–48, 2003.

[83] John Charnley. Fracture of femoral prostheses in total hip replacement: a clinical study. *Clinical orthopaedics and related research*, 111:105–120, 1975.

[84] Richard A. Brand, John J. Callaghan, and Richard C. Johnston. Total hip reconstruction. *Iowa Orthop J.*, 11:19–42, 1991.

[85] S. Terry Canale and James H. Beaty. *Campbell's Operative Orthopaedics, 11th Edition*. Mosby, An Imprint of Elsevier, 2008.

[86] Matthew J. Kraay, James S. Rowbottom, and Matthew G. Razek. The acetabular component in primary total hip arthroplasty. In *Seminars in Arthroplasty*, volume 23, pages 163–166. Elsevier, 2012.

[87] Kristoff Corten, Richard W. McCalden, Yeesze Teo, Kory D. Charron, Steven J. MacDonald, and Robert B. Bourne. Midterm results of 506 solid trispiked reflection cementless acetabular components for primary total hip arthroplasty. *The Journal of arthroplasty*, 26(8):1350–1356, 2011.

[88] Charles A. Engh, Robert H. Hopper Jr., and C. Anderson Engh Jr. Long-term porous-coated cup survivorship using spikes, screws, and press-fitting for initial fixation. *The Journal of arthroplasty*, 19(7):54–60, 2004.

[89] David A. Fisher. 5-year review of second-generation acetabular cup with dome screws. *The Journal of arthroplasty*, 14(8):925–929, 1999.

[90] Richard Iorio, Richard Puskas, William L. Healy, John F. Tilzey, Lawrence M. Specht, and Michael S. Thompson. Cementless acetabular fixation with and without screws: Analysis of stability and migration. *The Journal of Arthroplasty*, 25(2):309 – 313, 2010.

[91] Dean Pakvis, Joan Luites, Gijs van Hellemondt, and Maarten Spruit. A cementless, elastic press-fit socket with and without screws: A 2-year randomized controlled radiostereometric analysis of 37 hips. *Acta orthopaedica*, 83(5):481–487, 2012.

[92] Erwin W. Morscher. Current status of acetabular fixation in primary total hip arthroplasty. *Clinical orthopaedics and related research*, 274:172–193, 1992.

[93] Thomas P. Schmalzried, Sara Jane Wessinger, Gordon E. Hill, and William H. Harris. The harris-galante porous acetabular component press-fit without screw fixation: five-year radiographic analysis of primary cases. *The Journal of arthroplasty*, 9(3):235–242, 1994.

[94] Matthew Squire, William L. Griffin, J. Bohannon Mason, Richard D. Peindl, and Susan Odum. Acetabular component deformation with press-fit fixation. *The Journal of arthroplasty*, 21(6):72–77, 2006.

[95] David Emery, Annie Britton, Hugh Clarke, and Martin Grover. The stanmore total hip arthroplasty: a 15-to 20-year follow-up study. *The Journal of arthroplasty*, 12(7):728–735, 1997.

[96] A. O. El-Warrak, M. L. Olmstead, B. Von Rechenberg, and J. A. Auer. A review of aseptic loosening in total hip arthroplasty. *Veterinary and Comparative Orthopaedics and Traumatology*, 14(3):115–124, 2001.

[97] Lawrence D. Dorr, Zhinian Wan, and Thomas Gruen. Functional results in total hip replacement in patients 65 years and older. *Clinical orthopaedics and related research*, 336:143–151, 1997.

[98] Dan Haber and Stuart B. Goodman. Total hip arthroplasty in juvenile chronic arthritis: a consecutive series. *The Journal of arthroplasty*, 13(3):259–265, 1998.

[99] Young-Hoo Kim, S. H. Oh, and J. S Kim. Primary total hip arthroplasty with a second-generation cementless total hip prosthesis in patients younger than fifty years of age. *The Journal of Bone & Joint Surgery*, 85(1):109–114, 2003.

[100] R. B. Bourne and C. H. Rorabeck. A critical look at cementless stems: taper designs and when to use alternatives. *Clinical orthopaedics and related research*, 355:212–223, 1998.

[101] John C. Clohisy and William H. Harris. The harris-galante porous-coated acetabular component with screw fixation. an average ten-year follow-up study*. *The Journal of Bone & Joint Surgery*, 81(1):66–73, 1999.

[102] Craig J. Della Valle, Nathan W. Mesko, Laura Quigley, Aaron G. Rosenberg, Joshua J. Jacobs, and Jorge O. Galante. Primary total hip arthroplasty with a porous-coated acetabular componenta concise follow-up, at a minimum of twenty years, of previous reports*. *The Journal of Bone & Joint Surgery*, 91(5):1130–1135, 2009.

[103] Daniel Berry and Jay Lieberman. *Surgery of the Hip*. Elsevier, 2011.

[104] M. Ihle, S. Mai, D. Pfluger, and W. Siebert. The results of the titanium-coated rm acetabular component at 20 years a long-term follow-up of an uncemented primary total hip replacement. *Journal of Bone & Joint Surgery, British Volume*, 90(10):1284–1290, 2008.

[105] J. A. Bojescul, J. S. Xenos, John J. Callaghan, and C. G. Savory. Results of porous-coated anatomic total hip arthroplasty without cement at fifteen years a concise follow-up of a previous report*. *The Journal of Bone & Joint Surgery*, 85(6):1079–1083, 2003.

[106] David E. Hastings, Helen Tobin, and Marilyn Sellenkowitsch. Review of 10-year results of pca hip arthroplasty. *Canadian journal of surgery*, 41(1):48–51, 1998.

[107] William .L Healy, David J. Casey, Richard Iorio, and David Appleby. Evaluation of the porous-coated anatomic hip at 12 years. *The Journal of arthroplasty*, 17(7):856–863, 2002.

[108] Haruo Kawamura, Michael J. Dunbar, Paraic Murray, Robert B. Bourne, and Cecil H. Rorabeck. The porous coated anatomic total hip replacement a ten to fourteen-year follow-up study of a cementless total hip arthroplasty. *The Journal of Bone & Joint Surgery*, 83(9):1333–1338, 2001.

[109] Young-Hoo Kim, Jun-Shik Kim, and Soon-Ho Cho. Primary total hip arthroplasty with the aml total hip prosthesis. *Clinical orthopaedics and related research*, 360:147–158, 1999.

[110] Pacharapol Udomkiat, Lawrence D. Dorr, and Zhinian Wan. Cementless hemispheric porous-coated sockets implanted with press-fit technique without screws: average ten-year follow-up. *The Journal of Bone & Joint Surgery*, 84(7):1195–1200, 2002.

[111] Louis Matthew Kwong, Daniel O. O'Connor, Ronald C. Sedlacek, Robert J. Krushell, William J. Maloney, and William H. Harris. A quantitative¡ i¿ in vitro¡/i¿ assessment of fit and screw fixation on the stability of a cementless hemispherical acetabular component. *The Journal of arthroplasty*, 9(2):163–170, 1994.

[112] Peter F. Sharkey, William J. Hozack, John J. Callaghan, Yong Sik Kim, Daniel J. Berry, Arlen D. Hanssen, and David G. LeWallen. Acetabular fracture associated with cementless acetabular component insertion: a report of 13 cases. *The Journal of arthroplasty*, 14(4):426–431, 1999.

[113] S. A. Yerby, J. K. Taylor, and W. Murzic. Acetabular component interface: press-fit fixation. *Trans Orthop Res Soc*, 17:384, 1992.

[114] M. J. Curtis, R. H. Jinnah, V. D. Wilson, and D. S. Hungerford. The initial stability of uncemented acetabular components. *Journal of Bone & Joint Surgery, British Volume*, 74(3):372–376, 1992.

[115] Chiara Maria Bellini, Fabio Galbusera, Roberto Giacometti Ceroni, and Manuela Teresa Raimondi. Loss in mechanical contact of cementless acetabular prostheses due to post-operative weight bearing: a biomechanical model. *Medical engineering & physics*, 29(2):175–181, 2007.

[116] C. Hearn Won, T. C. Hearn, and M. Tile. Micromotion of cementless hemispherical acetabular components. does press-fit need adjunctive screw fixation? *Journal of Bone & Joint Surgery, British Volume*, 77(3):484–489, 1995.

[117] Paul G. Perona, Jeffrey Lawrence, Wayne G. Paprosky, Avinash G. Patwardhan, and Mark Sartori. Acetabular micromotion as a measure of initial implant stability in primary hip arthroplasty: An in vitro comparison of different methods of intial acetabular component fixation. *The Journal of arthroplasty*, 7(4):537–547, 1992.

[118] Bruno Olory, Eric Havet, Antoine Gabrion, Joël Vernois, and Patrice Mertl. Comparative in vitro assessment of the primary stability of cementless press-fit acetabular cups. *Acta orthopaedica belgica*, 70(1):31–37, 2004.

[119] A. Roth, T. Winzer, K. Sander, J. O. Anders, and R. A. Venbrocks. Press fit fixation of cementless cups: how much stability do we need indeed? *Archives of orthopaedic and trauma surgery*, 126(2):77–81, 2006.

[120] Jan Herman Kuiper and Rik Huiskes. Friction and stem stiffness affect dynamic interface motion in total hip replacement. *Journal of Orthopaedic Research*, 14(1):36–43, 1996.

[121] Daniel Kluess, Robert Souffrant, Wolfram Mittelmeier, Andreas Wree, Klaus-Peter Schmitz, and Rainer Bader. A convenient approach for finite-element-analyses of orthopaedic implants in bone contact: modeling and experimental validation. *Computer methods and programs in biomedicine*, 95(1):23–30, 2009.

[122] Iain R. Spears, Martin Pfleiderer, Erich Schneider, Ekkehard Hille, Georg Bergmann, and Michael M. Morlock. Interfacial conditions between a press-fit acetabular cup and bone during daily activities: implications for achieving bone in-growth. *Journal of biomechanics*, 33(11):1471–1477, 2000.

[123] Jui-Ting Hsu, Kuo-An Lai, Qingshan Chen, Mark E. Zobitz, Heng-Li Huang, Kai-Nan An, and Chih-Han Chang. The relation between micromotion and screw fixation in acetabular cup. *Computer methods and programs in biomedicine*, 84(1):34–41, 2006.

[124] I. Zivkovic, M. Gonzalez, and F. Amirouche. The effect of under-reaming on the cup/bone interface of a press fit hip replacement. *Journal of biomechanical engineering*, 132(4):041008, 2010.

[125] S. G. Clarke, A. T. M. Phillips, and A. M. J. Bull. Validation of fe micromotions and strains around a press-fit cup: introducing a new micromotion measuring technique. *Annals of biomedical engineering*, 40(7):1586–1596, 2012.

[126] S. Szmukler-Moncler, H. Salama, Y. Reingewirtz, and J. H. Dubruille. Timing of loading and effect of micromotion on bone-dental implant interface: review of experimental literature. *Journal of biomedical materials research*, 43(2):192–203, 1998.

[127] William J. Maloney, Murali Jasty, Dennis W. Burke, Daniel O. O'connor, Edward B. Zalenski, Charles Bragdon, and William H. Harris. Biomechanical and histologic investigation of cemented total hip arthroplasties: a study of autopsy-retrieved femurs after in vivo cycling. *Clinical orthopaedics and related research*, 249:129–140, 1989.

[128] Charles A. Engh, Daniel O'Connor, Murali Jasty, Thomas F. McGovern, J. Dennis Bobyn, and William H. Harris. Quantification of implant micromotion, strain shielding, and bone resorption with porous-coated anatomic medullary locking femoral prostheses. *Clinical orthopaedics and related research*, 285:13–29, 1992.

[129] Leo A. Whiteside, Stephen E. White, Charles A. Engh, and William Head. Mechanical evaluation of cadaver retrieval specimens of cementless bone-ingrown total hip arthroplasty femoral components. *The Journal of arthroplasty*, 8(2):147–155, 1993.

[130] M. Bernakiewicz, M. Viceconti, and A. Toni. Investigation of the influence of periprosthetic fibrous tissue on the primary stability of uncemented hip prostheses. *Computer methods in biomechanics & biomedical engineering—3. Gordon and Breach, NY, USA*, pages 21–26, 1999.

[131] Marco Viceconti, Luisa Monti, Roberto Muccini, Marek Bernakiewicz, and Aldo Toni. Even a thin layer of soft tissue may compromise the primary stability of cementless hip stems. *Clinical Biomechanics*, 16(9):765–775, 2001.

[132] Åke S Carlsson and Carl-Fredrik Gentz. Radiographic versus clinical loosening of the acetabular component in noninfected total hip arthroplasty. *Clinical orthopaedics and related research*, 185:145–150, 1984.

[133] Theodore T. Miller. Imaging of hip arthroplasty. *European journal of radiology*, 81(12):3802–3812, 2012.

[134] John M. Martell, R. H. D. Pierson, J. J. Jacobs, A. G. Rosenberg, M. Maley, and J. O. Galante. Primary total hip reconstruction with a titanium fiber-coated prosthesis inserted without cement. *JOURNAL OF BONE AND JOINT SURGERY-AMERICAN VOLUME-*, 75:554–554, 1993.

[135] Keith A. Fehring, John R. Owen, Anton A. Kurdin, Jennifer S. Wayne, and William A. Jiranek. Initial stability of press-fit acetabular components under rotational forces. *The Journal of arthroplasty*, 29(5):1038–1042, 2014.

[136] Iain R. Spears, Michael M. Morlock, Martin Pfleiderer, Erich Schneider, and Ekkehard Hille. The influence of friction and interference on the seating of a hemispherical press-fit cup: a finite element investigation. *Journal of biomechanics*, 32(11):1183–1189, 1999.

[137] Jui-Ting Hsu, Chih-Han Chang, Heng-Li Huang, Mark E. Zobitz, Weng-Pin Chen, Kuo-An Lai, and Kai-Nan An. The number of screws, bone quality, and friction coefficient affect acetabular cup stability. *Medical engineering & physics*, 29(10):1089–1095, 2007.

[138] Iain R. Spears, Martin Pfleiderer, Erich Schneider, Ekkehard Hille, and Michael M. Morlock. The effect of interfacial parameters on cup–bone relative micromotions: A finite element investigation. *Journal of Biomechanics*, 34(1):113–120, 2001.

[139] Francisco Romero, Farid Amirouche, Luke Aram, and Mark Gonzalez. Experimental and analytical validation of a modular acetabular prosthesis in total hip arthroplasty. *Journal of Orthopaedic Surgery and Research*, 2(1):7, 2007.

[140] Arne Hothan, Gerd Huber, Cornelius Weiss, Norbert Hoffmann, and Michael Morlock. Deformation characteristics and eigenfrequencies of press-fit acetabular cups. *Clinical Biomechanics*, 26(1):46–51, 2011.

[141] Michael D. Ries, Mark Harbaugh, Jeff Shea, and Richard Lambert. Effect of cementless acetabular cup geometry on strain distribution and press-fit stability. *The Journal of arthroplasty*, 12(2):207–212, 1997.

[142] G. Lowet and Georges Van der Perre. Ultrasound velocity measurement in long bones: measurement method and simulation of ultrasound wave propagation. *Journal of biomechanics*, 29(10):1255–1262, 1996.

[143] G. Lowet, Remy Van Audekercke, Georges Van der Perre, P. Geusens, Jan Dequeker, and Johan Lammens. The relation between resonant frequencies and torsional stiffness of long bones¡ i¿ in vitro¡/i¿. validation of a simple beam model. *Journal of biomechanics*, 26(6):689–696, 1993.

[144] S. G. Roberts, T. M. Hutchinson, S. B. Arnaud, B. J. Kiratli, R. B. Martin, and Charles R. Steele. Noninvasive determination of bone mechanical properties using vibration response: A refined model and validation¡ i¿ in vivo¡/i¿. *Journal of biomechanics*, 29(1):91–98, 1996.

[145] Georges Van der Perre and G. Lowet. In vivo assessment of bone mechanical properties by vibration and ultrasonic wave propagation analysis. *Bone*, 18(1):S29–S35, 1996.

[146] G. Nikiforidis, A. Bezerianos, A. Dimarogonas, and C. Sutherland. Monitoring of fracture healing by lateral and axial vibration analysis. *Journal of biomechanics*, 23(4):323–330, 1990.

[147] Yukio Nakatsuchi, Akira Tsuchikane, and Akio Nomura. Assessment of fracture healing in the tibia using the impulse response method. *Journal of orthopaedic trauma*, 10(1):50–62, 1996.

[148] N. Meredith, F. Shagaldi, D. Alleyne, L. Sennerby, and P. Cawley. The application of resonance frequency measurements to study the stability of titanium implants during healing in the rabbit tibia. *Clinical Oral Implants Research*, 8(3):234–243, 1997.

[149] S. J. Heo, L. Sennerby, M. Odersjö, G. Granström, A. Tjellström, and N. Meredith. Stability measurements of craniofacial implants by means of resonance frequency analysis. a clinical pilot study. *The Journal of Laryngology & Otology*, 112(06):537–542, 1998.

[150] Lukas Capek, Antonin Simunek, Radovan Slezak, and Ladislav Dzan. Influence of the orientation of the osstell¡ sup¿®¡/sup¿ transducer during measurement of dental implant stability using resonance frequency analysis: A numerical approach. *Medical engineering & physics*, 31(7):764–769, 2009.

[151] Haw-Ming Huang, Ching-Lai Chiu, Ching-Ying Yeh, and Sheng-Yang Lee. Factors influencing the resonance frequency of dental implants. *Journal of oral and maxillofacial surgery*, 61(10):1184–1188, 2003.

[152] Sheldon Winkler, Harold F. Morris, and J. Robert Spray. Stability of implants and natural teeth as determined by the periotest over 60 months of function. *Journal of Oral Implantology*, 27(4):198–203, 2001.

[153] Jurgen Zix, Stefan Hug, Gerda Kessler-Liechti, and Regina Mericske-Stern. Measurement of dental implant stability by resonance frequency analysis and damping capacity assessment: comparison of both techniques in a clinical trial. *The International journal of oral & maxillofacial implants*, 23(3):525–530, 2007.

[154] Sastra Kusuma Wijaya, Hisao Oka, Keiji Saratani, Takuya Sumikawa, and Takayoshi Kawazoe. Development of implant movement checker for determining dental implant stability. *Medical engineering & physics*, 26(6):513–522, 2004.

[155] John J. Elias, John B. Brunski, and Henry A. Scarton. A dynamic modal testing technique for noninvasive assessment of bone-dental implant interfaces. *The International journal of oral & maxillofacial implants*, 11(6):728–734, 1995.

[156] Lance C. Ramp, Michael S. Reddy, and Robert L. Jeffcoat. Assessment of osseointegration by nonlinear dynamic response. *The International journal of oral & maxillofacial implants*, 15(2):197–208, 1999.

[157] Fei Shao, W. Xu, A. Crocombe, and D. Ewins. Natural frequency analysis of osseointegration for trans-femoral implant. *Annals of biomedical engineering*, 35(5):817–824, 2007.

[158] Nicola J. Cairns, Mark J. Pearcy, James Smeathers, and Clayton J. Adam. Ability of modal analysis to detect osseointegration of implants in transfemoral amputees: a physical model study. *Medical & biological engineering & computing*, 51(1-2):39–47, 2013.

[159] A. P. Georgiou and J. L. Cunningham. Accurate diagnosis of hip prosthesis loosening using a vibrational technique. *Clinical Biomechanics*, 16(4):315–323, 2001.

[160] P. L. S. Li, N. B. Jones, and P. J. Gregg. Vibration analysis in the detection of total hip prosthetic loosening. *Medical engineering & physics*, 18(7):596–600, 1996.

[161] P. L. Li, N. B. Jones, and P. J. Gregg. Loosening of total hip arthroplasty. diagnosis by vibration analysis. *Journal of Bone & Joint Surgery, British Volume*, 77(4):640–644, 1995.

[162] I. Denayer and Georges Van der Perre. Detection of hip stem loosening using vibration analysis. *Journal of Biomechanics*, 31:165, 1998.

[163] S. V. N. Jaecques, C. Pastrav, A. Zahariuc, and Georges Van der Perre. Analysis of the fixation quality of cementless hip prostheses using a vibrational technique. In *Proceedings of ISMA 2004 International Conference on Noise and vibration engineering: 20–22 September 2004; Leuven*, pages 443–456, 2004.

[164] Michiel Mulier, Cesar Pastrav, and Georges Van der Perre. Per-operative vibration analysis: a valuable tool for defining correct stem insertion: preliminary report. *Ortopedia, traumatologia, rehabilitacja*, 10(6):576–582, 2007.

[165] Gang Qi, W. Paul Mouchon, and Teong E. Tan. How much can a vibrational diagnostic tool reveal in total hip arthroplasty loosening? *Clinical Biomechanics*, 18(5):444–458, 2003.

[166] Leonard C. Pastrav, Siegfried V. N. Jaecques, Ilse Jonkers, and Georges Van. Journal of orthopaedic surgery and research. *Journal of orthopaedic surgery and research*, 4:10, 2009.

[167] E. Varini, E. Bialoblocka-Juszczyk, M. Lannocca, A. Cappello, and Cristofolini. L. Assessment of implant stability of cementless hip prostheses through the frequency response function of the stem–bone system. *Sensors and Actuators A: Physical*, 163(2):526 – 532, 2010.

[168] Maurizio Lannocca, Elena Varini, Angelo Cappello, Luca Cristofolini, and Ewa Bialoblocka. Intra-operative evaluation of cementless hip implant stability: A prototype device based on vibration analysis. *Medical engineering & physics*, 29(8):886–894, 2007.

[169] Johannes Sebastian Rieger, Sebastian Jaeger, Christian Schuld, Jan Philippe Kretzer, and Rudi Georg Bitsch. A vibrational technique for diagnosing loosened total hip endoprostheses: an experimental sawbone study. *Medical engineering & physics*, 35(3):329–337, 2013.

[170] Petr Henys, Lukas Capek, Jaroslav Fencl, and Egon Prochazka. Evaluation of acetabular cup initial fixation by using resonance frequency principle. *Proceedings of the Institution of Mechanical Engineers, Part H: Journal of Engineering in Medicine*, 229(1):3–8, 2015.

[171] Petr Henyš and Lukáš Čpek. Numerical and experimental results from measuring spinal implant stability. *Journal of Vibroengineering*, 15(2), 2013.

[172] P. Henyš and L. Čapek. Measuring primary stability of cervical implant. *Computer methods in biomechanics and biomedical engineering*, 15(sup1):340–342, 2012.

[173] Leonard Pastrav. Monitoring of the fixation of orthopaedic implants by vibration analysis (monitoring van de fixatie van orthopedische implantaten aan de hand van trillingsanalyse). 2010.

[174] Robert Puers, Michael Catrysse, Glenn Vandevoorde, R. J. Collier, Emil Louridas, Franz Burny, M. Donkerwolcke, and Francoise Moulart. A telemetry system for the detection of hip prosthesis loosening by vibration analysis. *Sensors and Actuators A: Physical*, 85(1):42–47, 2000.

[175] U. Marschner, H. Grätz, B. Jettkant, D. Ruwisch, G. Woldt, W. J. Fischer, and B. Clasbrummel. Integration of a wireless lock-in measurement of hip prosthesis vibrations for loosening detection. *Sensors and Actuators A: Physical*, 156(1):145–154, 2009.

[176] Cathérine Ruther, U. Timm, H. Ewald, W. Mittelmeier, R. Bader, R. Schmelter, A. Lohrengel, D. Kluess, and S. K. Fokter. Current possibilities for detection of loosening of total hip replacements and how intelligent implants could improve diagnostic accuracy. *Recent Advances in Arthroplasty*, pages 363–386, 2012.

[177] Cathérine Ruther, Hannes Nierath, Hartmut Ewald, James L. Cunningham, Wolfram Mittelmeier, Rainer Bader, and Daniel Kluess. Investigation of an acoustic-mechanical method to detect implant loosening. *Medical engineering & physics*, 35(11):1669–1675, 2013.

[178] A. Rowlands, F. A. Duck, and J. L. Cunningham. Bone vibration measurement using ultrasound: Application to detection of hip prosthesis loosening. *Medical engineering & physics*, 30(3):278–284, 2008.

[179] Pascal Swider, Gaëtan Guérin, Joergen Baas, Kjeld Søballe, and Joan E. Bechtold. Characterization of bone-implant fixation using modal analysis: Application to a press-fit implant model. *Journal of biomechanics*, 42(11):1643–1649, 2009.

[180] A. C. Unger, H. Cabrera-Palacios, A. P. Schulz, C. H. Jürgens, and A. Paech. Acoustic monitoring (rfm) of total hip arthroplasty results of a cadaver study. *European journal of medical research*, 14(6):264, 2009.

[181] Michael C. Dahl, Patricia A. Kramer, Per G. Reinhall, Stephen K. Benirschke, Sigvard T. Hansen, and Randal P. Ching. The efficacy of using vibrometry to detect osteointegration of the agility total ankle. *Journal of Biomechanics*, 43(9):1840 – 1843, 2010.

[182] Jacques Riviere, Sylvain Haupert, Pascal Laugier, and Paul A. Johnson. Nonlinear ultrasound: Potential of the cross-correlation method for osseointegration monitoring. *The Journal of the Acoustical Society of America*, 132(3):EL202–EL207, 2012.

[183] Zannar Ossi, Wael Abdou, Robert L. Reuben, and Richard J. Ibbetson. Transmission of acoustic emission in bones, implants and dental materials. *Proceedings of the Institution of Mechanical Engineers, Part H: Journal of Engineering in Medicine*, 227(11):1237–1245, 2013.

[184] Andrew Top, Ghassan Hamarneh, and Rafeef Abugharbieh. Active learning for interactive 3d image segmentation. In *Medical Image Computing and Computer-Assisted Intervention–MICCAI 2011*, pages 603–610. Springer, 2011.

[185] Paul A. Yushkevich, Joseph Piven, Heather Cody Hazlett, Rachel Gimpel Smith, Sean Ho, James C. Gee, and Guido Gerig. User-guided 3d active contour segmentation of anatomical structures: significantly improved efficiency and reliability. *Neuroimage*, 31(3):1116–1128, 2006.

[186] Vicent Caselles, Francine Catté, Tomeu Coll, and Françoise Dibos. A geometric model for active contours in image processing. *Numerische mathematik*, 66(1):1–31, 1993.

[187] Andrew Top, Ghassan Hamarneh, and Rafeef Abugharbieh. Spotlight: Automated confidence-based user guidance for increasing efficiency in interactive 3d image segmentation. In *Medical Computer Vision. Recognition Techniques and Applications in Medical Imaging*, pages 204–213. Springer, 2011.

[188] The CGAL Project. *CGAL User and Reference Manual*. CGAL Editorial Board, 4.6 edition, 2015.

[189] Sung Joon Ahn, Wolfgang Rauh, and Hans-Jürgen Warnecke. Least-squares orthogonal distances fitting of circle, sphere, ellipse, hyperbola, and parabola. *Pattern Recognition*, 34(12):2283–2303, 2001.

[190] Andrew E. Long and Clifford A. Long. Surface approximation and interpolation via matrix svd. *College Mathematics Journal*, 32(1):20–25, 2001.

[191] William H. Press, Saul A. Teukolsky, William T. Vetterling, and Brian P. Flannery. Numerical recipes in c: the art of scientific computing, 1992. *Cité en*, page 92, 1992.

[192] William Schroeder, K. Martin, Lisa S. Avila, and C. Charles Law. The visualization toolkit user's guide, version 4.0. *Kitware, version*, 4, 2001.

[193] B. Helgason, F. Taddei, H. Pálsson, E. Schileo, L. Cristofolini, M. Viceconti, and S. Brynjólfsson. A modified method for assigning material properties to {FE} models of bones. *Medical Engineering & Physics*, 30(4):444 – 453, 2008.

[194] G. Chen, B. Schmutz, D. Epari, K. Rathnayaka, S. Ibrahim, M. A. Schuetz, and M. J. Pearcy. A new approach for assigning bone material properties from {CT} images into finite element models. *Journal of Biomechanics*, 43(5):1011 – 1015, 2010.

[195] F. Taddei, A. Pancanti, and M. Viceconti. An improved method for the automatic mapping of computed tomography numbers onto finite element models. *Medical Engineering & Physics*, 26(1):61 – 69, 2004.

[196] Haisheng Yang, Xin Ma, and Tongtong Guo. Some factors that affect the comparison between isotropic and orthotropic inhomogeneous finite element material models of femur. *Medical Engineering & Physics*, 32(6):553 – 560, 2010.

[197] T. San Antonio, M. Ciaccia, C. Müller-Karger, and E. Casanova. Orientation of orthotropic material properties in a femur {FE} model: A method based on the principal stresses directions. *Medical Engineering & Physics*, 34(7):914 – 919, 2012.

[198] Ralf Schneider, Gunter Faust, Urlich Hindenlang, and Peter Helwig. Inhomogeneous, orthotropic material model for the cortical structure of long bones modelled on the basis of clinical {CT} or density data. *Computer Methods in Applied Mechanics and Engineering*, 198(27–29):2167 – 2174, 2009.

[199] Dieter H. Pahr and Philippe K. Zysset. A comparison of enhanced continuum {FE} with micro {FE} models of human vertebral bodies. *Journal of Biomechanics*, 42(4):455 – 462, 2009.

[200] X. Neil Dong and X. Edward Guo. The dependence of transversely isotropic elasticity of human femoral cortical bone on porosity. *Journal of biomechanics*, 37(8):1281–1287, 2004.

[201] E. Dall'Ara, C. Karl, G. Mazza, G. Franzoso, P. Vena, M. Pretterklieber, D. Pahr, and P. Zysset. Tissue properties of the human vertebral body sub-structures evaluated by means of microindentation. *Journal of the Mechanical Behavior of Biomedical Materials*, 25(0):23 – 32, 2013.

[202] N. K. Sharma, D. K. Sehgal, R. K. Pandey, and Ruchita Pal. Finite element simulation of cortical bone under different loading and anisotropic yielding situations. In *Proceedings of the World Congress on Engineering and Computer Science 2012*, volume 2. WCECS, 2012.

[203] N.K. Sharma, D.K. Sehgal, and R.K. Pandey. Comparative study of locational variation in shear and transverse elastic modulus of buffalo cortical bone. {*IERI*} *Procedia*, 1(0):205 – 210, 2012. 2012 International Conference on Mechanical, Industrial, and Manufacturing Engineering, Singapore, June 27-28, 2012.

[204] Y. J. Yoon, G. Yang, and S. C. Cowin. Estimation of the effective transversely isotropic elastic constants of a material from known values of the material's orthotropic elastic constants. *Biomechanics and modeling in mechanobiology*, 1(1):83–93, 2002.

[205] Patrick Guillaume, Peter Verboven, Steve Vanlanduit, Herman Van Der Auweraer, and Bart Peeters. A poly-reference implementation of the least-squares complex frequency-domain estimator. In *Proceedings of IMAC*, volume 21, pages 183–192, 2003.

[206] Herman Van Der Auweraer, P. Guillaume, Peter Verboven, and S. Vanlanduit. Application of a fast-stabilizing frequency domain parameter estimation method. *Journal of dynamic systems, measurement, and control*, 123(4):651–658, 2001.

[207] Peter Verboven, Eli Parloo, Patrick Guillaume, and Marc Van Overmeire. Autonomous modal parameter estimation based on a statistical frequency domain maximum likelihood approach. In *Proceedings, International Modal Analysis Conference (IMAC)*, page 15111517, 2001.

[208] Bart Cauberghe, Patrick Guillaume, Peter Verboven, Eli Parloo, and Steve Vanlanduit. A poly-reference implementation of the maximum likelihood complex frequency-domain estimator and some industrial applications. In *Proceedings of the 22nd International Modal Analysis Conference*, 2004.

[209] Peter Verboven, Patrick Guillaume, Bart Cauberghe, Eli Parloo, and Steve Vanlanduit. Stabilization charts and uncertainty bounds for frequency-domain linear least squares estimators. *Proceedings of the 21st IMAC, Kissimmee, FL*, 2003.

[210] P. Vacher, B. Jacquier, and A. Bucharles. Extensions of the mac criterion to complex modes. In *Proceedings of the International Conference on Noise and Vibration Engineering*, 2010.

[211] Randall J Allemang. The modal assurance criterion–twenty years of use and abuse. *Sound and vibration*, 37(8):14–23, 2003.

[212] L. D. Mitchell. Increasing the sensitivity of the modal assurance criteria (mac) to small mode shape changes: The imac. In *PROCEEDINGS-SPIE THE INTERNATIONAL SOCIETY FOR OPTICAL ENGINEERING*, volume 1, pages 64–69. SPIE INTERNATIONAL SOCIETY FOR OPTICAL, 1998.

[213] D. Christian Wirtz, T. Pandorf, F. Portheine, K. Radermacher, N. Schiffers, P. Prescher, D. Weichert, and F. Uwe Niethard. Concept and development of an orthotropic {FE} model of the proximal femur. *Journal of Biomechanics*, 36(2):289 – 293, 2003.

[214] Béatrice Couteau, Marie-Christine Hobatho, Robert Darmana, Jean-Claude Brignola, and Jean-Yves Arlaud. Finite element modelling of the vibrational behaviour of the human femur using ct-based individualized geometrical and material properties. *Journal of biomechanics*, 31(4):383–386, 1998.

[215] Roger Scholz, Falk Hoffmann, Sandra von Sachsen, Welf-Guntram Drossel, Carsten Klöhn, and Christian Voigt. Validation of density–elasticity relationships for finite element modeling of human pelvic bone by modal analysis. *Journal of biomechanics*, 46(15):2667–2673, 2013.

[216] Reimund Neugebauer, M. Werner, C. Voigt, H. Steinke, R. Scholz, S. Scherer, and M. Quickert. Experimental modal analysis on fresh-frozen human hemipelvic bones employing a 3d laser vibrometer for the purpose of modal parameter identification. *Journal of biomechanics*, 44(8):1610–1613, 2011.

[217] Thomas Kailath. *Linear systems*, volume 1. Prentice-Hall Englewood Cliffs, NJ, 1980.

[218] Patrick Guillaume, Rick Pintelon, and Johan Schoukens. Parametric identification of multivariable systems in the frequency domain- a survey. *ISMA 21*, pages 1069–1082, 1996.

[219] Ward Heylen and Paul Sas. *Modal analysis theory and testing*. Katholieke Universteit Leuven, Departement Werktuigkunde, 2006.

[220] E. C. Levy. Complex curve fitting. *IRE transactions on automatic control*, 4(1):37–43, 1959.

[221] C. K. Sanathanan and Judith Koerner. Transfer function synthesis as a ratio of two complex polynomials. *Automatic Control, IEEE Transactions on*, 8(1):56–58, 1963.

[222] Rik Pintelon, Patrick Guillaume, Gerd Vandersteen, and Yves Rolain. Analyses, development, and applications of tls algorithms in frequency domain system identification. *SIAM journal on matrix analysis and applications*, 19(4):983–1004, 1998.

[223] Henri Gavin. The levenberg-marquardt method for nonlinear least squares curve-fitting problems. *Department of Civil and Environmental Engineering, Duke University*, 2011.

[224] Ananth Ranganathan. The levenberg-marquardt algorithm. *Tutoral on LM Algorithm*, pages 1–5, 2004.

[225] Manolis I. A. Lourakis. A brief description of the levenberg-marquardt algorithm implemented by levmar. *Foundation of Research and Technology*, 4:1–6, 2005.

[226] Peter Verboven. Frequency-domain system identification for modal analysis. *Vrije Universiteit Brussel, Brussels*, 2002.

[227] Bart Cauberghe. Applied frequency-domain system identification in the field of experimental and operational modal analysis. *Mechanical Engineering Department, Vrije Universiteit Brussel, Brussels*, 2004.

[228] M. Balda. Lmfsolve. m: Levenberg-marquardt-fletcher algorithm for nonlinear least-squares problems, 2009.

[229] R. Pintelon, P. Guillaume, and Joannes Schoukens. Uncertainty calculation in (operational) modal analysis. *Mechanical systems and signal processing*, 21(6):2359–2373, 2007.

[230] P. Verboven, B. Cauberghe, P. Guillaume, S. Vanlanduit, and E. Parloo. Modal parameter estimation and monitoring for on-line flight flutter analysis. *Mechanical Systems and Signal Processing*, 18(3):587–610, 2004.

[231] T. De Troyer, P. Guillaume, R. Pintelon, and S. Vanlanduit. Fast calculation of confidence intervals on parameter estimates of least-squares frequency-domain estimators. *Mechanical Systems and Signal Processing*, 23(2):261–273, 2009.

[232] Patrick Guillaume, Joannes Schoukens, and R. Pintelon. Sensitivity of roots to errors in the coefficient of polynomials obtained by frequency-domain estimation methods. *Instrumentation and Measurement, IEEE Transactions on*, 38(6):1050–1056, 1989.

[233] Richard S. Pappa, Kenny B. Elliott, and Axel Schenk. Consistent-mode indicator for the eigensystem realization algorithm. *Journal of Guidance, Control, and Dynamics*, 16(5):852–858, 1993.

[234] Vicente Hernandez, Jose E. Roman, and Vicente Vidal. SLEPc: A scalable and flexible toolkit for the solution of eigenvalue problems. *ACM Trans. Math. Software*, 31(3):351–362, 2005.

[235] V. Hernandez, J. E. Roman, and V. Vidal. SLEPc: Scalable Library for Eigenvalue Problem Computations. *Lecture Notes in Computer Science*, 2565:377–391, 2003.

[236] E. Romero and J. E. Roman. A parallel implementation of Davidson methods for large-scale eigenvalue problems in SLEPc. *ACM Trans. Math. Software*, 40(2):13:1–13:29, 2014.

[237] Lisandro D. Dalcin, Rodrigo R. Paz, Pablo A. Kler, and Alejandro Cosimo. Parallel distributed computing using python. *Advances in Water Resources*, 34(9):1124–1139, 2011.

[238] Tom Lauwagie, Ward Heylen, H. Sol, and Omer Van der Biest. Validation of a vibration based identification procedure for layered materials. In *Proc. of the Int. Conf. on Noise and Vibration Engineering*, pages 1325–1336. Citeseer, 2004.

[239] Tom Lauwagie and Eddy Dascotte. Layered material identification using multi-model updating. In *Proceedings of the 3rd International Conference on Structural Dynamics Modeling-Test, Analysis, Correlation and Validation-Madeira Island, Portugal*, 2002.

[240] Tom Lauwagie. Vibration-based methods for the identification of the elastic properties of layered materials. *status: published*, 2005.

[241] Tom Lauwagie, H. Sol, G. Roebben, Ward Heylen, and Y. Shi. Validation of the resonalyser method: an inverse method for material identification. In *Publications at ISMA (International Conference on Noise and Vibration Engineering)*, pages 687–694, 2002.

[242] Dieter Kraft et al. *A software package for sequential quadratic programming*. DFVLR Obersfaffeuhofen, Germany, 1988.

[243] Eric Jones, Travis Oliphant, Pearu Peterson, et al. SciPy: Open source scientific tools for Python, 2001–. [Online; accessed 2015-04-14].

[244] Stefan Van Der Walt, S. Chris Colbert, and Gael Varoquaux. The numpy array: a structure for efficient numerical computation. *Computing in Science & Engineering*, 13(2):22–30, 2011.

[245] Fernando Perez and Brian E. Granger. Ipython: a system for interactive scientific computing. *Computing in Science & Engineering*, 9(3):21–29, 2007.

[246] Frédéric Bastien, Pascal Lamblin, Razvan Pascanu, James Bergstra, Ian J. Goodfellow, Arnaud Bergeron, Nicolas Bouchard, and Yoshua Bengio. Theano: new features and speed improvements. Deep Learning and Unsupervised Feature Learning NIPS 2012 Workshop, 2012.

[247] James Bergstra, Olivier Breuleux, Frédéric Bastien, Pascal Lamblin, Razvan Pascanu, Guillaume Desjardins, Joseph Turian, David Warde-Farley, and Yoshua Bengio. Theano: a CPU and GPU math expression compiler. In *Proceedings of the Python for Scientific Computing Conference (SciPy)*, June 2010. Oral Presentation.

[248] Ronald L. Iman and Jon C. Helton. An investigation of uncertainty and sensitivity analysis techniques for computer models. *Risk Analysis*, 8(1):71–90, 1988.

[249] Ronald L. Iman and Jon C. Helton. The repeatability of uncertainty and sensitivity analyses for complex probabilistic risk assessments. *Risk Analysis*, 11(4):591–606, 1991.

[250] A. Saltelli and J. Marivoet. Non-parametric statistics in sensitivity analysis for model output: A comparison of selected techniques. *Reliability Engineering & System Safety*, 28(2):229 – 253, 1990.

[251] D. M. Hamby. A review of techniques for parameter sensitivity analysis of environmental models. *Environmental monitoring and assessment*, 32(2):135–154, 1994.

[252] Eric D. Smith, Ferenc Szidarovszky, William J. Karnavas, and ATerry Bahill. Sensitivity analysis, a powerful system validation technique. *Open Cybernetics & Systemics Journal*, 2:39–56, 2008.

[253] P. Mohanty, P. Reynolds, and A. Pavic. Automated interpretation of stability plots for analysis of a non-stationary structure. In *25th International Modal Analysis Conference (IMAC XXV)*, 2007.

[254] Yves Govers. *Parameter identification of structural dynamic models by inverse statistical analysis*. PhD thesis, Kassel, Univ., Diss., 2012, 2012.

[255] E. Reynders, J. Houbrechts, and G. De Roeck. Fully automated (operational) modal analysis. *Mechanical Systems and Signal Processing*, 29(0):228 – 250, 2012.

[256] Richard S. Pappa, George H. James, and David C. Zimmerman. Autonomous modal identification of the space shuttle tail rudder. *Journal of Spacecraft and Rockets*, 35(2):163–169, 1998.

[257] Marco Scionti, Jeroen Lanslots, Ivan Goethals, Antonio Vecchio, H. Van der Auweraer, B. Peeters, and Bart De Moor. Tools to improve detection of structural changes from in-flight flutter data. In *Proceedings of the Eighth International Conference on Recent Advances in Structural Dynamics*, 2003.

[258] Ivan Goethals, Bart Vanluyten, and Bart De Moor. Reliable spurious mode rejection using self learning algorithms. In *Proceedings of the International Conference on Noise and Vibration Engineering (ISMA 2004), Leuven, Belgium*, pages 991–1003, 2004.

[259] F. Pedregosa, G. Varoquaux, A. Gramfort, V. Michel, B. Thirion, O. Grisel, M. Blondel, P. Prettenhofer, R. Weiss, V. Dubourg, J. Vanderplas, A. Passos, D. Cournapeau, M. Brucher, M. Perrot, and E. Duchesnay. Scikit-learn: Machine learning in Python. *Journal of Machine Learning Research*, 12:2825–2830, 2011.

[260] M. J. Desforges, J. E. Cooper, and J. R. Wright. Mode tracking during flutter testing using the modal assurance criterion. *Proceedings of the Institution of Mechanical Engineers, Part G: Journal of Aerospace Engineering*, 210(1):27–37, 1996.

[261] L. Čapek, P. Henyš, and Fencl J. Tool for measuring of implant stability, 2014.

[262] L. Dzan, P. Henyš, L. Čapek, and A. Šimůnek. Makrodesign implantátu-typy a tvary používaných závitů a jejich hodnocení metodou konečných prvků. *Czech Stomatology & Practical Dentistry/Česká stomatologie a praktické zubní lékařství*, 113(4), 2013.

[263] L. Capek, A. Simunek, P. Henys, and L. Dzan. The role of implant's surface treatment to its preload. *Computer methods in biomechanics and biomedical engineering*, 17(sup1):8–9, 2014.

[264] Michal Ackermann, Lukáš Čapek, Petr Henyš, and Cyril Dody. Evaluation of contact pressure by using pressurex films. In *14th Conference on Human Biomechanics*, page 2, 2012.

[265] Maxime Billon, Lukáš Čapek, Martin Kaláb, Petr Henyš, and Petr Hájek. Analysis of the force needed for the closure of the sternum after median sternotomy. In *14th Conference on Human Biomechanics*, page 3, 2012.

[266] Enrico Schileo, Cristina Falcinelli, Luca Balistreri, Petr Henys, Fabio Baruffaldi, Sigurdur Sigurdsson, Vilmundur Gudnason, Stephanie Boutroy, and Fulvia Taddei. Association of ct-based finite element estimates of femur strength with fracture status in three clinical studies on postmenopausal women. 2014.

Appendix A

Sensitivity Data

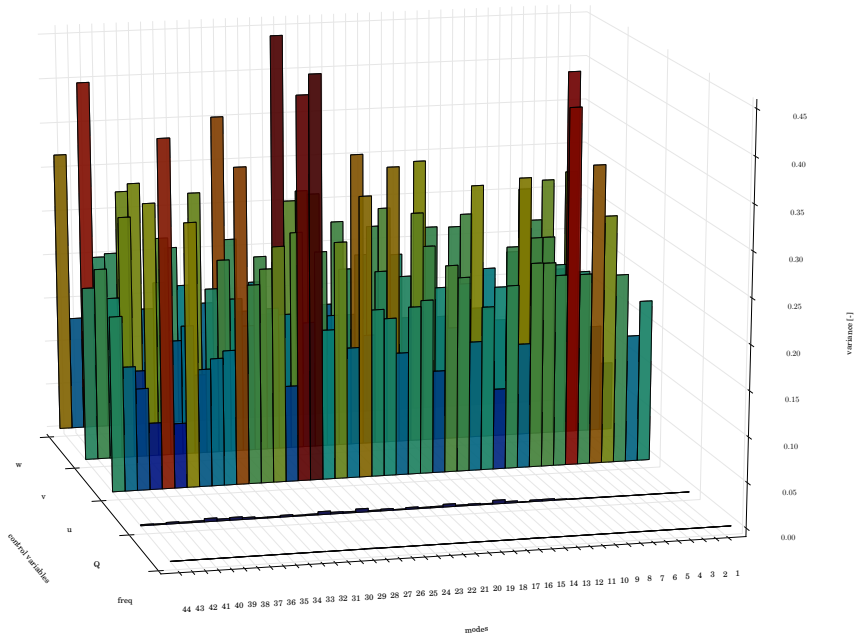

(a) variance

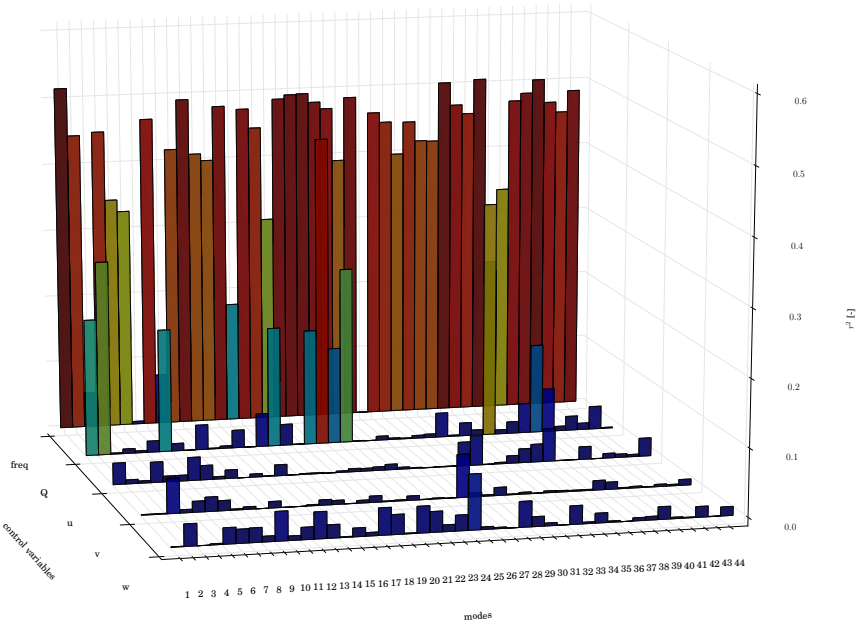

(b) determination coefficient

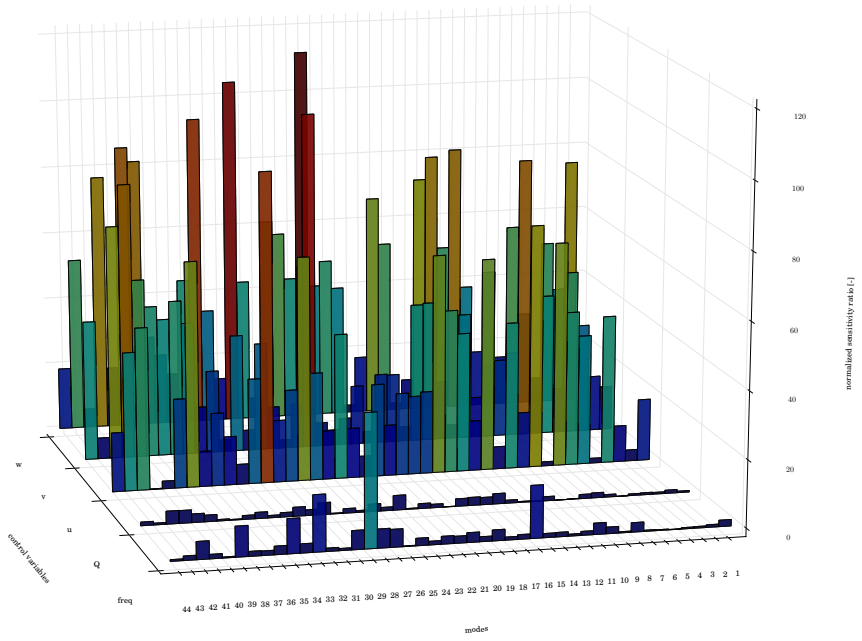

(c) Sensitivity ratio (-2.8)

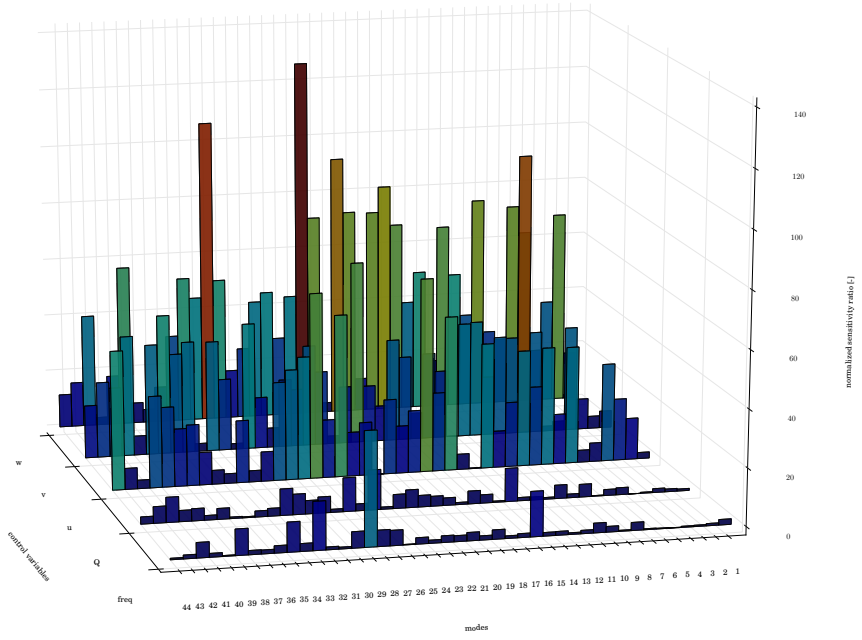

(d) Sensitivity ratio (-0.9)

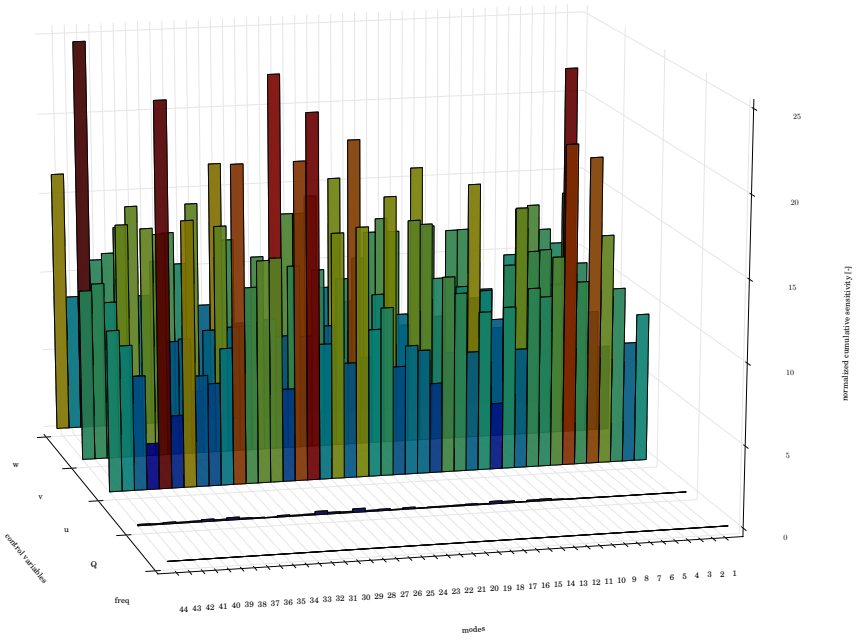

(e) cumulative sensitivity

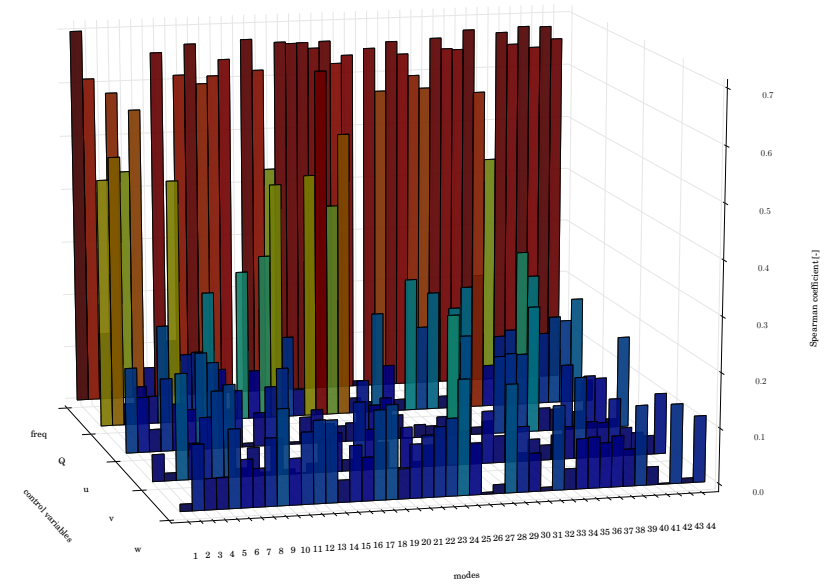

(f) rank - order correlation coeff.

Figure A.-2: Control variables for all 44 modes

Appendix B

Correlation Data - Cup

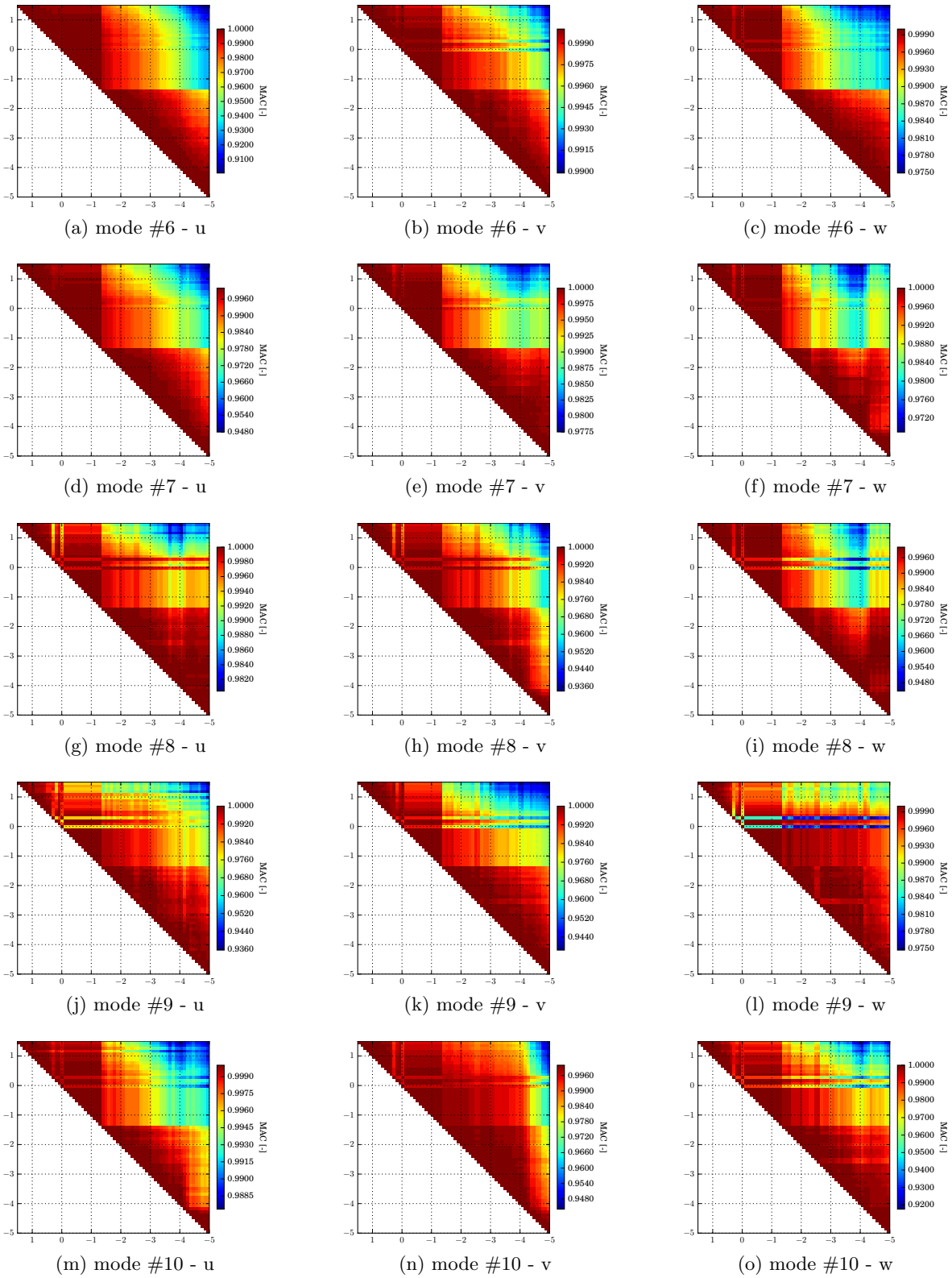

(a) mode #6 - u (b) mode #6 - v (c) mode #6 - w

(d) mode #7 - u (e) mode #7 - v (f) mode #7 - w

(g) mode #8 - u (h) mode #8 - v (i) mode #8 - w

(j) mode #9 - u (k) mode #9 - v (l) mode #9 - w

(m) mode #10 - u (n) mode #10 - v (o) mode #10 - w

Figure B.1: MAC for acetabular cup - 6:10 modes

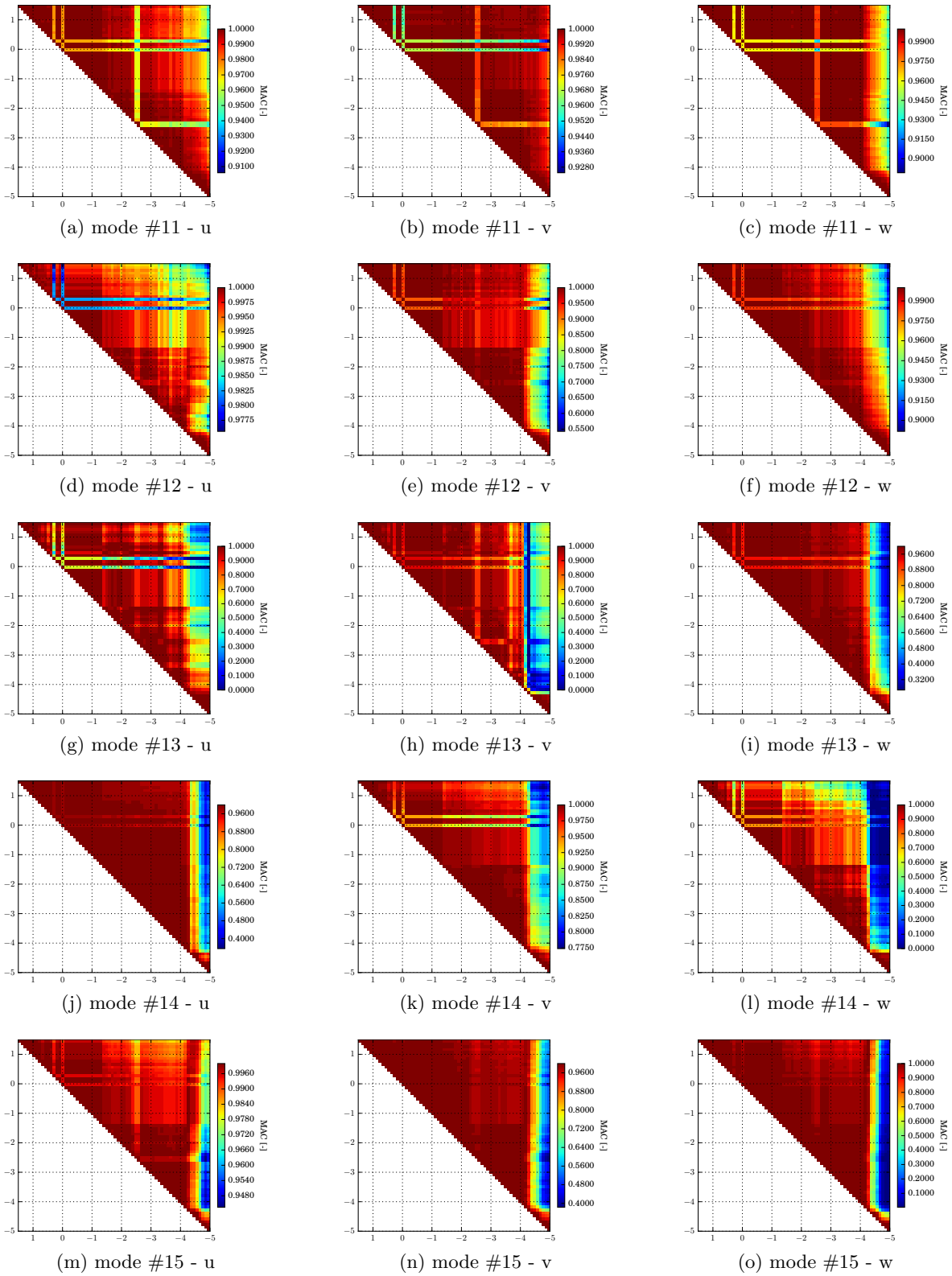

(a) mode #11 - u (b) mode #11 - v (c) mode #11 - w

(d) mode #12 - u (e) mode #12 - v (f) mode #12 - w

(g) mode #13 - u (h) mode #13 - v (i) mode #13 - w

(j) mode #14 - u (k) mode #14 - v (l) mode #14 - w

(m) mode #15 - u (n) mode #15 - v (o) mode #15 - w

Figure B.2: MAC for acetabular cup - 11:15 modes

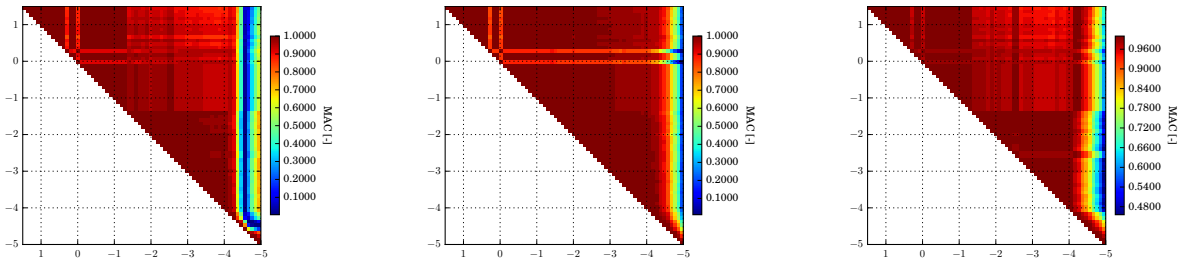

(a) mode #16 - u (b) mode #16 - v (c) mode #16 - w

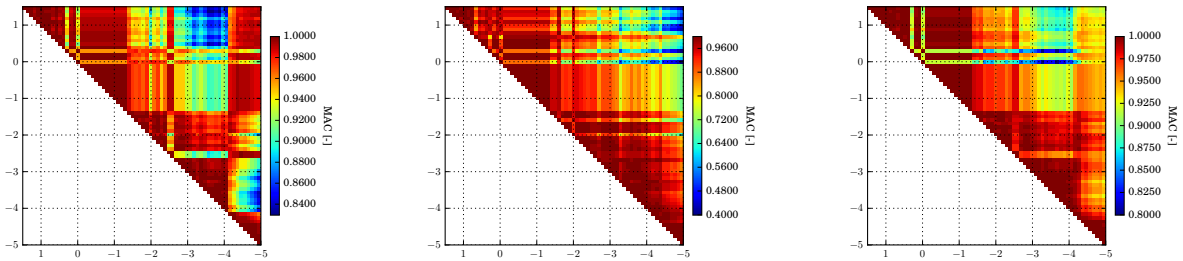

(d) mode #17 - u (e) mode #17 - v (f) mode #17 - w

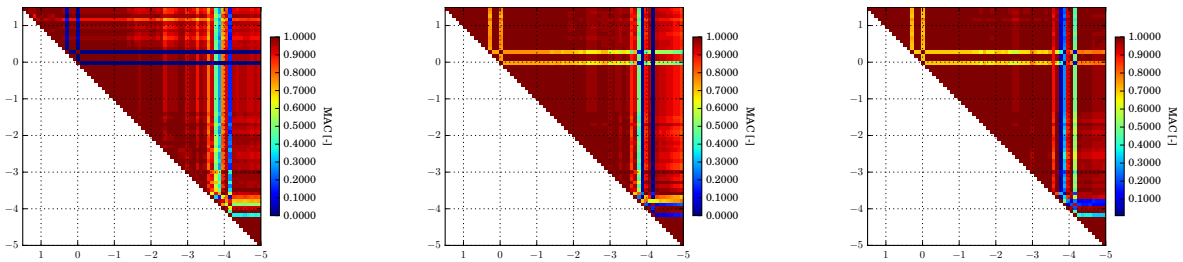

(g) mode #18 - u (h) mode #18 - v (i) mode #18 - w

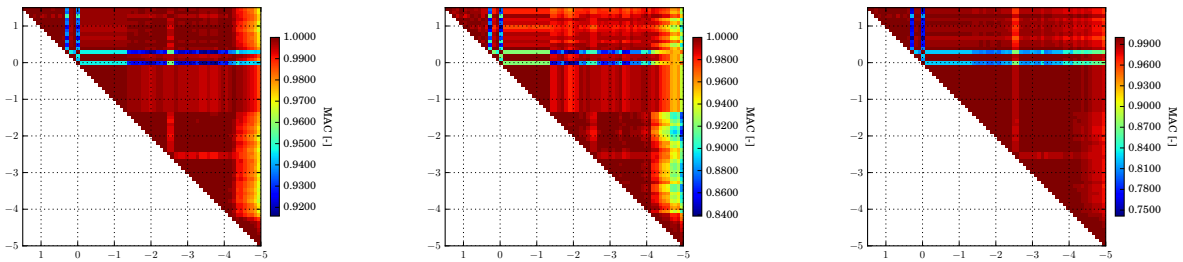

(j) mode #19 - u (k) mode #19 - v (l) mode #19 - w

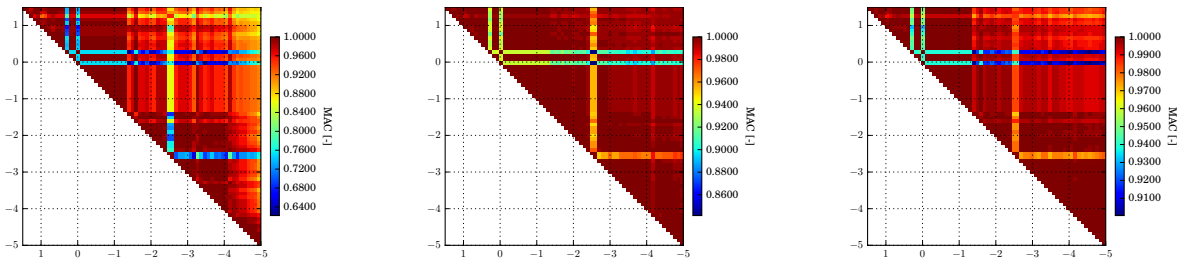

(m) mode #20 - u (n) mode #20 - v (o) mode #20 - w

Figure B.3: MAC for acetabular cup - 16:20 modes

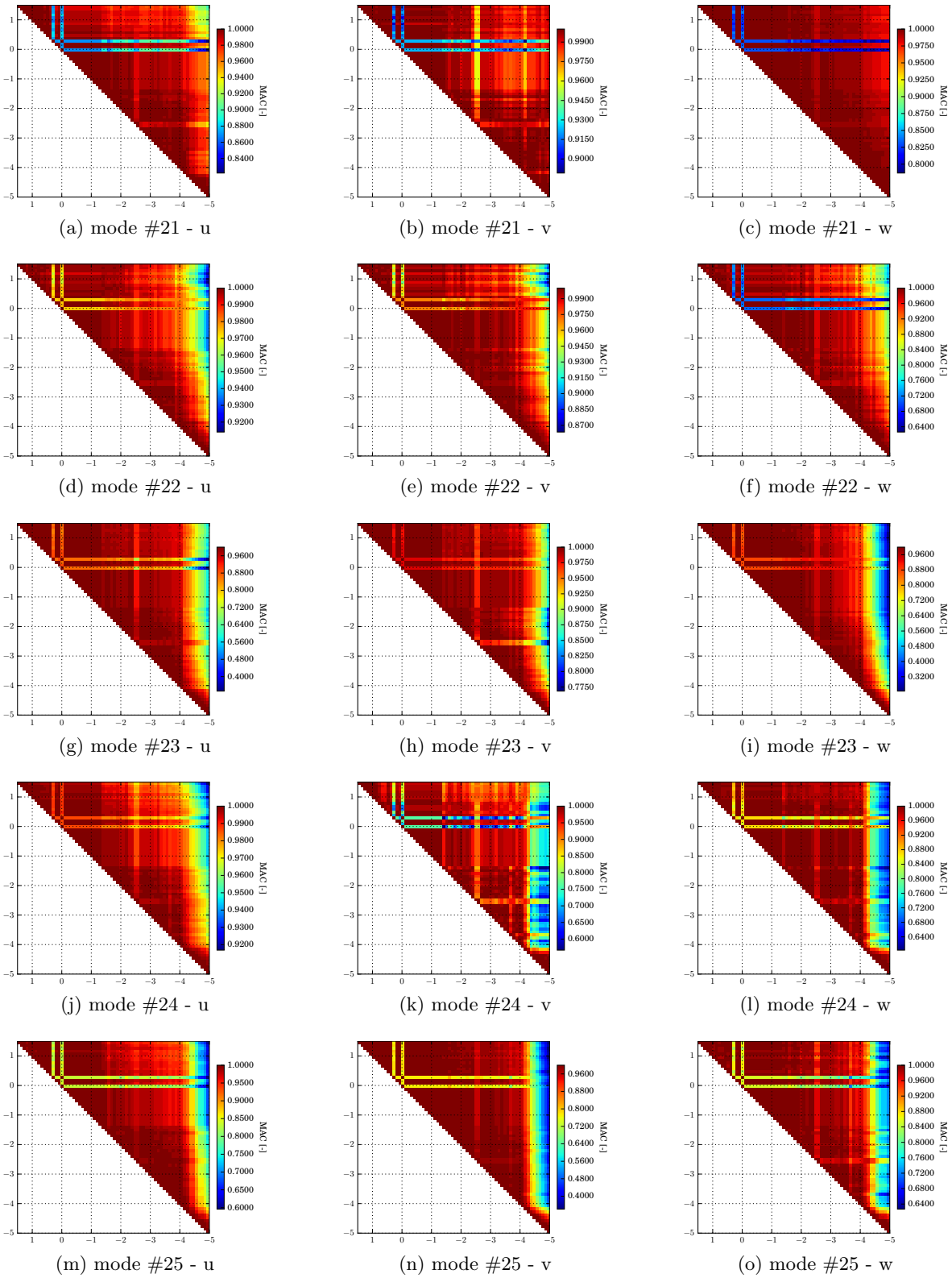

(a) mode #21 - u (b) mode #21 - v (c) mode #21 - w

(d) mode #22 - u (e) mode #22 - v (f) mode #22 - w

(g) mode #23 - u (h) mode #23 - v (i) mode #23 - w

(j) mode #24 - u (k) mode #24 - v (l) mode #24 - w

(m) mode #25 - u (n) mode #25 - v (o) mode #25 - w

Figure B.4: MAC for acetabular cup - 21:25 modes

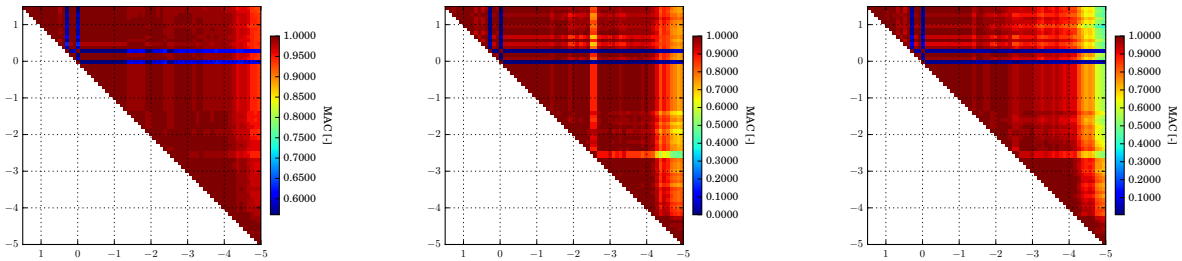

(a) mode #26 - u (b) mode #26 - v (c) mode #26 - w

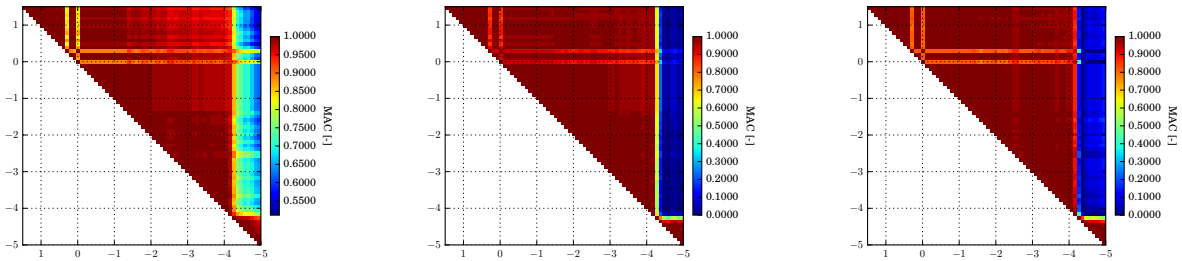

(d) mode #27 - u (e) mode #27 - v (f) mode #27 - w

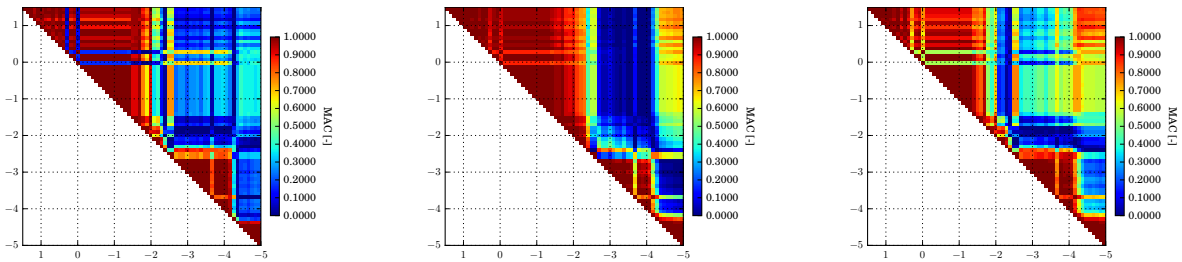

(g) mode #28 - u (h) mode #28 - v (i) mode #28 - w

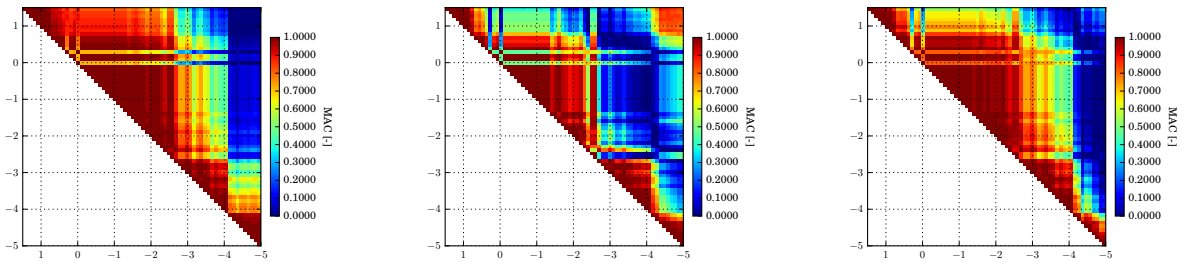

(j) mode #29 - u (k) mode #29 - v (l) mode #29 - w

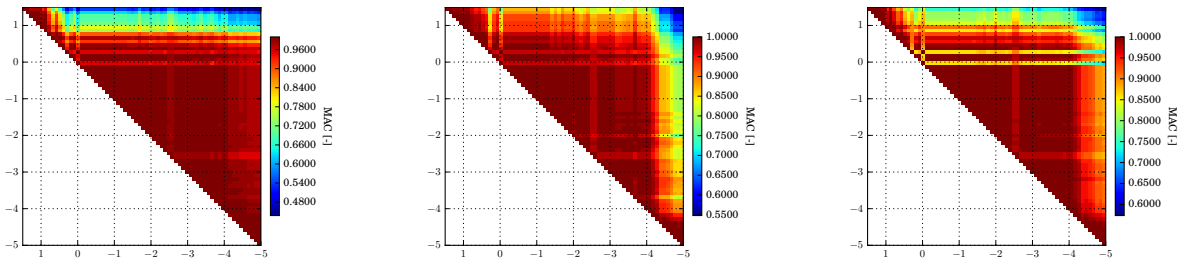

(m) mode #30 - u (n) mode #30 - v (o) mode #30 - w

Figure B.5: MAC for acetabular cup - 26:30 modes

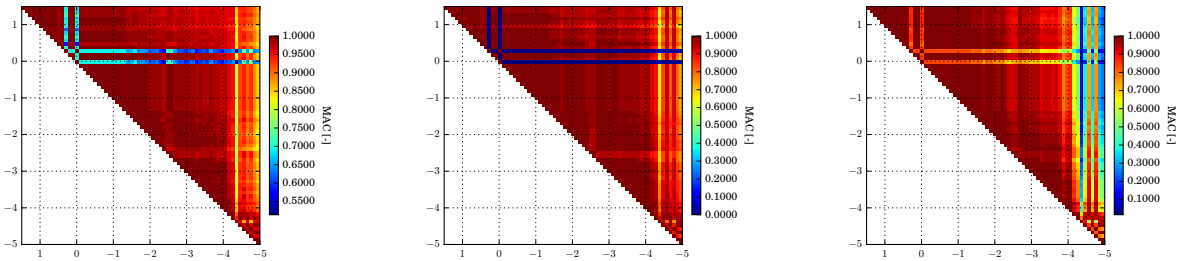

(a) mode #31 - u (b) mode #31 - v (c) mode #31 - w

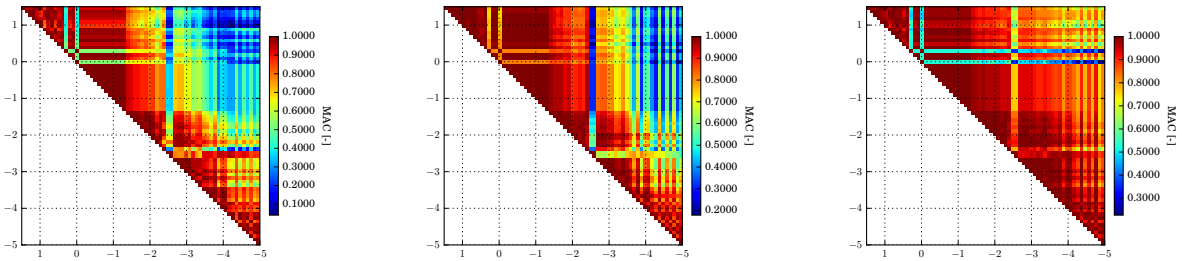

(d) mode #32 - u (e) mode #32 - v (f) mode #32 - w

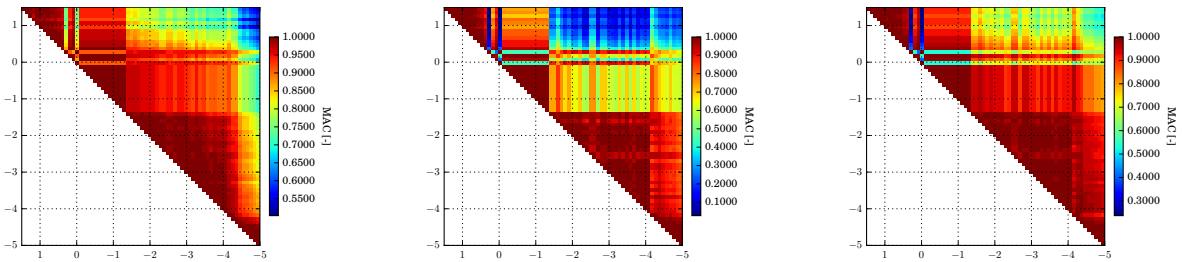

(g) mode #33 - u (h) mode #33 - v (i) mode #33 - w

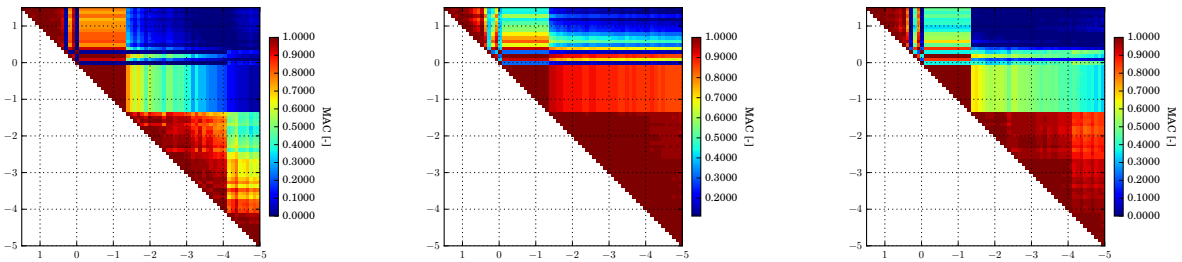

(j) mode #34 - u (k) mode #34 - v (l) mode #34 - w

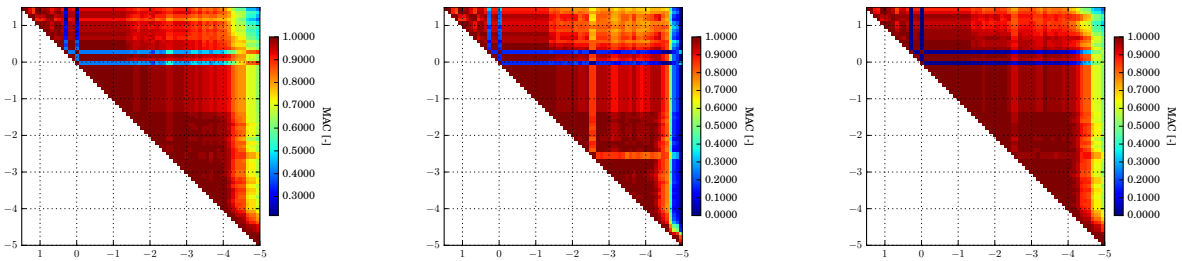

(m) mode #35 - u (n) mode #35 - v (o) mode #35 - w

Figure B.6: MAC for acetabular cup - 31:35 modes

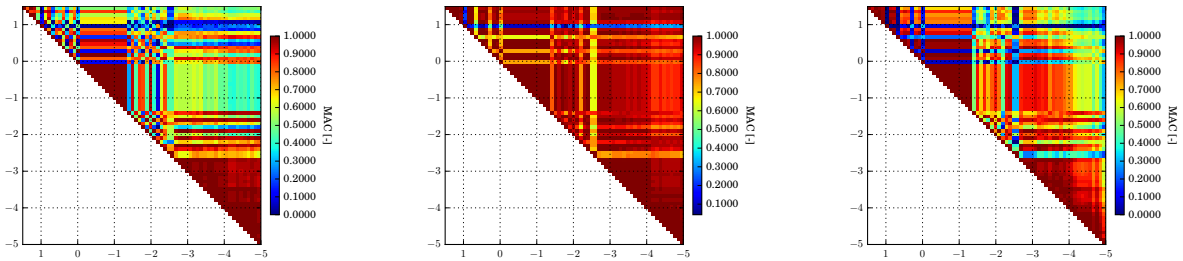

(a) mode #36 - u (b) mode #36 - v (c) mode #36 - w

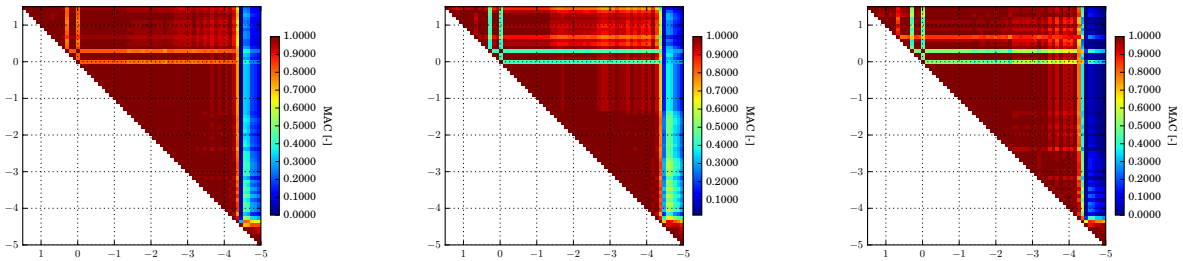

(d) mode #37 - u (e) mode #37 - v (f) mode #37 - w

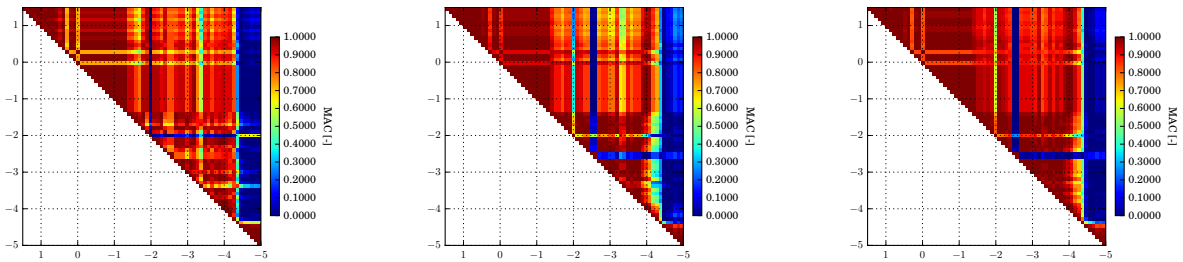

(g) mode #38 - u (h) mode #38 - v (i) mode #38 - w

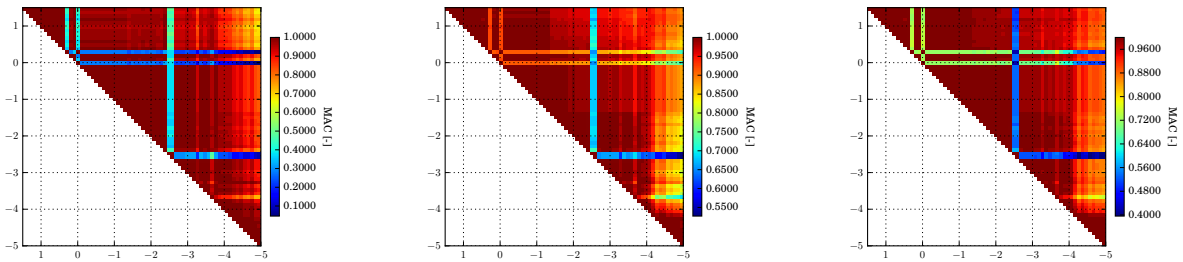

(j) mode #39 - u (k) mode #39 - v (l) mode #39 - w

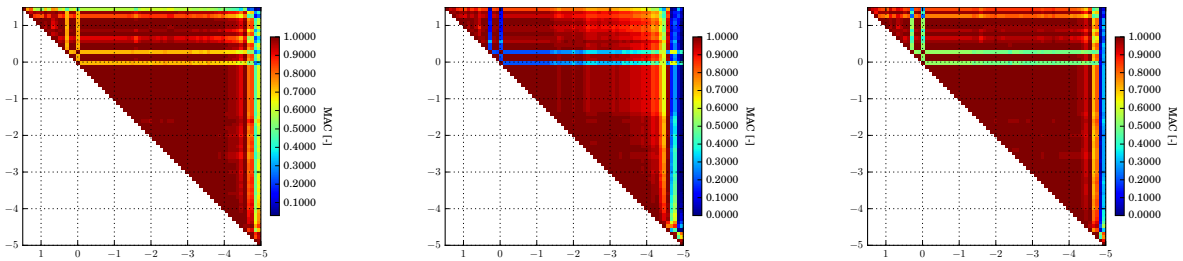

(m) mode #40 - u (n) mode #40 - v (o) mode #40 - w

Figure B.7: MAC for acetabular cup - 36:40 modes

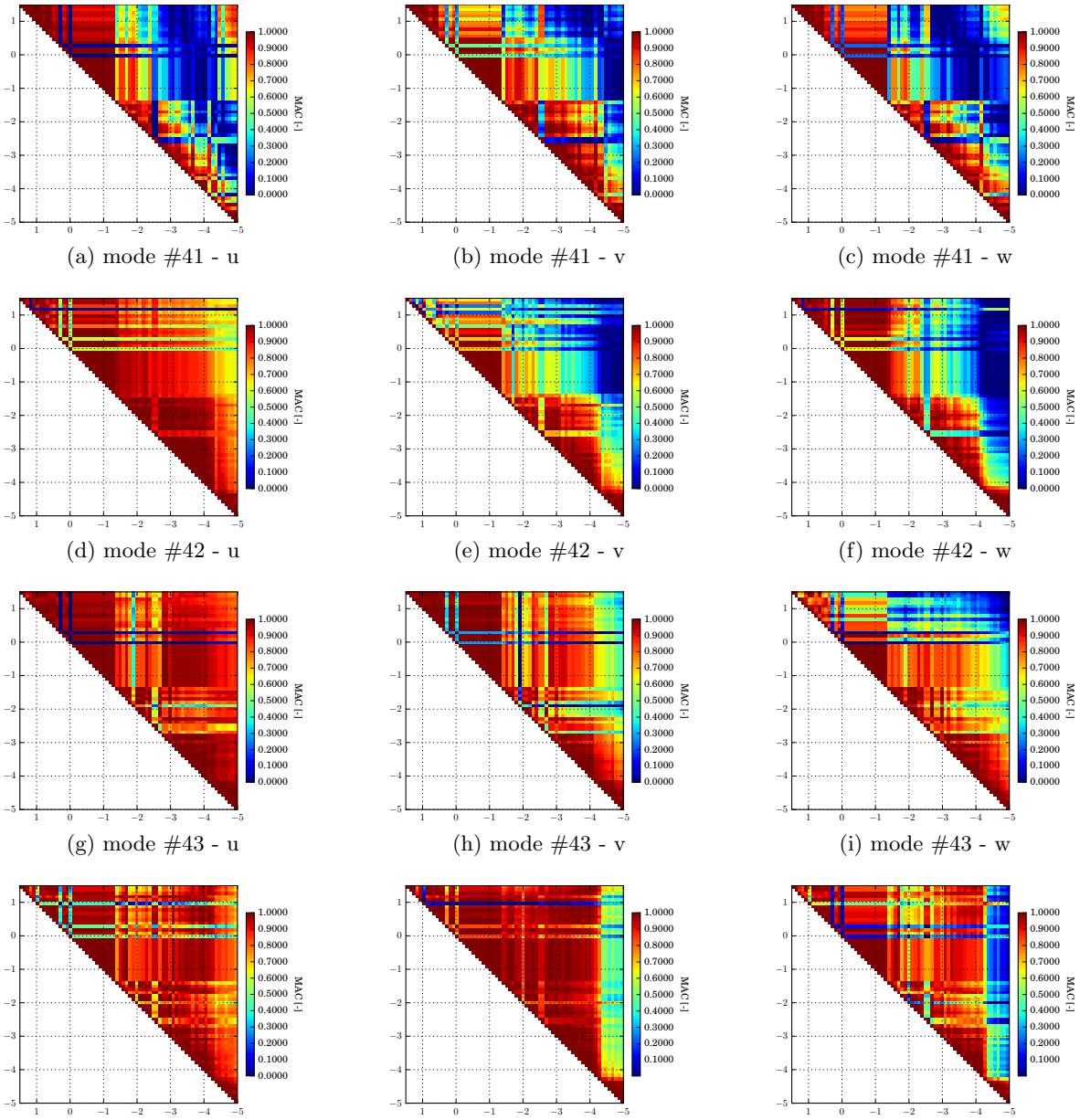

(a) mode #41 - u (b) mode #41 - v (c) mode #41 - w

(d) mode #42 - u (e) mode #42 - v (f) mode #42 - w

(g) mode #43 - u (h) mode #43 - v (i) mode #43 - w

(j) mode #44 - u (k) mode #44 - v (l) mode #44 - w

Figure B.8: MAC for acetabular cup - 41:44 modes

Appendix C

Correlation Data - Beam

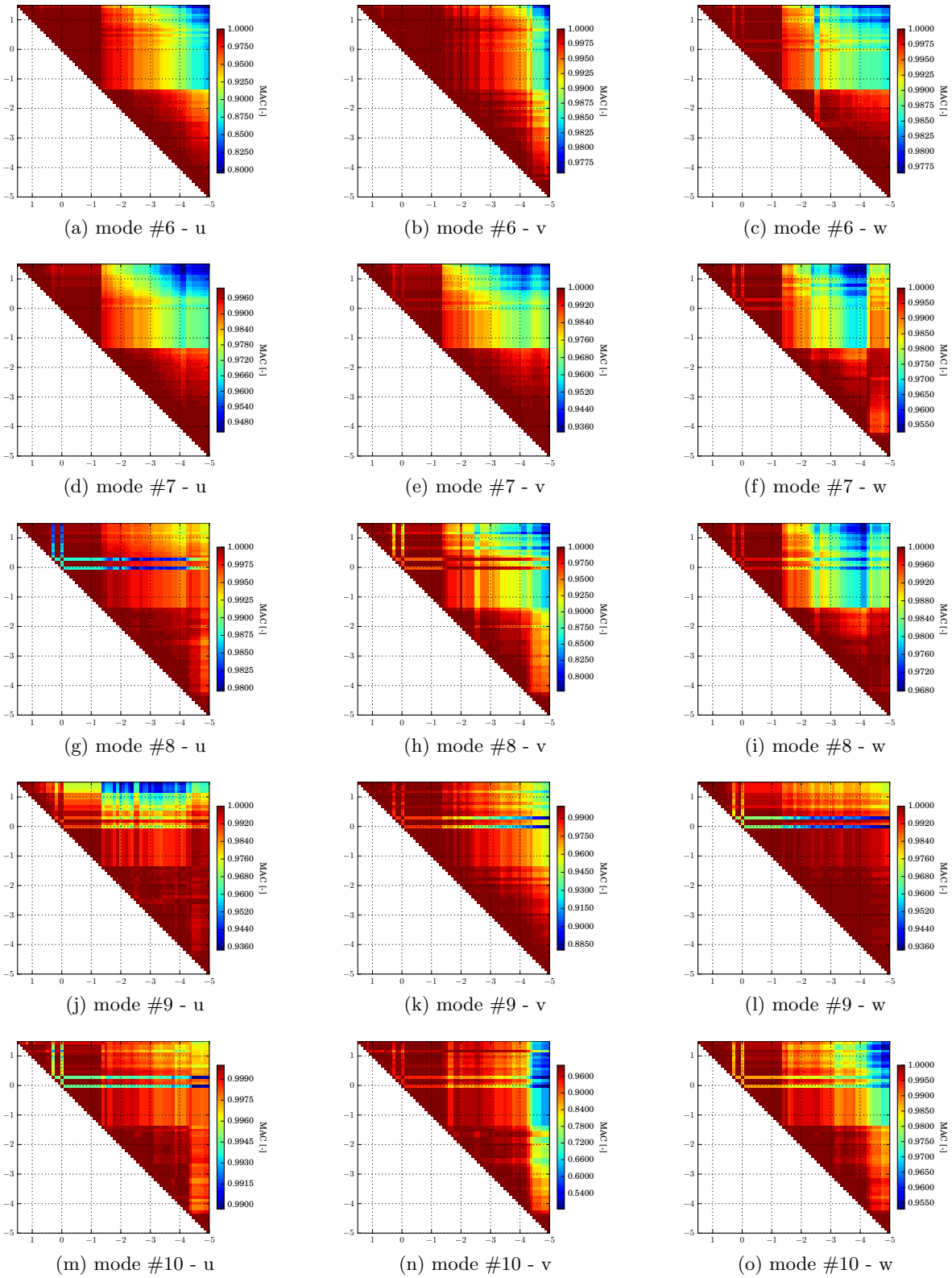

(a) mode #6 - u (b) mode #6 - v (c) mode #6 - w

(d) mode #7 - u (e) mode #7 - v (f) mode #7 - w

(g) mode #8 - u (h) mode #8 - v (i) mode #8 - w

(j) mode #9 - u (k) mode #9 - v (l) mode #9 - w

(m) mode #10 - u (n) mode #10 - v (o) mode #10 - w

Figure C.1: MAC for beam - 6:10 modes

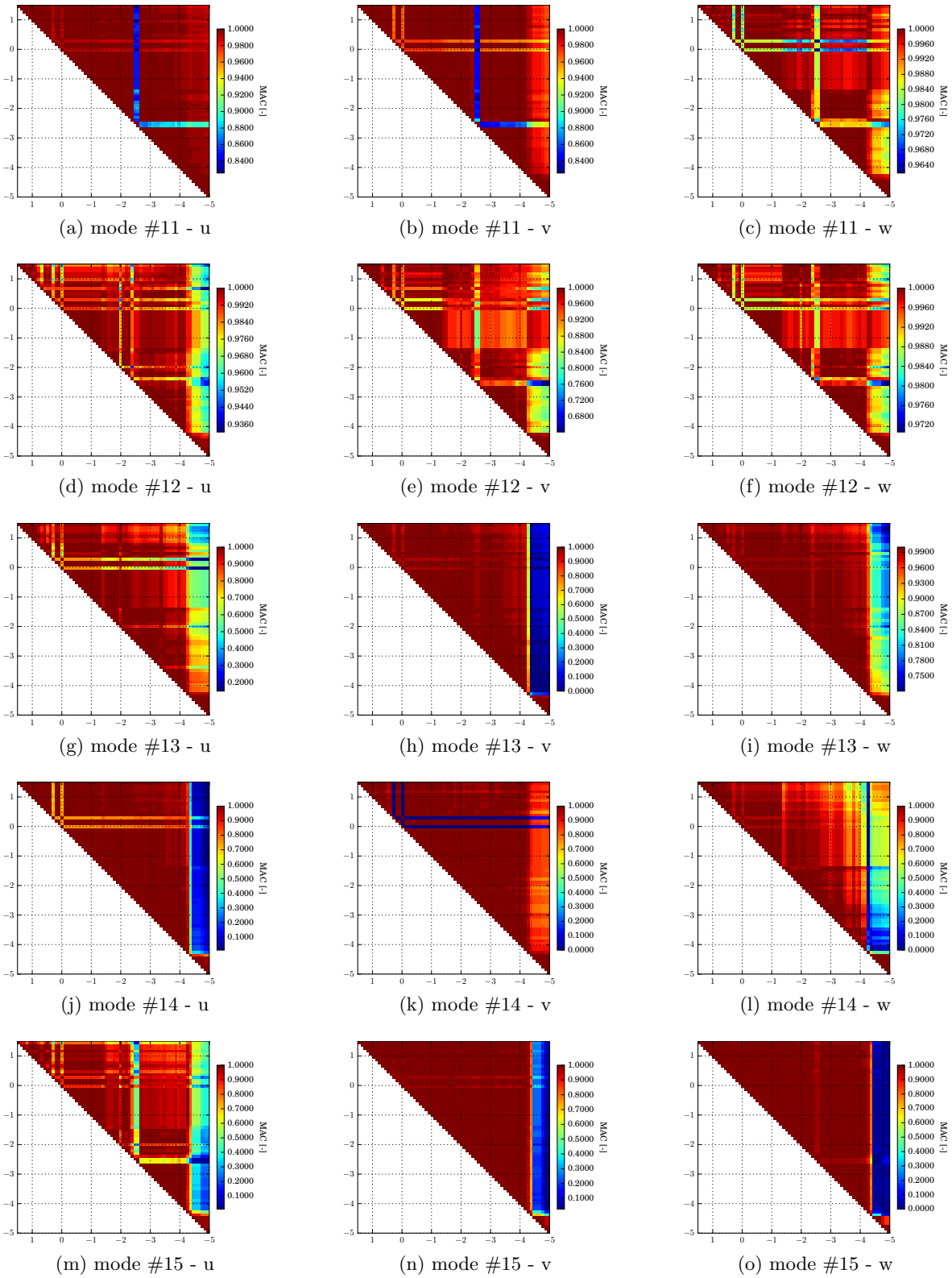

(a) mode #11 - u (b) mode #11 - v (c) mode #11 - w

(d) mode #12 - u (e) mode #12 - v (f) mode #12 - w

(g) mode #13 - u (h) mode #13 - v (i) mode #13 - w

(j) mode #14 - u (k) mode #14 - v (l) mode #14 - w

(m) mode #15 - u (n) mode #15 - v (o) mode #15 - w

Figure C.2: MAC for beam - 11:15 modes

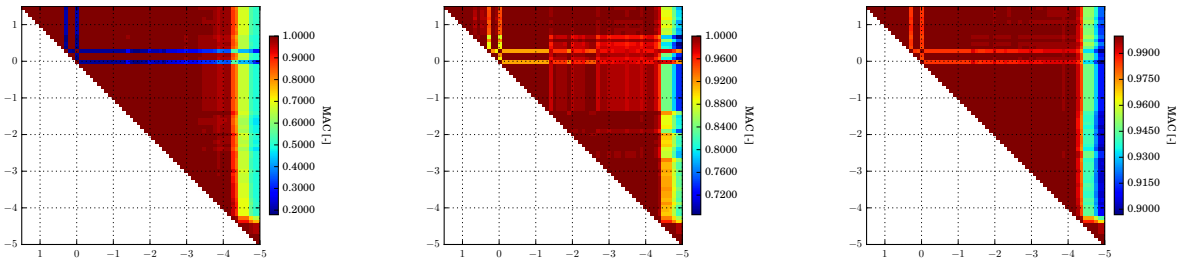

(a) mode #16 - u (b) mode #16 - v (c) mode #16 - w

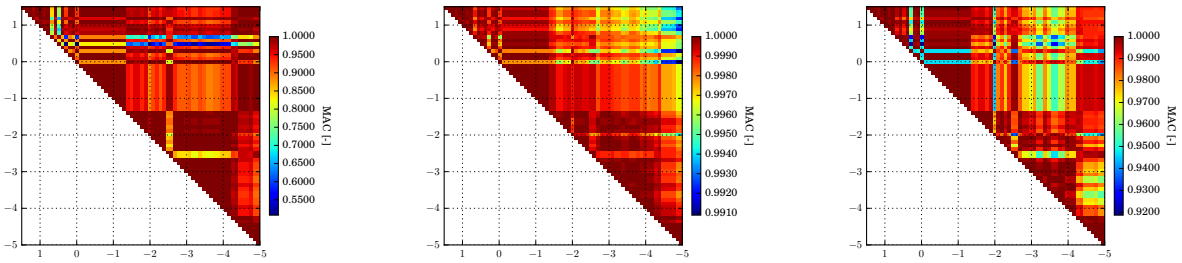

(d) mode #17 - u (e) mode #17 - v (f) mode #17 - w

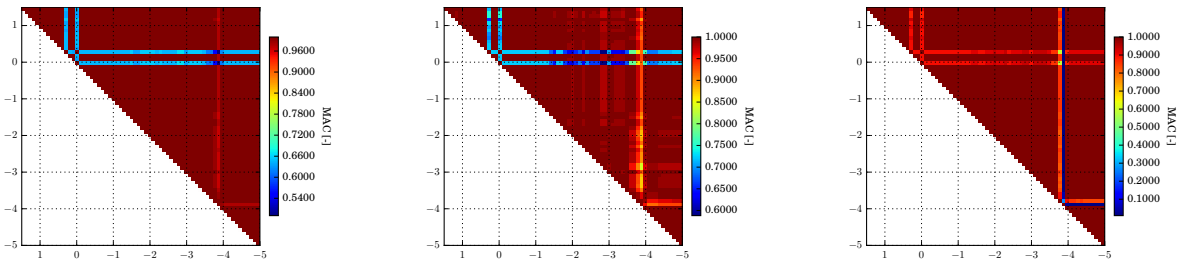

(g) mode #18 - u (h) mode #18 - v (i) mode #18 - w

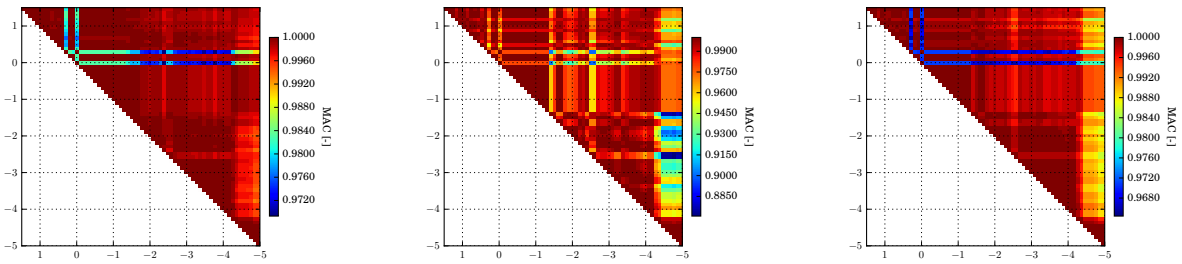

(j) mode #19 - u (k) mode #19 - v (l) mode #19 - w

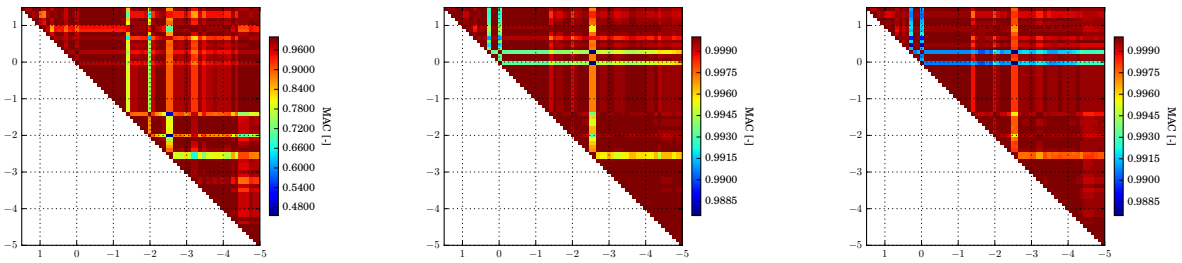

(m) mode #20 - u (n) mode #20 - v (o) mode #20 - w

Figure C.3: MAC for beam - 16:20 modes

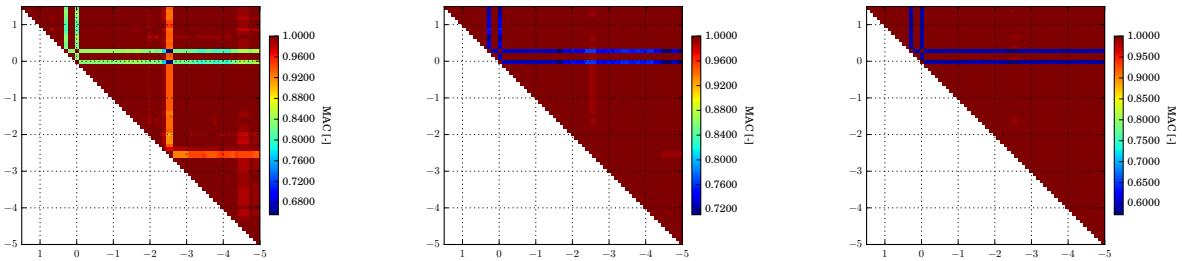

(a) mode #21 - u (b) mode #21 - v (c) mode #21 - w

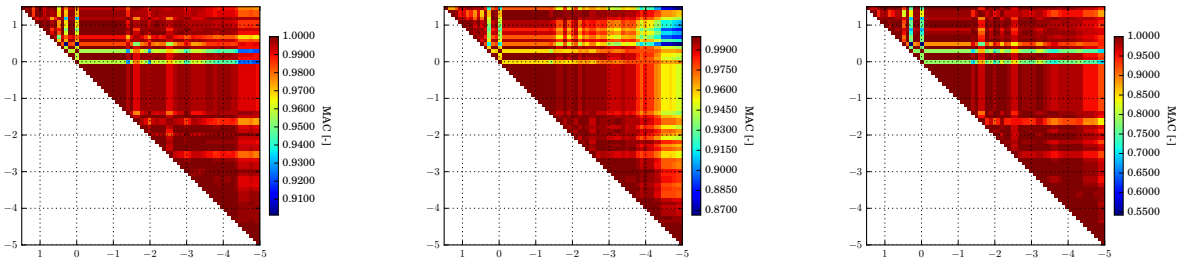

(d) mode #22 - u (e) mode #22 - v (f) mode #22 - w

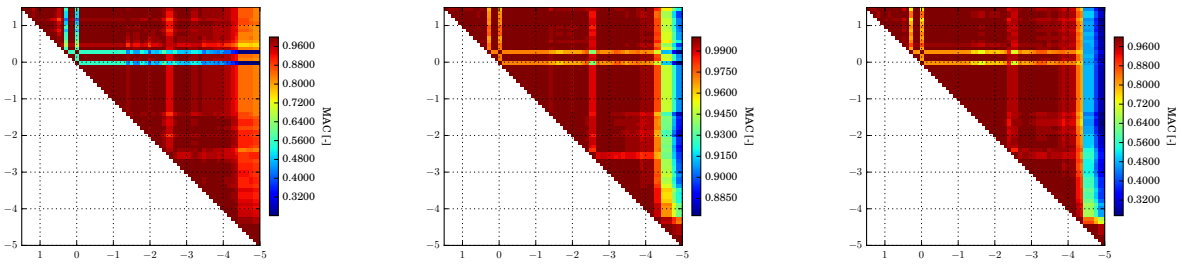

(g) mode #23 - u (h) mode #23 - v (i) mode #23 - w

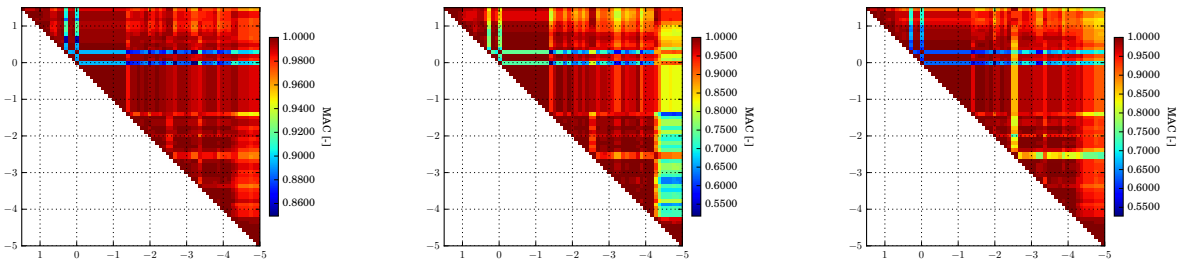

(j) mode #24 - u (k) mode #24 - v (l) mode #24 - w

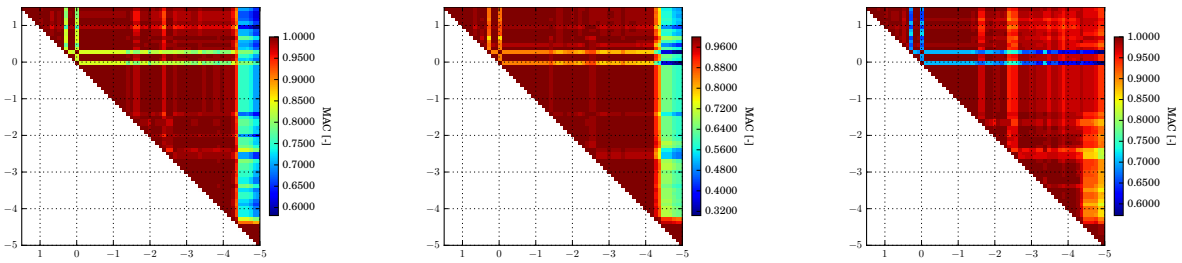

(m) mode #25 - u (n) mode #25 - v (o) mode #25 - w

Figure C.4: MAC for beam - 21:25 modes

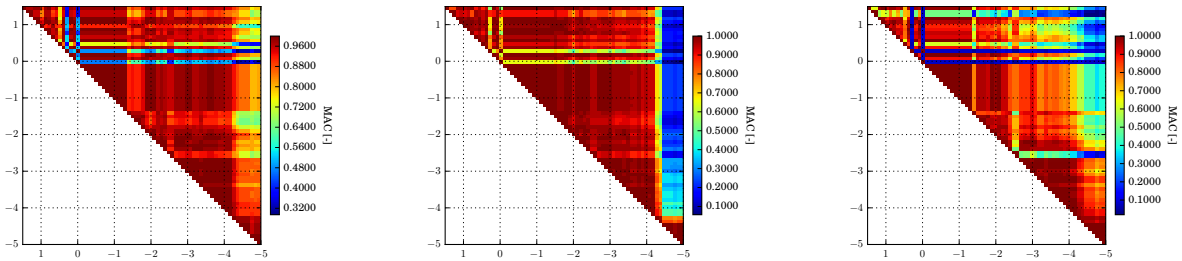

(a) mode #26 - u (b) mode #26 - v (c) mode #26 - w

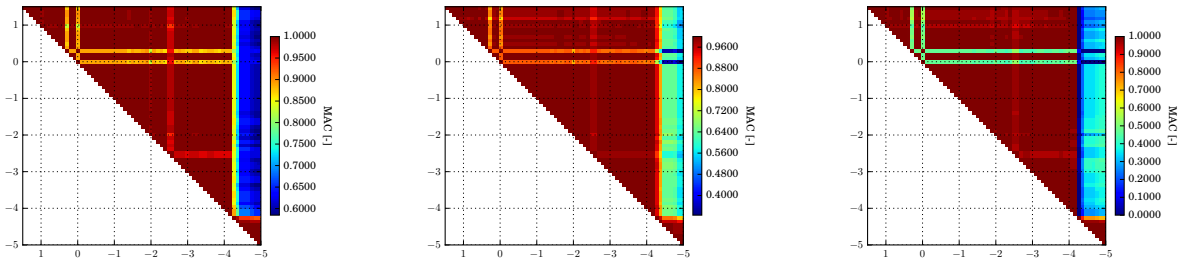

(d) mode #27 - u (e) mode #27 - v (f) mode #27 - w

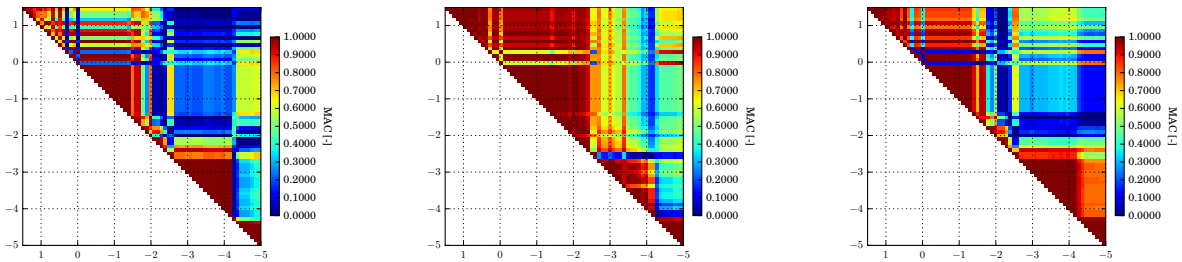

(g) mode #28 - u (h) mode #28 - v (i) mode #28 - w

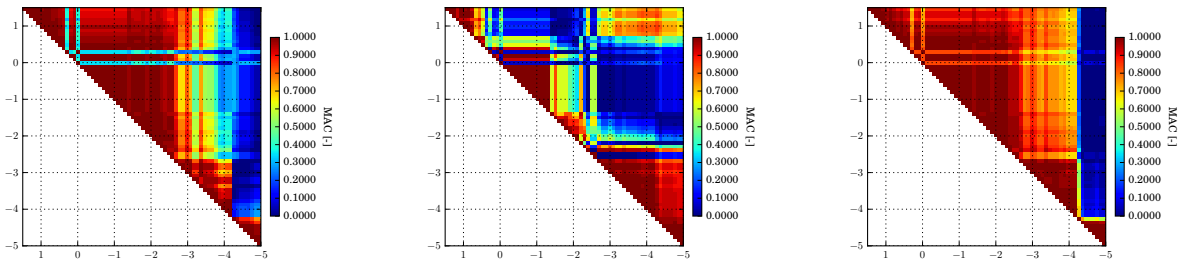

(j) mode #29 - u (k) mode #29 - v (l) mode #29 - w

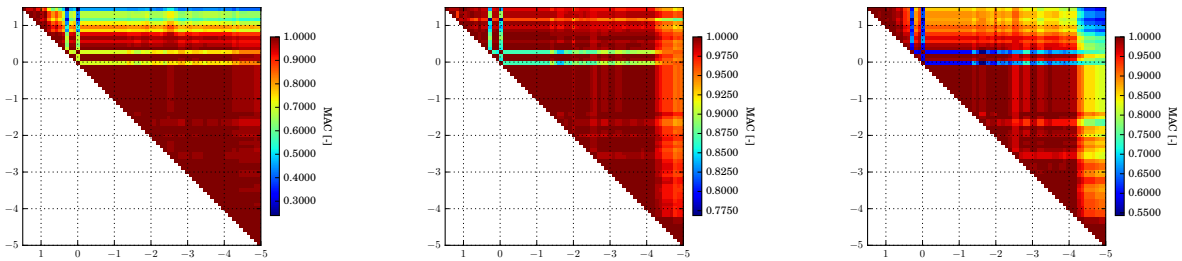

(m) mode #30 - u (n) mode #30 - v (o) mode #30 - w

Figure C.5: MAC for beam - 26:30 modes

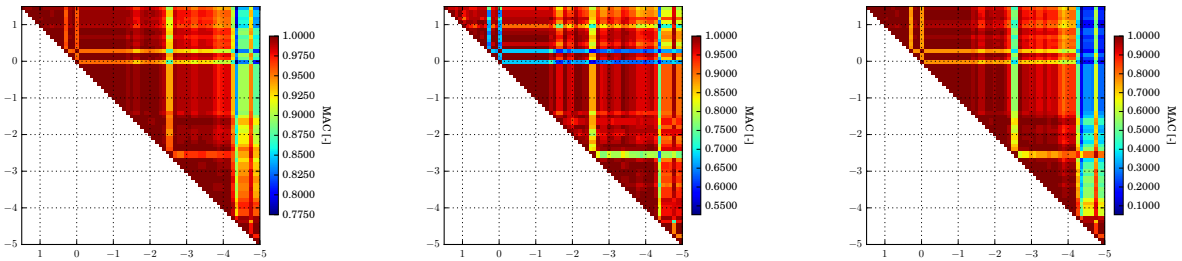

(a) mode #31 - u

(b) mode #31 - v

(c) mode #31 - w

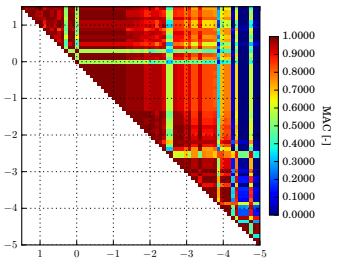

(d) mode #32 - u

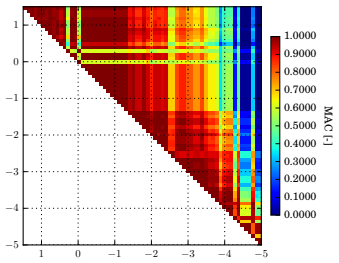

(e) mode #32 - v

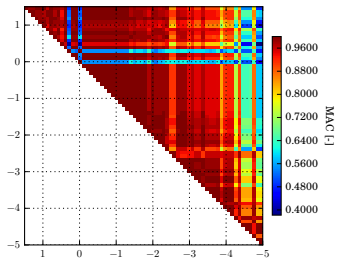

(f) mode #32 - w

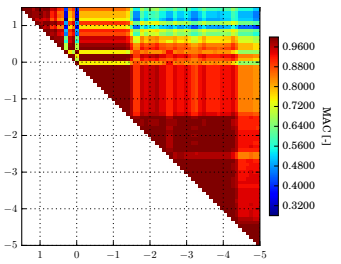

(g) mode #33 - u

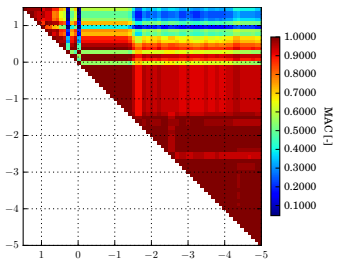

(h) mode #33 - v

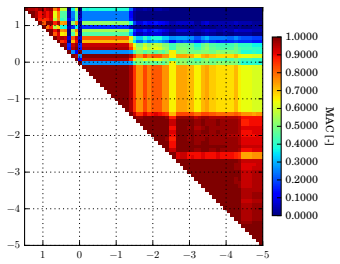

(i) mode #33 - w

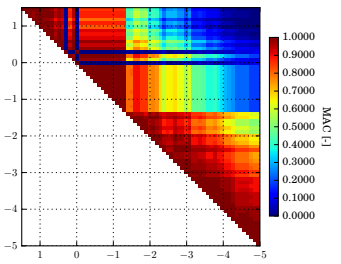

(j) mode #34 - u

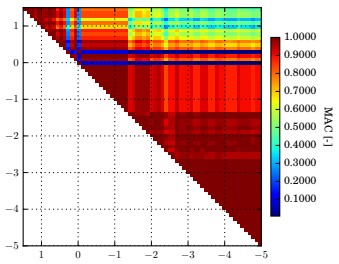

(k) mode #34 - v

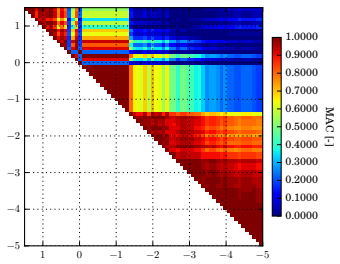

(l) mode #34 - w

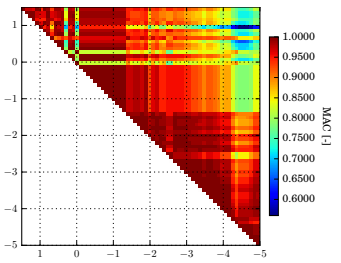

(m) mode #35 - u

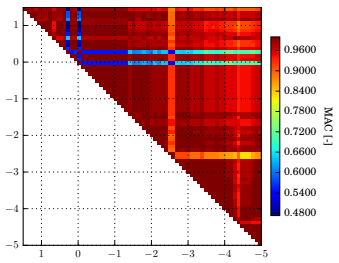

(n) mode #35 - v

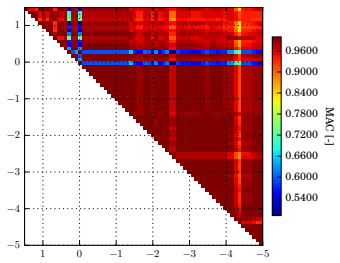

(o) mode #35 - w

Figure C.6: MAC for beam - 31:35 modes

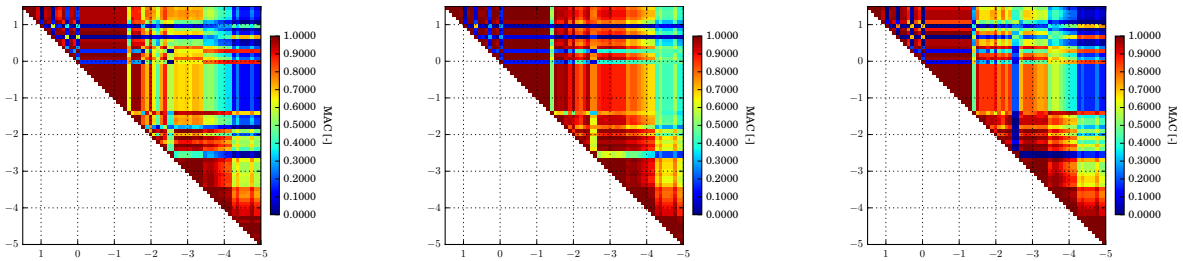

(a) mode #36 - u (b) mode #36 - v (c) mode #36 - w

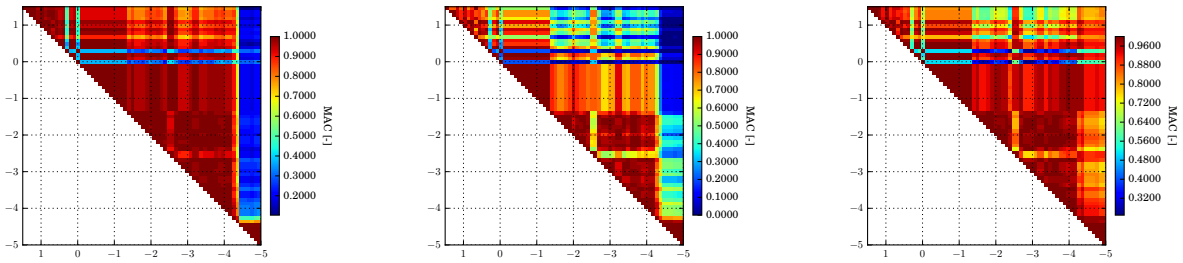

(d) mode #37 - u (e) mode #37 - v (f) mode #37 - w

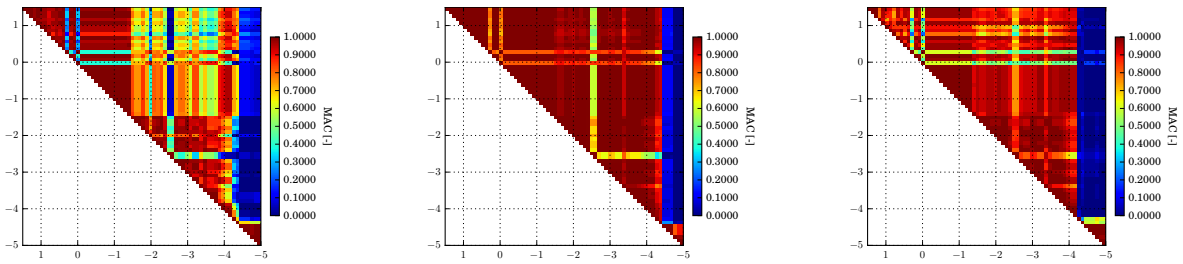

(g) mode #38 - u (h) mode #38 - v (i) mode #38 - w

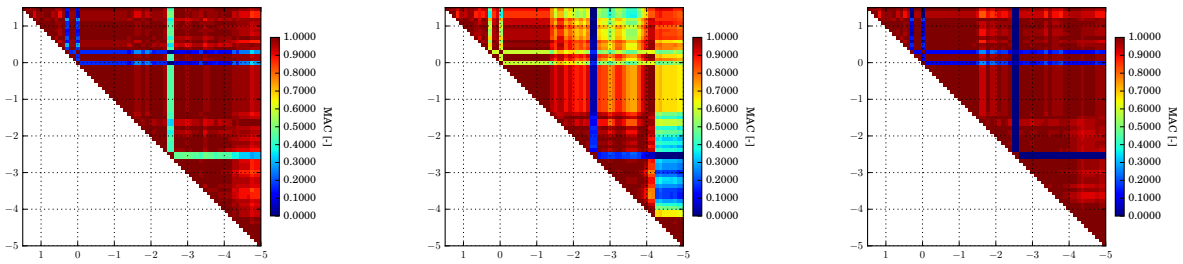

(j) mode #39 - u (k) mode #39 - v (l) mode #39 - w

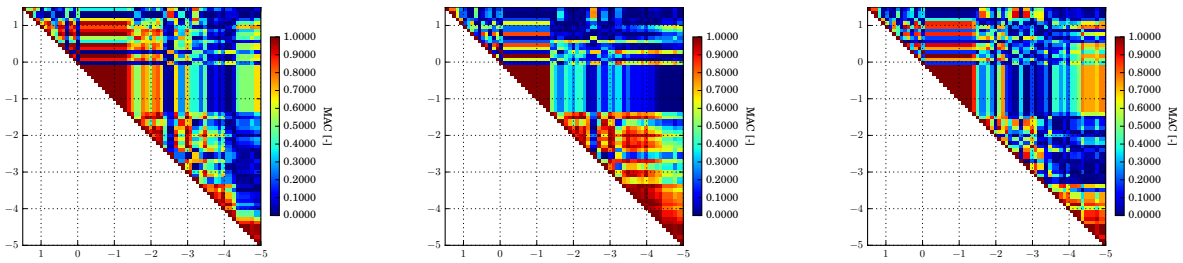

(m) mode #40 - u (n) mode #40 - v (o) mode #40 - w

Figure C.7: MAC for beam - 36:40 modes

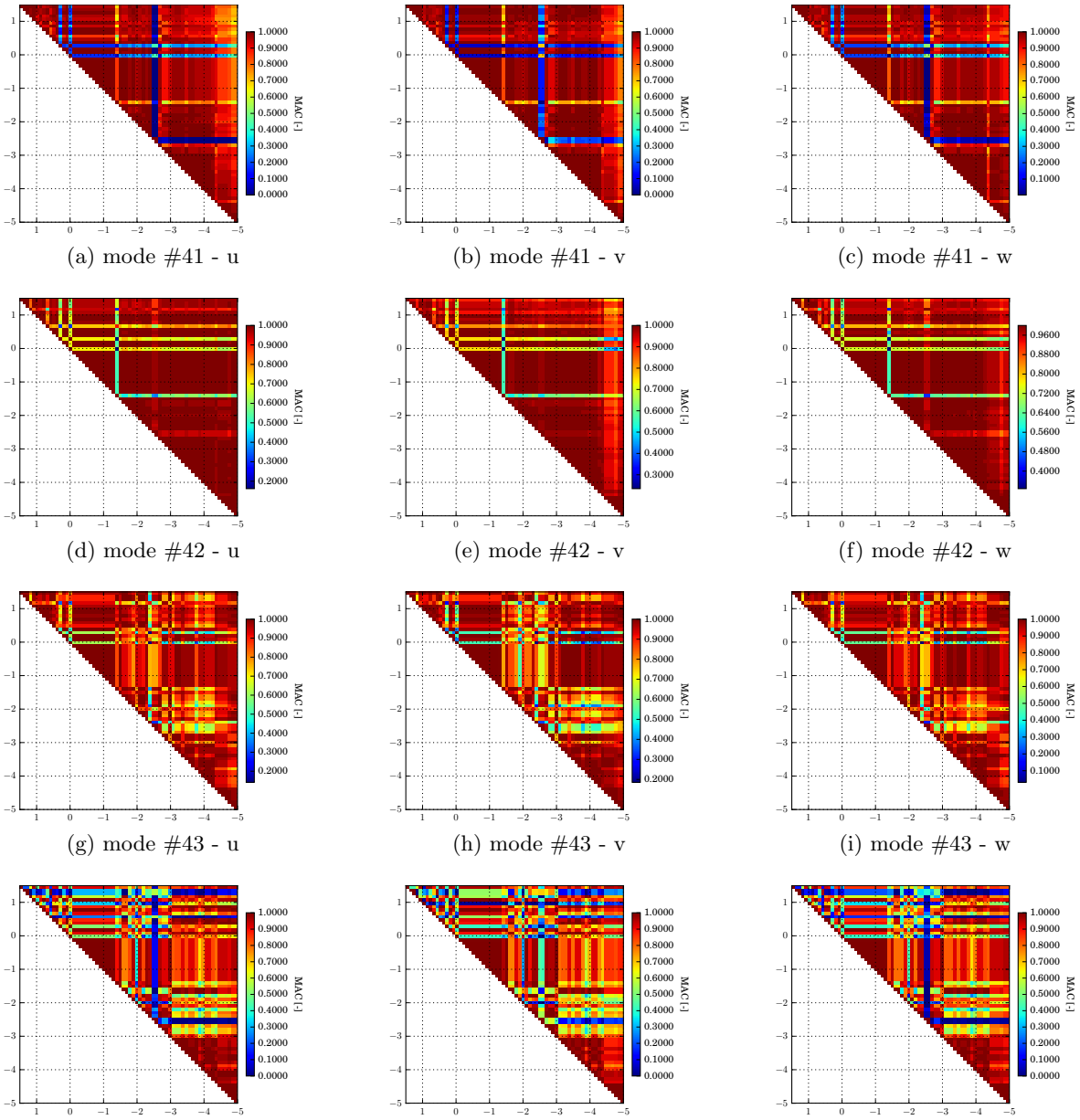

(a) mode #41 - u (b) mode #41 - v (c) mode #41 - w

(d) mode #42 - u (e) mode #42 - v (f) mode #42 - w

(g) mode #43 - u (h) mode #43 - v (i) mode #43 - w

(j) mode #44 - u (k) mode #44 - v (l) mode #44 - w

Figure C.8: MAC for beam - 41:44 modes

Appendix D

Modal Data Evaluation

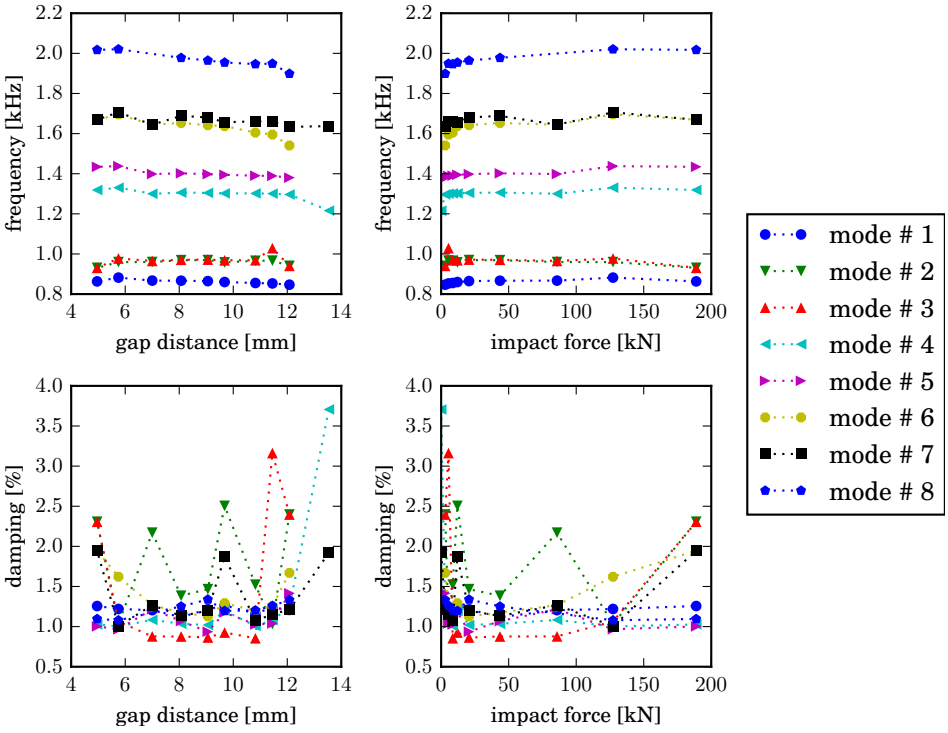

(a) frequency range 100 - 2100 Hz

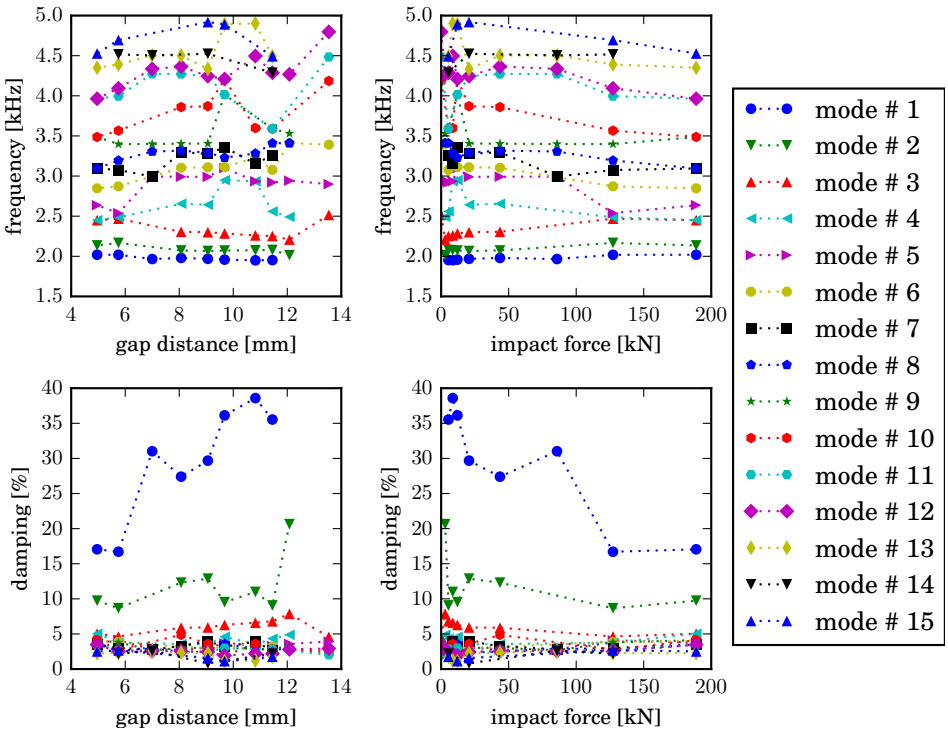

(b) frequency range 1900 - 5000 Hz

Figure D.1: Evaluation of modal properties for implant # 2

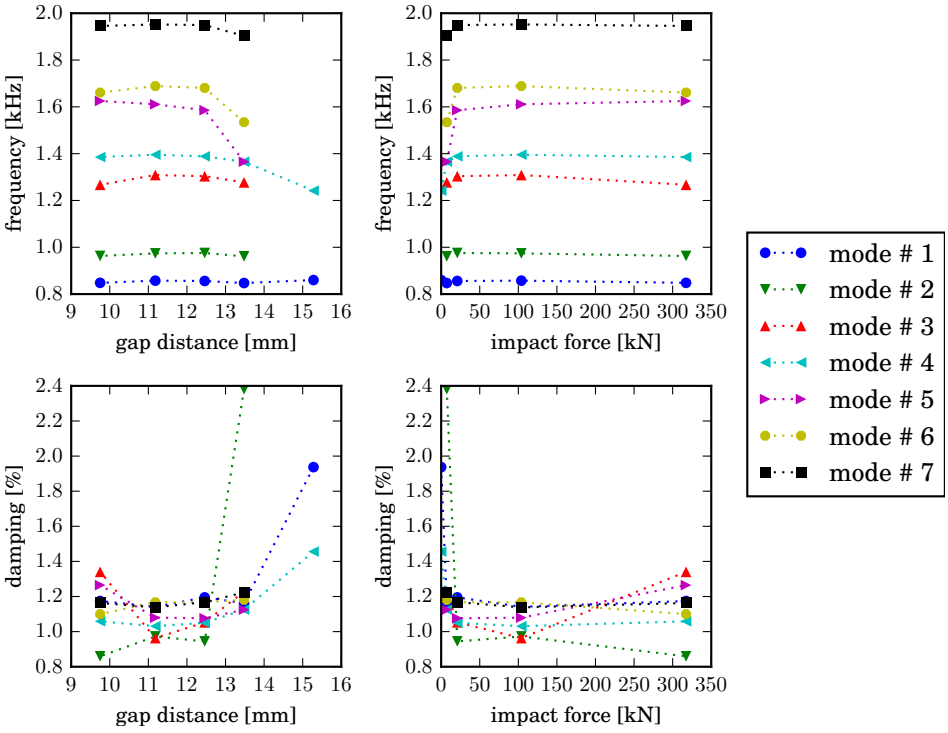

(a) frequency range 100 - 2100 Hz

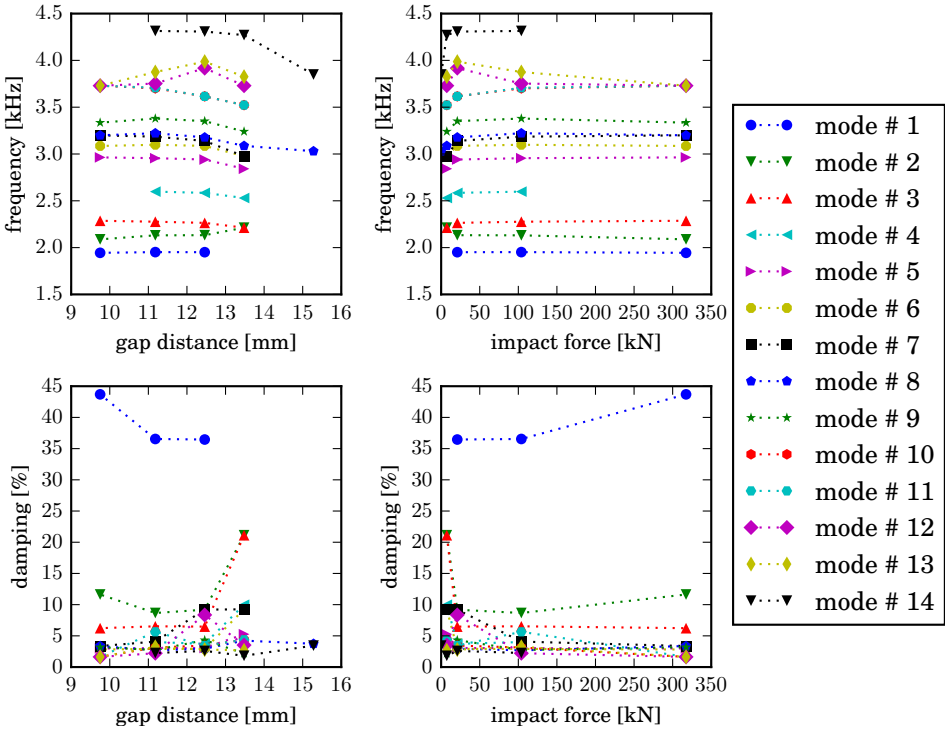

(b) frequency range 1900 - 5000 Hz

Figure D.2: Evaluation of modal properties for implant # 3

Appendix E

Modal Data Correlation Matrices

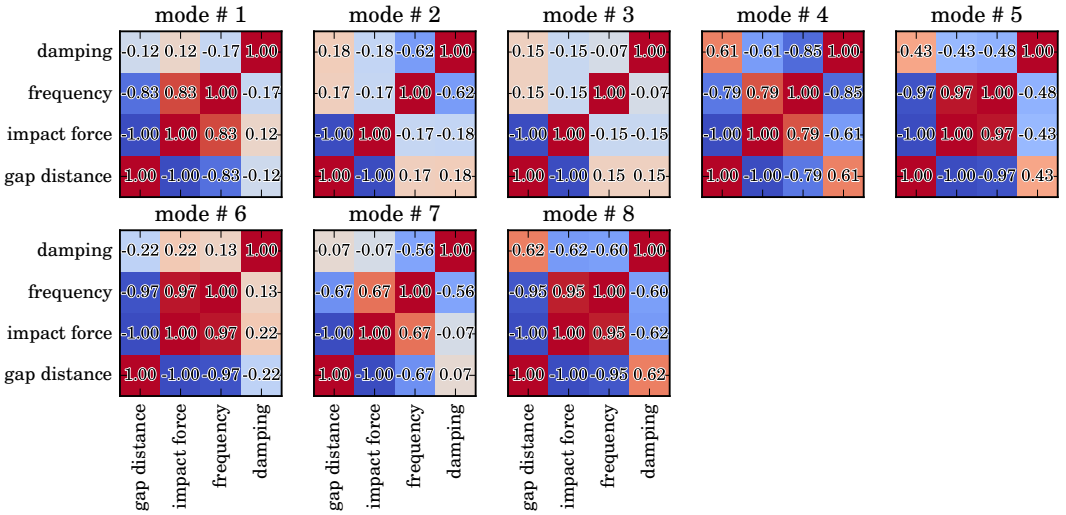

(a) frequency range 100 - 2100 Hz

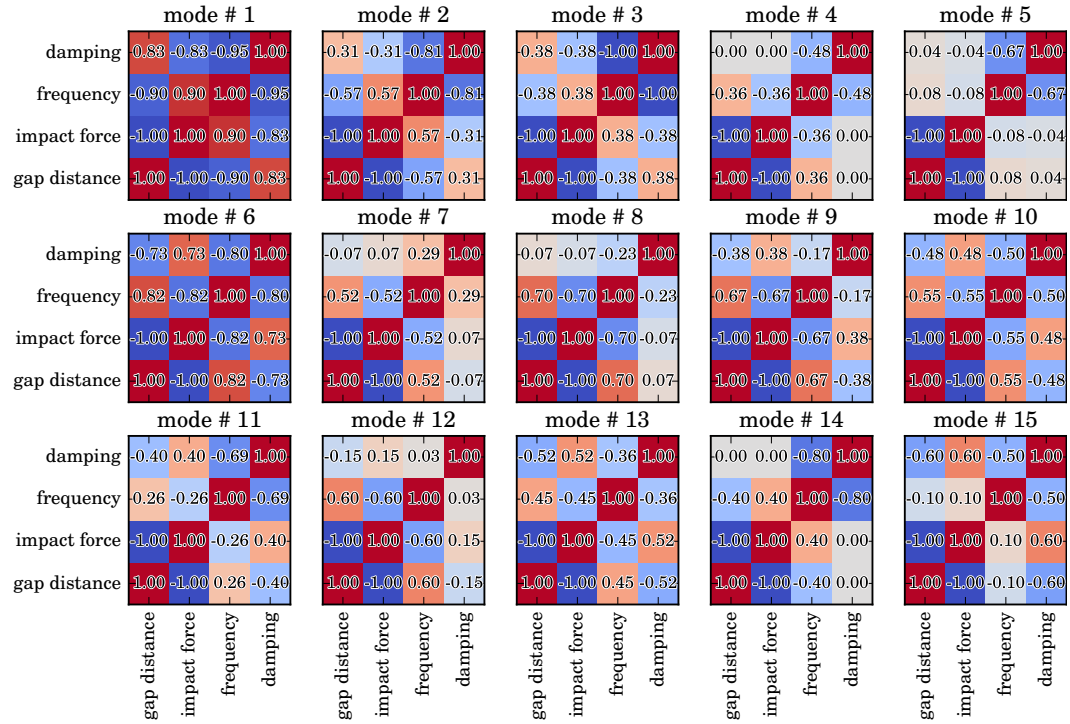

(b) frequency range 1900 - 5000 Hz

Figure E.1: Correlation of modal properties for implant # 2

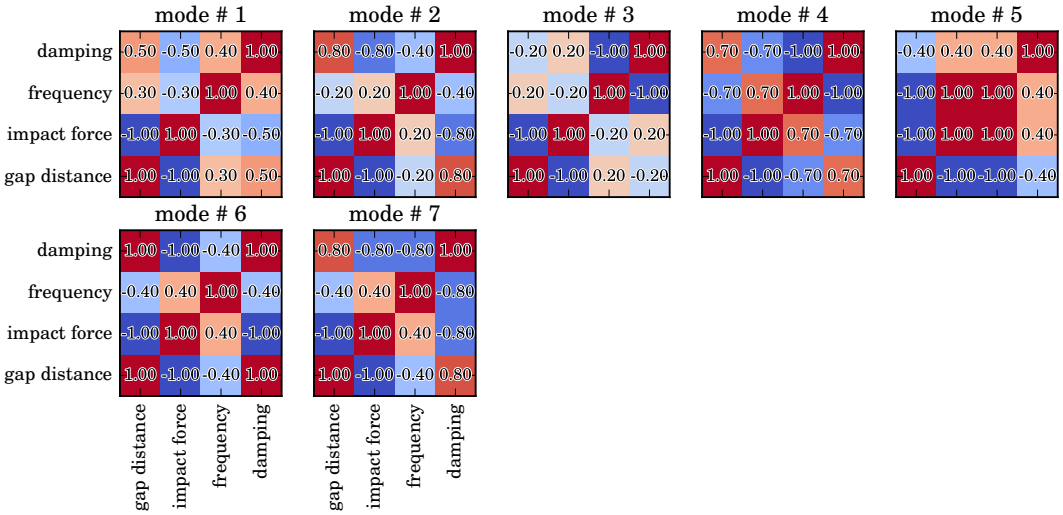

(a) frequency range 100 - 2100 Hz

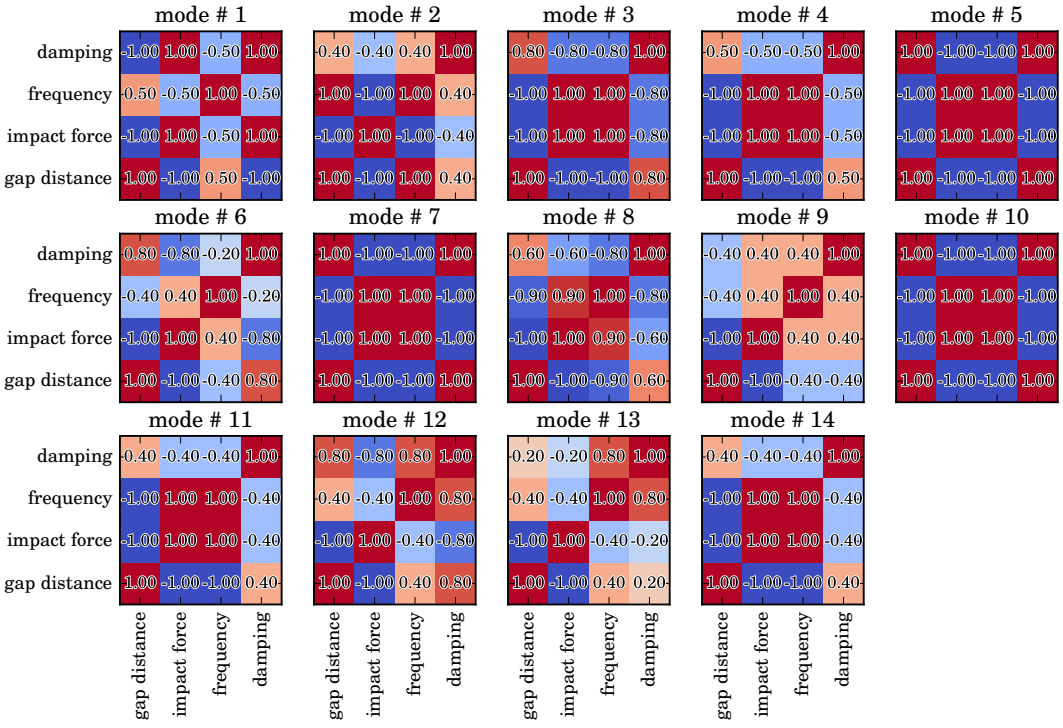

(b) frequency range 1900 - 5000 Hz

Figure E.2: Correlation of modal properties for implant # 3

Appendix F

Modal Shapes of Cups

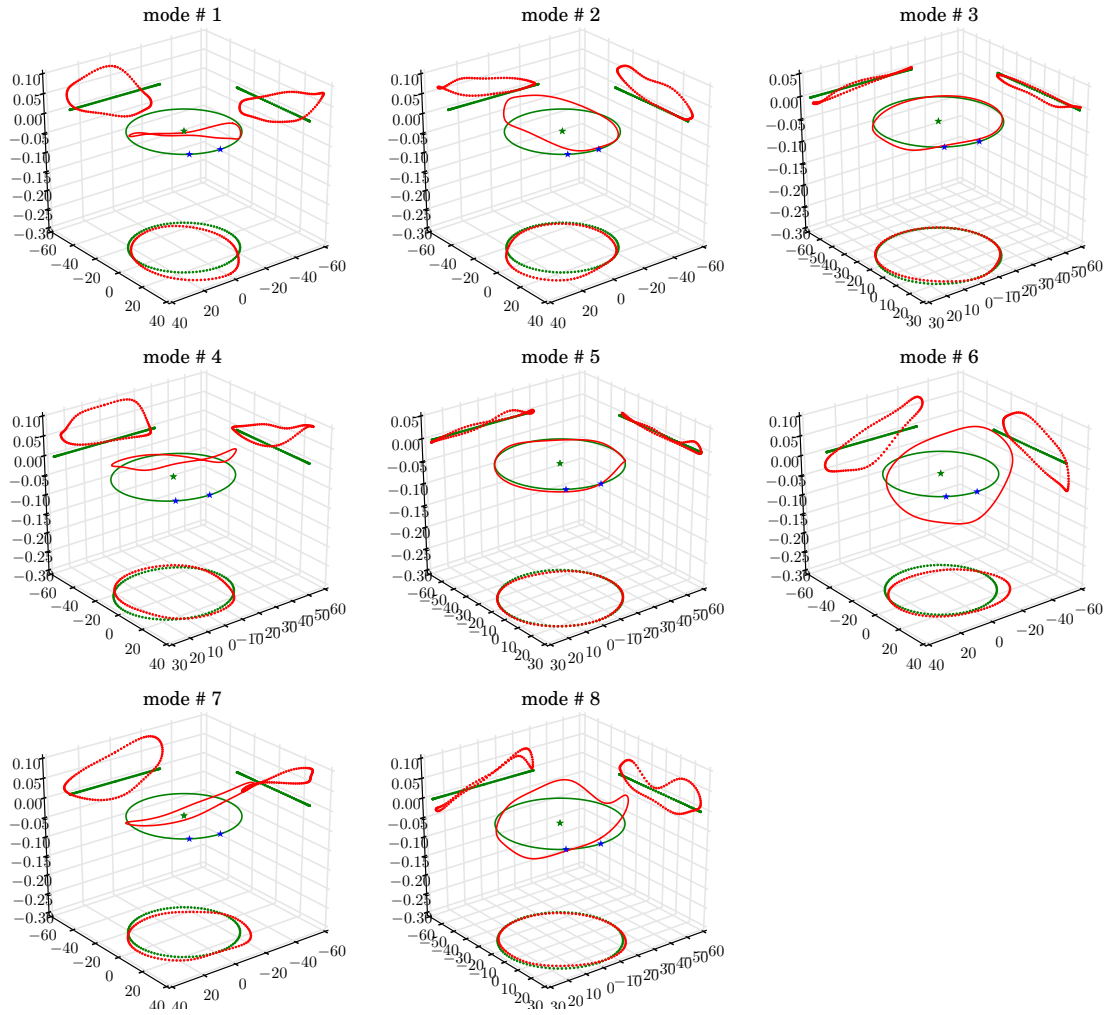

Figure F.1: Modal shape for implant # 2

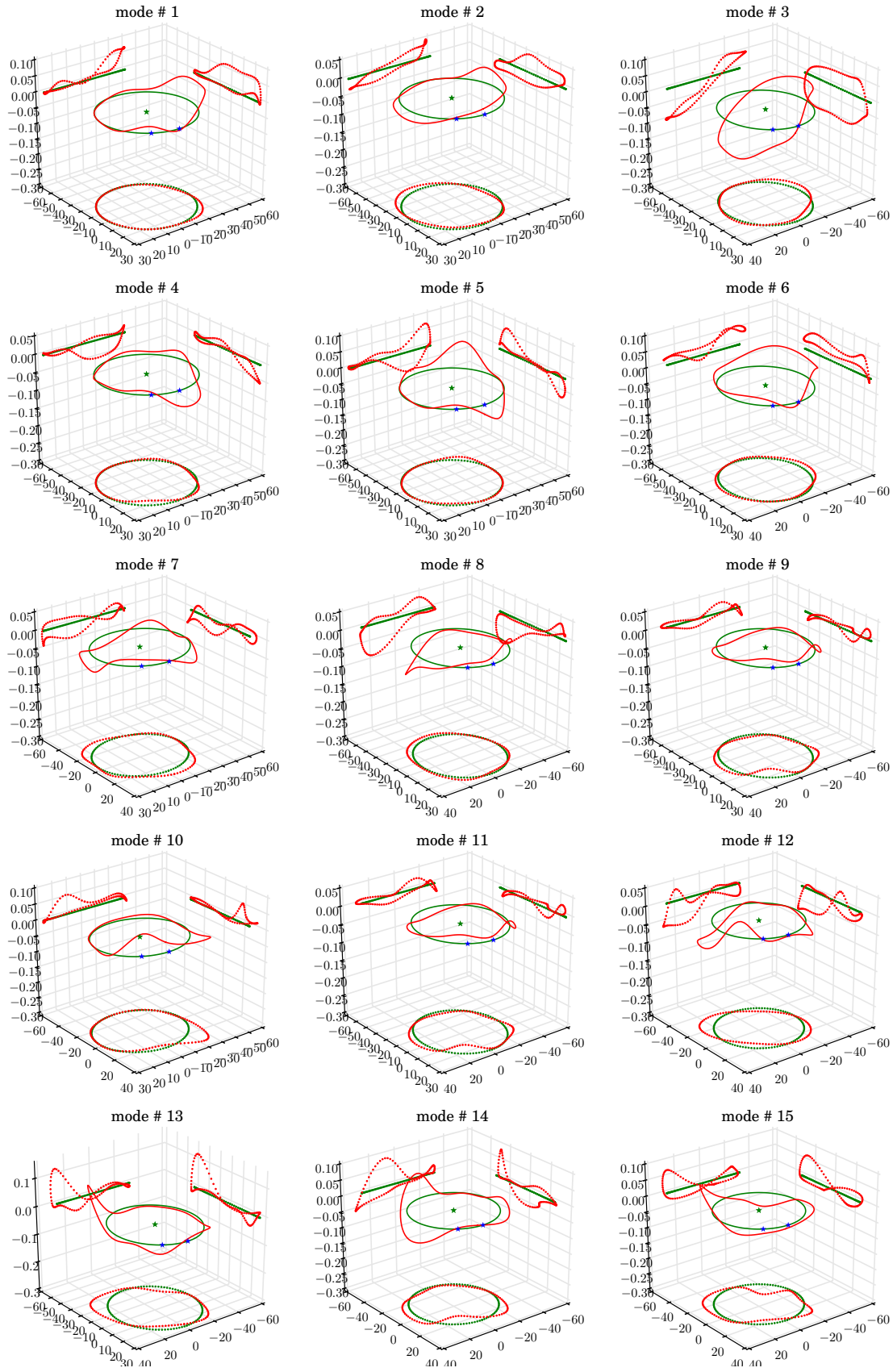

Figure F.2: Modal shape for implant # 2

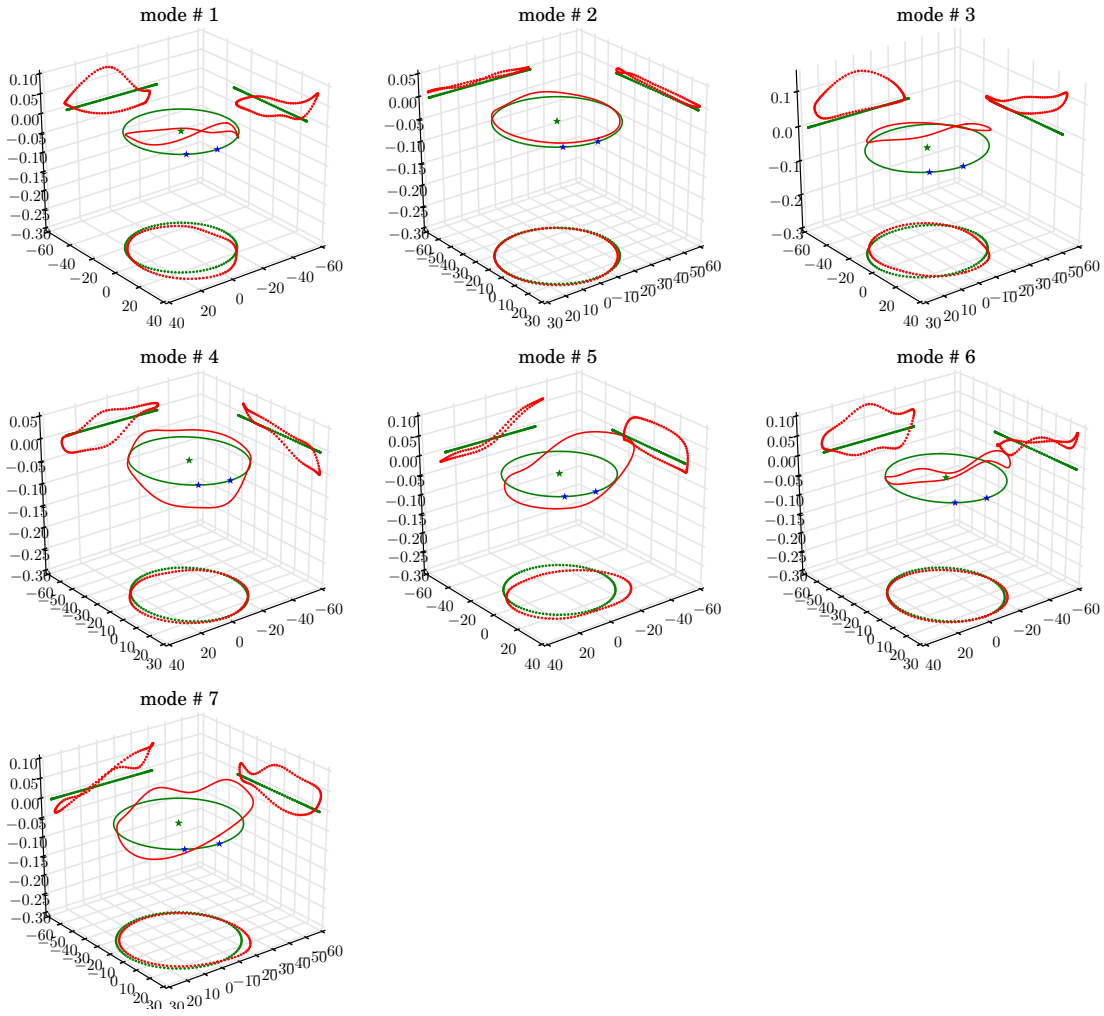

Figure F.3: Modal shape for implant # 3

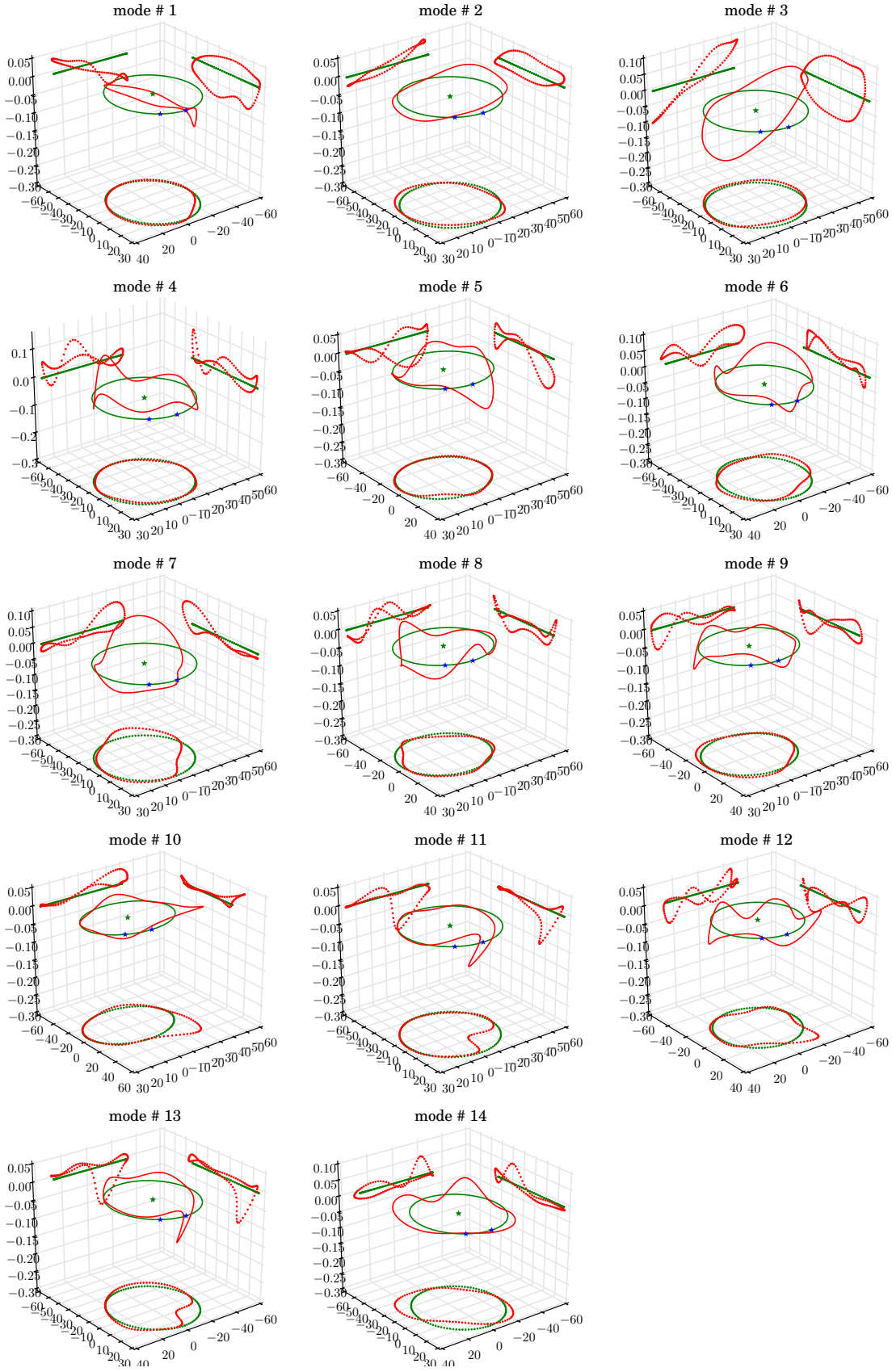

Figure F.4: Modal shape for implant # 3

Appendix G

Modal Shape Correlation Data

G.1 Model Performance

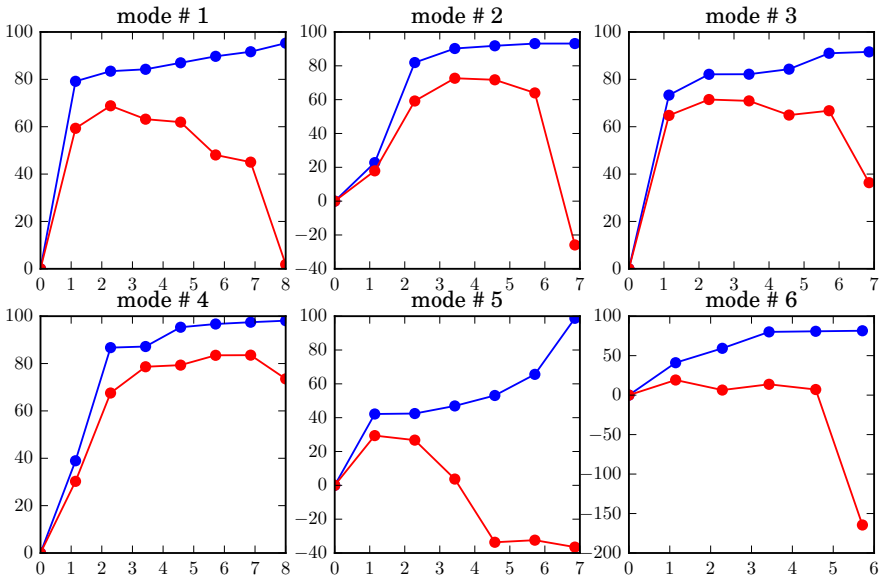

Figure G.1: Cumulative variance explained by data [%] - implant # 1 - 2100

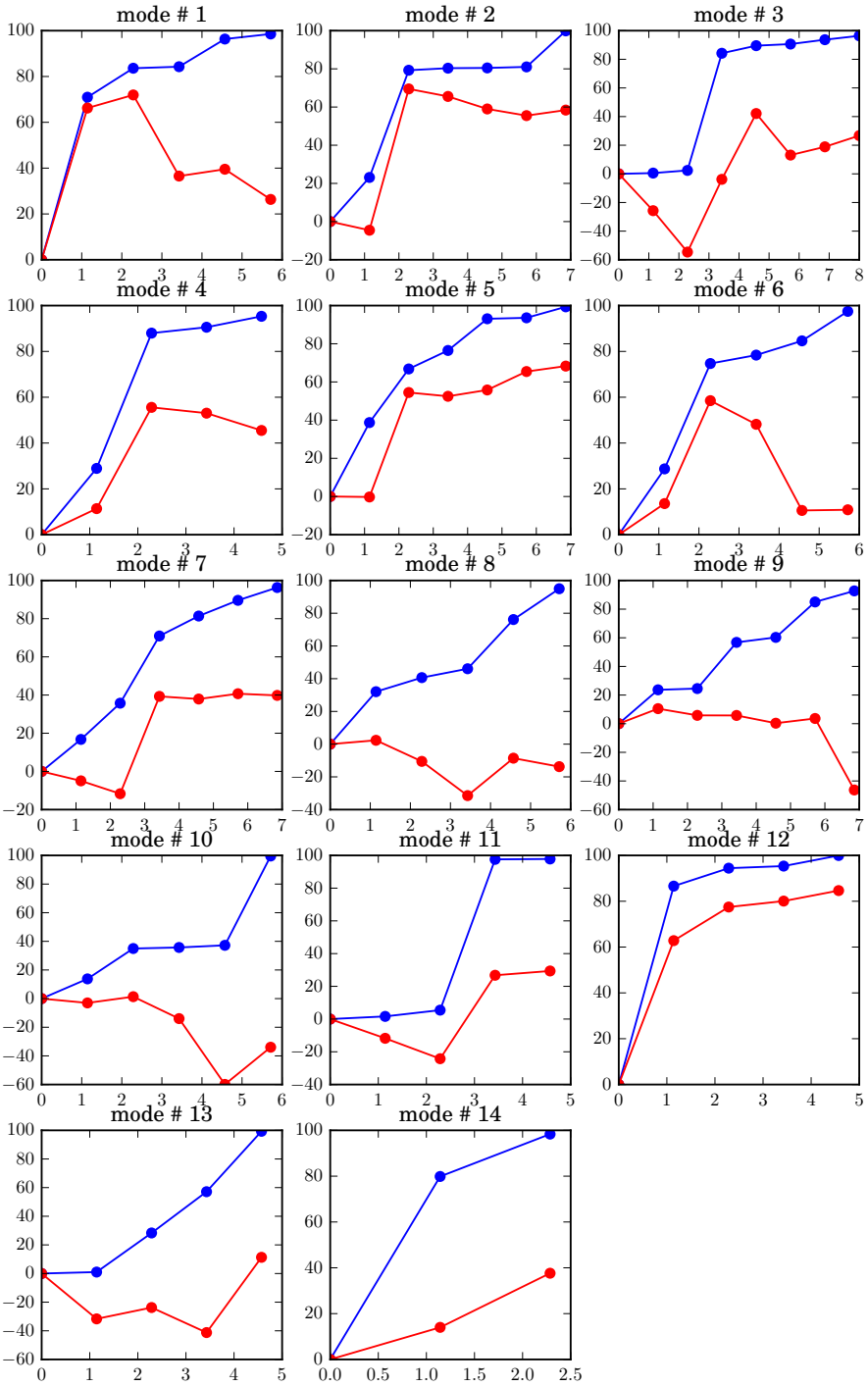

Figure G.2: Cumulative variance explained by data [%] - implant # 1 - 5000

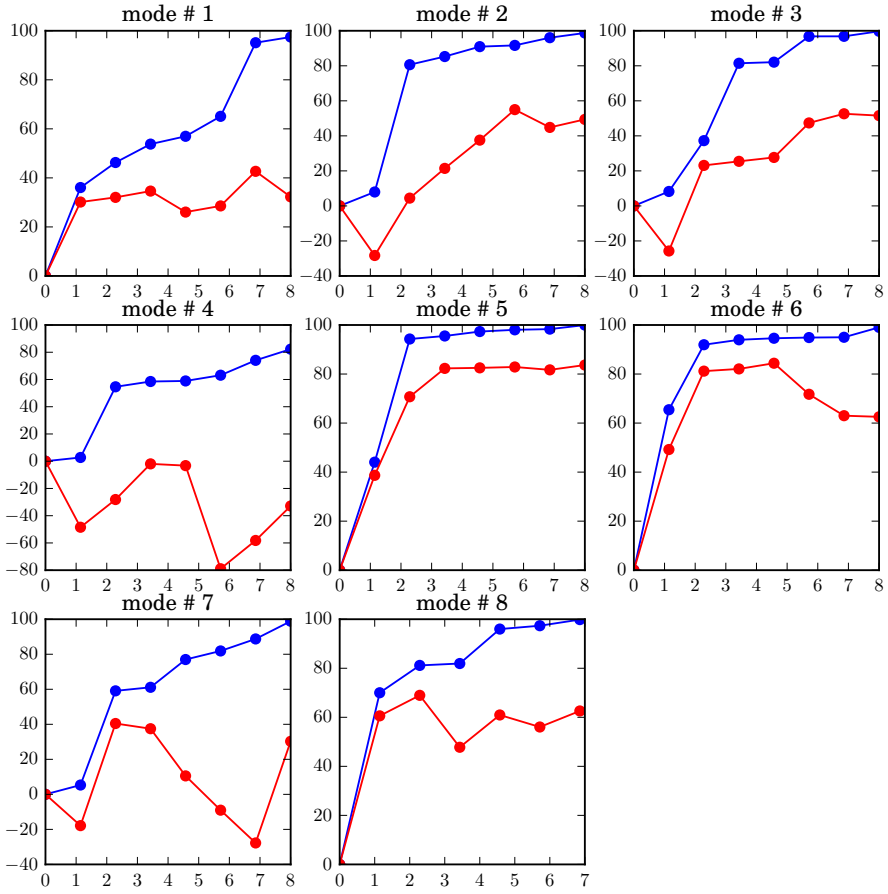

Figure G.3: Cumulative variance explained by data [%] - implant # 2 - 2100

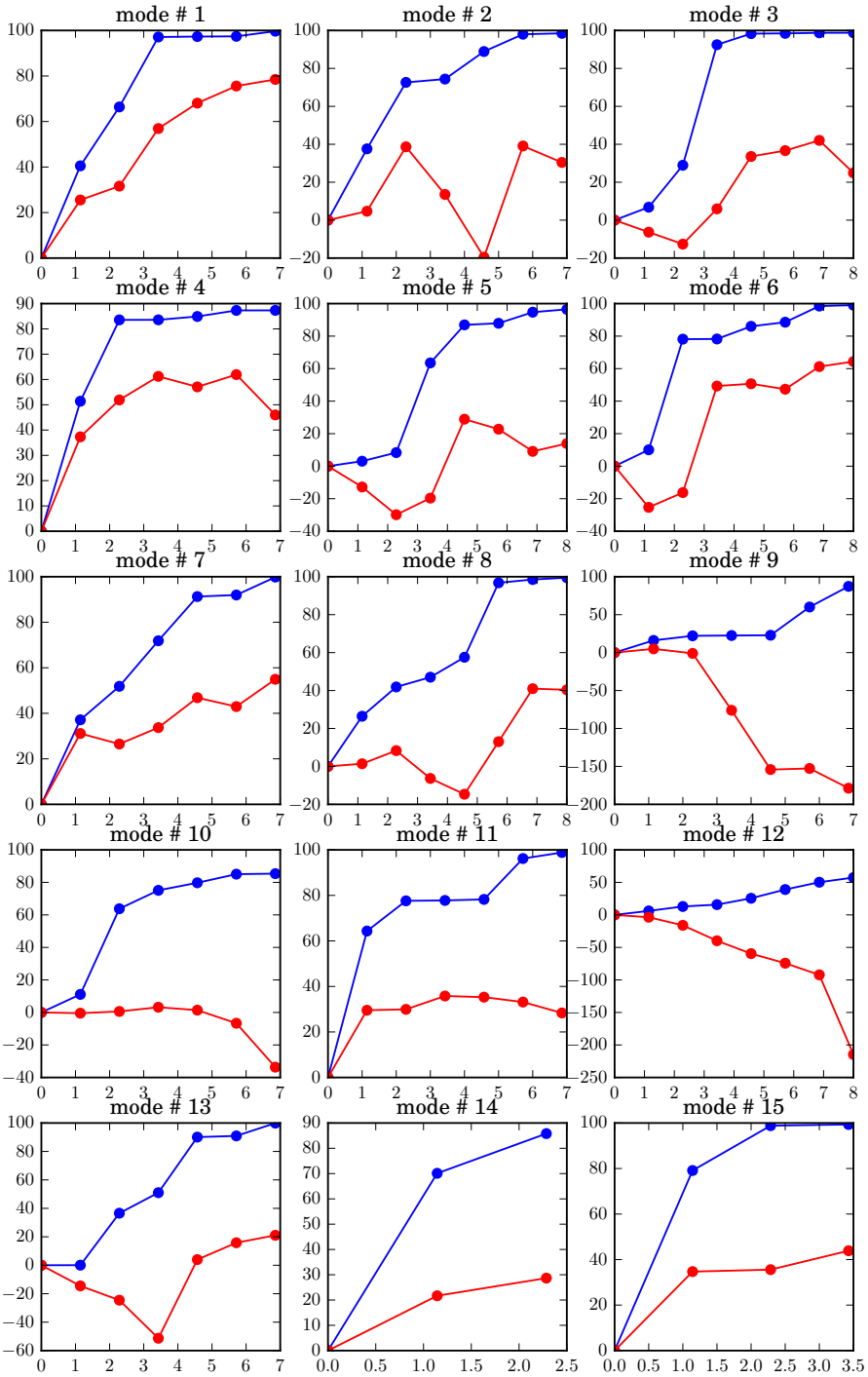

Figure G.4: Cumulative variance explained by data [%] - implant # 2 - 5000

G.2 Model Accuracy

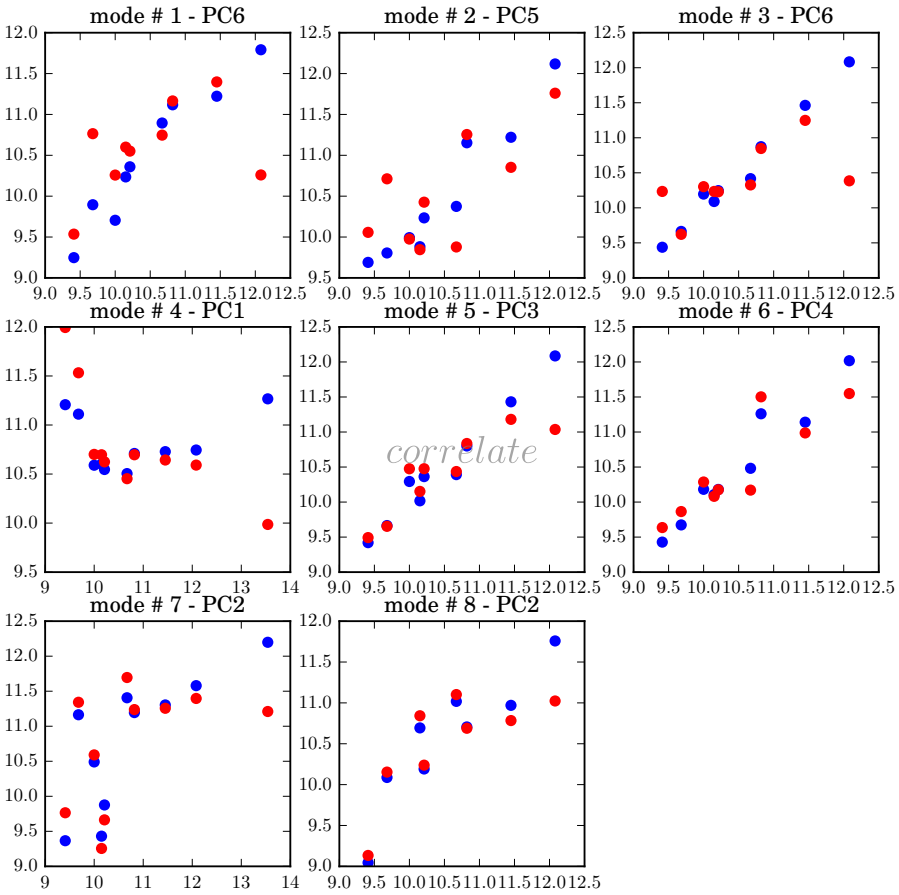

Figure G.5: Performance of PCR for implant # 2 in range 100 - 2100 Hz - gap distance [mm]

Table G.1: Regression parameters for implant # 2 - frequency range 100 - 2100 Hz and gap distance [mm]

	Calibration data				Predictive data			
# mode	Slope [-]	interp. [mm]	RMSE [mm]	R^2[−]	Slope [-]	interp. [mm]	RMSE [mm]	R^2[−]
1.	0.92	0.83	0.22	0.92	0.27	7.65	0.74	0.32
2.	0.92	0.75	0.21	0.92	0.56	4.63	0.56	0.61
3.	0.98	0.20	0.11	0.98	0.32	6.99	0.65	0.48
4.	0.05	10.24	1.15	0.05	-0.33	14.43	1.63	-
5.	0.96	0.36	0.15	0.96	0.60	4.09	0.41	0.79
6.	0.93	0.65	0.20	0.93	0.72	2.94	0.39	0.81
7.	0.58	4.43	0.76	0.59	0.33	7.12	1.07	0.34
8.	0.81	2.02	0.36	0.81	0.53	4.82	0.56	0.65

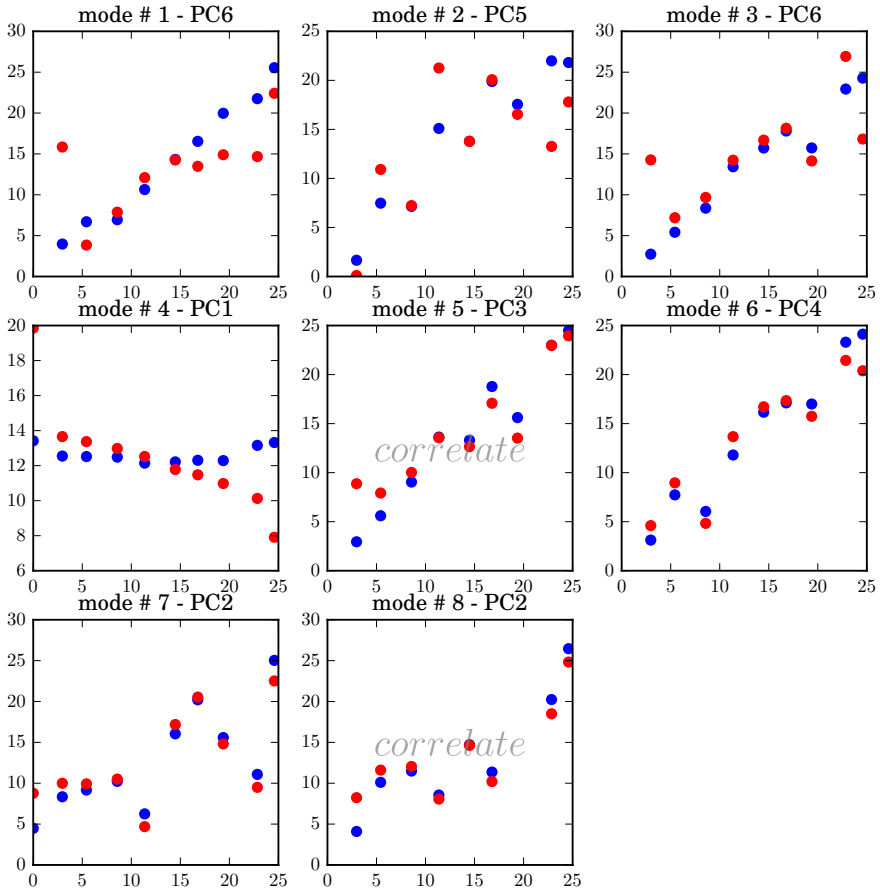

Figure G.6: Performance of PCR for implant # 2 in range 100 - 2100 Hz - impact force [kN]

Table G.2: Regression parameters for implant # 2 - frequency range 100 - 2100 Hz and impact force [N]

	Calibration data				Predictive data			
# mode	Slope [-]	interp. [N]	RMSE [N]	R^2[−]	Slope [-]	interp. [N]	RMSE [N]	R^2[−]
1.	0.98	254.31	960.94	0.98	0.44	7.02e3	5.49e3	0.53
2.	0.90	1.33e3	2.21e3	0.90	0.57	5.43e3	5.79e3	0.49
3.	0.96	622.71	1.51e3	0.95	0.51	8.31e3	5.28e3	0.57
4.	0.01	1.26e4	7.96e3	0.01	-0.32	1.68e4	1.06e4	-
5.	0.94	764.13	1.66e3	0.94	0.71	4.65e3	3.09e3	0.85
6.	0.95	640.72	1.52e3	0.95	0.76	2.99e3	2.83e3	0.87
7.	0.59	5.14e3	5.09e3	0.59	0.39	7.78e3	6.48e3	0.45
8.	0.81	2.48e3	3.14e3	0.81	0.59	5.61e3	4.34e3	0.75

Table G.3: Regression parameters for implant # 2 - frequency range 2100 - 5000 Hz and gap distance [mm]

	Calibration data				Predictive data			
# mode	Slope [-]	interp. [mm]	RMSE [mm]	R^2[−]	Slope [-]	interp. [mm]	RMSE [mm]	R^2[−]
1.	0.99	0.01	0.02	0.99	0.52	4.92	0.29	0.82
2.	0.70	3.15	0.45	0.70	0.15	8.81	0.79	0.30
3.	0.98	0.12	0.13	0.99	0.11	9.42	0.12	0.23
4.	0.78	2.23	0.38	0.78	0.46	5.73	0.61	0.58
5.	0.91	0.99	0.36	0.91	0.11	9.32	1.15	0.24
6.	0.99	0.03	0.06	0.99	0.50	5.47	0.86	0.61
7.	0.99	3.49e-6	2.56e-4	0.99	0.394	6.13	0.50	0.49
8.	0.99	0.09	0.07	0.99	0.24	7.94	0.70	0.40
9.	0.16	8.77	0.77	0.16	-0.06	11.07	0.93	0.06
10.	0.82	1.92	0.51	0.82	-0.08	11.65	1.39	-
11.	0.86	1.42	0.45	0.86	0.19	8.32	1.14	0.35
12.	0.05	10.26	1.16	0.05	-0.11	12.02	1.33	-
13.	0.99	2.08e-6	1.95e-4	0.99	0.17	8.41	0.57	0.33
14.	0.79	2.11	0.30	0.79	-0.14	11.84	0.79	0.20
15.	0.98	0.12	0.08	0.99	0.06	9.59	0.69	0.41

Table G.4: Regression parameters for implant # 2 - frequency range 2100 - 5000 Hz and impact force [N]

	Calibration data				Predictive data			
# mode	Slope [-]	interp. [N]	RMSE [N]	R^2[−]	Slope [-]	interp. [N]	RMSE [N]	R^2[−]
1.	0.99	81.01	458.95	0.99	0.52	6.62e3	3.61e3	0.75
2.	0.75	3.33e3	3.64e3	0.75	0.29	1.04e3	6.08e3	0.47
3.	0.98	162.35	942.89	0.98	0.43	6.91e3	5.65e3	0.61
4.	0.88	1.56e3	2.49e3	0.88	0.46	6.72e3	4.99e3	0.64
5.	0.82	2.14e3	3.28e3	0.82	0.23	1.11e3	7.21e3	0.33
6.	0.98	192.88	1.01e3	0.98	0.48	6.63e3	5.14e3	0.67
7.	0.99	49.26	357.90	0.99	0.51	8.47e3	4.52e3	0.61
8.	0.97	287.78	1.02e3	0.97	0.24	1.05e4	6.12e3	0.42
9.	0.16	1.23e4	6.67e3	0.16	-0.07	1.59e4	8.19e3	0.03
10.	0.68	4.14e3	4.44e3	0.68	-0.06	1.35e4	8.69e3	0.06
11.	0.69	4.44e3	4.41e3	0.69	0.21	1.23e4	7.22e3	0.36
12.	0.07	1.17e4	7.68e3	0.07	-0.11	1.36e4	9.08e3	nan
13.	0.99	27.99	269.80	0.99	0.04	1.56e4	6.91e3	0.08
14.	0.92	1.23e3	1.84e3	0.92	-0.02	1.59e4	6.94e3	0.36
15.	0.99	12.36	200.60	0.99	0.08	1.44e4	6.55e3	0.46

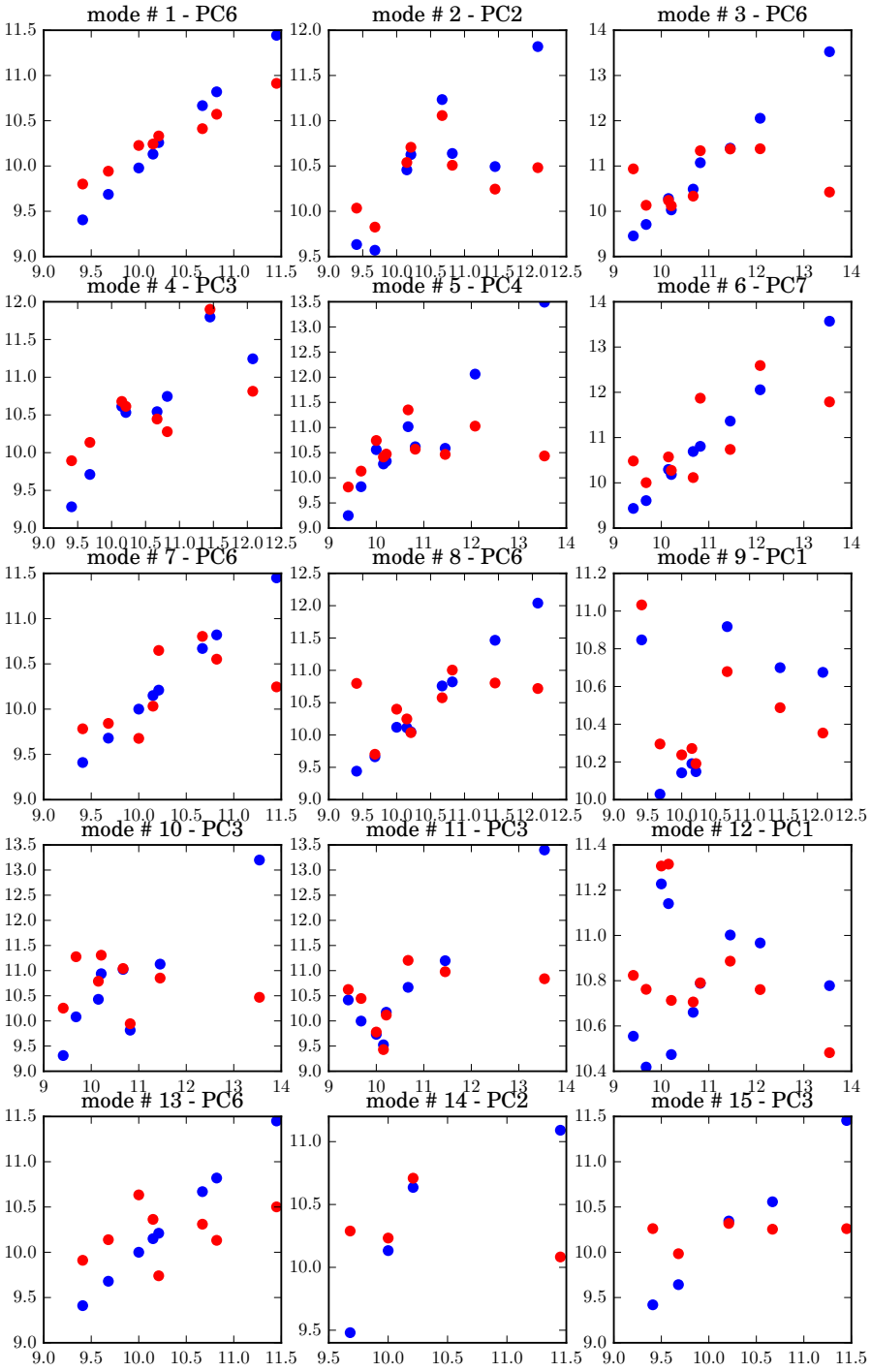

Figure G.7: Performance of PCR for implant # 2 in range 2100 - 5000 Hz - gap distance [mm]

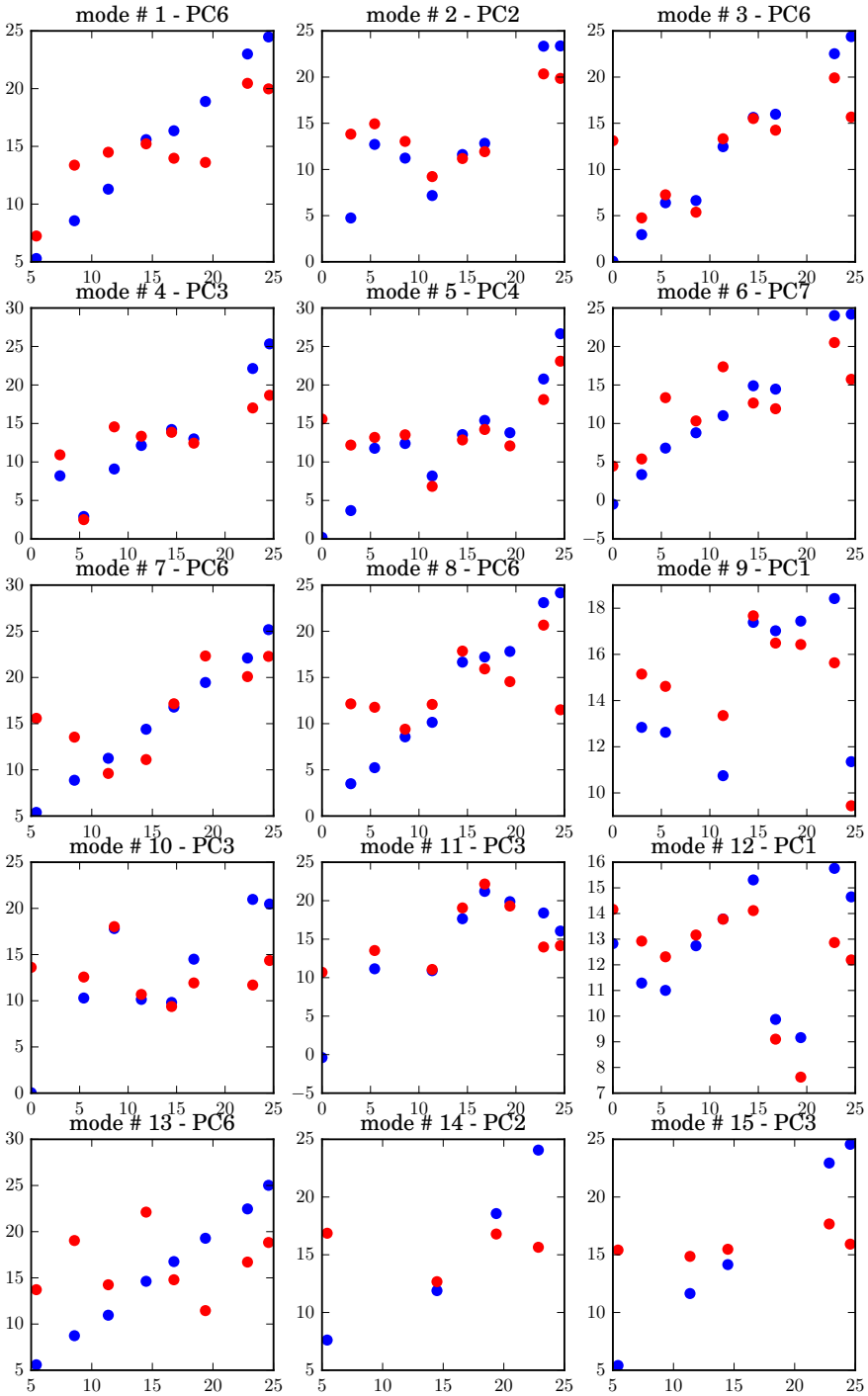

Figure G.8: Performance of PCR for implant # 2 in range 2100 - 5000 Hz - impact force [kN]

Appendix H

Raw FRF Correlation Data

H.1 Model Performance

H.1.1 Radial DOFs

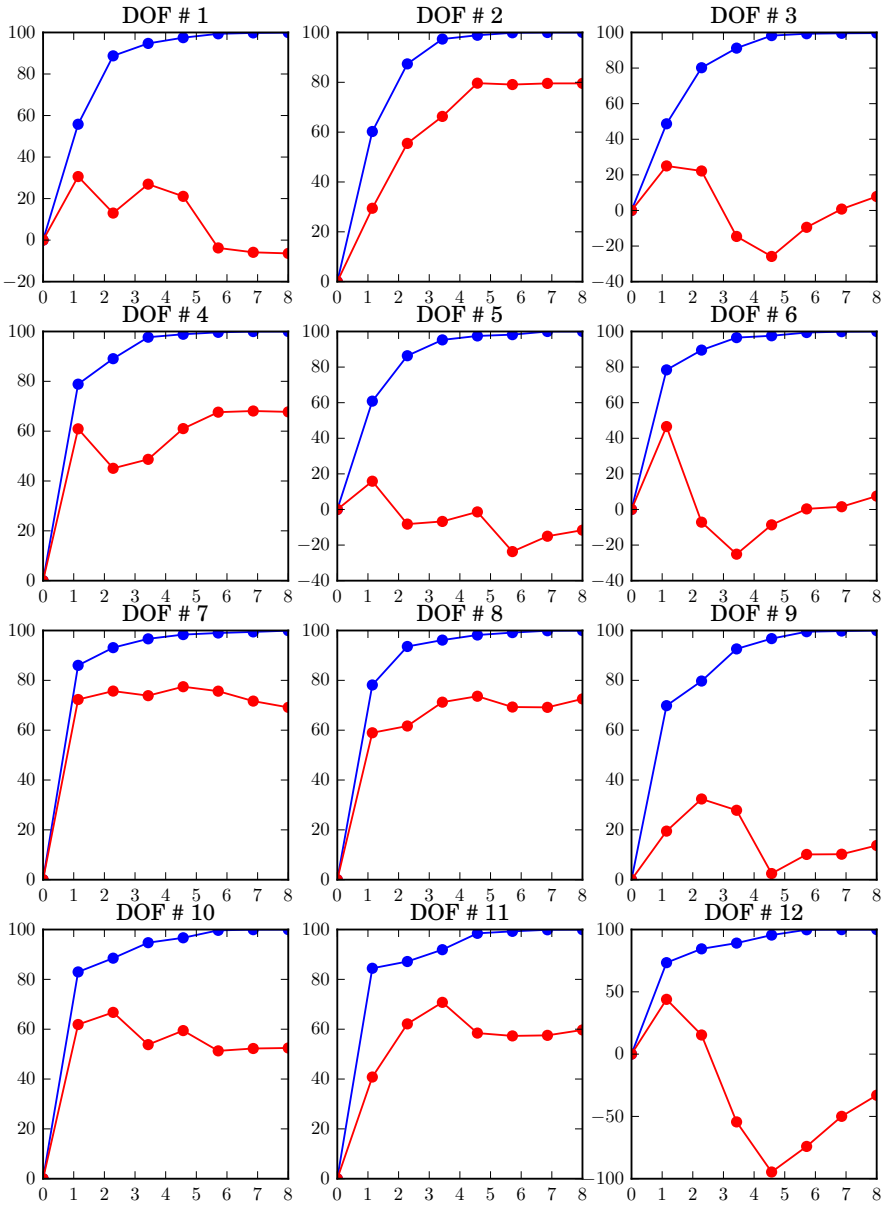

Figure H.1: Cumulative variance explained by data [%] - implant # 1 - 2100 - rad. DOF

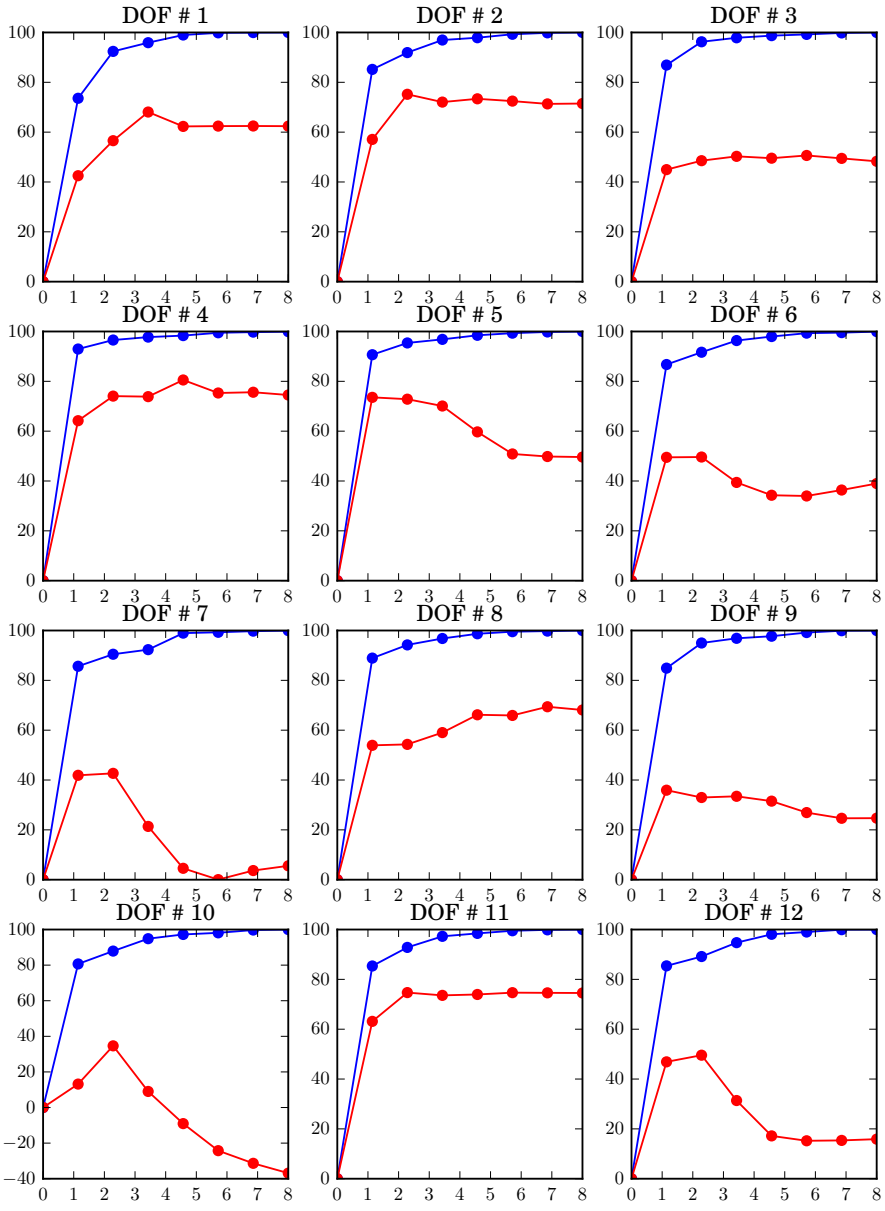

Figure H.2: Cumulative variance explained by data [%] - implant # 1 - 5000 - rad. DOF

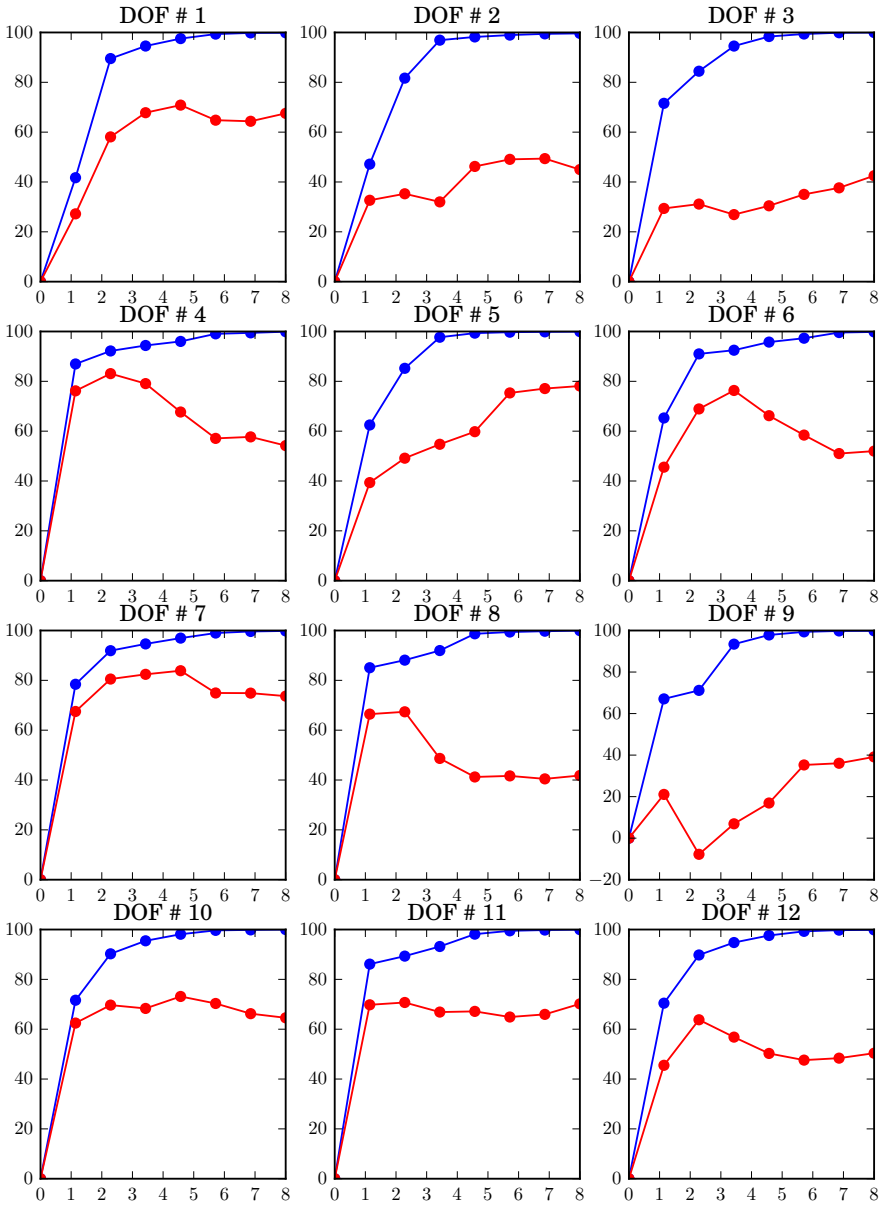

Figure H.3: Cumulative variance explained by data [%] - implant # 2 - 2100 - rad. DOF

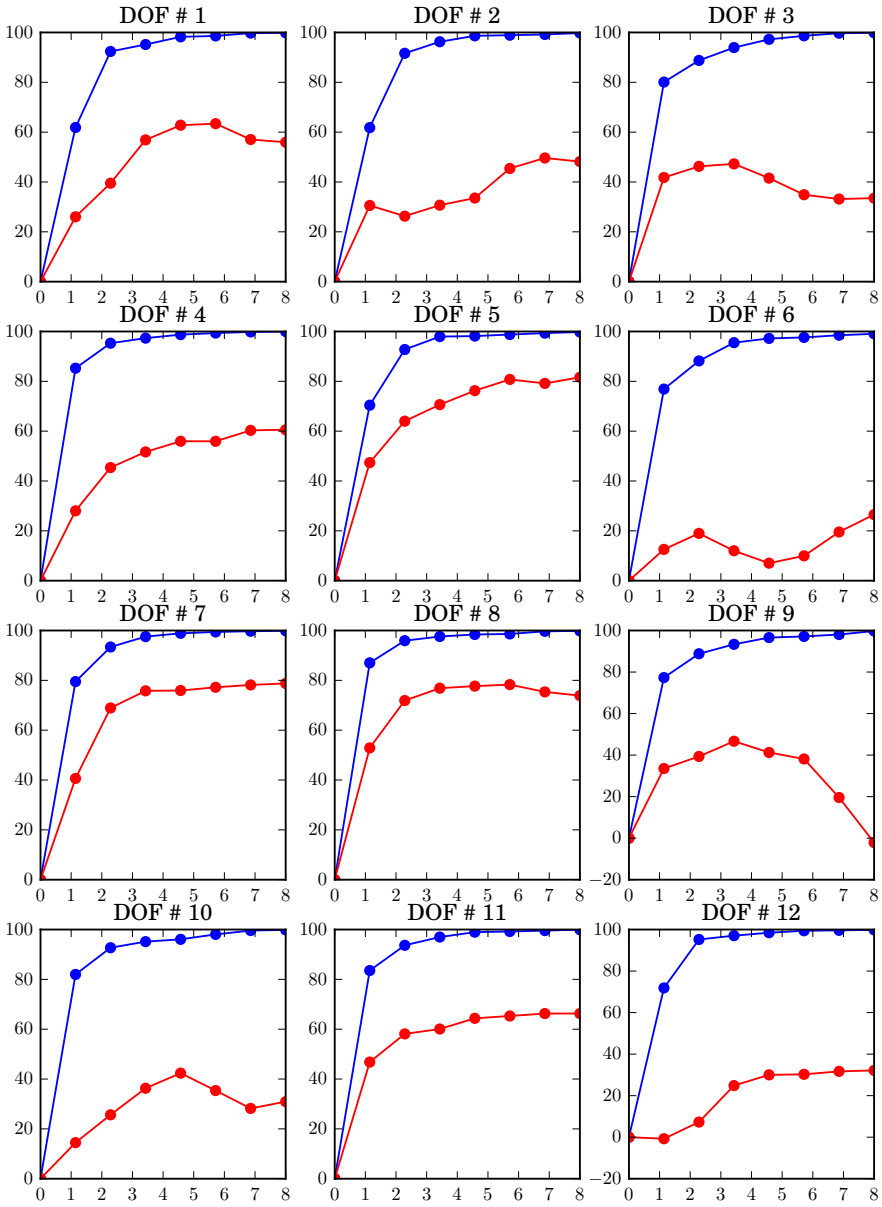

Figure H.4: Cumulative variance explained by data [%] - implant # 2 - 5000 - rad. DOF

H.1.2 Axial DOFs

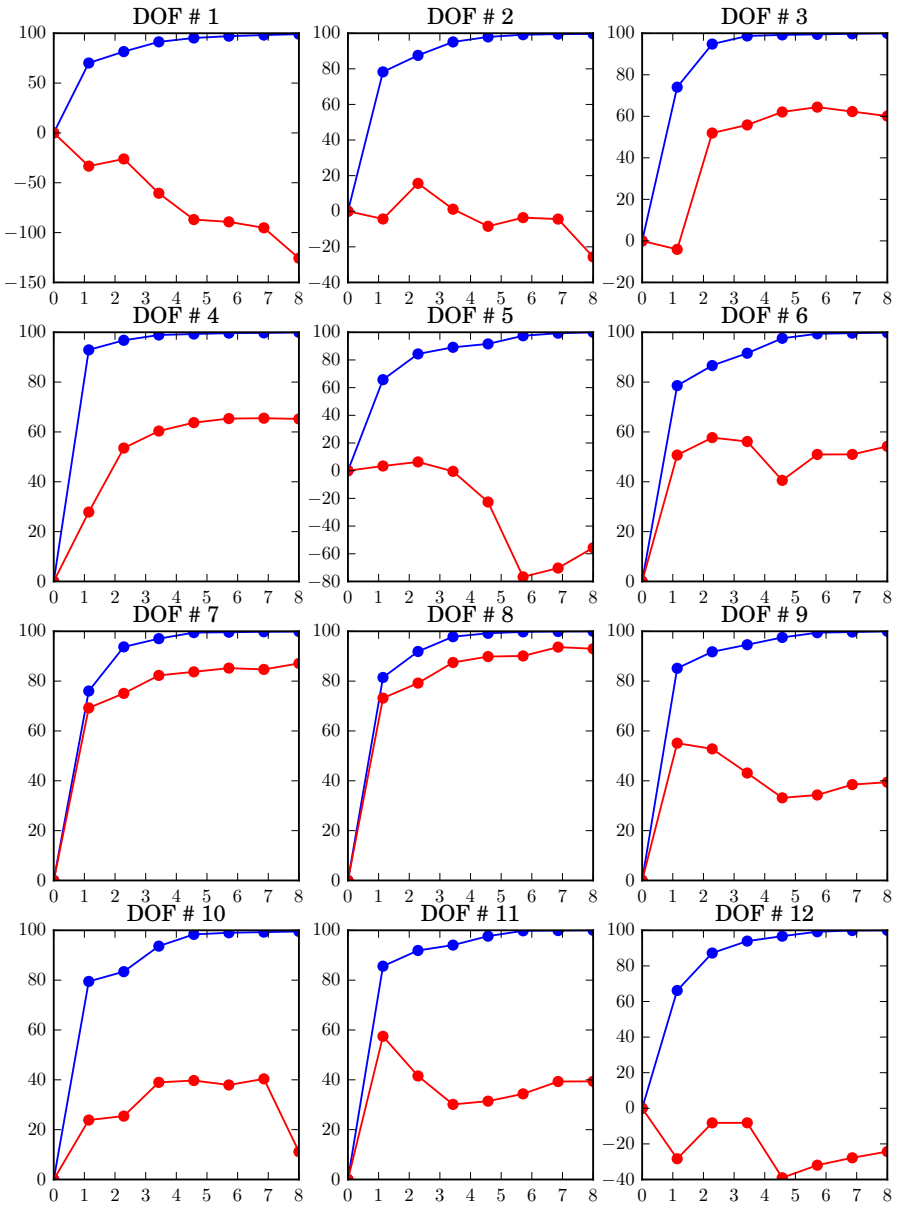

Figure H.5: Cumulative variance explained by data [%] - implant # 1 - 2100 - ax. DOF

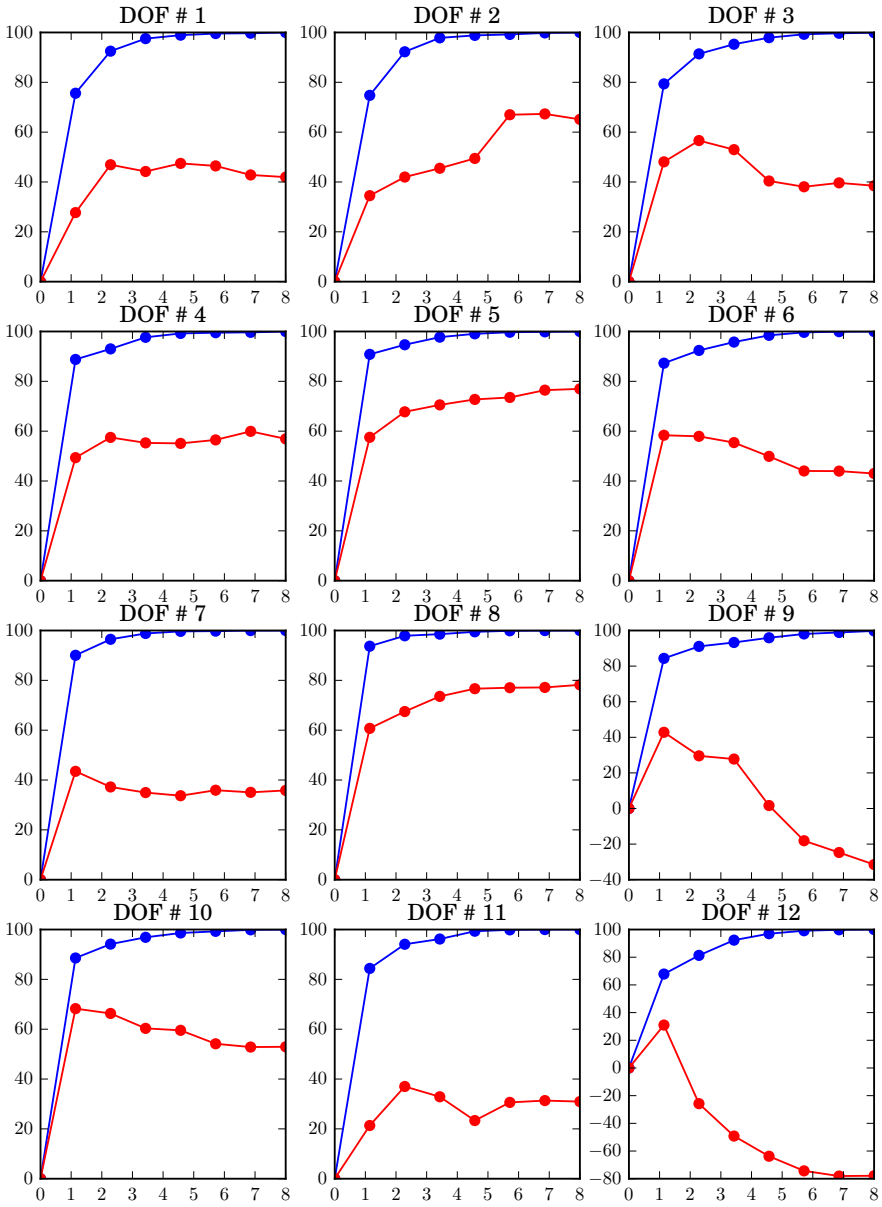

Figure H.6: Cumulative variance explained by data [%] - implant # 1 - 5000 - ax. DOF

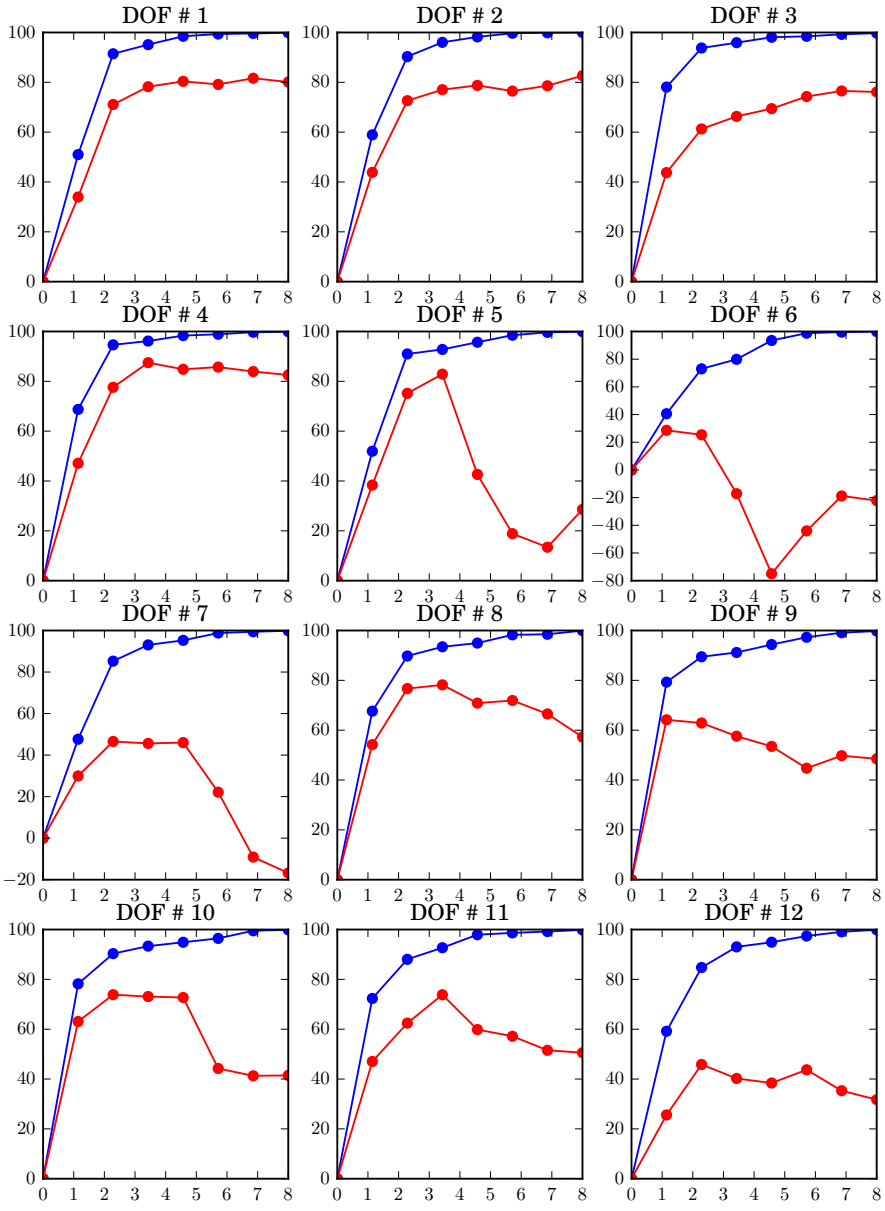

Figure H.7: Cumulative variance explained by data [%] - implant # 2 - 2100 - ax. DOF

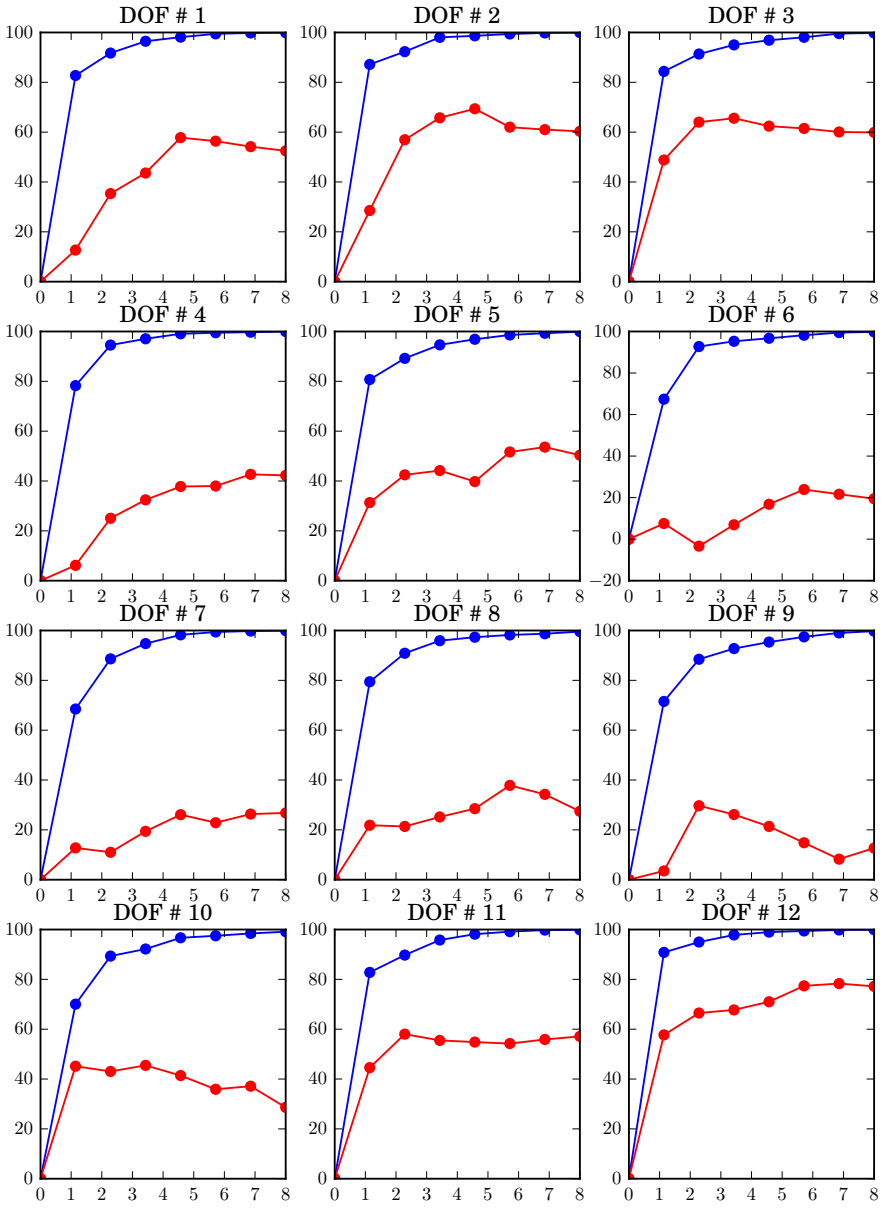

Figure H.8: Cumulative variance explained by data [%] - implant # 2 - 5000 - ax. DOF

H.2 Model Accuracy

H.2.1 Radial DOFs

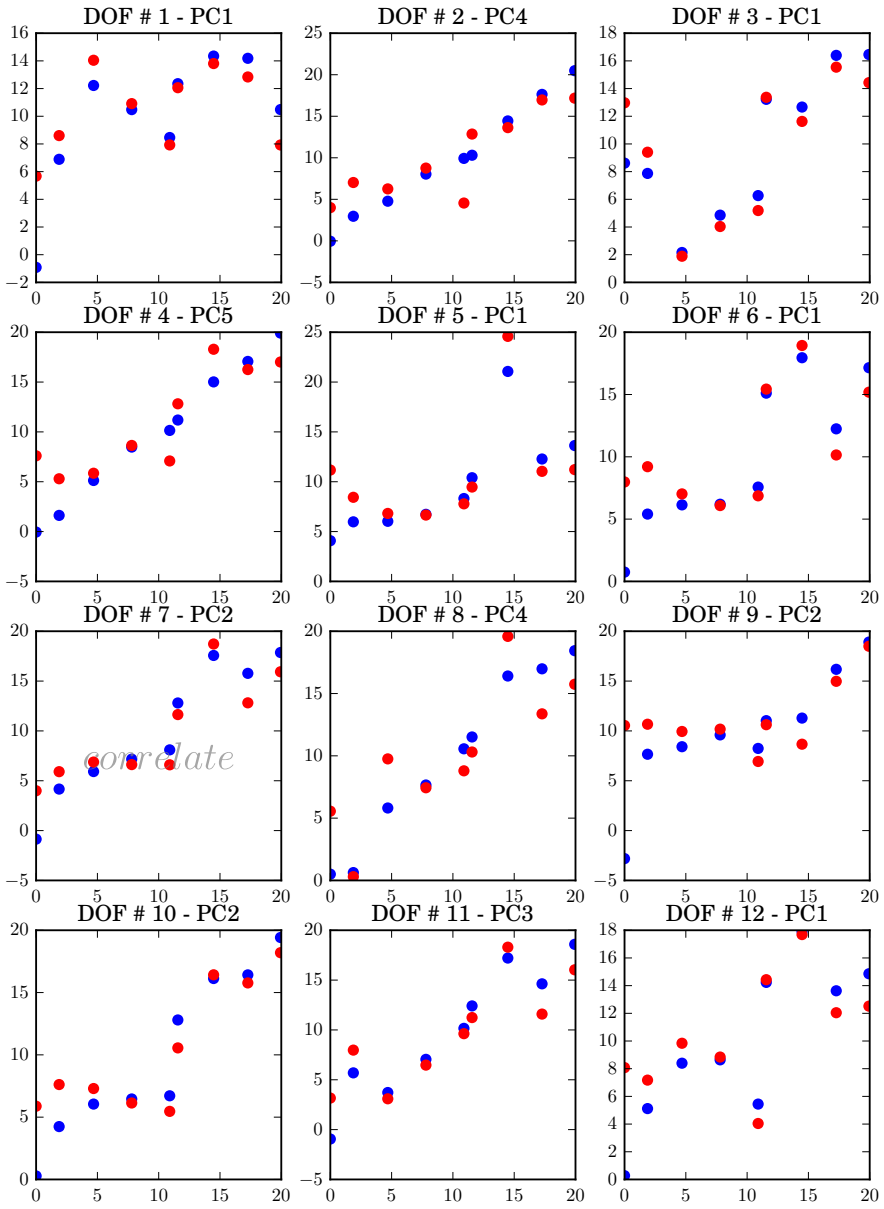

Figure H.9: Performance of PLSR for implant # 1 - 2100 - rad. DOF - polar gap distance [mm]

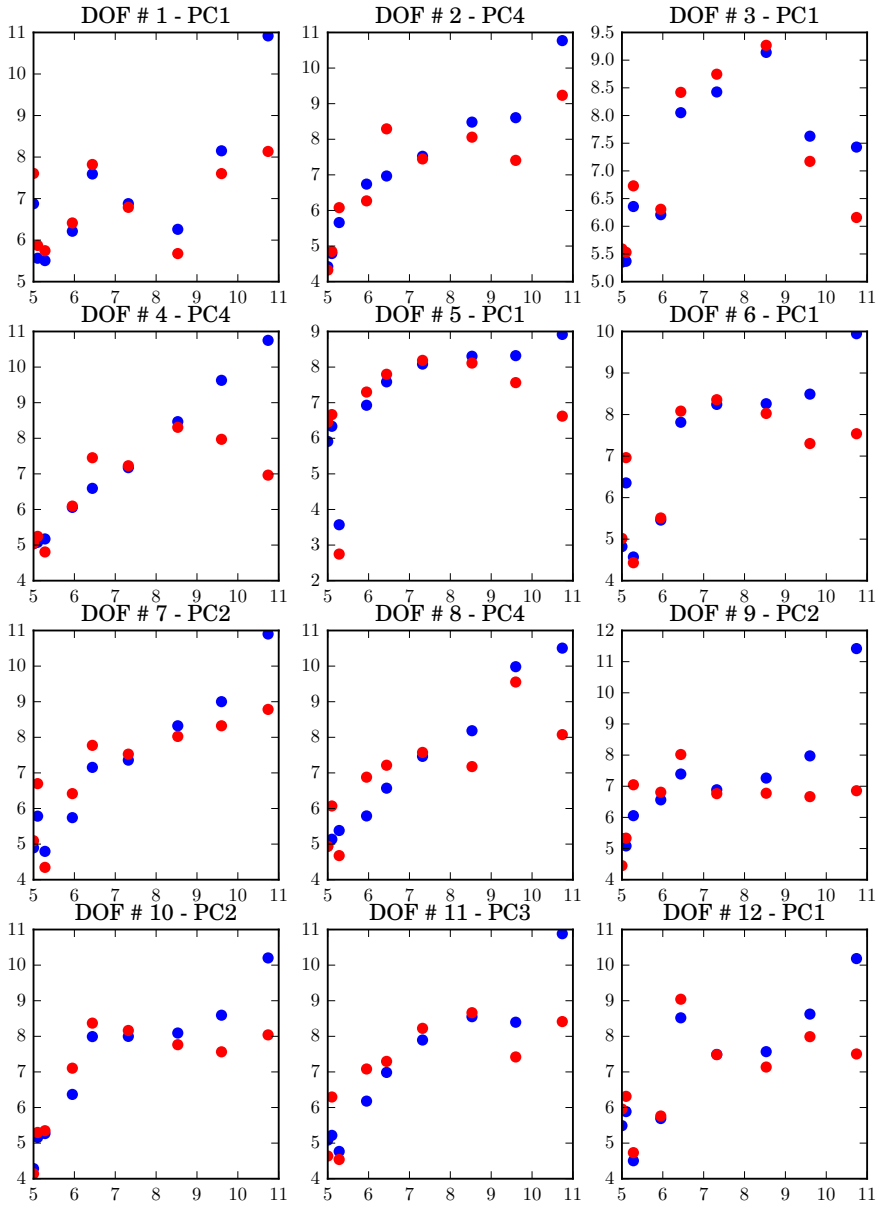

Figure H.10: Performance of PLSR for implant # 1 - 2100 - rad. DOF - impact force [N]

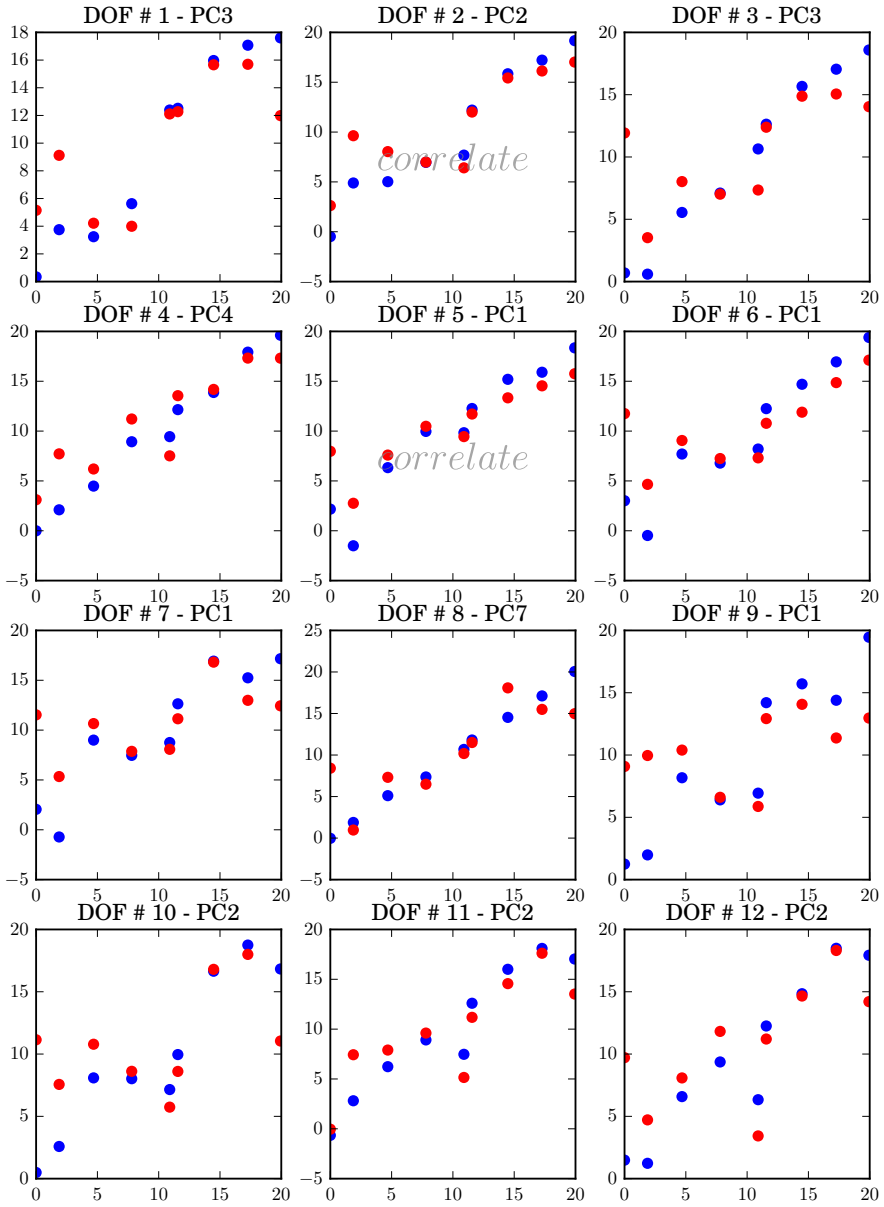

Figure H.11: Performance of PLSR for implant # 1 - 5000 - rad. DOF - polar gap distance [mm]

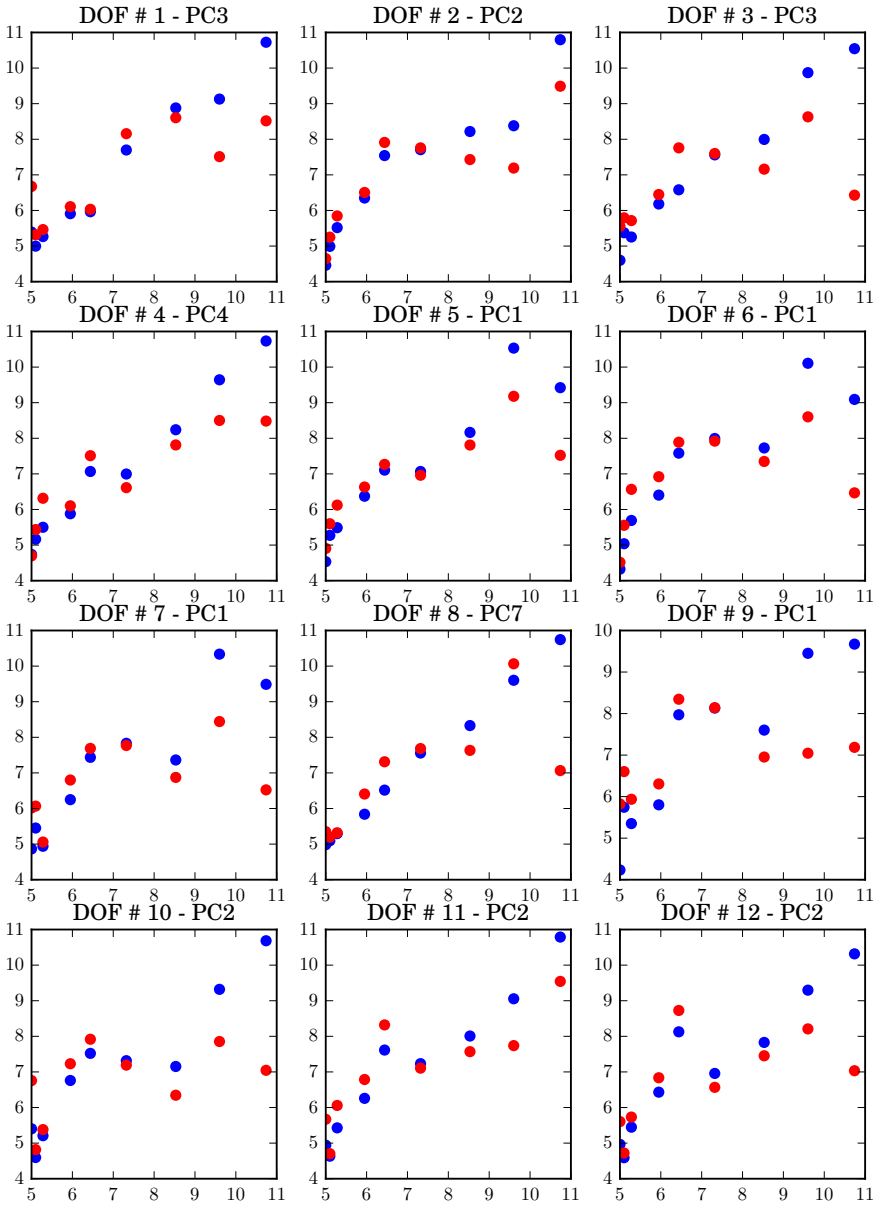

Figure H.12: Performance of PLSR for implant # 1 - 5000 - rad. DOF - impact force [N]

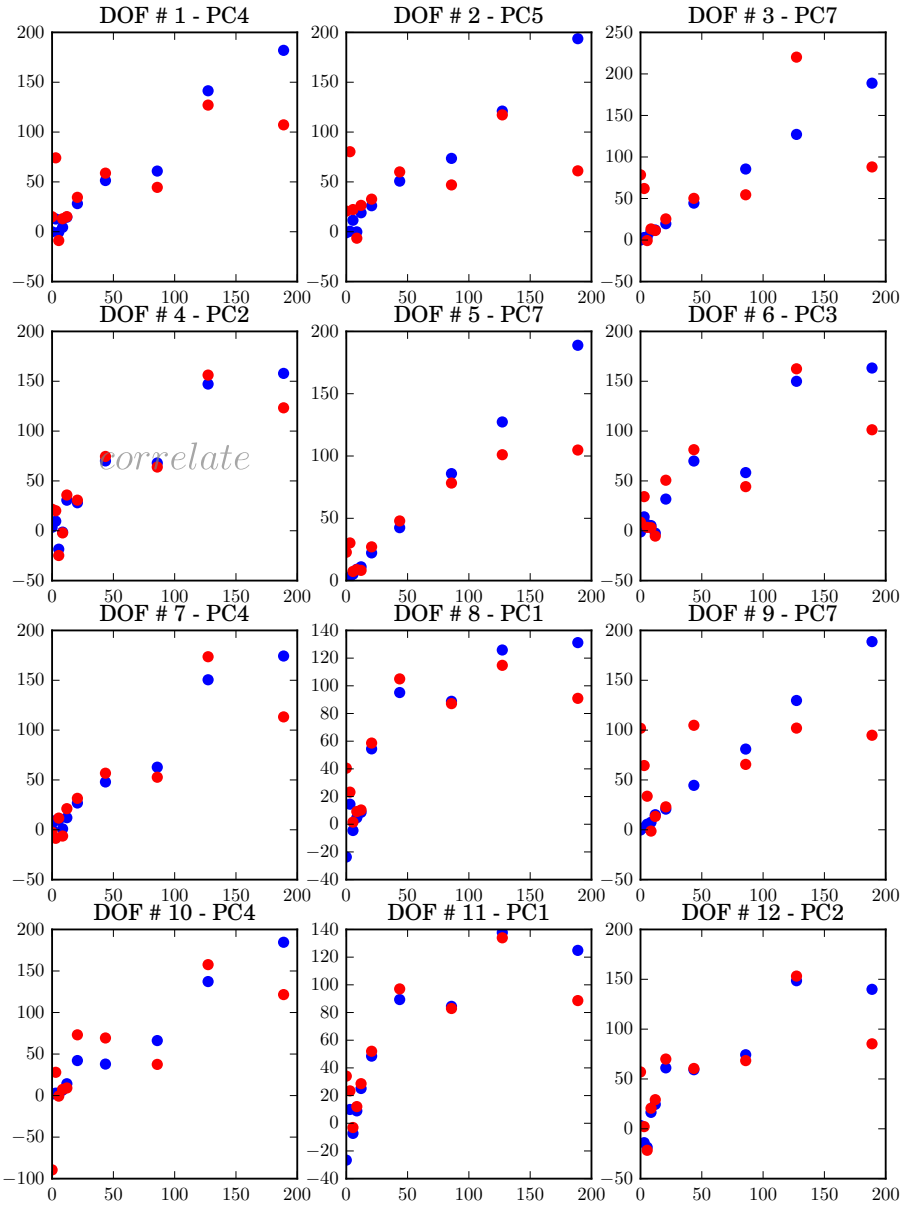

Figure H.13: Performance of PLSR for implant # 2 - 2100 - rad. DOF - polar gap distance [mm]

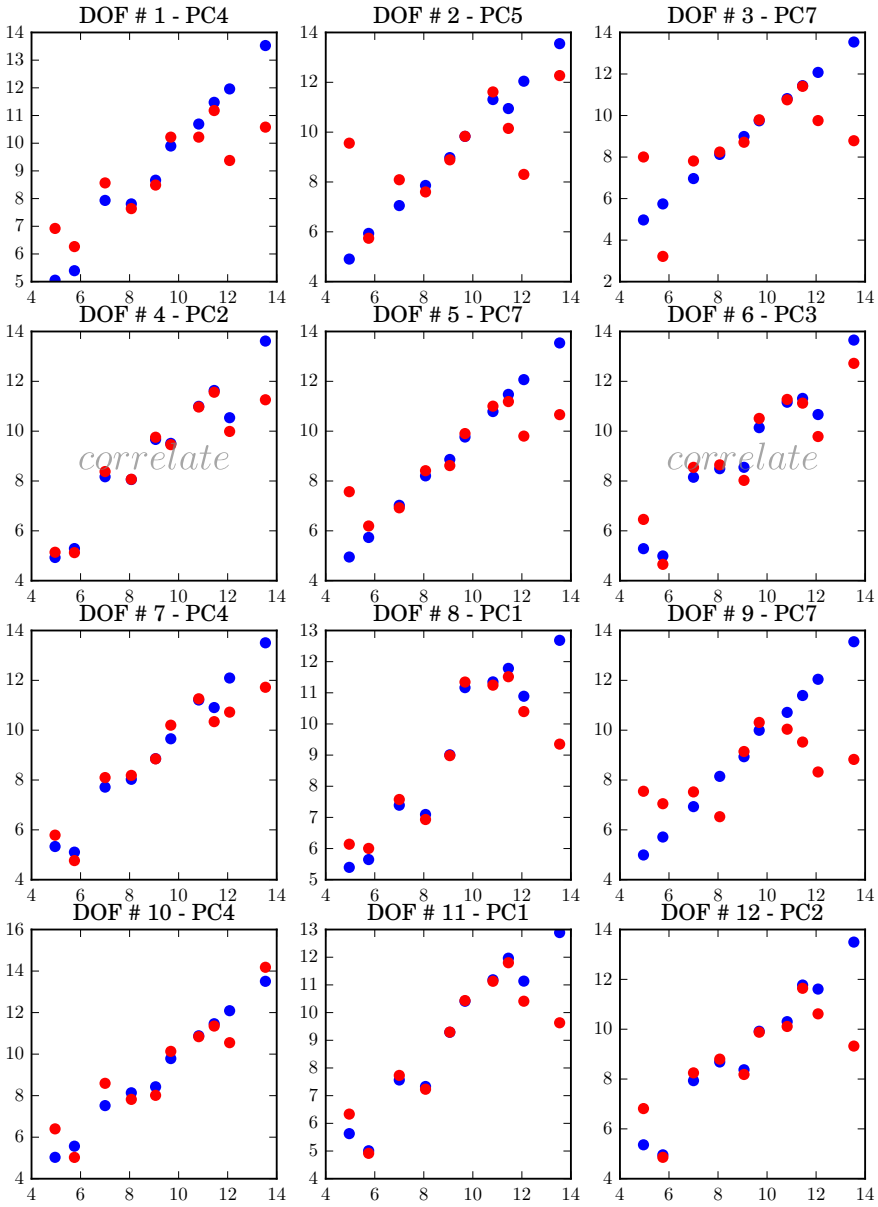

Figure H.14: Performance of PLSR for implant # 2 - 2100 - rad. DOF - impact force [N]

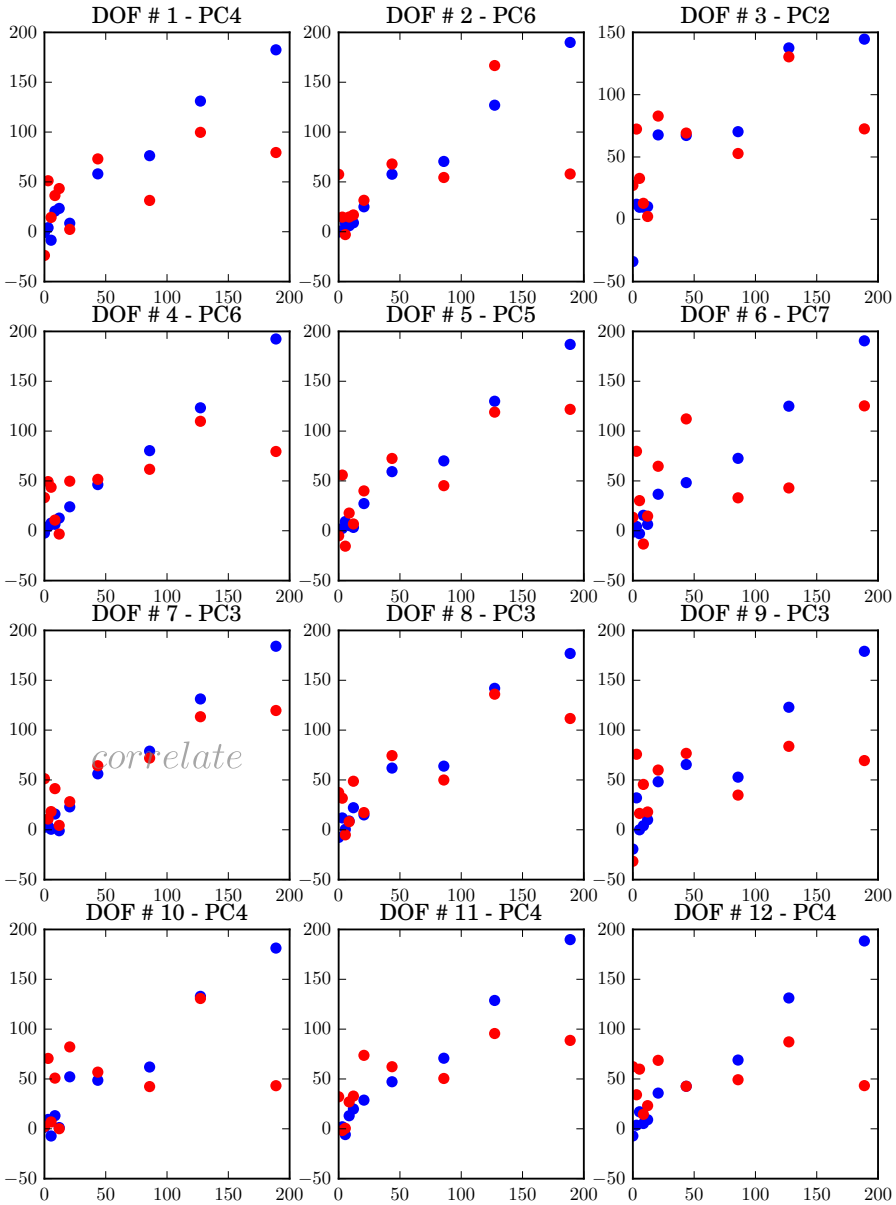

Figure H.15: Performance of PLSR for implant # 2 - 5000 - rad. DOF - polar gap distance [mm]

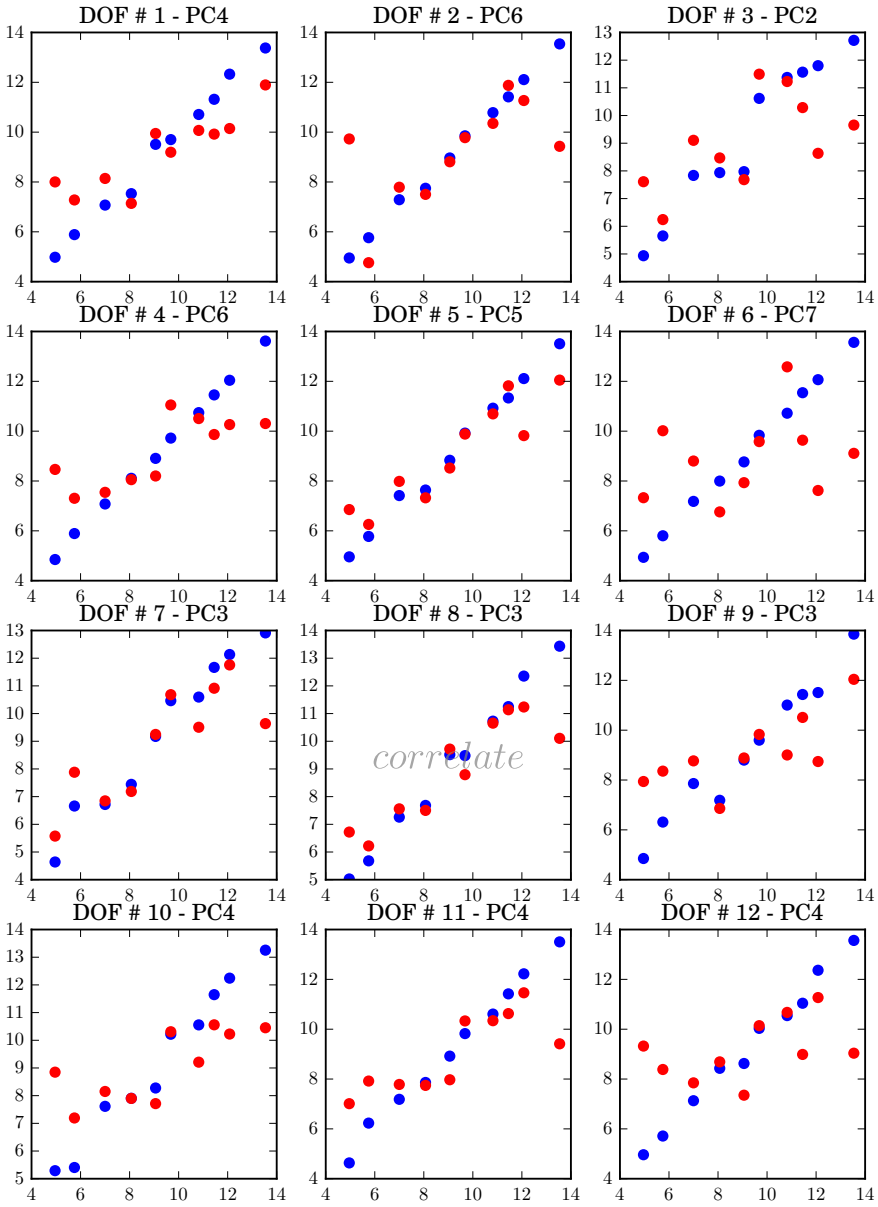

Figure H.16: Performance of PLSR for implant # 2 - 5000 - rad. DOF - impact force [N]

H.2.2 Axial DOFs

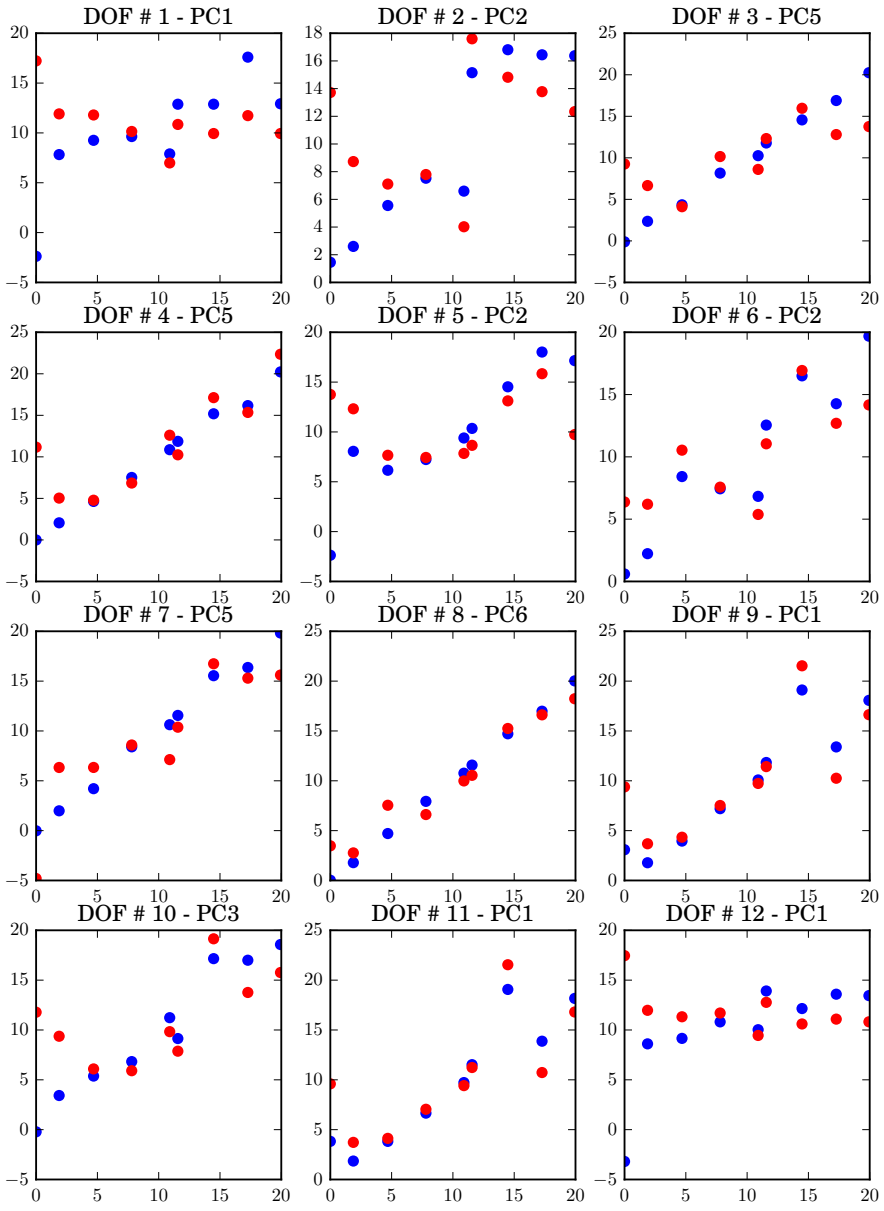

Figure H.17: Performance of PLSR for implant # 1 - 2100 - ax. DOF - polar gap distance [mm]

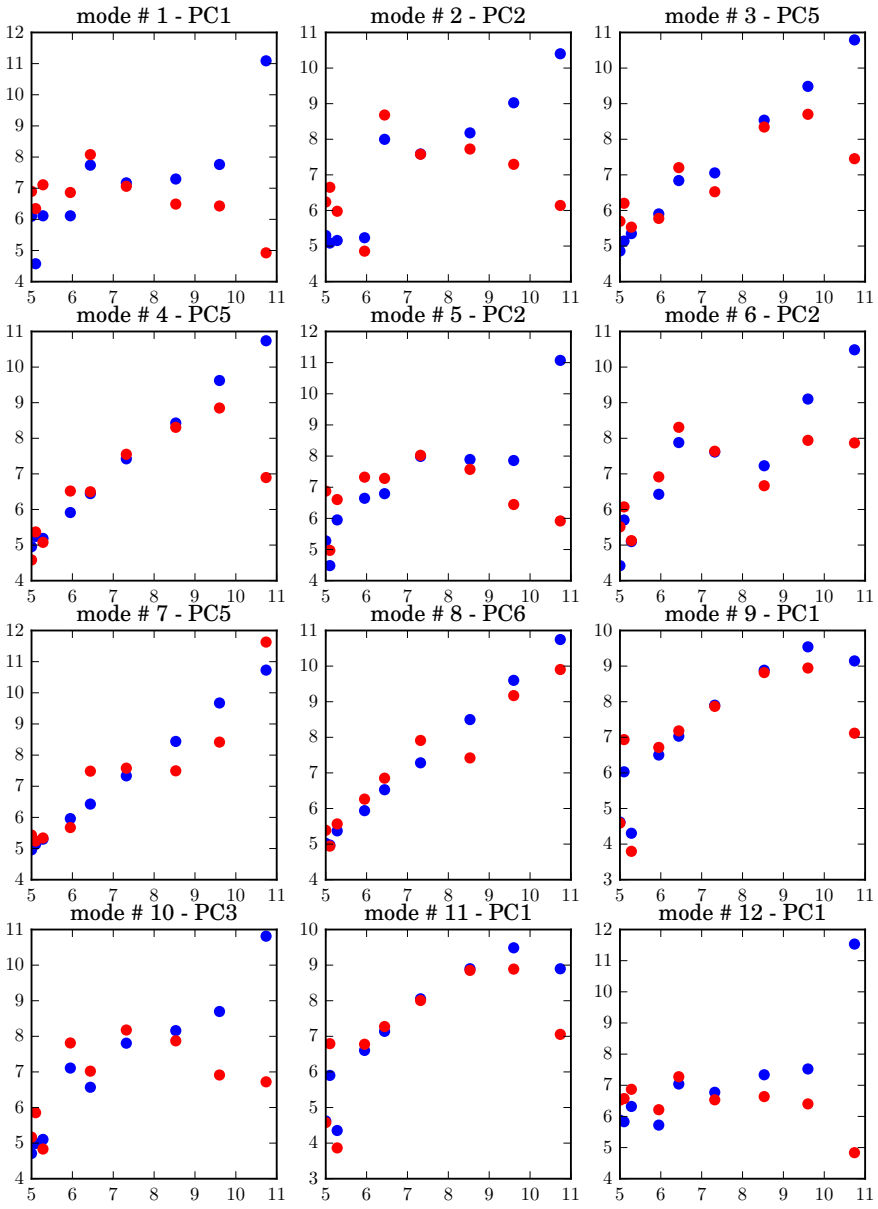

Figure H.18: Performance of PLSR for implant # 1 - 2100 - ax. DOF - impact force [N]

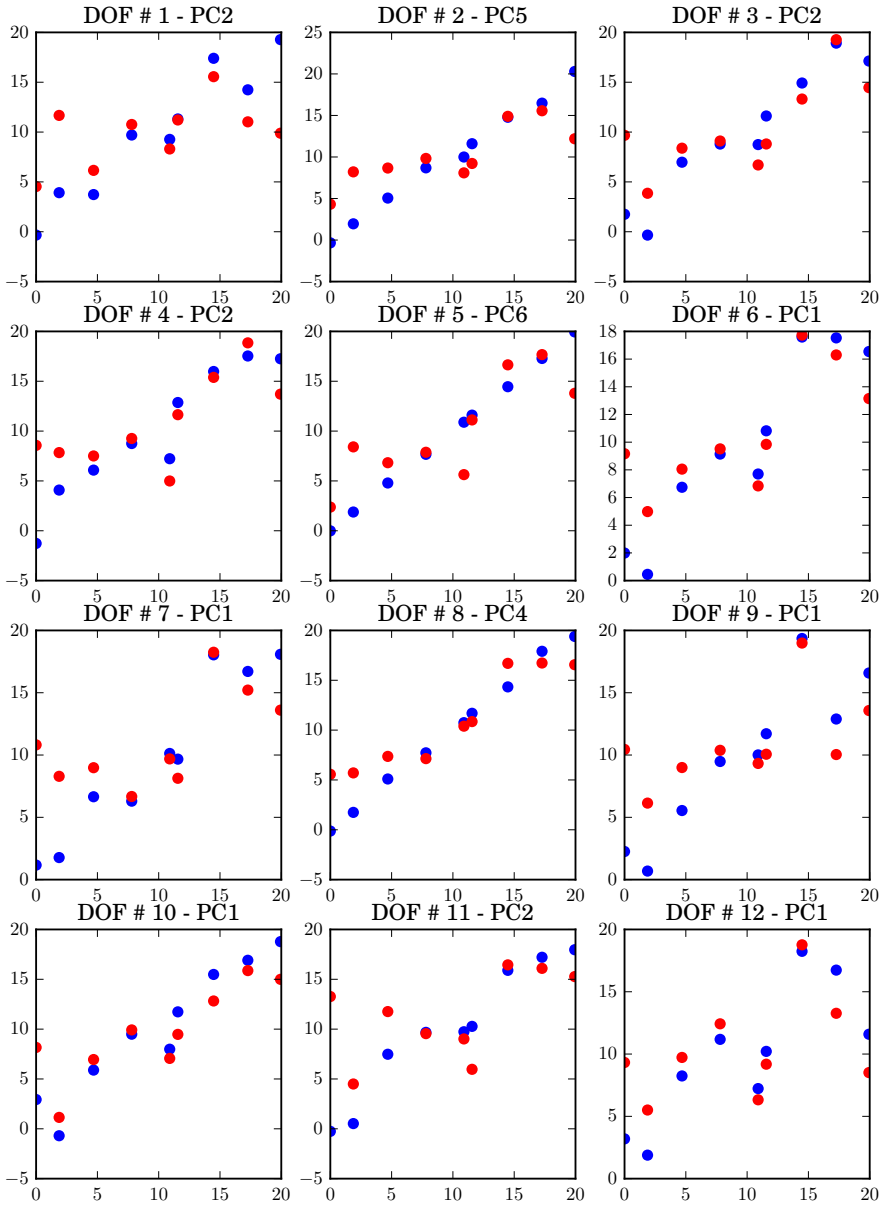

Figure H.19: Performance of PLSR for implant # 1 - 5000 - ax. DOF - polar gap distance [mm]

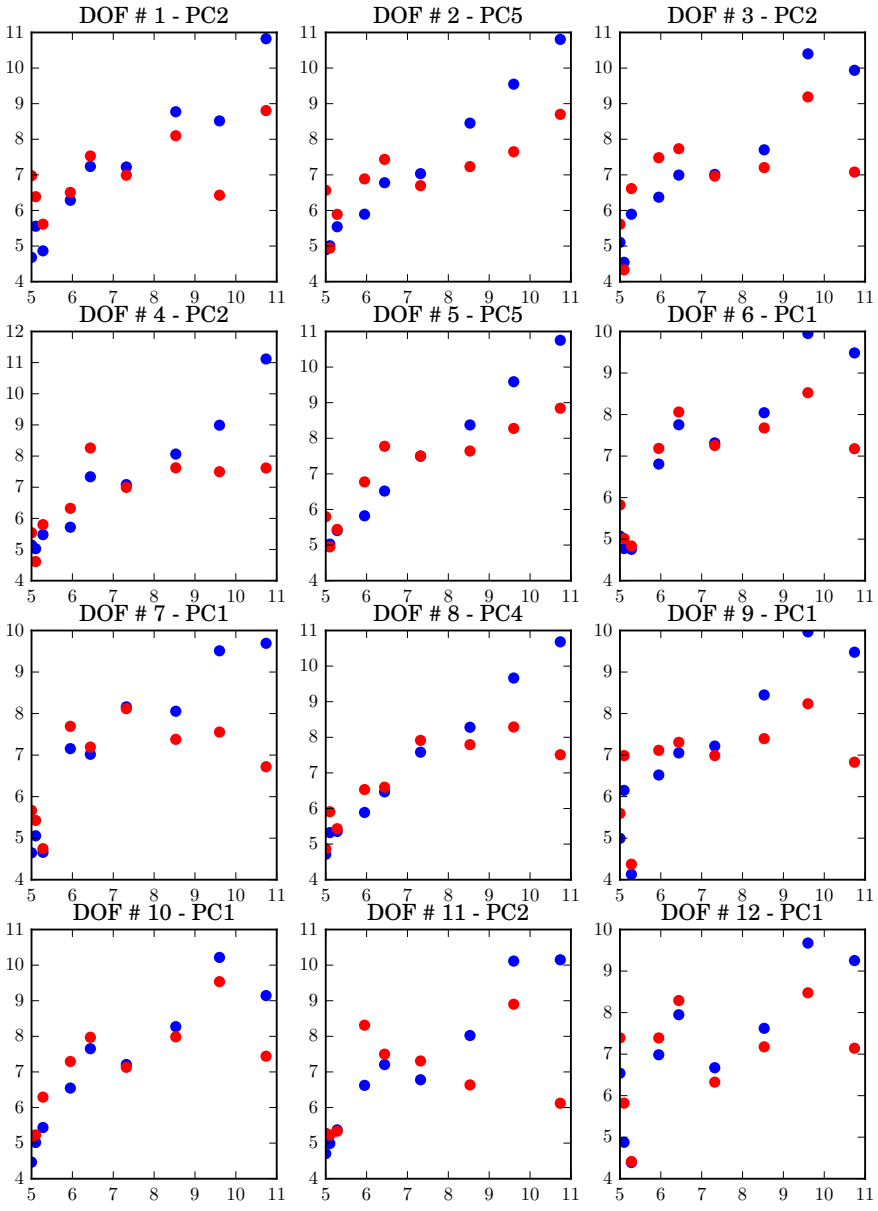

Figure H.20: Performance of PLSR for implant # 1 - 5000 - ax. DOF - impact force [N]

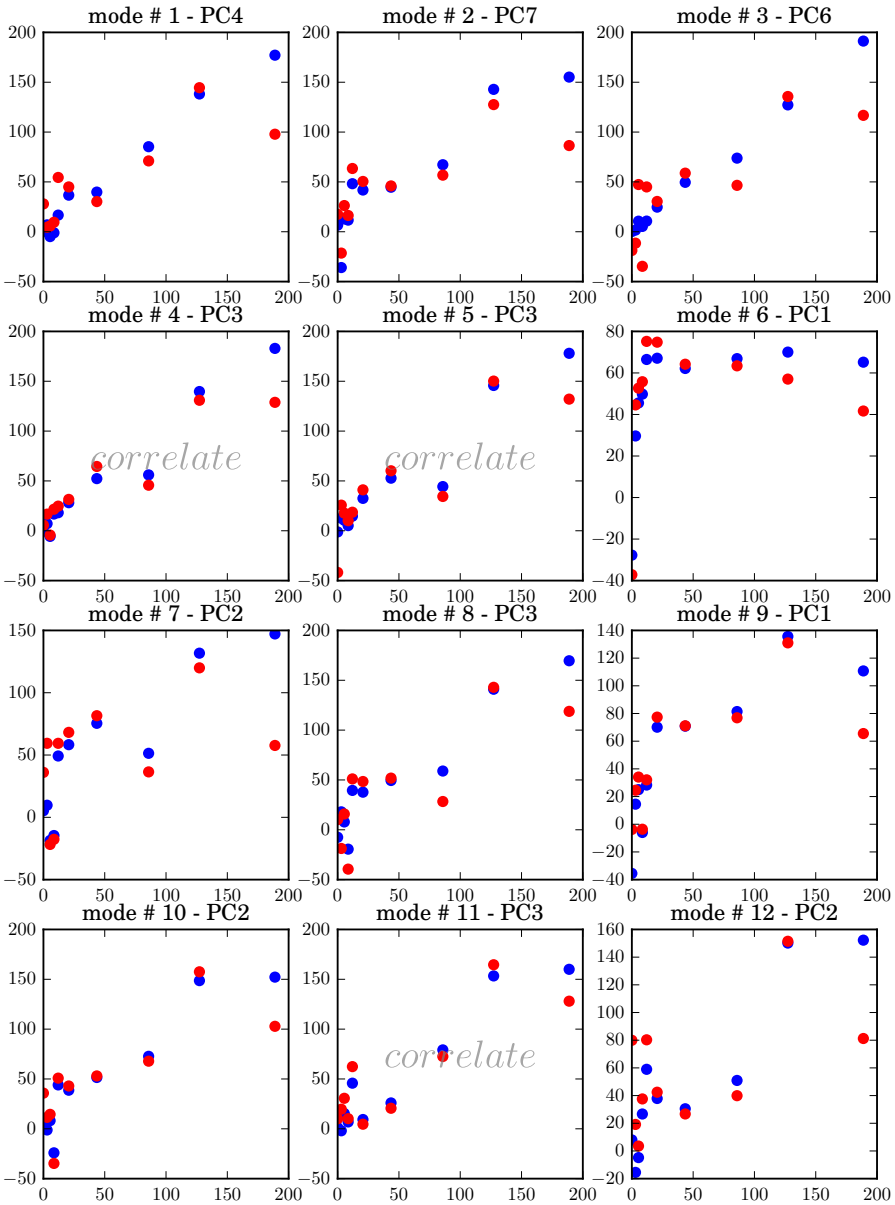

Figure H.21: Performance of PLSR for implant # 2 - 2100 - ax. DOF - polar gap distance [mm]

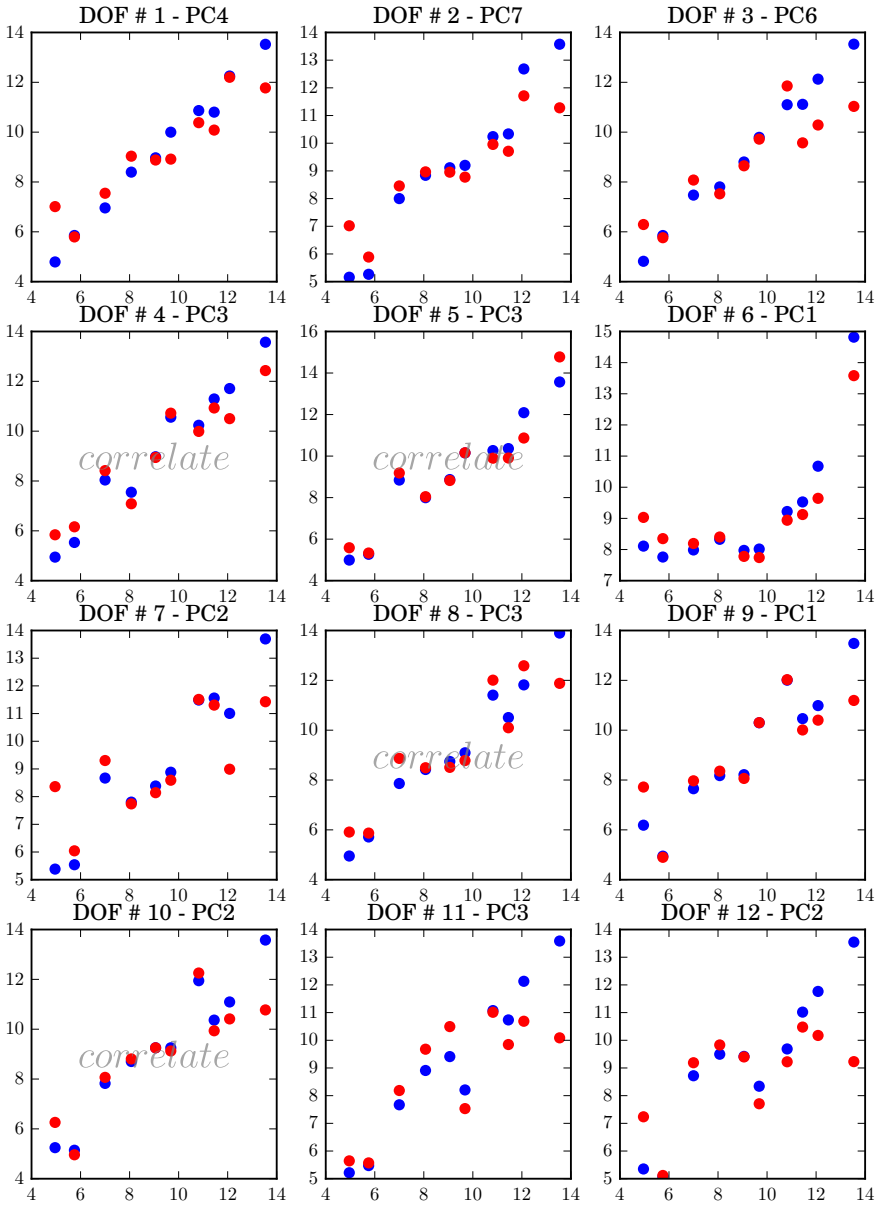

Figure H.22: Performance of PLSR for implant # 2 - 2100 - ax. DOF - impact force [N]

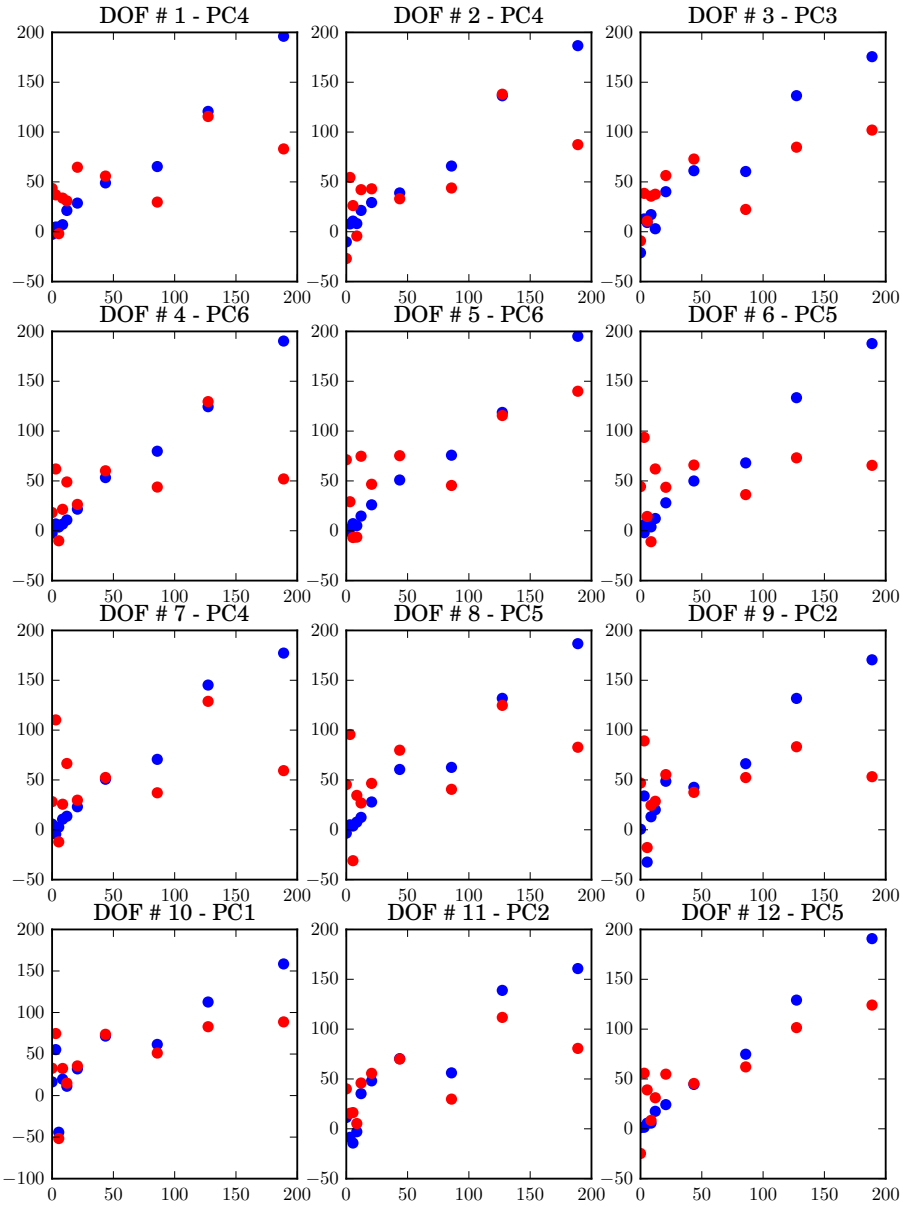

Figure H.23: Performance of PLSR for implant # 2 - 5000 - ax. DOF - polar gap distance [mm]

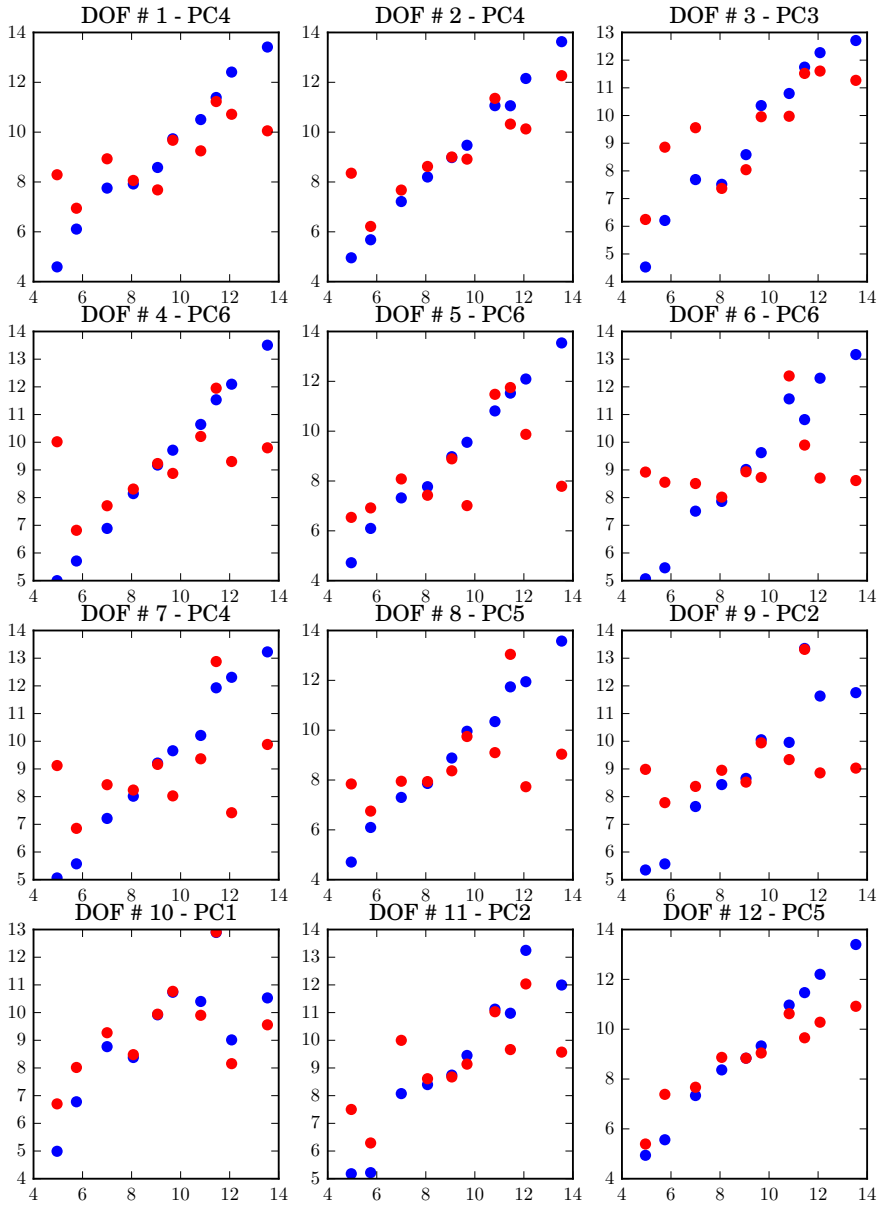

Figure H.24: Performance of PLSR for implant # 2 - 5000 - ax. DOF - impact force [N]